

Structural and Biochemical Studies of Membrane Proteins CFTR and  
GLUT1 Yield New Insights into the Molecular Basis of Cystic Fibrosis  
and Biology of Glucose Transport

A Dissertation Presented

By

Kailene Souza Simon

Submitted to the Faculty of the

University of Massachusetts Graduate School of Biomedical Sciences, Worcester  
in partial fulfillment of the requirements for the degree of

DOCTOR OF PHILOSOPHY

May 24, 2019

BIOCHEMISTRY AND MOLECULAR PHARMACOLOGY

Structural and Biochemical Studies of Membrane Proteins CFTR and Glut1 Yield  
New Insights into the Molecular Basis of Cystic Fibrosis and Biology of  
Glucose Transport

A Dissertation Presented

By

KAILENE SOUZA SIMON

This work was undertaken in the Graduate School of Biomedical Sciences  
Biochemistry and Molecular Pharmacology

Under the mentorship of

---

Gregory D. Hurlbut, Ph.D., Thesis Advisor

---

Anthony Carruthers, Ph.D., Thesis Co-Advisor

---

Reid Gilmore, Ph.D., Member of Committee

---

Brian Kelch, Ph.D., Member of Committee

---

Jill Zitzewitz, Ph.D., Member of Committee

---

Nael McCarty, Ph.D., External Member of Committee

---

Celia Schiffer, Ph.D., Chair of Committee

---

Mary Ellen Lane, Ph.D.,  
Dean of the Graduate School of Biomedical Sciences

May 24, 2019

## DEDICATION

For Bennett and Emerson, who were my reasons for starting this journey...  
and for Andrew, whose constant support was the reason I finished.

## ACKNOWLEDGMENTS

Six years ago, I made the decision to return to school for my doctorate in biochemistry. And six years ago, with a husband pursuing his own degree, a one-year old son, and a daughter on the way, I realized how much love and support I am surrounded by. Though arriving at this point was not always easy, and the path was far from straight, the overwhelming encouragement I have received and the continued willingness of so many to make this possible has been truly humbling.

I would not have been able to undertake nor complete this doctoral degree without the unwavering support of Dr. Anthony Carruthers. He, along with Dr. Kendall Knight and Dr. Seng Cheng, helped me to lay the groundwork for this unique arrangement. I will forever be grateful for this opportunity and for their willingness to work with me to make it happen. Perhaps most importantly, I thank them sincerely for believing that a 34 year-old woman in her third trimester of pregnancy was a worthwhile educational investment. Their decision to support me - when others before them had not – has changed my life immeasurably.

I owe a debt of gratitude to my mentor, Dr. Gregory Hurlbut, for welcoming me into his lab without hesitation and for his steadfast support ever since. I am sincerely appreciative of the opportunity to have embarked on this journey with him and the stellar team of scientists he has assembled, and for his insistence to hold my work to a high standard. Lastly, I thank him for the trust he placed in me

to see his scientific vision through and for the freedom he provided to create my own. I am a better scientist and person for having worked with him.

I would like to thank my fellow members of the Hurlbut lab, both past and present, who have been so consistently helpful (and wonderfully sympathetic toward my exhausting schedule), and have made the last four and a half years truly great. To Robin Ziegler, Dr. Stefan Kaczmarek, Steve Altmann, Scott Bercury, Dr. Brendan Hilbert, Dr. Rod Moreland, Dr. Devin Wolfe, Kristin Taylor, Jeff Bajko, Qiuming Chu, Mei Duguid, Joe Foley and Aliza Majewski, thank you all sincerely for helping me navigate my journey. To Dr. Ronald Scheule, whose enthusiasm for my educational pursuits helped me get through the first two years of school, thank you for providing a bit of “academia” to my life. And to my colleagues in Waltham, particularly Dr. Michael Kothe, Dr. Joseph Batchelor and Dr. David Stepp, thank you for your willingness to be my first “rotation lab” and to spend countless hours contributing to a project that was not in your job description. My sincerest thanks to all of my colleagues at Sanofi, not only for their contributions to this thesis, but also, and most importantly, for their friendship. I could not have survived this without them.

Thank you to my Qualifying Exam Committee, Thesis Research Advisory Committee and Dissertation Exam Committee members: Dr. Reid Gilmore, Dr. Celia Schiffer, Dr. Brian Kelch, Dr. Jill Zitzewitz, Dr. Haley Melikian and Dr. Nael McCarty. I truly appreciate their willingness to take part in my somewhat unconventional graduate school experience and their patience while I figured it

all out. I have learned a great deal from each of them about how to think more critically, more independently, more like a scientist.

Much of what I accomplished in this body of work could not have happened without the patience, guidance and true kindness of Dr. Gregory Hendricks, Dr. Lara Strittmatter, Dr. Chen Xu and the rest of the UMass Electron Microscopy facilities. I did not start this degree as a structural biologist, but have evolved in that direction, perhaps accidentally, but certainly due in large part to their involvement in it.

When I think about the experiences I have been afforded over the last few years and the benefits of my unconventional approach, the opportunity to collaborate with the Dafforn Lab at the University of Birmingham is among my most cherished. I sincerely thank Dr. Timothy Dafforn and the entire SMALP community for being my surrogate academic lab and for inviting me to be part of a fabulous community of engaged, collaborative scientists who represent the best of what the structural biology field has to offer. I am especially grateful for having met Dr. Naomi Pollock, who has been by my side, either in person or in spirit, for the past three years, and has never questioned my sanity, even as we worked in the lab until the sun came up, which may have happened once or twice. I have learned so much working with her and am so thankful for our relationship, both professional and personal, and for her amazing ability to know when I needed advice, support, or just someone to check in on me; somehow

she always knew. I look forward to many more years of great collaboration and great friendship with her.

Finally, thank you to my family and friends for the immense support – emotional, moral, physical, scientific, or otherwise. I am remarkably lucky to have you all in my life and in my children's lives; constantly providing the village it took for this thesis to become a reality. I specifically want to thank Dr. Claire Davies and Dr. Richard Gregory, colleagues who were friends that have become family. To Claire, thank you for 17 years of friendship and for providing inspiration (perhaps unknowingly) on how to succeed as a woman in science without compromising your success as a mother. You have accomplished a great deal professionally, while never losing sight of your priorities, and have exhibited such grace in the process. And to Rick, thank you for hiring me 13 years ago and sharing with me your love of science. Joining your lab represented a turning point in my career and perhaps one of the best professional decisions I have ever made. Thank you for everything you have done to support me, including offer to mentor me through a PhD. Although the timing perhaps wasn't right for the PhD, you saw something in my abilities that I had not yet seen myself.

Most importantly, thank you sincerely to my family. My decision to return to school was a family affair from the very beginning, made only possible and at all feasible because of their unflinching willingness to help Andrew and me navigate raising a family while both pursuing doctorates. To say we would not

have accomplished this without their love and support is a vast understatement. So to my parents, Stephen and Patricia, and to my in-laws, Anne and Kevin, thank you for helping us in all ways possible so that we could both 'have it all.' To my siblings, Stevie, Christopher and Ashley, your friendship and constant encouragement have meant more to me than you know. I am so fortunate to have the three of you, and now Genna, in my life.

Ashley, thank you for your beautiful contributions to this thesis, and for bringing my work to life through your artistic talent. I have loved collaborating with you on this.

To my amazing children, Bennett and Emerson, who have only ever known a mother who worked much more than she would have liked, thank you for your patience with me while I pursued this degree, and for the daily reminders that you are the best thing that ever happened to me.

And finally, thank you to my husband, Andrew. Thank you for always believing in me, even when I didn't believe in myself. Thank you for instilling a love of science in our children, and for helping me build this life full of chaos, laughter, and love. Thank you for being my partner in everything that matters in this world.



## ABSTRACT

Integral membrane proteins (IMPs) assume critical roles in cell biology and are key targets for drug discovery. Given their involvement in a wide range of diseases, the structural and functional characterization of IMPs are of significant importance. However, this remains notoriously challenging due to the difficulties of stably purifying membrane-bound, hydrophobic proteins. Compounding this, many diseases are caused by IMP mutations that further decrease their stability. One such example is cystic fibrosis (CF), which is caused by misfolding or dysfunction of the epithelial cell chloride channel cystic fibrosis transmembrane conductance regulator (CFTR). Roughly 70% of CF patients world-wide harbor the  $\Delta F508$ -CFTR mutation, which interrupts CFTR's folding, maturation, trafficking and function. No existing treatment sufficiently addresses the consequences of  $\Delta F508$ , and the substantial instability that results from this mutation limits our ability to study  $\Delta F508$ -CFTR in search of better treatments. To that end, my colleagues at Sanofi generated homology models of full-length wild-type and  $\Delta F508$ -CFTR +/- second-site suppressor mutations (SSSMs) V510D and R1070W, and performed molecular dynamics (MD) simulations for each model. Using information obtained from this analysis, I tested several hypotheses on the mechanism by which  $\Delta F508$  destabilizes full-length CFTR and how SSSMs suppress this effect. Leveraging studies of the purified NBD1 subdomain and of full-length CFTR in a cellular context, I confirmed the prediction of a key salt-bridge interaction between V510D and K564 important to second-site suppression. Furthermore, I identified a novel

class of SSSMs that support a key prediction from these analyses: that helical unraveling of TM10, within CFTR's second transmembrane domain, is an important contributor to  $\Delta F508$ -induced instability. In addition, I developed a detergent-free CFTR purification method using styrene-maleic acid (SMA) copolymer to extract the channel directly from its cell membrane along with the surrounding lipid content. The resulting particles were stable, monodisperse discs containing a single molecule of highly-purified CFTR. With this material, I optimized grid preparation techniques and carried out cryo-EM structural analysis of WT-hCFTR which resulted in 2D particle class averages which were consistent with an ABC transporter shape characteristic of CFTR, and a preliminary 3D reconstruction. This result establishes a foundation for future characterization of  $\Delta F508$ -CFTR in its native state. I have also applied this SMA-based purification method to the facilitated glucose transporter GLUT1 (SLC2A1). SLC2A1 mutations contribute to a rare and developmentally debilitating disease called GLUT1-deficiency syndrome. Using SMA, I successfully extracted GLUT1 in its native state. With the application of this method, I was able to purify endogenous GLUT1 from erythrocytes, in complex with several associated proteins as well as the surrounding lipids, in its monomeric, dimeric and tetrameric forms without the use of cross-linking or chimeric mutations. These results point to the potential for studying isolated IMPs without the use of destabilizing detergents and thereby offer a pathway to analysis of wild-type and mutant membrane protein structure, function and pharmacodynamics.

## TABLE OF CONTENTS

DEDICATION .....	iii
ACKNOWLEDGMENTS .....	iv
ABSTRACT .....	ix
TABLE OF CONTENTS .....	xi
LIST OF TABLES .....	xv
LIST OF FIGURES .....	xvi
LIST OF COPYRIGHTED MATERIALS .....	xxi
LIST OF ABBREVIATIONS .....	xxii
CHAPTER I: INTRODUCTION .....	1
1.1    Membrane proteins in human disease .....	1
1.1.1    The challenge of membrane protein characterization .....	3
1.1.2    Cryo-Electron Microscopy and the “resolution revolution” .....	7
1.2    Cystic Fibrosis Transmembrane Conductance Regulator .....	10
1.2.1    Structure, function and clinical relevance .....	10
1.2.2    Structural determination of CFTR .....	14
1.2.3    Cystic Fibrosis .....	22
1.3    GLUT1 .....	38
1.3.1    Function and clinical relevance .....	38
1.3.2    Structural determination .....	43
1.3.3    Evidence of GLUT1 oligomerization .....	47
1.4    Membrane Protein Nanoparticles .....	50
1.4.1    Preface .....	50
1.4.2    Abstract .....	51
1.4.3    Introduction .....	52
1.4.4    Overview of membrane mimetics .....	59
1.4.5    Latest applications of SMALPs .....	62
1.4.6    Understanding and Developing the Polymer Family .....	68
1.4.7    Perspectives .....	73

1.5	Scope of Thesis .....	76
CHAPTER II: DETERMINING THE MOLECULAR MECHANISM OF SUPPRESSOR MUTATION V510D AND THE CONTRIBUTION OF HELICAL UNRAVELING TO THE $\Delta$ F508-CFTR DEFECT.....		
2.1	Preface.....	78
2.2	Abstract.....	79
2.3	Introduction .....	80
2.4	Results .....	84
2.4.1	CFTR homology model and molecular dynamics simulation .....	84
2.4.2	The role of K564 on V510D-mediated suppression on the $\Delta$ F508 trafficking defect.....	99
2.4.3	The impact of V510D on the structure and stability of NBD1 .....	105
2.4.4	Evaluation of Helical Unraveling .....	114
2.5	Discussion.....	123
2.5.1	Presence and position of residue K564 is key to V510D suppression of the $\Delta$ F508 trafficking defect .....	127
2.5.2	The occurrence and subsequent rescue of TMD2 helical unraveling in $\Delta$ F508-CFTR.....	129
2.6	Materials and Methods .....	135
	Homology Modeling .....	135
	Molecular Dynamics Simulations .....	135
	Construct generation and expression of full-length hCFTR mutants.....	137
	NBD1 Analysis .....	139
CHAPTER III: STYRENE-MALEIC ACID COPOLYMER EXTRACTION: A BREAKTHROUGH IN CFTR LIPID PARTICLE PURIFICATION AND STABILIZATION.....		
3.1	Preface.....	144
3.2	Abstract.....	145
3.3	Introduction .....	147
3.4	Results .....	153
3.4.1	Expression of CFTR.....	155

3.4.2	Encapsulation and purification of CFTR using Styrene Maleic Acid Co-Polymer (SMA).....	157
3.4.3	Evaluation of alternative polymers for CFTR purification .....	170
3.4.4	Lipid evaluation of CFTR-SMALPs .....	176
3.5	DISCUSSION.....	186
3.6	Materials and Methods .....	192
	Protein expression and purification .....	192
	Polymer preparation.....	198
	CFTR Expression Cell Lines .....	199
	Electron Microscopy.....	201
CHAPTER IV: CAPTURING THE PHYSIOLOGICAL COMPLEXES OF GLUT1 FROM RBCS: SMALP SOLUBILIZATION.....		202
4.1	Preface.....	202
4.2	Abstract .....	203
4.3	Introduction .....	205
4.4	Results .....	215
4.4.1	SMA solubilization and purification of GLUT1 oligomers from Expi293F™ expression cells.....	215
4.4.2	GLUT1 oligomerization detection using Native PAGE .....	219
4.4.3	SMA solubilization and purification of untagged GLUT1 oligomers from erythrocyte membranes .....	224
4.5	Discussion.....	234
4.6	Materials and Methods .....	236
	Protein expression and purification .....	236
	Erythrocyte membrane complex purification .....	240
	Microscopy .....	244
	Cytoskeleton dynamics .....	245
CHAPTER V: DISCUSSION.....		246
APPENDIX I .....		255
6.1	Appendix I .....	255

6.2	CFTR Cryo-EM .....	255
6.2.1	Reduction of particle heterogeneity with stabilizing modifications .....	257
6.2.2	Optimization of cryo-EM grid preparation for CFTR-SMALP structural analysis .....	261
6.2.3	Current 2D and 3D cryo-EM models of hCFTR-SMALPs show both open and closed conformations of the protein .....	267
6.3	Discussion.....	273
BIBLIOGRAPHY .....		275

## LIST OF TABLES

TABLE 1.1	CURRENT LIST OF FULL-LENGTH CFTR CRYO-EM STRUCTURES OF SUB-NANOMETER RESOLUTION. ....	21
TABLE 1.2	SELECTED ALTERNATIVE AND FUNCTIONALIZED AMPHIPATHIC POLYMERS.....	70
TABLE 2.1	RMSD VALUES BY DOMAIN FOR THE FULL-LENGTH WT-CFTR HOMOLOGY MODEL .....	87
TABLE 2.2	$\Delta$ F508/V510D-NBD1 STRUCTURE DETERMINATION/REFINEMENT STATISTICS.....	113
TABLE 3.1	SUMMARY OF THE FOUR CLASSES OF LIPIDS ANALYZED IN DETAIL FROM EXPI-293-GENERATED SAMPLES .....	178
TABLE 6.1	BINDING AFFINITIES ( $K_D$ ) OF ADP, ATP AND ATP- $\gamma$ -S TO WT-NBD1	258

## LIST OF FIGURES

FIGURE 1.1	TOTAL ACCUMULATED (TOP) OR PER-YEAR (BOTTOM) NUMBER OF UNIQUE MEMBRANE PROTEIN STRUCTURES DEPOSITED TO THE PROTEIN DATA BANK (PDB).....	6
FIGURE 1.2	TOPOLOGY OF CFTR.....	12
FIGURE 1.3	CRYO-EM STRUCTURES OF HUMAN CFTR IN THE OPEN AND CLOSED CONFORMATIONS. ....	13
FIGURE 1.4	CLASSIFICATION OF CFTR MUTATIONS AND CORRESPONDING THERAPEUTIC STRATEGIES .....	27
FIGURE 1.5	CRYSTAL STRUCTURE OF GLUT1.....	46
FIGURE 1.6	POLYMERIZATION OF STYRENE AND MALEIC ANHYDRIDE.....	54
FIGURE 1.7	A SCHEMATIC REPRESENTATION OF THE PREPARATION OF SMALP MP USING SMA .....	55
FIGURE 1.8	GROWTH OF PUBLICATIONS DESCRIBING MEMBRANE PROTEINS PURIFIED USING SMALP TECHNOLOGY AND ITS ASSOCIATED DERIVATIVES FROM 2009 TO 2018 (YEAR-TO-DATE).....	58
FIGURE 1.9	CRYO-EM STRUCTURES OF TWO PROTEINS IN SMALPS .....	65
FIGURE 2.1	CFTR HOMOLOGY MODELS OF FULL-LENGTH WT AND $\Delta F508$ CFTR HIGHLIGHT DIFFERENCES AT V510 LOOP.....	85
FIGURE 2.2	STRUCTURAL COMPARISON AND CORRESPONDING RMSD VALUES OF ICL AND NBD REGIONS FOR THE HUMAN WT-CFTR HOMOLOGY MODEL AND THE PUBLISHED CRYO-EM STRUCTURE OF HCFTR.....	89
FIGURE 2.3	CFTR MD SIMULATION PREPARATIONS. ....	90
FIGURE 2.4	QUALITY CONTROL ANALYSIS FOR MOLECULAR DYNAMICS SIMULATIONS OF WT, $\Delta F508$ , $\Delta F508/V510D$ AND $\Delta F508/R1070W$ CFTR.....	91
FIGURE 2.5	CFTR RESIDUES OF INTEREST FOR MD SIMULATION. ....	92
FIGURE 2.6	% OCCURRENCE OF SECONDARY STRUCTURE CHANGES WAS CONSISTENT WITH REPORTED STABILITY DATA FOR CFTR VARIANTS $\Delta F508$ , $\Delta F508+V510D$ AND $\Delta F508 + R1070W$ . ....	93
FIGURE 2.7	SALT BRIDGE INTERACTIONS WITH V510D.....	95



FIGURE 2.8	MOLECULAR DYNAMICS SIMULATIONS OF WT, $\Delta$ F508, $\Delta$ F508/V510D AND $\Delta$ F508/R1070W SHOW EVIDENCE OF HELICAL UNRAVELING .....	97
FIGURE 2.9	SUPERPOSITION OF TM10 ALPHA HELICAL REGION TAKEN FROM THE FIRST AND LAST FRAME OF MD SIMULATIONS .....	98
FIGURE 2.10	PRESENCE AND POSITION OF RESIDUE K564 IS KEY TO V510D SUPPRESSION OF THE $\Delta$ F508 TRAFFICKING DEFECT.....	101
FIGURE 2.11	ELECTROPHYSIOLOGICAL ANALYSES OF FRT CELLS EXPRESSING $\Delta$ F508-CONTAINING CFTR MUTANTS +/- V510D AND K564A .	105
FIGURE 2.12	REMOVAL OF K564 DECREASES NBD1 THERMAL STABILITY IN THE PRESENCE AND ABSENCE OF V510D AS INDICATED BY DSLS AND NANO-DSF THERMAL SHIFT ASSAYS.....	109
FIGURE 2.14	PRELIMINARY WESTERN BLOT ANALYSIS OF HELICAL STABILIZATION MUTATIONS ALONG TMS 10 AND 11 .....	115
FIGURE 2.15	WESTERN BLOT AND C/B RATIO ANALYSIS OF HELICAL STABILIZATION MUTATIONS ALONG TMS 10 AND 11 .....	116
FIGURE 2.16	NBD1 STABILIZATION IS CRITICAL FOR P1050R RESCUE OF ICL-4 STABILIZED $\Delta$ F508.....	119
FIGURE 2.17	NBD1 STABILIZATION AND K564/V510D INTERACTIONS ARE CRITICAL FOR P1050R RESCUE OF $\Delta$ F508 .....	121
FIGURE 2.18	THE ROLE OF NBD1 STABILIZATION ON $\Delta$ F508-CFTR RESCUE DOES NOT REQUIRE DUAL CORRECTION BY V510D WHEN P1050R HELICAL STABILIZATION IS ADDED.....	122
FIGURE 3.1	TEM ANALYSIS OF DETERGENT-PURIFIED HCFTR AT LOWER AND HIGHER MAGNIFICATIONS .....	154
FIGURE 3.2	COMPARISON OF HCFTR EXPRESSION LEVELS IN SF21 INSECT CELLS AND EXPI293 HEK CELLS .....	156
FIGURE 3.3	EXPERIMENTAL PARAMETERS TO EVALUATE CFTR PRODUCTION IN EXPI293 HEK CELLS AND SF21INSECT CELLS .....	157
FIGURE 3.4	SDS-PAGE ANALYSIS OF SIZE EXCLUSION CHROMATOGRAPHY COLUMN ELUTION FRACTIONS TO EVALUATE HEK CELL AND SF21 CELL CFTR SOLUBILIZATION USING SMA. OF CONDITIONS. ....	159

FIGURE 3.5	TEM MICROGRAPHS OF CFTR AND SAV1866 SMALPS .....	159
FIGURE 3.6	CARTOON SCHEMATIC OF FULL-LENGTH HCFTR IN A SMALP .....	160
FIGURE 3.7	SCHEMATIC OVERVIEW OF THE PROTOCOL FOR SMA PURIFICATION OF CFTR FROM MAMMALIAN CELL MEMBRANES.....	161
FIGURE 3.8	SDS-PAGE SILVER STAIN & WESTERN BLOT OF ELUTED CFTR...	162
FIGURE 3.9	SDS-PAGE SILVER STAIN AND WESTERN BLOT OF SEC PURIFIED CFTR .....	163
FIGURE 3.10	SEC PURIFICATION OF DETERGENT-PURIFIED CFTR .....	164
FIGURE 3.11	EM NEGATIVE STAINING OF PURIFIED CFTR IN SMALPS OR DETERGENT MICELLES .....	166
FIGURE 3.12	NATIVE PAGE ANALYSIS OF CFTR-SMALPS .....	168
FIGURE 3.13	MASS SPECTRAL ANALYSIS OF SEC-PURIFIED CFTR-SMALPS SHOWS HIGH-PURITY CFTR PROTEIN .....	169
FIGURE 3.14	INITIAL ANALYSIS OF CFTR SOLUBILIZATION USING DIBMA.....	172
FIGURE 3.15	IMIDAZOLE ELUTION FRACTIONS FOR CFTR-DIBMALPS PRIOR TO PHOSPHORYLATION TREATMENT WITH PKA .....	173
FIGURE 3.16	FRACTIONAL ANALYSIS OF SIZE-EXCLUSION CHROMATOGRAPHY OF PKA-TREATED CFTR-DIBMALPS .....	174
FIGURE 3.17	LIPID PROFILES OF EXPI293-SMALPS .....	180
FIGURE 3.18	LIPID PROFILES COMPARING THE CONTENT OF GFP- TRANSFECTED CFSME <sub>0</sub> - SMALPS, CFSME <sub>0</sub> -TOTAL MEMBRANE, CFTR- SMALPS AND CFTR-CONTAINING CFSME <sub>0</sub> - MEMBRANES.....	183
FIGURE 3.19	COMPARISON OF LIPIDOMICS DATA FOR TWO CELL LINES, CFSME <sub>0</sub> - LUNG CELLS AND EXPI293 EXPRESSION CELLS.....	185
FIGURE 4.1	THE MORPHOLOGY OF RESEALED RED BLOOD CELL GHOSTS IS IMPACTED BY THE PRESENCE OR ABSENCE OF ATP .....	212
FIGURE 4.2	OVERVIEW OF THE PROTOCOL FOR SMA PURIFICATION OF HGLUT1 FROM EXPI293 CELL MEMBRANES.....	215
FIGURE 4.3	CARTOON SCHEMATIC OF MONOMERIC GLUT1 IN A SMALP .....	216
FIGURE 4.4	SEC CHROMATOGRAM OF HGLUT1-SMALP PURIFICATION AND FRACTIONATION, SDS-PAGE SILVER STAIN GEL AND WESTERN BLOT OF SEC PURIFIED GLUT1 .....	218

FIGURE 4.5 NATIVE PAGE SILVER STAIN (TOP) AND WESTERN BLOT (BOTTOM) OF SEC PURIFIED GLUT1 FRACTIONS .....	220
FIGURE 4.6 TEM ANALYSIS OF HGLUT1-SMALPS .....	221
FIGURE 4.7 QUANTITATIVE COMPARISON OF THE TOP TEN MOST PREVALENT PROTEINS IN GLUT1-SMALP FRACTIONS .....	222
FIGURE 4.8 NATIVE PAGE SILVER STAIN (TOP) AND WESTERN BLOT (BOTTOM) OF SEC PURIFIED GLUT1 FRACTIONS .....	223
FIGURE 4.9 RBC MEMBRANE PELLETS BEFORE AND AFTER SMA SOLUBILIZATION .....	225
FIGURE 4.10 UNSEALED RBC GHOSTS UNTREATED (LEFT) AND TREATED WITH 2.5% SMA SOLUTION FOR 30 SECONDS .....	227
FIGURE 4.11 AMP-CONTAINING RESEALED RBC GHOSTS IN THE ECHINOCYTE MORPHOLOGY, UNTREATED (LEFT) AND TREATED WITH 2.5% SMA SOLUTION FOR 30 SECONDS .....	227
FIGURE 4.12 RESEALED RBC GHOST + ATP TREATED WITH 1% SMA FOR 30 SECOND (LEFT) AND TREATED WITH 1% TRITON-X FOR 30 SECONDS .....	228
FIGURE 4.13 SEC TRACES SHOW POTENTIAL DIFFERENCES IN ELUTION OF RBC SMALPS AFTER TREATMENT WITH ACTIN MODULATORS .....	230
FIGURE 4.14 SMA EXTRACTION OF RBC MEMBRANE PROTEINS .....	233
FIGURE 6.1 EVALUATION OF THE IMPACT OF GLYCEROL REMOVAL ON CFTR- SMALPS USING NEGATIVE STAIN TEM ANALYSIS AND SDS-PAGE SILVER STAINING .....	256
FIGURE 6.2 COMPARISON OF AFFINITY BINDING OF ATP, ADP AND ATP- $\gamma$ -S TO NBD1 USING SURFACE PLASMON RESONANCE .....	258
FIGURE 6.3 PHOSPHORYLATION OF CFTR-SMALPS WITH PKA CATALYTIC SUBUNIT .....	260
FIGURE 6.4 INCONSISTENCIES IN GRAPHENE OXIDE GRID COATING LED TO VARIATION IN PARTICLE DISTRIBUTION .....	264
FIGURE 6.5 AGARD/CHENG GRAPHENE OXIDE COATING PROTOCOL .....	266
FIGURE 6.6 CRYO-EM MICROGRAPH IMAGES OF HCFTR-SMALPS CAPTURED USING THE TALOS ARCTICA (200 KVA) .....	267

FIGURE 6.7 2D CLASS AVERAGING OF CFTR-SMALP CRYO-EM PARTICLES AND THE RESULTING 3D MODEL .....	268
FIGURE 6.8 2D CLASS AVERAGES OF CFTR-SMALPS FROM ~3,000 NEGATIVELY STAINED TEM PARTICLES .....	269
FIGURE 6.9 2D CLASS AVERAGES FROM NEGATIVELY STAINED TEM PARTICLES OF CFTR-SMALPS WITH STABILIZING LIGAND BOUND.....	270
FIGURE 6.10 CRYO-EM CLASS-AVERAGING OF CFTR-SMALP .....	272

## LIST OF COPYRIGHTED MATERIALS

Membrane protein nanoparticles: the shape of things to come  
*Kailene S. Simon, Naomi L. Pollock, Sarah C. Lee* Biochemical Society  
Transactions Dec 2018,46(6)1495-1504; **DOI:** 10.1042/BST20180139

## LIST OF ABBREVIATIONS

2S	NBD1 stabilizing mutations F494N/Q637R
3DEM	3-dimensional electron microscopy
3S	NBD1 stabilizing mutations F494N/Q637R/F429S
$\Delta$ F508	Disease mutation of CFTR which results in cystic fibrosis
ABC	ATP-binding cassette
ACIII	Alternative Complex III
AD	Alzheimer's disease
ALS	Amyotrophic Lateral Sclerosis
Å	Angstrom
ApoA1	Apolipoprotein A-1
APols	Amphipols
ARNT	Aryl Hydrocarbon Nuclear Translocator
BRET	Bioluminescent Förster Resonance Energy Transfer
CCB	Cytochalasin B
CCD	Charge Coupled Device
CE	Cholesteryl Ester
CF	Cystic Fibrosis
CFF	Cystic Fibrosis Foundation
CFRD	CF-related diabetes
CFSME	Cystic Fibrosis Submucosal Epithelial Cells
CFTR	Cystic Fibrosis Transmembrane Conductance Regulator
CHS	Cholesteryl Hemisuccinate

CIP	Calf Intestinal Alkaline Phosphatase
cryo-EM	Cryo-Transmission Electron Microscopy
CV	Column Volumes
cyt aa3	aa3-type cytochrome c oxidase
DDD	Direct Detection Device
DDM	n-dodecyl- $\beta$ -D-maltopyranoside
DIBMA	Diisobutylene Maleic Acid
DSF	Differential scanning fluorimetry
DSLS	Differential Static Light Scattering
DTT	Dithiothreitol
E2	17 $\beta$ -estradiol
ECL	Extracellular Loop
ENaC	Epithelial Sodium Channel
ENT1	Equilibrative Nucleotide Transporter-1
Ephys	Electrophysiology
ERAD	Endoplasmic Reticulum-Associated Protein Degradation
FA-3	3 $\alpha$ -hydroxy-7 $\alpha$ ,12 $\alpha$ -di-((O- $\beta$ -D-maltosyl)-2-hydroxyethoxy)-cholane
FEV1	Forced Expiratory Volume
FPmax	Maximal current post Forskolin and CFTR potentiator addition
FRET	Forster Resonance Energy Transfer
FRT	Fisher Rat Thyroid
G1DS	GLUT1-deficiency syndrome
GLUT	Glucose Transporters
GLUT-i1	Glucose transporter-inhibitor 1

GLUT-i2	Glucose transporter-inhibitor 2
GO	Graphene Oxide
GPCR	G-protein coupled receptor
Gt	Transepithelial conductance
HDX-MS	Hydrogen Deuterium Exchange Mass Spectrometry
HRP	Horseradish Peroxidase
ICL	Intracellular Loop
IMP	Integral Membrane Protein
lo	Liquid-Ordered Phase
Isc	Transepithelial current
KTN1	Kinectin
LCP	Lipidic Cubic Phase
MCT1	Monocarboxylate Transporter 1
MD	Molecular Dynamics
MFS	Major Facilitator Superfamily
MNG-10	Decyl Maltose Neopentyl Glycol
MP	Membrane Protein
MS	Mass Spectrometry
MSP	Membrane Scaffold Protein
nanoDSF	Nano Differential Scanning Fluorimetry
NBDs	Nucleotide Binding Domains
NTM	Nontuberculous Mycobacteria
NYSBC	New York Structural Biology Center
PC	Phosphatidylcholine



PDB	Protein Data Bank
PE	Phosphatidylethanolamine
P-gp	P-glycoprotein 1
PIS	Precursor Ion Scanning
PKA	Protein Kinase A
PL	Phospholipids
PoLP	Polymer-Based Lipid Particle
POPC	1-palmitoyl-2-oleoyl-sn-glycero-3-phosphocholine
PS	Phosphatidylserine
PTM	Post-Translational Modification
R-domain	Regulatory Domain
RBCs	Red Blood Cells
RE	Regulatory Extension
RI	Regulatory Insertion
RLU	Relative Luminescence Unit
RMSD	Root-Mean-Square Deviation
SEC	Size Exclusion Chromatography
SEM	Scanning Electron Microscopy
SLC	Solute Linked Carrier
SMA	Styrene-Maleic Acid
SMALP	Styrene-Maleic Acid Lipid Particle
SMA <sub>nh</sub>	Styrene-Maleic Anhydride
SMA-QA	Styrene Maleimide Quaternary Ammonium
SMA-SH	Thiolated Styrene-Maleic Acid

SMI	Styrene Maleic Imide
SPR	Surface Plasmon Resonance
SS	Secondary Structure
SSSM	Second-Site Suppressor Mutation
Tagg	Aggregation Temperature
TEM	Transmission Electron Microscopy
TG	Triglycerides
TM	Transmembrane
T <sub>m</sub>	Melting Temperature
TMD	Transmembrane Domain
VC	Viable Cells
WT	Wild-Type

## CHAPTER I: INTRODUCTION

### 1.1 Membrane proteins in human disease

In 1958, the first crystal structure of a protein, myoglobin, was determined to a resolution of 6Å (Kendrew *et al.*, 1958). Within two years this structural model was improved to 2Å (Kendrew *et al.*, 1960). It was 25 more years before the first high-resolution structure of a membrane protein – the photosynthetic reaction center of *Rhodospseudomonas viridis* – would be solved (Deisenhofer *et al.*, 1985). In the early 1980's, the first studies to demonstrate reversible unfolding of a membrane protein were published (Huang *et al.*, 1981; London and Khorana, 1982); however, not until 1995 was this behavior quantitatively measured and reported (Booth *et al.*, 1995), 33 years after the same was accomplished with ribonuclease (Haber and Anfinsen, 1962). And while still meaningful, these landmark membrane protein (MP) experiments were all performed with thermostable, endogenously expressed and readily available bacterial proteins like photosystems (Kurusu *et al.*, 2003; Palczewski *et al.*, 2000), ATP synthases (Abrahams *et al.*, 1994; Liu *et al.*, 2004) and electron transport chain complexes (Sakai and Tsukihara, 1998; Sun *et al.*, 2014). In fact, this was true for nearly all structural and functional analysis of  $\alpha$ -helical MPs, with the occasional exception being a mammalian protein recombinantly expressed in bacteria (Palczewski *et al.*, 2000). This remained the case until 2005, when Long

*et al.* published the first eukaryotic MP structure at atomic resolution for a mammalian voltage-dependent K<sup>+</sup> channel using recombinant expression (Long *et al.*, 2005).

While this discrepancy in structural analysis between soluble and membrane-bound proteins isn't at all surprising, considering the tendency of eukaryotic proteins to be low-expressing and highly unstable, it is unfortunate for a number of reasons. MPs occupy a valuable place within the drug discovery landscape, given the extensive relationship between integral MP (IMP) dysregulation and human disease. In fact, protein folding defects are implicated in nearly all types of disease (Sanders and Myers, 2004). Often times, it is a single point mutation or incorrect molecular interaction that triggers misfolding, making them attractive candidates for pharmacological folding chaperones (Marinko *et al.*, 2019; Sanders and Myers, 2004). Accordingly, MPs are the target of nearly 70% of drugs currently approved by the FDA (Niesen *et al.*, 2017). Yet even though they hold such a significant role in human health and disease, and represent 30% of the human genome (Uhlen *et al.*, 2015), MPs only account for a small fraction of published protein structures. In fact, of the >150,000 structures deposited into the protein data bank (PDB), only 884, or 0.59%, are of membrane proteins (White, 2019).

### 1.1.1 The challenge of membrane protein characterization

Important gaps in our understanding of MP biology, especially those that relate to protein structure, can be attributed to several factors: low expression levels, limited stability when purified, prevalence of hydrophobic residues, and the need for an ordered and stabilizing environment provided by exogenous lipids or detergents, to name a few (Niesen *et al.*, 2017; Seddon *et al.*, 2004; Yang *et al.*, 2014). For these, one key limitation underlies all: MPs are defined by their endogenous location within a lipid bilayer, and have evolved to exist there for a purpose and occupy certain roles accordingly (Bigay and Antonny, 2012; Hirama *et al.*, 2017). It therefore stands to reason that removing MPs from their preferred context can change their intrinsic properties (i.e., structure and function), as MPs often rely on the lateral pressure and proximity of certain phospholipids for support (Bayburt and Sligar, 2010; Niesen *et al.*, 2017). Proteins adopt conformations that result in local energy minima in relation to their surrounding environment. Consequently, removing MPs from their normal membrane context can have deleterious effects, altering their kinetic and structural characteristics.

With that said, there are reasonable membrane mimetics that can be employed for the purpose of solubilizing MPs; however, it is necessary to consider the impact these may have on the protein of interest. The current methods for purifying full-length MPs into detergent micelles often result in

suboptimal yields of functional protein with limited stability (Hildebrandt *et al.*, 2017; Yang *et al.*, 2014). In addition, detergent molecules such as n-Dodecyl  $\beta$ -D-maltoside (DDM), a standard for MP purification, often interfere with biophysical characterization.

Moreover, if we hope to fully understand the endogenous characteristics of a membrane protein, it behooves us to consider the lipid bilayer that accompanies it. Just as there exists a canonical understanding that protein structure and function are inextricably linked, the same holds true for the wide array of lipids that comprise a eukaryotic cell membrane. Indeed, the Fluid Mosaic Model of non-specific lipid-protein interactions that once served as the standard for our understanding of the lipid bilayer has, in recent decades, been replaced by a more deliberate model of lateral organization (Corradi *et al.*, 2018; Singer and Nicolson, 1972; van Meer *et al.*, 2008). This is of particular importance when considering that lipids are involved in the regulation of MP trafficking, localization, oligomerization and activity, and are known to act as messengers in receptor signaling cascades (Contreras *et al.*, 2011; van Meer *et al.*, 2008). Hence, to fully form our understanding of how a MP functions, our interpretation of its structure should not solely consist of the amino acids that define its secondary and tertiary structure, but should reflect the lipids that surround it as well. And whenever possible, including these lipids in the analysis is preferable, albeit challenging with methods currently available.

However, despite the continued difficulty inherent in studying MPs and the relatively modest progress made in the field of MP structural biology, examining the rate at which new atomic-level MP structures are being deposited to the PDB confirms that the field is experiencing exponential growth (Figure 1.1). From the time the first MP high resolution structure was solved in 1985 to about the year 2000, the annual rate of new structures being reported was in the single digits (White, 2019). Around the year 2000, however, technological advances like the development of lipidic cubic phase (LCP) (which is still the preferred method for creating MP crystals) and improvements in automation and analysis software helped propel MP structural analysis forward (Pebay-Peyroula *et al.*, 1997). Despite this, atomic resolution of MPs is still challenging with the standard methodology, particularly given the difficulty of creating an ordered crystal with an inherently disordered protein.

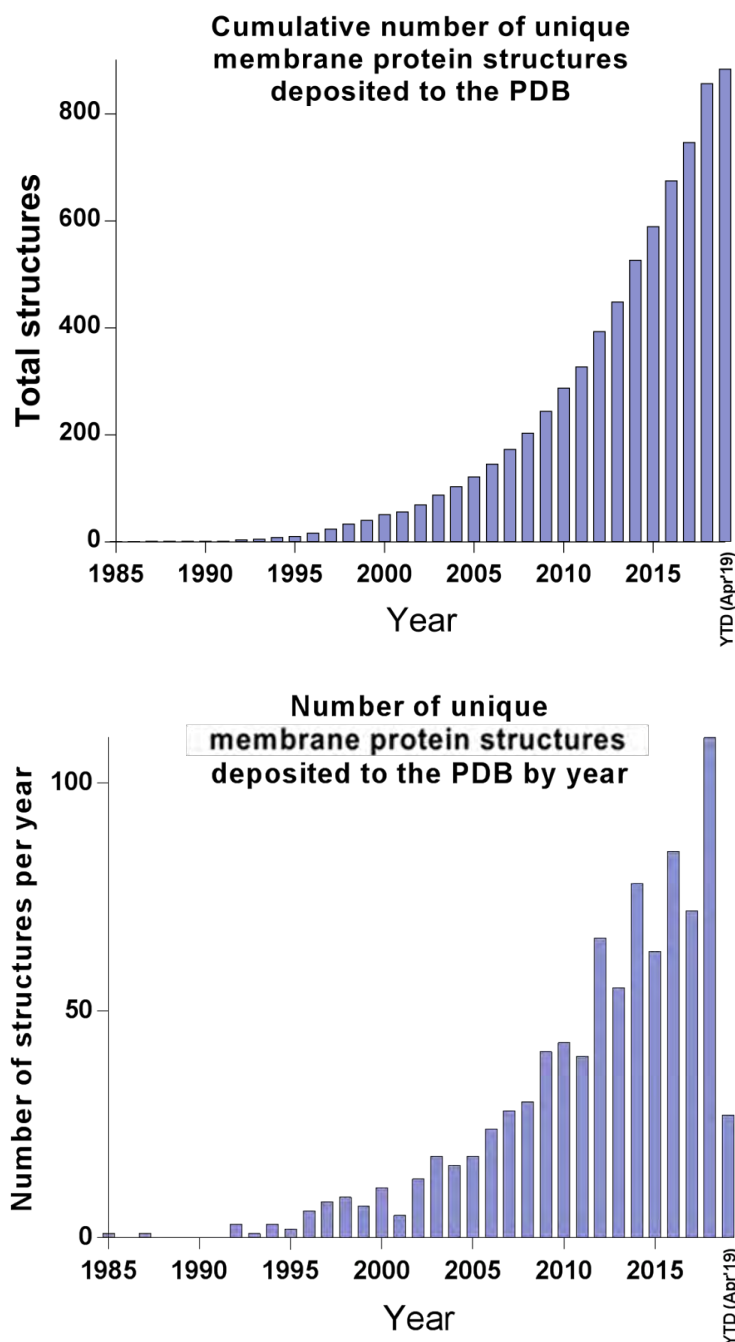


**Figure 1.1 Total accumulated (top) or per-year (bottom) number of unique membrane protein structures deposited to the protein data bank (PDB).**

Graph adapted from Membrane Proteins of Known 3D Structure Database; Data compiled by the White Lab, UC Irvine, values are as of April 9, 2019;

<https://blanco.biomol.uci.edu/mpstruc/>



### 1.1.2 Cryo-Electron Microscopy and the “resolution revolution”

The advent of the cryo-EM “revolution” has provided a new path to high-quality, high-resolution structures of MPs. This method offers structural biologists not only a way to visualize MPs, but also provides insight into their function, given that particles of any conformation can be captured (Qiu *et al.*, 2018; Zhang *et al.*, 2017), a significant limitation of crystallography. Electron microscopy has been in use for nearly 100 years, and has allowed scientists to view structures at a resolution that visible light wavelength never could (de Jonge *et al.*, 2014; Gordon, 2014), yet the use of such a powerful source of energy for imaging is not without certain drawbacks. Particle damage due to beam heat, staining with heavy metal salt like uranyl acetate, and the required removal of water molecules that interfere with imaging limited the resolution that could be obtained (Frank, 2006). Then in 1960, Humberto Fernández-Morán published on the concept of suspending particles in ice as a means of capturing them in their native state with water molecules intact (Fernandez-Moran, 1960); a concept that was perhaps ahead of its time. It took about 15 years for that concept to be a tangible reality, when Taylor and Glaeser (Taylor and Glaeser, 1974, 1976) published the first evidence of imaging a frozen, hydrated specimen with true success; thus providing the basis for cryo-EM. Around the same time, Henderson and Unwin successfully applied the concept of class-averaging to acquire a 3-dimensional model of a 7-transmembrane protein embedded in a purple-colored

membrane patch of *H. halobium*, a specimen that provided the basis for much of the early work surrounding 3-dimensional electron microscopy (3DEM) (Henderson, 1977; Henderson and Unwin, 1975).

While the concept of frozen specimen preparation solved the issue of dehydration effects and (to a certain extent) particle damage, it also introduced a level of variation and imaging interruption due to crystalline ice formation. This issue was overcome with the introduction of vitreous ice formation (Brüggeller and Mayer, 1980; Dubochet and McDowell, 1981), a biological concept that, amusingly, was characterized as “bending nature” by a dubious journal editor (Dubochet, 2012). From there, developments in thin film vitrification and image processing (Dubochet *et al.*, 1988; Frank, 2006) helped to establish this method as a tangible approach to atomic-level microscopy, and not simply a “niche” method (Callaway, 2015). And in between the landmark findings of Dubochet and Frank were the small, step-wise advances in sample preparation, 2D- and 3D-particle averaging, phase contrast imaging, and direct electron detection (Bammes *et al.*, 2012; Murata and Wolf, 2018).

In 2008, Direct Electron (San Diego, CA) changed the landscape of MP structural biology with the development of the direct detection device (DDD) for electron microscopy (Jin *et al.*, 2008; Milazzo *et al.*, 2011). This technology was created as a radiation-tolerant alternative to the charge coupled device (CCD) system, which required the use of a resolution-limiting scintillation screen to allow

for electron-to-photon conversion (Jin *et al.*, 2008; Xuong *et al.*, 2004). In 2011, FEI (The Netherlands) followed with the commercial launch of its first direct electron detector, the “Falcon” (Kuijper *et al.*, 2015). The availability of this improved detection system was responsible for the second significant increase in the rate of MP structure determination (White, 2019). Two years later, Gatan, Inc. (Pleasanton, CA) followed the release of the Falcon with the Gatan K2, and in 2015 they introduced the Gatan K2 Summit direct electron detector, which was responsible for the most significant increase in the number of high resolution maps obtained using cryo-EM (White, 2019).

Today, cryo-EM is widely seen as the standard for high-resolution structural analysis. The method lends itself to particle visualization across a wide range of conformations, molecular sizes - published structures range from low kilo-Daltons up to mega-Daltons – and specimen types (Liu *et al.*, 2018; Murata and Wolf, 2018). With the exponential wealth of knowledge that has sprung from the early discoveries of scientists like Jacques Dubochet, Joachim Frank and Richard Henderson, cryo-EM will likely continue to change the course of biology.

## 1.2 Cystic Fibrosis Transmembrane Conductance Regulator

### 1.2.1 Structure, function and clinical relevance

Cystic fibrosis transmembrane conductance regulator (CFTR) is an ATP-gated, phosphorylation-regulated chloride channel found in the apical membrane of epithelial cells. It contains 1480 amino acid residues and measures ~170kD in size (Meng *et al.*, 2019; Riordan, 2008; Sheppard and Welsh, 1999). CFTR is a large, multi-pass protein that comprises five domains: two transmembrane domains (TMD1 and TMD2) each with six transmembrane (TM)  $\alpha$ -helices, two cytoplasmic nucleotide-binding domains (NBD1 and NBD2) and a regulatory (R) domain with multiple PKA and PKC phosphorylation sites (Figure 1.2) (Amaral and Kunzelmann, 2011; Chiaw *et al.*, 2011; Hegedűs *et al.*, 2009; Hunt *et al.*, 2013; Lewis *et al.*, 2010; Linsdell, 2014). Although a member of the ATP-binding cassette (ABC) transporter family (ABCC7), which normally function as active transporters, CFTR instead utilizes its ATP binding domains as a non-catalytic gating mechanism. Upon ATP binding to the NBDs, CFTR is held in an outward-facing, open conformation, facilitating passive transport of chloride ions down a concentration gradient (Dean *et al.*, 2001; Pezzulo *et al.*, 2012). CFTR channel gating is driven by phosphorylation and dephosphorylation, primarily of the R domain (Cheng *et al.*, 1991; Rich *et al.*, 1993). When in the inactive, or closed state, the unstructured R domain appears to reside (at least in part) in an

inhibitory position within a cavity between TMDs 1 and 2, interfering with the dimerization of the NBDs (Zhang *et al.*, 2017). However, upon phosphorylation by the cAMP-dependent protein kinase (PKA), CFTR undergoes a significant conformational change that starts with movement of the R domain away from the channel opening, which allows ATP-driven dimerization of NBD1 and NBD2 and subsequent channel opening (Zhang *et al.*, 2017). See Figure 1.3 for cryo-EM structures in both the open and closed conformations. In the two structures, the visible portion of the largely unstructured R domain is represented by a purple helix. Remaining residues of the domain that were disordered and not visualized in the final map are not present in the PDB and not included in the figure.

The two heterodimeric NBDs are each characterized by the presence of nucleotide-binding Walker motifs A and B: NBD1 containing the sequences GSTGAGKTS and LYLLDSP, and NBD2, GRTGSGKST and ILLLDEP, for A and B, respectively. Although both NBDs have the capacity to bind ATP, it is the Walker B domain of NBD2, specifically Glu1371, which is necessary for ATP hydrolysis (Stratford *et al.*, 2007). NBD1 is catalytically inactive due to the replacement of the Walker-B carboxylate residue (often a Glu or His) needed to facilitate ATP recognition and hydrolysis, which is instead a Ser residue (Ser573) (Lewis *et al.*, 2004). Immediately preceding the Walker B site is a highly conserved sequence motif 'linker peptide' (LSGGQQ/R/KQR) that is shared among members of the ABC transport family (Chen and Hwang, 2008; Schneider and Hunke, 1998).

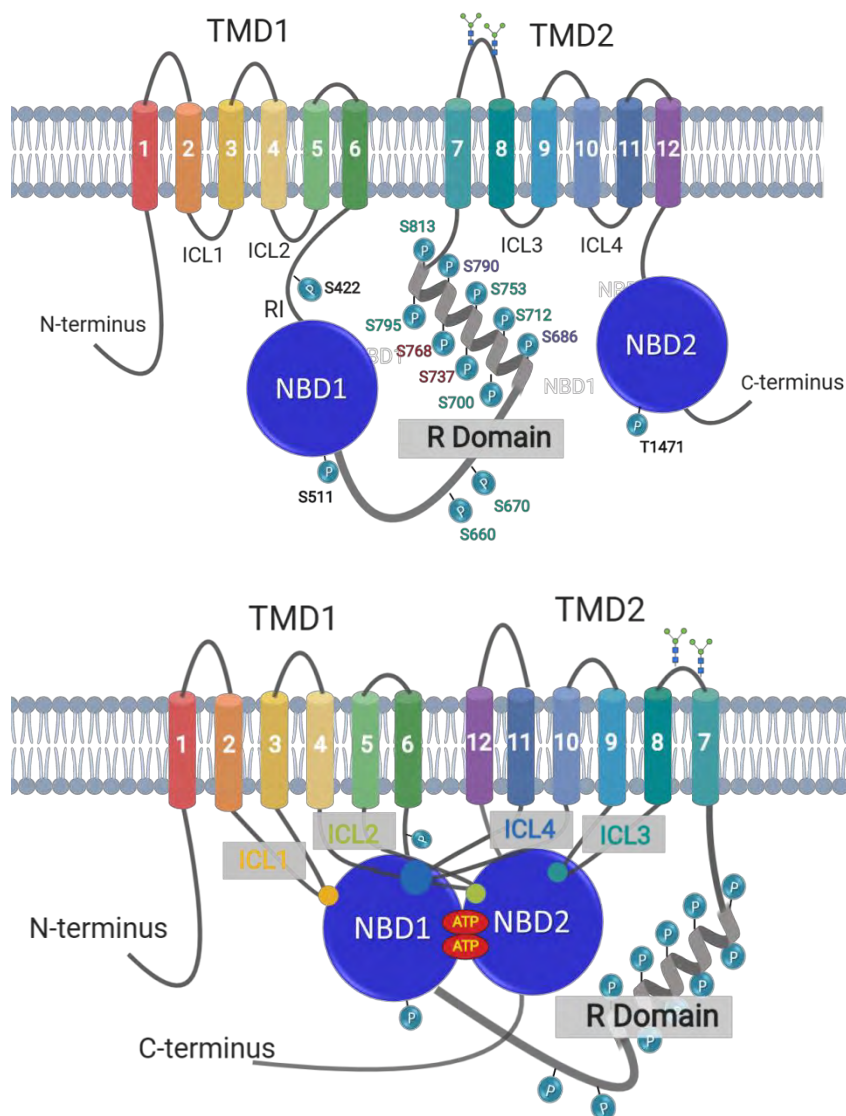


**Figure 1.2 Topology of CFTR in both the closed (top) and open (bottom) conformations.** These topologies show the two transmembrane domains (TMDs), two nucleotide binding domains (NBDs), the adjacent regulatory insertion (RI), and the regulatory domain (R domain), which is the site of several CFTR phosphorylation sites (top) (Hegedűs *et al.*, 2009). Residues phosphorylated by PKA are denoted in green (stimulatory) or red (inhibitory) (Wilkinson *et al.*, 1997), while PKC sites are purple (Chappe *et al.*, 2004). Residues not known to be involved in channel activation are shown as black.

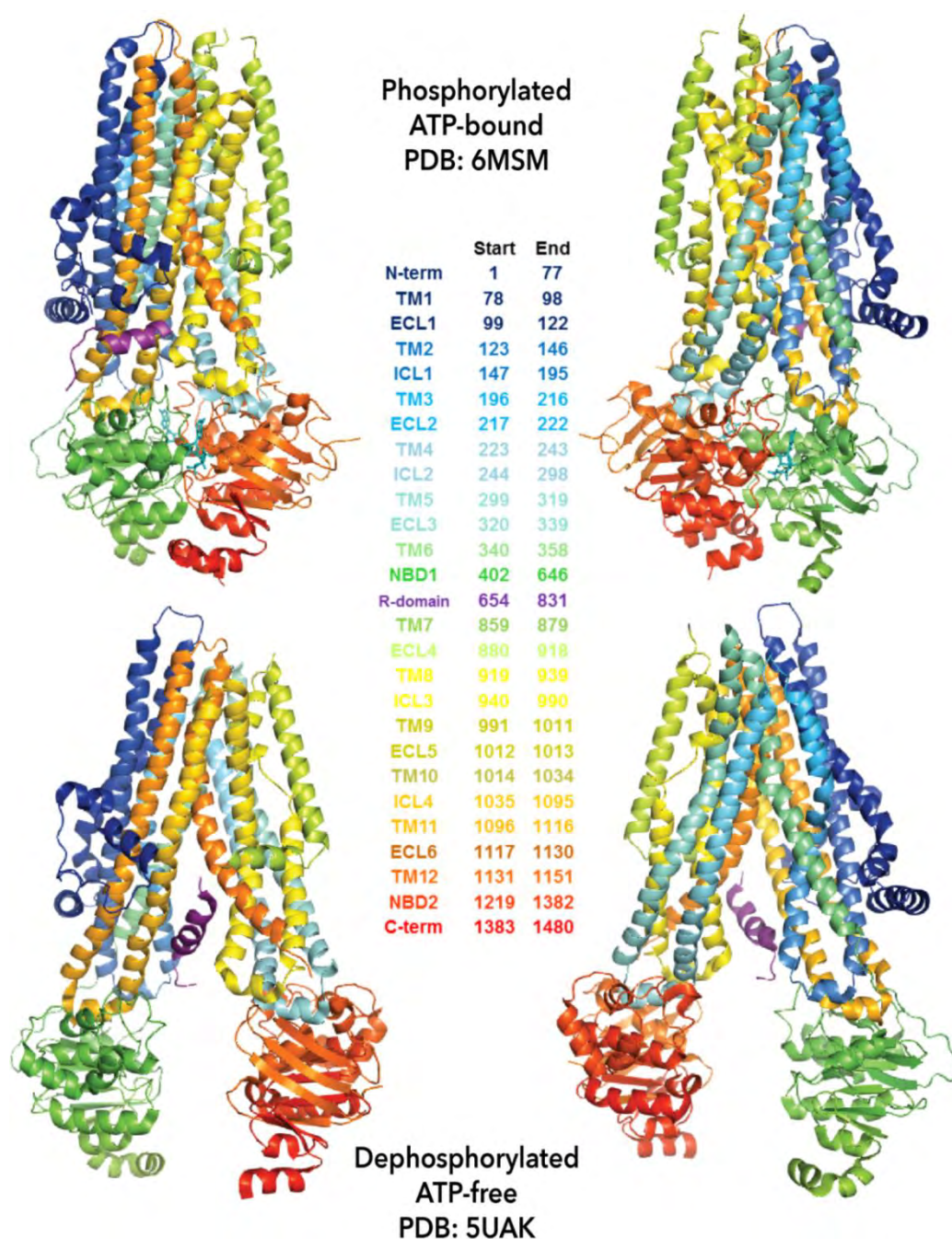


**Figure 1.3 Cryo-EM structures of human CFTR in the open and closed conformations.** Domain names and TM helix numbers are listed with color-coding as they appear in the corresponding structural models. Structures were obtained from the protein data bank (PDB IDs 6MSM and 5UAK; (Liu *et al.*, 2017; Zhang *et al.*, 2018b) and models were prepared using PyMol (2015).

### 1.2.2 Structural determination of CFTR

It has now been well-established that CF is the direct result of genetic mutations that cause the loss of CFTR function (Cheng *et al.*, 1990; Rich *et al.*, 1990; Riordan *et al.*, 1989b). It has also been well-established that the scope and severity of this disease is directly related to the mutation or combination of mutations the patient possesses (Brodie *et al.*, 2015; Welsh and Smith, 1993a), and that if the CFTR defect(s) can be addressed, channel conductance and subsequently the patient's overall health can be greatly improved. It stands to reason, then, that a clear picture of the structure and function of CFTR is of paramount importance to CF drug discovery efforts. And accordingly, it has been the subject of much extensive research for the last thirty years (Callebaut *et al.*, 2004; Callebaut *et al.*, 2017; Hunt *et al.*; Mornon *et al.*, 2008; Rosenberg *et al.*, 2004; Rosenberg *et al.*, 2012; Zhang and Chen, 2016).

### Homology modeling of CFTR

Until recently, the standard models for full-length CFTR structure were based on homology models comprised of (once available) NBD1 [PDB ID: 2pze] and NBD2 [PDB ID: 3gd7] crystal structures (Dalton *et al.*, 2012; Lewis *et al.*, 2010), paired with known structures of homologous bacterial efflux transporters Sav1866 (Dawson and Locher, 2007; Dawson and Locher, 2006), MsbA (Ward *et al.*, 2007) and p-glycoprotein (Aller *et al.*, 2009). Despite having broad similarities to these orthologous ABC transporters (two domains comprised of 6



$\alpha$ -helices each and similar cytoplasmic NBDs), there were striking differences between P-glycoprotein 1 (P-gp) and some orthologs of ATP-binding protein MsbA compared to Sav1866, namely the distance between the two NBDs and the overall orientation of the TMDs. Taking into account structural analysis of the CFTR sequence and the predicted lengths of loops and helices, Sav1866 was most often used as a starting point for molecular modeling (Callebaut *et al.*, 2004; Lewis *et al.*, 2004).

Indeed, before the availability of cryo-EM made structural analysis of membrane proteins a more attainable goal, there was a great deal of information to be collected from CFTR homology models. For example, in early 2008 Serohijos *et al.* first described the interaction between F508 and ICL4 (“...Phe508 mediates a tertiary interaction between the surface of NBD1 and a cytoplasmic loop (CL4) in the c-terminal membrane spanning domain”) (Serohijos *et al.*, 2008). Later that year, Mornon *et al.*, who, like Serohijos, used Sav1866 as a starting point for modeling CFTR in an outward-facing conformation, provided a slightly more in-depth analysis, highlighting “an intricate H-bond network (involving especially the ICL4 R1070 and the main chain of NBD1 F508),” which, they proposed, stabilized the interface between TMD2 and NBD1 (Mornon *et al.*, 2008). However, despite the overall similarities these models possessed and the great deal of early information they provided, discrepancies between models did exist with regard to side-chain rotamers and relative positions of residues adjacent to the membrane (Hunt *et al.*, 2013), as well as the

lack of precedent for the R domain which is specific to CFTR, once again highlighting the importance of a high-resolution structure of full-length human CFTR.

### **Experimental structural determination of CFTR**

Despite a dedicated effort toward obtaining structural information about CFTR, most attempts have been met with frustration in the form of an atomic resolution “ceiling,” due largely to the limitations of available technology, and the difficulties inherent in working with the large, hydrophobic and generally unstable CFTR. In 2004, the first successful 2D crystallization and TEM imaging of n-dodecyl- $\beta$ -maltopyranoside (DDM)-purified human CFTR, albeit of very limited resolution, was published (Rosenberg *et al.*, 2004). Later a 9-Å resolution map of CFTR in its apo form was obtained using the sitting droplet method of 2D crystallization (as opposed to the hanging drop method previously employed) (Rosenberg *et al.*, 2012). While this work represented significant progress in the field of CFTR structural biology, the model relied heavily on high-resolution data previously reported for Sav1866 (PDB ID: 2HYD). For several years, this was the highest resolution (non-homology) structural model of full-length, wild-type CFTR that existed.

In 2016 the first high-resolution, full-length atomic model of CFTR – of any species – was resolved. These structural analyses showed zebrafish and human CFTR in both the dephosphorylated (closed) (Zhang and Chen, 2016; Zhang *et*

*al.*, 2017) and phosphorylated (open) conformations (Liu *et al.*, 2017; Zhang *et al.*, 2018b), and offers novel insights about the structure and function of CFTR. (The human CFTR cryo-EM structures are seen in Figure 1.3.)

Zebrafish CFTR shares 55% sequence identity with human CFTR, including 42 of the 46 missense mutational sites that lead to CF in humans. Its successful purification as a larger, more stable sample of CFTR into detergent micelles than is usually possible with its human ortholog (Zhang and Chen, 2016) facilitated the high-resolution structure determination. In addition to obtaining a 3.7 Å structural model in the dephosphorylated (ATP-free) state, the Chen lab showed ATPase-mediated channel activity of CFTR, lending support to the validity of the structural model (Zhang and Chen, 2016). A dephosphorylated human CFTR structural model - this time at 3.9 Å - followed soon thereafter, displaying remarkable similarity to its zebrafish counterpart (Liu *et al.*, 2017). Within a year and a half, two more structures were published from the lab: one zebrafish and one human CFTR, both in the phosphorylated, ATP-bound, “open” conformation (Zhang *et al.*, 2017; Zhang *et al.*, 2018b).

This work was important not only because it represented the first time a high-resolution CFTR structure had been published, but because of the number of insights this collection of models provided about both the open and closed conformations and because it offered concrete evidence to support years of biophysical analysis on CFTR’s helical positioning (Gao and Hwang, 2016;

Serohijos *et al.*, 2008; Wang and Linsdell, 2012; Zhou *et al.*, 2010). These models confirmed a “head-to-tail” dimerization of the two NBDs upon ATP binding, and although not fully visible, presented a partial view of the CFTR-specific R-domain, along with evidence that phosphorylation of this unstructured region may be the gatekeeper responsible for CFTR conformational changes (Zhang *et al.*, 2017). Perhaps most importantly, this work provided valuable information on how several CF-causing mutations might lead to channel dysfunction, offering up a roadmap for structure-based drug design (Liu *et al.*, 2017; Zhang and Chen, 2016; Zhang *et al.*, 2017; Zhang *et al.*, 2018b).

Yet while Jue Chen's collection of CFTR structures does represent a significant step forward in the field of CFTR structural biology, some limitations remain in the model determination and the overall interpretation of the results. As previously mentioned, the first publication released from the Chen lab was of zebrafish CFTR in a dephosphorylated or “closed” conformation (PDB ID: 5UAR, (Zhang and Chen, 2016). In this paper, Zhang mentions that in the course of model determination, because the “densities corresponding to the NBDs are not as sharply resolved, (they) relied on the crystal structures of mouse NBD1 and human NBD2 (PDB: 1Q3H and 3GD7, respectively) to guide model building” (Zhang and Chen, 2016).

This approach was again used by the Chen lab when determining the structure of dephosphorylated human CFTR (PDB ID: 5UAK, (Liu *et al.*, 2017),

however human NBD1 and NBD2 were docked into the cryo-EM map as opposed to murine NBD1. Using the human NBD crystal structures as a guide, side-chain positions were then adjusted to conform to the EM density (Liu *et al.*, 2017). Additionally, to determine positioning of TMD1 and TMD2 in their model of hCFTR, the authors relied on their structure of zebrafish CFTR as a starting point, and reworked their human CFTR cryo-EM map around the zebrafish model. In instances where densities were weak, “the residues were kept as they were in the models” (Liu *et al.*, 2017). It is unlikely that this represented an optimal approach for modeling human CFTR, given the modest sequence homology (55%) between human and zebrafish CFTR, the lack of an obvious evolutionary common thread, and the vast differences in their overall stability. In fact, work has since been published highlighting differences in the functional properties of the two isoforms, including differences in gating patterns and the strong preference of zCFTR to reside in the closed conformation (Zhang *et al.*, 2018a).

When the phosphorylated, open conformation zCFTR structure was published later that year, it included a point mutation made to the consensus site within NBD2 (E1372 in zCFTR and E1371 in human CFTR) in order to abolish ATP hydrolysis and hinder the rate of pore-closing by ~1,000-fold (Vergani *et al.*, 2005). And in 2018, the successively published model of phosphorylated, open channel hCFTR was again based on an initial model of ATP-bound zebrafish CFTR (Zhang *et al.*, 2018b). According to Zhang *et al.*, a comparison of hCFTR

and the zCFTR structure it was modeled after highlighted major structural differences in the two orthologs: most notably displacement of equivalent residues up to 6Å and structural shifts in TMs 1, 6 and 12 between the two structures, and differences in nucleotide binding symmetry between human (symmetrical) and zebrafish (asymmetrical) NBDs (Zhang *et al.*, 2018b). Moreover, because Chen's lab has created their phosphorylated hCFTR structural model using a hydrolysis-null version of CFTR that had been held in an open conformation, they were unable to confirm that this observed structural conformation is true, despite making several claims about the channel gating properties and functional data. In such cases, the potential for variability that is introduced when dealing with detergent purification cannot be overlooked, particularly with such a large protein. It is well-established that detergent purification does introduce variability and instability to membrane proteins, and in some cases such as with digitonin, may bias the protein toward a specific (in the case of CFTR, closed) protein conformation. There is mounting evidence that membrane protein function is sensitive to the composition of the bilayer in which it is embedded, with a preference for lipid compositions that resemble the native environment (Bigay and Antonny, 2012; Corradi *et al.*, 2018; Fang *et al.*, 2010; Hildebrandt *et al.*, 2017; Teo *et al.*, 2019; van Meer *et al.*, 2008). Moreover there is direct evidence that cholesterol is essential for proper CFTR structure and function (Abu-Arish *et al.*, 2015; Fang *et al.*, 2010). With this in mind, the replacement of this environment with exogenous detergents – particularly one

that is known to precipitate sterols, such as digitonin (Bloor and Knudson, 1916; Zhong *et al.*, 2010) - should be carefully considered, and the results of such studies carefully interpreted.

In an area of study where experimental structural data is limited, it can be easy to make sweeping assumptions about a protein's characteristics based on a snapshot. It can, however, be very misleading, and scrutiny should be applied, particularly when such data is used to inform the next iteration of studies (Abreu *et al.*, 2019), or perhaps inform the next generation of drug development.

A list of the 7 full-length structures of CFTR (<10 Å) is seen in Table 1.1.

**Table 1.1 Current list of full-length CFTR cryo-EM structures of sub-nanometer resolution.** Table adapted from Meng *et al.*, 2019.

Year published	Species	EMDB code	PDB code	Protein state	Resolution	Mutations	Reference
2011	Human	1966	4A82	Dephosphorylated, ATP-free (predicted)	9Å	None	<a href="#">Rosenberg et al, 2011</a>
2016	Zebrafish	8461	5UAR	Dephosphorylated, ATP-free	3.73Å	None	<a href="#">Zhang et al, 2016</a>
2017	Human	8516	5UAK	Dephosphorylated, ATP-free	3.9Å	None	<a href="#">Liu et al, 2017</a>
2017	Zebrafish	8782	5W81	Phosphorylated, ATP-bound	3.4Å	E1371Q	<a href="#">Zhang et al, 2017</a>
2018	Chicken	7793	6D3R	Dephosphorylated, thermostabilized	4.3Å	H1404S/1441X/ΔRI	<a href="#">Fay et al, 2017</a>
2018	Chicken	7794	6D3S	Phosphorylated, thermostabilized	6.6 Å	H1404S/1441X/ΔRI	<a href="#">Fay et al, 2017</a>
2018	Human	9230	6MSM	Phosphorylated, ATP-bound	3.2Å	E1371Q	<a href="#">Zhang et al, 2018</a>

### 1.2.3 Cystic Fibrosis

#### CF pathophysiology

Cystic Fibrosis (CF) is a genetic disease caused by loss-of-function CFTR mutations. CF primarily affects exocrine tissues within the respiratory and digestive systems, notably the lungs, intestines, pancreas and sweat glands (Amaral and Kunzelmann, 2011). In these tissues, CFTR serves as the primary apical conduit for important anions, including chloride, bicarbonate and thiocyanate. Through this function, CFTR controls the movement of water to and from the cell surface as well as the apical pH, which together regulate the viscosity of luminal secretions, especially mucus (Rich *et al.*, 1990). In the lung, when CFTR function is lost, anions are prohibited from moving to the apical surface of the lung epithelial cells, causing dehydration and acidification of the airway surface liquid. This, in turn, increases viscosity of the normal mucosal layer and impairs mucociliary clearance (McKoy *et al.*, 2016). As a result, mucus builds up and blocks oxygen transfer, trapping bacteria that thrive in low-pH environments. In addition, the immune response that follows is rendered largely ineffective, as the lymphocytes, neutrophils and phagocytes that respond also become trapped, further contributing to the build-up (Southern *et al.*, 2019). These factors make patients particularly vulnerable to lung infections and inflammation, which continue to be the leading causes of morbidity and mortality in people with cystic fibrosis (Pezzulo *et al.*, 2012). Despite recent progress in treatment options for CF such as CFTR potentiators and correctors (discussed in



greater detail below) and increased prevalence of newborn screening, the median life span for a patient living with CF in the US, Canada or the UK is only about 37.5 years (CFF.org, 2018). However, given the rapid advancements in CF therapies, a patient born between 2013 and 2017 is expected to survive into their mid-40's. This number decreases, however, for patients living in developing countries such as India, Bolivia and Mexico, where newborn screening and access to healthcare are not readily available (Mirtajani *et al.*, 2017; Spoonhower and Davis, 2016).

### **CFTR mutations**

In 1989, the gene for CFTR was first identified (Kerem *et al.*, 1989; Riordan *et al.*, 1989a), and the molecular basis of cystic fibrosis was described shortly thereafter (Cheng *et al.*, 1990). Within two more years, nearly 300 mutations had been reported (Tsui, 1992) and the first four classes of mutations were defined (Welsh and Smith, 1993b). Since then, the classes have evolved and increased in number as our understanding of the disease and the list of known CF mutations has expanded. There are currently 6 traditional mutational classes categorizing over 2,000 reported CF-causing mutations; however, this classification model continues to evolve as the development of new drugs targeting specific CF phenotypes advances (De Boeck and Amaral, 2016; Marson *et al.*, 2016).

The current classification of CF mutations is as follows:

- I. **Production mutations** – This type of mutation encodes a premature stop codon within the open reading frame, resulting in truncated and non-functional CFTR variants. This category also includes nonsense mutations, deletions and splicing mutations.
- II. **Processing mutations** – This class results from folding defect mutations of CFTR, which ultimately prevent trafficking to the apical cell surface.
- III. **Gating mutations** – With these mutations, CFTR reaches the cell surface but fails to activate channel opening. These proteins are non-functional.
- IV. **Conduction mutations** – CFTR is processed normally, yet has abnormal channel function, which results in limited activity.
- V. **Insufficient protein mutations** – This class results from splice variants in which an insufficient quantity of functional CFTR or irregular CFTR proteins are produced due to incorrect mRNA splicing.
- VI. **Stability mutations** – CFTR is produced with normal function, but is recovered more rapidly from the cell surface as a result of these mutations. One example is rescued  $\Delta F508$  (r $\Delta F508$ ), which is partially functional and benefits from CFTR gating potentiators.

The most common CFTR mutation occurs in approximately 70% of patients worldwide and results in the deletion of a phenylalanine at position 508 within NBD1 ( $\Delta$ F508-CFTR) (De Boeck and Amaral, 2016; Dean *et al.*, 2001; Goor *et al.*, 2009).  $\Delta$ F508 prevalence is higher for patients in the United States (~88%) and throughout Europe (~80%) (CFF, 2017; CFF.org, 2018; Orenti *et al.*, 2018; Prinz *et al.*, 2019). Despite the rather modest change in sequence that the loss of F508 causes, loss of this residue prevents proper folding of NBD1, which consequently disrupts the interface between NBD1 and the intracellular loop 4 (ICL4) within membrane spanning domain 2 (TMD2) (Serohijos *et al.*, 2008). The resulting protein is far less stable at physiologic temperatures, with a thermostability that is about 10°C less than that of wild-type CFTR, and it is quickly recognized by the endoplasmic reticulum-associated protein degradation (ERAD) pathway before it can traffic to the cell membrane (Brodsky, 2001).

Additional mutations can impair normal channel function by impacting gating or conductance once the protein is embedded in the cell membrane. Figure 1.4 outlines the six (current) classifications of CF-causing mutations and lists the therapeutic approach that would be required for effective treatment.

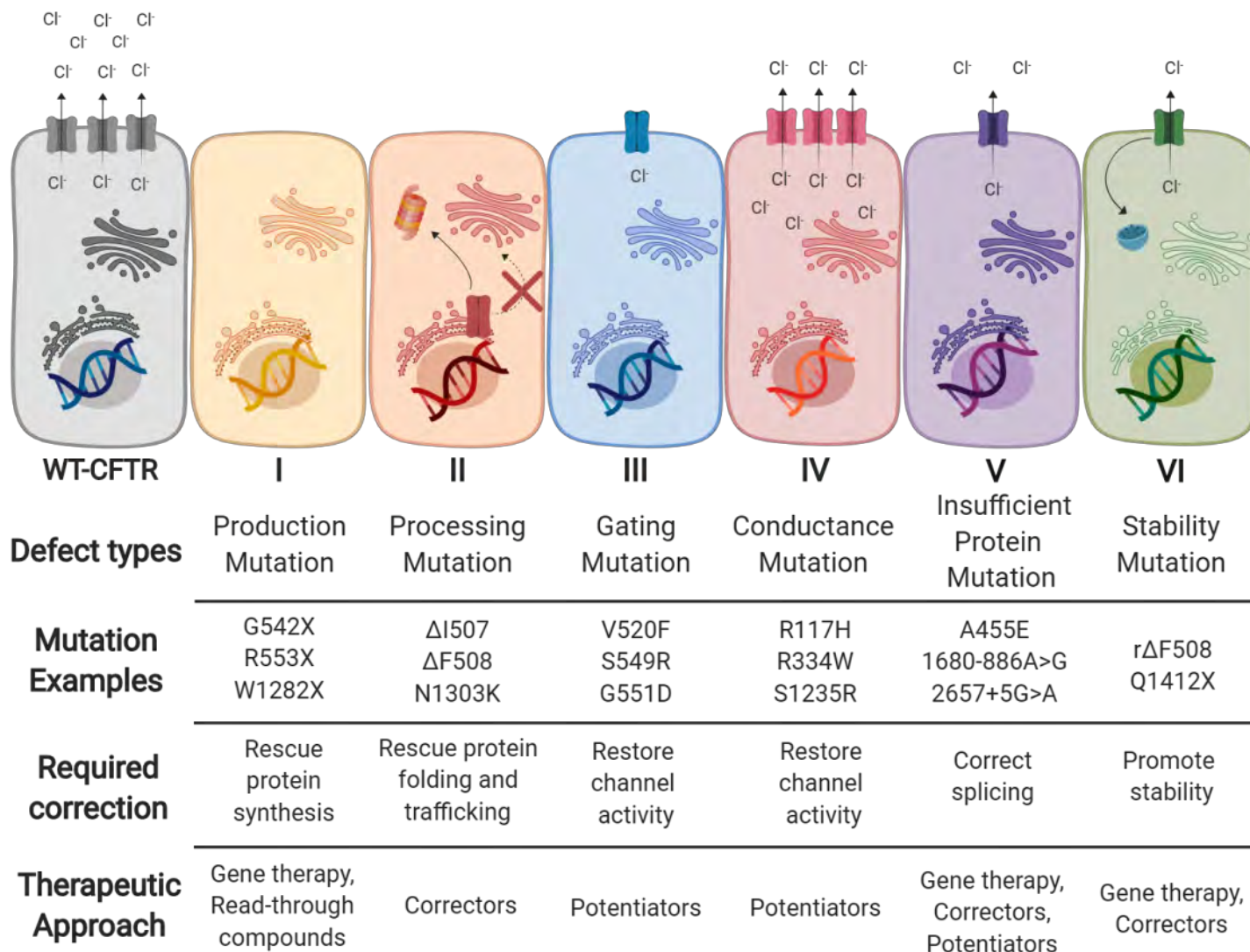


**Figure 1.4 Classification of CFTR mutations and corresponding therapeutic strategies** The current classification system for cystic fibrosis mutations encompasses six classes of defects in addition to wild type (WT). Each mutational class is designated by its impact on CFTR biogenesis, maturation, stability and function. Therapeutic strategies are discussed in greater detail in the Treatment Options section of this chapter. Figure on previous page. Adapted from (Vallières and Elborn, 2014).

### **Second-site suppressor mutations that correct the $\Delta F508$ -CFTR defect**

Although no existing therapy fully corrects the  $\Delta F508$  defect, various second-site suppressor mutations (SSSM) have been identified, in part through patient genotyping, which reduce the impact of the  $\Delta F508$  mutation. In 1990, secondary mutation R553Q was identified in a CF patient homozygous for  $\Delta F508$  who exhibited near-normal sweat test chloride levels and yet suffered from typical CF symptoms of gastrointestinal and pulmonary disease (Dörk T, 1991; Teem *et al.*, 2007). Further genotyping of CF patient samples revealed a series of SSSMs (I539T, G550E, R553Q, and R555K) located within NBD1, which were capable of reducing the impact of the  $\Delta F508$  mutation by increasing CFTR trafficking and function, resulting in a milder disease phenotype (Teem *et al.*, 2007). These mutations, known commonly as R mutations (revertant) or -3M mutations (when R553M is used), increase the thermal stability of NBD1, but they do not reestablish the NBD1:ICL4 interface that is lost with  $\Delta F508$  (He *et al.*, 2010). However, when these NBD1 stabilizing mutations exist alongside a small molecule or SSSM that corrects the NBD1:ICL4 interaction, a vast improvement

can be seen in CFTR global assembly and channel function (He *et al.*, 2015; He *et al.*, 2010).

In addition to NBD1, several CF-causing point mutations have been reported in the cytoplasmic loops; the most prevalent being ICL4, where mutations have been observed at 36 of the ~60 residues comprising the loop (Krasnov *et al.*, 2008; Seibert *et al.*, 1996). Within ICL4, Arg1070, which resides at the NBD1:ICL4 interface, has been the site of three different missense mutations: R1070W, R1070P and R1070Q. Patients who have the latter two mutations present with a classic CF phenotype, while those with R1070W experience a much milder phenotype and live a normal lifespan. Of the 29 patients worldwide who have been identified with R1070W, clinical data is available for 24, and of these, 16 reportedly also carry  $\Delta F508$  (Krasnov *et al.*, 2008). In nearly all cases of this mutation, disease phenotype was significantly ameliorated and patients had pancreatic-sufficient CF, suggesting that R1070W was acting to suppress the  $\Delta F508$  mutation in patients. In the years since clinical data was first reported, much work has been done to better understand this secondary mutation, which may reduce the  $\Delta F508$  defect by replacing the missing aromatic ring of F508 with a tryptophan at the ICL4 interface (Kalid, 2010; Loo, 2010).

In 2007, Wang *et al.* first reported that the SSSM V510D improved trafficking in normal and Cys-less mutants of  $\Delta F508$ -CFTR, despite reported

inactivity of the mutant in iodide efflux assays (Wang *et al.*, 2007). Shortly thereafter, Mornon *et al.* used evidence obtained through molecular modeling to propose that V510D likely compensates for the loss of F508 by creating a salt bridge with arginine 1070 (R1070) of CFTR's intracellular loop 4, restoring an important domain-domain interaction lost in  $\Delta F508$  that appears important to CFTR folding, stability and apical localization (Mornon *et al.*, 2008). Three years later, fellow members of Wang's lab reported that in addition to rescuing trafficking, V510D is also capable of increasing  $\Delta F508$ -CFTR half-life by about 5-fold, similar to that of WT protein (Loo *et al.*, 2010).

Although the rescue effects of these suppressor mutations have been repeatedly confirmed, their mechanism of action is, in many cases, not fully defined. A more thorough understanding, however, may provide a solid platform for the design and optimization of therapeutics that address the  $\Delta F508$  defect more effectively.

### **Clinical biomarkers of cystic fibrosis**

Since 2010, every state in the U.S. has incorporated testing for cystic fibrosis into its standard newborn screening panel. This evaluation is done by testing for elevated blood levels of immunoreactive trypsinogen, or IRT. Additionally, genetic testing to look for specific mutations can be conducted, particularly if one or both parents are carriers or if certain risk factors are identified. Another means of diagnosis is the sweat test, which can be

administered once a child reaches two weeks old. For this test, a patient's skin is treated with a chemical to induce perspiration, and the resulting sweat is tested for chloride content. Given that CFTR is involved in normal chloride transport out of epithelial cells, CF patients have a greater concentration of chloride ions leave their body through perspiration. Hence, a higher-than-normal level of measured sweat chloride signals the presence of defective CFTR, and a diagnosis of CF may be suspected.

Once a patient has been positively diagnosed with CF, there are clinical biomarkers that can be utilized to monitor disease progression and comorbidities such as lung infection, as well as to evaluate therapeutic efficacy. Doctors often measure C-reactive protein levels in a patient's blood as a biomarker for inflammation (Levy *et al.*, 2007). Calprotectin, a neutrophil protein also detected through a blood test, has been shown to predict pulmonary exacerbations and lung function decline with good correlation (Muhlebach *et al.*, 2016; Schechter, 2018). The most well-established biomarker for CF disease progression is forced expiratory volume in 1 sec, or FEV1, which assesses a patient's pulmonary function by measuring the maximal amount of air that a patient can forcefully exhale in one second (Szczesniak *et al.*, 2017).

### **Treatment options: mutation-dependent therapies**

A number of therapeutics in development seek to ameliorate CF pathology by targeting specific mutations, either by aiding proper CFTR folding and



stabilization (correctors), by improving channel performance (potentiators), or by overriding a premature termination codon (read-through compounds) (Rabeh MW 2012). In some situations, gene therapy may be the most effective approach for functional protein recovery. At this point, only the first two types of therapies have been approved by the FDA and are available to patients.

### *Potentiators*

This class of drugs leads to increased CFTR chloride flow. Potentiators are effective in cases of gating and conductance mutations such as G551D, where the CFTR that is at the cell surface does not adequately manage the flow of chloride out of the cell (Bompadre *et al.*, 2007). In 2012, the FDA approved Vertex's CFTR potentiator, Kalydeco® (Ivacaftor), for patients with the G551D gating mutation, making it the first drug available to patients that addresses the underlying cause of CF, rather than managing the symptoms (Eckford *et al.*, 2012). While this marked a major milestone in the field, the patient population that most benefits from Kalydeco® is relatively small, about 5%, and in non-clinical studies, it has been shown to further destabilize temperature-rescued  $\Delta F508$ -CFTR (Meng *et al.*, 2017b). However, as described below, in recent years Kalydeco® has been approved for use in patients with severe processing mutations like  $\Delta F508$  in combination with another class of CFTR modulators known as correctors (CFF.org, 2019b) (<https://www.cff.org/trials/pipeline>.) When paired with a corrector, potentiators can also improve CFTR efficiency in patients with processing defects by increasing the amount of current achieved in cases

where a corrector is used to traffic misfolded CFTR to the cell surface (CFF, 2017; Meng *et al.*, 2019).

### *Correctors*

Nearly half of all CF patients have two copies of the  $\Delta F508$  mutation, a processing defect that leads to the misfolding and subsequent degradation of ~99% of translated CFTR. Despite the rather modest change in sequence that the loss of F508 causes, the resulting protein is far less stable at physiologic temperatures, with a thermostability that is about 10°C less than that of wild-type CFTR. As a consequence,  $\Delta F508$ -CFTR is quickly recognized by the endoplasmic reticulum-associated protein degradation (ERAD) pathway before it has the chance to traffic to the apical cell membrane (Brodsky, 2001). The use of an effective corrector to guide proper tertiary folding and trafficking, and stabilize the protein once at the cell surface, offers tremendous therapeutic potential for patients living with this mutation. There are currently two CFTR correctors available to patients, Lumacaftor and Tezacaftor. Neither has been FDA approved for single agent use; however, they have both been approved as combination therapies with the potentiator, Ivacaftor, as Orkambi® and Symdeko®, respectively (CFF.org, 2019b; Walker, 2015). It should be noted, however, that the impact seen with these currently-approved therapies is modest. In one study of CF patients harboring Class II mutations, an approximately 2.5%-6% increase in FEV<sub>1</sub>% was reported for patients being treated with Vertex combination therapy Orkambi® (lumacaftor-ivacaftor) (Southern *et al.*, 2018).

### *Amplifiers*

The limited response seen with potentiators and correctors may be attributed to insufficient substrate availability at the cell surface, due in large part to the rapid degradation of mutant protein that occurs with many CF-causing mutations. This presumption is supported by the greater therapeutic benefit that Orkambi® provides for patients homozygous for  $\Delta F508$  as compared to heterozygous (Drew *et al.*, 2016). In such cases, a therapeutic that increases the amount of CFTR made by the cell could have advantageous effects when paired with potentiators or correctors (Biswas *et al.*, 2017). This class of therapeutic, known as “amplifiers,” increases the steady-state of CFTR protein available in the cell through post-transcriptional amplification of CFTR mRNA, irrespective of mutation (Drew *et al.*, 2016). Currently, clinical trials are underway for a CFTR amplifier, PTI-428 (Proteostasis Therapeutics, Cambridge, MA), which is being evaluated both alone and in combination with Symdeko® in  $\Delta F508$  homozygous patients (CFF.org, 2019b).

### **Treatment options: mutation-agnostic treatments**

#### *Mucociliary clearance*

As mentioned previously, infection as a result of mucous accumulation in the airways is a major complication for patients with cystic fibrosis. As such, the management of mucous build-up is an important component of their daily treatment regimens. In addition to several mechanical airway clearance

techniques (physical therapy, high-frequency chest compression, intrapulmonary percussive ventilation, *etc.*), prescribed treatments such as mucolytics and airway hydrators can also help mobilize mucous and reduce the likelihood of infection (Southern *et al.*, 2019). Because a significant component of the mucous build-up is polymerized DNA and filamentous actin that results from the degradation of trapped white blood cells, inhalable recombinant human DNase treatments, such as Pulmozyme® (dornase alfa), may be effective (Aitken *et al.*, 1992; Shak *et al.*, 1990; Southern *et al.*, 2019). A second type of mucolytic known as OligoG and currently in phase 2 clinical trials, works to detach pulmonary mucin fibers through calcium chelation, a necessary component of mucin unfolding and detachment in healthy cells (Ermund *et al.*, 2017).

Improvements in hydration can also help to reduce mucous levels, and can be effected in multiple ways. The first is with the inhalation of 6% or 7% hypertonic saline, administered twice daily to increase the concentration of sodium ions at the apical surface of the lungs, and in so doing, increase water levels at these surfaces by creating an osmotic gradient (Wark and McDonald, 2018). The second option, which is already approved for use in Australia and the U.K., is the inhalation of mannitol, a naturally-occurring osmotic agent. In the U.S., Australian-based company Pharmaxis is currently in phase 3 trials with Bronchitol®, an inhaled dry-powder form of mannitol (Burness, 2012; De Boeck, 2017). Another therapeutic option in the drug development pipeline that leads to improved hydration and mucociliary clearance is the inhibition of the epithelial

sodium channel (ENaC). While several early candidates have been unsuccessful in the clinic (limited bioavailability and short duration of activity have proven problematic) (Moore and Tarran, 2018), testing is currently in phase 2 for several ENaC inhibitors which may prevent further influx of water and sodium ions into the cell, instead restoring it at the cell surface (Butler *et al.*, 2015).

#### *Anti-inflammatory/Anti-infective therapy*

Because lung infection-related complications continue to be the most significant comorbidity associated with cystic fibrosis, one of the more critical components of a CF patient's treatment regimen is the use of antibiotics (Levy *et al.*, 2007; Martin *et al.*, 2016). As the CF therapeutic landscape continues to evolve, so must the treatments available to combat this issue. A new subset of research pertaining to lung infection deals specifically with how microorganisms in the lung interact with CFTR-modulating compounds. Another significant area of study for CF researchers is how to manage the spread of nontuberculous mycobacteria (NTM), a difficult-to-treat and constantly evolving family of bacteria that can lead to severe lung infection and sometimes death (Gilljam *et al.*, 2004; Maiz-Carro and Navas-Elorza, 2002; Viviani *et al.*, 2016).

Moreover, because a prolonged inflammatory response can lead to lung damage, the use of anti-inflammatory drugs may help slow the progression of CF. Recently, several candidates have proven unsuccessful in the clinic; however, as this type of drug must be able to moderate inflammatory cells and

the corresponding cytokines without completely suppressing the patient's immune system, finding such a balance has proven challenging (Chmiel *et al.*, 2013). While a handful of clinical trials remain ongoing, the standard of care for combatting inflammation in CF patients continues to be high-dose ibuprofen.

#### *Nutritional/Gastro-intestinal supplements*

In addition to the lungs, patients with CF must also manage complications related to their digestive system, specifically the pancreas, liver and intestines that can sometimes lead to liver disease and CF-related diabetes (CFRD). The reduction in hydration and bicarbonate levels in the luminal space of the digestive system as a result of defective CFTR can render digestive enzymes inactive, leading to a condition known as pancreatic insufficiency (Eggermont, 1996; Littlewood, 1992). To combat this, patients must adhere to a routine of digestive supplements to ensure absorption of nutrients is possible in the small intestines. Moreover, the aberrantly thickened mucus, mucostasis, and pancreatic obstruction that result from defective CFTR can lead to autodigestion of the pancreatic tissue, and cause CF-related diabetes. To ensure that this serious comorbidity is detected and managed as early as possible, it is recommended that people with CF that are 10 years-old and up get tested for CFRD every year (CFF.org, 2019a).

CF patients must work with their physicians to decide which combination of approaches is most suitable. Strict adherence to the regimen of treatments

must be met for long-term survival. While great progress is being made in CF therapeutic availability, no truly effective treatment option currently exists. In order for patients to have a realizable chance at living a full life, scientists must continue to draw upon the clinical successes as well as the failures that have occurred in recent years, remain mindful of what CFTR biology is telling us, and continue to tap into vast research networks like those provided by the Cystic Fibrosis Foundation.

## 1.3 GLUT1

### 1.3.1 Function and clinical relevance

Glucose Transporter I, or GLUT1, is an integral membrane facilitative glucose transporter found ubiquitously throughout the human body (Yeagle, 2016). GLUT1 belongs to the major facilitator superfamily (MFS), an extensive class of transporters that is present in many different organisms, and is responsible for the movement of a broad range of organic molecules across the lipid bilayer through thermodynamically passive means (Pao *et al.*, 1998). Unlike other major transporter super-families such as the ABC transporters, which require ATP binding and hydrolysis to catalyze transport, MFS transporters act in response to a chemiosmotic gradient of their preferred solute (Jones and George, 2004; Pao *et al.*, 1998).

In humans, MFS orthologs are known as solute linked carriers (SLCs), and represent about half of all human transporter/channel genes expressed (Hediger *et al.*, 2004). Within the family of SLCs, glucose transporters (GLUTs) belong to the SLC2 family, of which GLUT1 (encode by the *SLC2A* gene) is a member (Reddy *et al.*, 2012). The SLC2 transport family comprises 14 transporters: GLUTs 1-12, GLUT13 (also called H(+)-myo-inositol transporter or HMIT), and GLUT14, which until 2002 was presumed to be a pseudogene of GLUT3 (Amir Shaghaghi *et al.*, 2017; Jones *et al.*, 2000b; Joost *et al.*, 2002; Wu



and Freeze, 2002). Most SLC2 family members function as uniporters, facilitating the passive movement of sugars between cells and across tissues, with the exception of HMIT, which handles the exchange of protons and inositol, primarily in the brain (Uldry *et al.*, 2004).

Because glucose is utilized as a metabolic substrate by many cell types, and can be utilized by the human body at a rate upwards of 200 g/day (Berg JM *et al.*, 2002), it must be readily available at sufficient concentrations in the blood, and must be capable of permeating tissues and crossing the blood-brain barrier. The latter requirement is particularly important, given that the brain is responsible for consuming the majority share of available glucose (Berg JM *et al.*, 2002). Basal levels of circulating glucose serum levels tend to be between 4-12 mM, which is necessary given this metabolic burden (Wright, 2009). To ensure widespread availability of glucose throughout the body, GLUT1 is expressed in high abundance within the lipid bilayers of erythrocytes and the endothelial cells lining the cardiovascular system (Kayano *et al.*, 1990). It is also highly expressed in cardiomyocytes, astrocytes, and in the endothelial cells that line the blood-brain barrier, ensuring continuous transport of glucose to the brain (Cura and Carruthers, 2012; Hertz *et al.*, 2007; Luiken *et al.*, 2004; Maher *et al.*, 1994).

## GLUT1 Deficiency Syndrome

Given the significant role transport proteins play in cellular metabolism and homeostasis, their proper function is critical to human health. Under-expression or dysregulation of metabolic transporters can often lead to severe clinical outcomes due to the body's inability to process certain molecules. Such is the case with glutamate transporter SLC1A2, which is implicated in the pathogenesis of amyotrophic lateral sclerosis (ALS) and Alzheimer's disease (AD) (Hediger *et al.*, 2013). Similarly, when defects arise within *SLC2A1*, the result is GLUT1-deficiency syndrome (G1DS), a genetic disorder stemming from loss of function to GLUT1 which is characterized by a range of neurological symptoms such as motor dysfunction, seizures, acquired microcephaly and intellectual disabilities (Gras *et al.*, 2014b). G1DS can be diagnosed by evaluating glucose levels in the cerebrospinal fluid relative to the patient's blood; elevated serum levels indicate ineffective transfer of glucose from the blood to its required destinations (Gras *et al.*, 2014a).

Around 100 different GLUT1 mutations have been reported, most of which are heterozygous *de novo* mutations, giving rise to random occurrences of the disease, although a handful of familial cases have been described (Klepper *et al.*, 2009; Wang *et al.*, 2005). Reported cases have included missense, nonsense, insertion, deletion, frameshift and splice mutations, with no apparent correlation between genotype and phenotype (Klepper and Voit, 2002; Wang *et al.*, 2005). Bi-allelic mutations to *SLC2A1* result in a near-total loss of residual GLUT1

function and, as a result, are more often than not embryonic lethal (Wang *et al.*, 2005). To date, the only treatment option for patients with G1DS is a ketogenic diet (KD), which reduces or eliminates the body's dependence on glucose, and instead provides high-fat and moderate-protein fuel alternatives.

### **GLUT1, tumor cells, and the Warburg Effect**

While a loss-of-function mutation to *SLC2A1* leads to G1DS, the opposite expression pattern can be just as detrimental. It has been well-established that in order to maintain an accelerated rate of growth and proliferation, cancer cells default to a metabolic pattern of increased glucose uptake and fermentation, even in aerobic conditions, rather than undergo oxidative phosphorylation (a process 10-100 times slower) as a means of energy production (Liberti and Locasale, 2016). This observation, known as the Warburg Effect, says that cancer cells must consume significantly higher amounts of glucose to facilitate this inefficient process and provide sufficient biomass for tumor growth (Molenaar *et al.*, 2009). And often times, the required kinetics of glucose transport acts as a rate-limiting step. In some cancers, GLUT1 protein expression may increase to meet the growing demand for glucose by the tumor cells, as evidence of GLUT1 overexpression has been detected in a range of cancer types, including ovarian, lung, brain, pancreatic and thyroid cancers (Chan *et al.*, 2011; Feng *et al.*, 2017; Wang *et al.*, 2007). This overexpression is thought to result from a variety of tissue-specific interactions with GLUT1 promoter enhancer elements (Amann *et al.*, 2011; Macheda *et al.*, 2005).

Solid tumor studies of breast and colorectal cancers have shown a direct correlation between areas of hypoxia and upregulated GLUT1 expression (Chen *et al.*, 2001; Kim *et al.*, 2013; Korkeila *et al.*, 2011). This has also been seen in studies involving ovarian and lung carcinoma cells, where *in vitro* induction of hypoxic conditions leads to an increase in GLUT1 mRNA levels (Chen *et al.*, 2001; Zhang *et al.*, 1999). When this relationship was studied in murine hepatocellular carcinoma, researchers found that GLUT1 upregulation resulted when a complex comprised of HIF-1 $\alpha$  and aryl hydrocarbon nuclear translocator (ARNT) bound to the GLUT1 promoter (Okino *et al.*, 1998). In other cases, upregulation isn't driven by hypoxia-induced gene regulation, but by hormones, particularly estrogen (Macheda *et al.*, 2005; Wellberg *et al.*, 2016). This (perhaps indirect) correlation is proposed to be due to an increase in glucose metabolism that occurs upon treatment with 17 $\beta$ -estradiol (E<sub>2</sub>) (Lippman *et al.*, 1987). While GLUT1 mRNA levels were not seen to change with hormone treatment, the increased consumption of glucose by the cells points to the potential for therapeutic intervention via GLUT1 inhibition. In fact, several studies have recently shown that the use of small molecule inhibitors of GLUT1 can be effective in reducing tumor size and sensitizing cells to radiation that were previously impervious (Peng *et al.*, 2019; Zhang *et al.*, 2010; Zhao *et al.*, 2016).

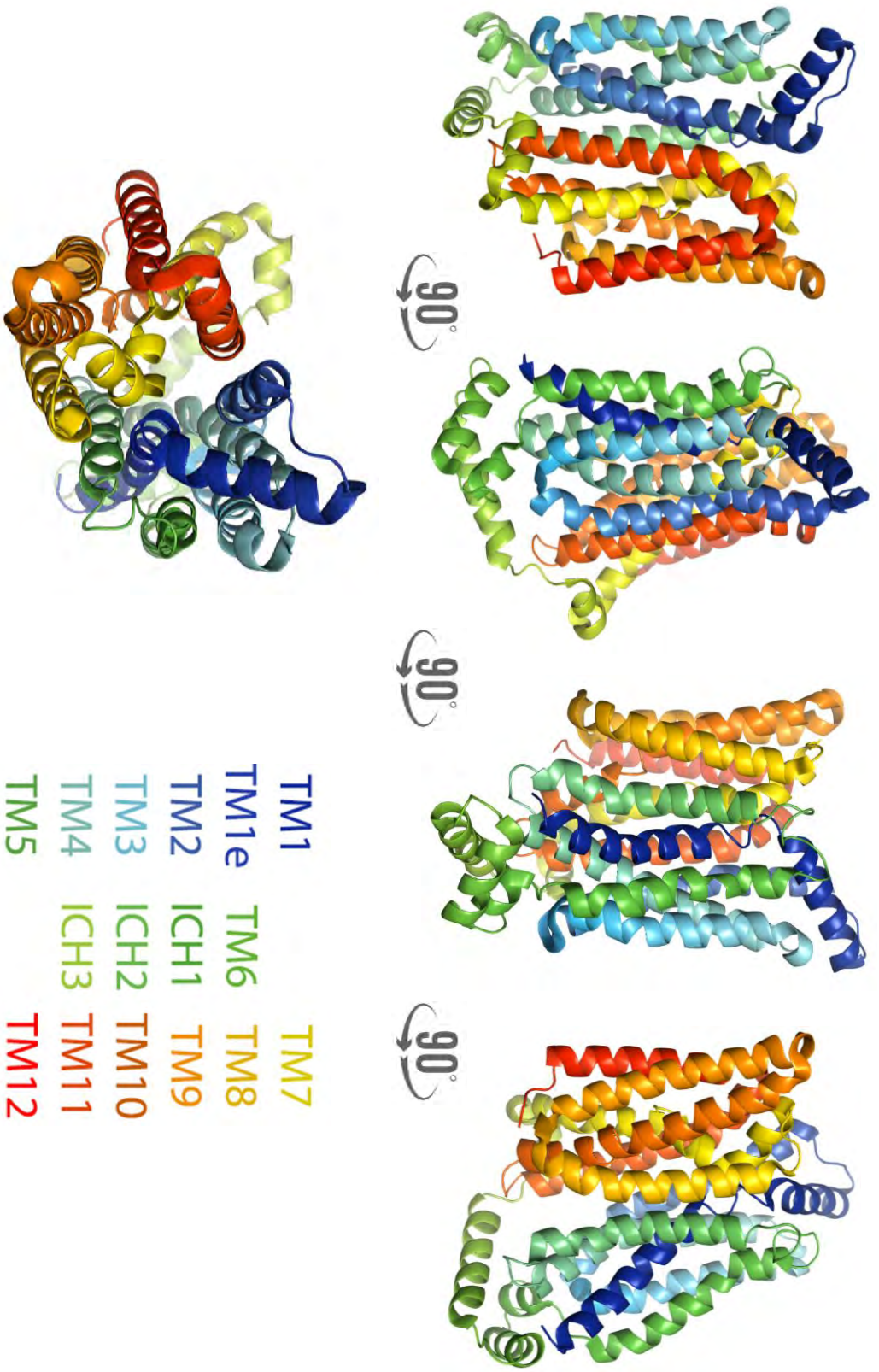
### 1.3.2 Structural determination

Similar to other members of the MFS family, GLUT1 topology consists of 12 transmembrane  $\alpha$ -helices, arranged in two inverted domains of six pseudo-repeats, generally referred to as the amino- and carboxy-terminal domains (Colas *et al.*, 2016). The two domains are connected by a long cytoplasmic loop. GLUT1 contains 492 amino acids, has a predicted molecular weight of ~55 kDa, and has a single site (N45) of N-linked glycosylation. In humans, two distinct degrees of glycosylation have been described, which results in a range of detected molecular weights between 45-60 kDa in biochemical studies (Asano *et al.*, 1991). Complex glycosylation patterns tend to occur in erythroid GLUT1, as compared to GLUT1 expressed in non-vascular brain cells such as astrocytes and oligodendrocytes (Maher *et al.*, 1994).

As previously discussed, the task of elucidating the structure of a complex membrane protein is often difficult due to the refractive nature of large, unstructured MPs to create organized crystals. However, the relatively small size of GLUT1 coupled with the symmetrical nature of its 12  $\alpha$ -helices and lack of large intracellular domains have aided in its crystallization.

In 2014, the Yan lab at the University of Beijing successfully solved the structure of GLUT1 to 3.2Å (PDB ID: 4PyP) (Deng *et al.*, 2014). To facilitate crystallization, two stabilizing mutations were added to the recombinant protein. The first was N45T, which prevented heterogeneity of GLUT1 due to

glycosylation, and the second was E329Q, which is reported to lock the protein in a static endofacial conformation. The crystallized protein, which was detergent-purified, exists as a monomer in an inward-facing orientation (see Figure 1.5) (Deng *et al.*, 2014; Schurmann *et al.*, 1997).



Top-down view

**Figure 1.5 Crystal structure of GLUT1** (PDB: 4PYP) For each of the four lateral perspectives, the structure was rotated approximately 90° CCW. The lower perspective is a top-down, extracellular view. Structure was obtained from RCSB (<http://www.rcsb.org>) (Deng, 2014) and formatted using PyMOL ("The PyMol Molecular Graphics System," 2015) (Figure on previous page.)

Shortly after the first apo structure was published, three more high-resolution structures were released by the Stroud lab, all of which were inhibitor-bound forms of human GLUT1 (Kapoor *et al.*, 2016). The first, a co-structure with cytochalasin B, was resolved to 3.0Å (PDB: 5EQI); the second, bound with glucose transporter-inhibitor 1 (GLUT-i1), was resolved to 2.9Å (PDB: 5EQG); and the third, bound with glucose transporter-inhibitor 2 (GLUT-i2), resolved to 2.99Å (PDB: 5EQH) (Kapoor *et al.*, 2016).

The four crystal structures that have been deposited to the PDB to date all display a detergent-purified, monomeric form of GLUT1 in the inward-open conformation. This representation of the transporter is in contrast to biochemical evidence demonstrating that endogenous GLUT1 exists as non-covalently bound homodimers and homotetramers (Hebert and Carruthers, 1991; Hebert and Carruthers, 1992).



### 1.3.3 Evidence of GLUT1 oligomerization

In studies that evaluated oligomerization state of cholate-solubilized GLUT1 under native (-DTT) and reducing (+DTT) conditions, distinct size populations were detected for each treatment group using sucrose-gradient ultracentrifugation and size-exclusion chromatography (Hebert and Carruthers, 1991). More recent studies have been performed that utilized Bioluminescent Förster Resonance Energy Transfer (BRET) to determine whether oligomeric state is dependent upon high levels of expression for dynamic aggregation to occur (Looyenga *et al.*, 2016). They also addressed whether oligomerization is the result of the elevated GLUT1 concentration found in erythrocyte membranes, or if it is possible in any cell type and if a high concentration is required for higher-order oligomers to form. With this work, the investigators were able to detect the formation of higher-order oligomers of GLUT1 by labeling the N- and C-terminus of GLUT1 with mCherry and NanoLuc, respectively, and measuring the levels of intermolecular BRET (a measure of oligomerization using this model) that resulted with increased GLUT1 expression levels (Looyenga *et al.*, 2016). What they found was that while a minimum concentration threshold of cell-surface GLUT1 may be required to catalyze the formation of higher-order oligomers (they estimated this to have an  $EC_{50}$  of  $1.27 \times 10^3$  molecules/ $\mu m^2$ ), the requirement was only about 3-fold higher than endogenous expression levels of GLUT1 in a 293T cell, and less than what exists for a red blood cell ( $2.21 \times 10^3$

molecules/ $\mu\text{m}^2$ ). In other words, GLUT1 oligomers could biologically exist on any cell type that expresses it. Moreover, when membrane complexes were disrupted with the addition of detergents, results indicated that although NanoLuc donor signal intensity was unchanged, no BRET signal was detected, suggesting a total loss of oligomeric structures in detergent (Looyenga *et al.*, 2016). This is consistent with earlier biophysical studies demonstrating that some detergents stabilize GLUT1 oligomeric structure while others results in reversible dissociation of GLUT1 tetramers into dimers and monomers (Graybill *et al.*, 2006).

Earlier studies demonstrate that purified, cholate-solubilized GLUT1 (which retains its native oligomeric structure) also co-purifies with sufficient lipid to form a lipid bilayer annulus surrounding the protein (Hebert and Carruthers, 1991). The oligomeric state of GLUT1 under different conditions is an important distinction to consider when evaluating the protein's role as a solute transporter. GLUT1 structural analysis (Deng *et al.*, 2014) and extensive biochemical studies on the monomeric protein (De Zutter *et al.*, 2013) indicate that the sugar translocation pathway consists of 8 amphipathic  $\alpha$ -helices (TMs 1, 2, 4, 5, 7, 8, 10 and 11) that are protected by four hydrophobic  $\alpha$ -helices (TM3, 6, 9 and 12), an arrangement presumed to be the basic functional catalytic unit of GLUT1 (De Zutter *et al.*, 2013). When present as a dimer, GLUT1 subunits are thought to function independently, despite being associated. However, in its tetrameric form, GLUT1 has been shown to display augmented capacity to transport

glucose (Zottola *et al.*, 1995). This difference in glucose transport suggests that GLUT1 may exhibit cooperative interactions between exofacial and endofacial glucose binding sites that present in this tetrameric form (Blodgett *et al.*, 2008; Blodgett *et al.*, 2007).

Understanding the specific kinetic behavior of GLUT1 across different cell types becomes important when considering how best to treat GLUT1-related diseases. Although G1DS represents a loss-of-function disorder, and the opposite is true in cancer, the ability to modulate GLUT1 activity with small molecules - whether activators or inhibitors - relies on a deeper understanding of its endogenous structure and predicted transport behavior. Due to the impact of oligomeric state on glucose transport kinetics, the ability to characterize the native protein structure is important, not only with regard to structure-based drug design, but also to predict the downstream augmentation or disruption of glucose transport that may result from ligand binding. It becomes important to understand whether tumor cells primarily contain GLUT1 in tetrameric form, for example, and what the impact may be on interrupting this endogenous state. Yet when standard membrane protein solubilization methods are used for this characterization, such information is often lost. Through the use of a non-denaturing solubilization method, it is possible to capture this structural information, which may potentially create a link between the impact of oligomeric state and glucose transport.

## 1.4 Membrane Protein Nanoparticles

### 1.4.1 Preface

Text and figures are reproduced from a published review that originally appeared in Biochemistry Society Transactions. This article focuses on recent progress in the field of polymer purification of membrane proteins, the limitations inherent in using styrene-maleic acid (SMA) and predictions for this area of research.

Simon, K.S., N.L. Pollock, and S.C. Lee, *Membrane protein nanoparticles: the shape of things to come*. Biochem Soc Trans, 2018. 46(6): p. 1495-1504.

Figure 1.6. Polymerization of styrene and maleic anhydride. Reprinted from “The styrene–maleic acid copolymer: a versatile tool in membrane research,” by Dörr, J.M., Scheidelaar, S., Koorengevel, M.C. *et al.* Eur Biophys J, (2016) 45: 3. 3-21. Copyright by Springer Berlin Heidelberg.

Figure 1.7. A schematic representation of the preparation of SMALP MP using SMA. Adapted from Dörr *et al.*, 2015 (full citation above).

Figure 1.9 Cryo-EM structures of two proteins in SMALPs. Figure contains data that originally appeared in two published articles.

- Panels A and B were reprinted from “Using a SMALP platform to determine a sub-nm single particle cryo-EM membrane protein structure” by Parmar, M., Rawson, S., Scarff, C.A., Goldman, A., Dafforn, T.R., Muench, S.P., and Postis, V.L.G., (2018), BBA Biomembranes, 1860(2), 378-383. Copyright 2018 by Elsevier.
- Panels C and D were reprinted from “Structure of the alternative complex III in a supercomplex with cytochrome oxidase” by Sun, C., Benlekbir, S., Venkatakrishnan, P., Wang, Y., Hong, S., Hosler, J. (2018) Nature 557, 123–126

Creative Commons User License: <https://creativecommons.org/licenses/by/4.0/>

### 1.4.2 Abstract

The use of styrene-maleic acid (SMA) for the purification of a wide range of membrane proteins (MPs) from both prokaryotic and eukaryotic sources has begun to make an impact in the field of MP biology. This method is growing in popularity as a means to purify and thoroughly investigate the structure and function of MPs and biological membranes. The amphiphilic SMA copolymer can effectively extract MPs directly from a native lipid bilayer to form discs approximately 10 nm in diameter. The resulting lipid particles, or SMALPs, contain SMA, protein and membrane lipid. MPs purified in SMALPs are able to retain their native structure and, in many cases, functional activity, and growing evidence suggests that MPs purified using SMA have enhanced thermal stability compared to detergent-purified proteins. The SMALP method is versatile and is compatible with a wide range of cell types across taxonomic domains. It can readily be adapted to replace detergent in many protein purification methods, often with only minor changes made to the existing protocol. Moreover, biophysical analysis and structural determination may now be a possibility for many large, detergent-destabilized MPs. Here we review recent advances in the area of SMALP purification and how it is impacting the field of MP biology, critically assess recent progress made with this method, address some of the associated technical challenges which may remain unresolved, and discuss

opportunities for exploiting SMALPs to expand our understanding of structural and functional properties of MPs.

### 1.4.3 Introduction

Proteins embedded within lipid-based membranes mediate the interactions between cells and their environment, define the boundaries of intracellular organelles and influence the passage of most molecules into and out of the cells. In short, they are of critical importance. However, the study of membrane proteins (MPs) presents several challenges: they are not typically abundant and can be difficult to stably purify and subsequently characterize. As a result, our understanding of the structure and function of MPs has failed to keep pace with our burgeoning knowledge of soluble proteins, limiting our understanding of fundamental biological processes and impacting our ability to treat diseases.

Detergent purification has been essential in the MP methodological toolkit and has allowed us to answer important questions surrounding the structure and function of key targets (Birch *et al.*, 2018). Head-and-tail detergents like dodecyl  $\beta$ -D-maltoside (DDM) act as a simple replacement for the lipid bilayer and provide a membrane mimetic. Detergent micelles are dynamic, and over time, detergent molecules will fully replace lipids adjacent to the MP. Without these lipids, many MPs no longer function natively. Indeed, purified MPs are generally considered to be unstable and susceptible to aggregation. There is an increasing

understanding that this instability is not an intrinsic quality of MPs, but a result of their removal from the lipid bilayer. Therefore, many recent advances in MP biochemistry have focused on preserving stability by developing purification methods that provide better membrane mimetics. These mimetics can be grouped into four classes: next-generation detergents (Birch *et al.*, 2018), amphipols (Le Bon *et al.*, 2018; Zoonens and Popot, 2014b), nanodiscs (Denisov and Sligar, 2017), and styrene-maleic acid lipid particles (SMALPs). While the first three technologies are essential for membrane protein science, they have been thoroughly reviewed elsewhere. The focus of this review is SMALPs, and the evolution of this method to involve new polymers and experimental progress.

The use of the styrene-maleic acid (SMA) copolymer allows the direct isolation of proteins and their local lipids from the surrounding crude membrane (Figure 1.6). SMA, which results from the hydrolysis of precursor styrene-maleic anhydride (SMA<sub>anh</sub>), consists of alternating styrene and maleic acid moieties, forming an amphipathic copolymer.

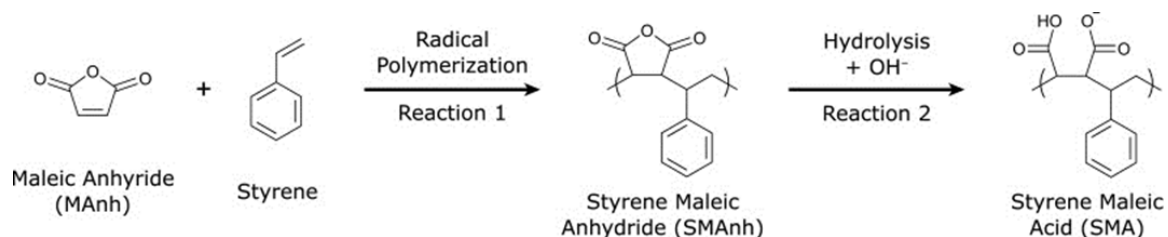


**Figure 1.6 Polymerization of styrene and maleic anhydride** at a 2:1 or 3:1 ratio followed by hydrolysis of the maleic anhydride moieties results in a styrene maleic acid copolymer suitable for use in the extraction of transmembrane proteins from cell membranes. The alternating hydrophobic (styrene) and hydrophilic (maleic acid) moieties of SMA render it amphipathic and capable of inserting into biological membranes.

The resulting SMA copolymers contain distinct ratios of styrene:maleic acid, depending on the polymerization reaction that is utilized to create the SMAAnh precursor. These differences in the SMA can modulate their properties in membrane protein purification. Isolation of transmembrane proteins using SMA creates monodisperse lipid discs of 10-11 nm in diameter containing the protein of interest as well as its surrounding native lipid bilayer (Knowles *et al.*, 2009) (See Figure 1.7).



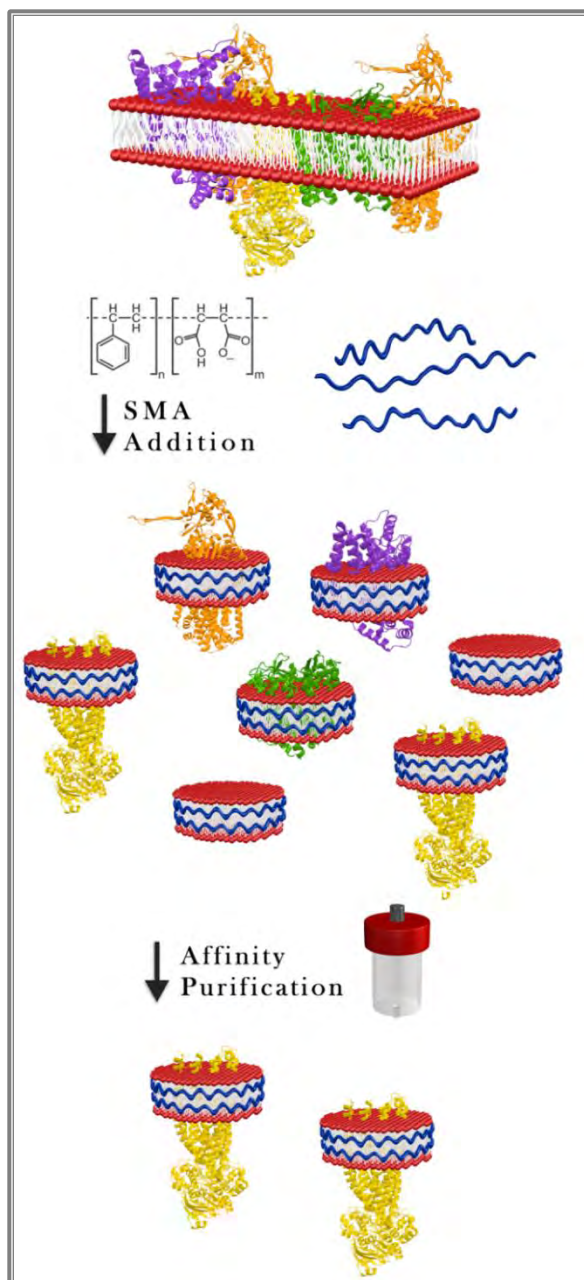


**Figure 1.7 A schematic representation of the preparation of SMALP MP using SMA** When SMA is added to the MP preparation, it inserts into the lipid bilayer forming a SMALP. The SMALP contains MP and the proximal lipid bilayer surrounded by SMA polymer. The SMALPs containing the MP of interest can be purified by affinity chromatography. Thus, the MP can be purified within its local lipid environment, which maintains structural integrity and stability. (Figure by Ashley Souza and adapted from Dörr *et al.* (Dörr *et al.*, 2016)).

Previous work with SMA has focused on its application as a drug delivery system for enhanced bioavailability of hydrophobic molecules, as an antiviral treatment, and as a tumor-targeting agent due to its enhanced cell permeability and size, which makes it well-suited for invading the compromised vasculature of tumors (Daruwalla *et al.*; Fang *et al.*, 2009; Greish *et al.*, 2004). More recently, however, SMA copolymer has been used to extract a variety of  $\alpha$ -helical and  $\beta$ -barrel transmembrane proteins, with much success (Gulati *et al.*, 2014; Orwick-Rydmark *et al.*, 2012; Parmar *et al.*, 2018). For this application, SMA copolymers with a ratio of either 2:1 or 3:1 are most often utilized (Orwick-Rydmark *et al.*, 2012; Prabudiansyah *et al.*, 2015). By capitalizing on the properties of SMA as an amphipathic copolymer capable of permeating a cell membrane, we can create SMA lipid particles (SMALPs) that contain an intact MP in its native form, with a lipid composition likely to reflect the native membrane environment. In contrast, detergent-purified proteins typically do not retain interactions with lipids or other proteins.

One significant advantage of the SMA purification method is the absence of detergent from the protocol. As a consequence, proteins purified in this way can be extracted along with both their natural lipid support-system and any interacting proteins. Not only does this provide useful information about associated proteins and their potential roles in regulating MPs, but it also offers a means for identifying the endogenous lipid composition surrounding the protein of interest (Jamshad *et al.*, 2015; Landreh *et al.*, 2016; Lee, 2004, 2005). Another

advantage is the remarkable stability of proteins that have been purified into SMALPs. It is common for protein-SMALPs to remain intact and monodisperse at 4°C for at least a week, and to have the ability to undergo several rounds of freeze/thaw with minimal loss to particle integrity or protein function (Lee and Pollock, 2016; Logez *et al.*, 2016).

In 2016 we presented a summary of research using the SMALP technology (Lee and Pollock, 2016). We considered its advantages and limitations. As part of that discussion, we explored three potential future directions for the SMALP field: 1) expanding our understanding of amphipathic copolymers and the means of improving their utility; 2) using SMALPs to solve high-resolution structures of MPs, and 3) exploring the potential of using SMALPs to better understand the local lipids surrounding an MP. It is a remarkable testament to the utility of this method that progress has already been made in all three areas and that the number of publications pertaining to this technology has tripled since 2016 (Figure 1.8). In this section, we will return to these predictions. We will also discuss new developments related to SMA and its associated methods, and consider what could and should be next.

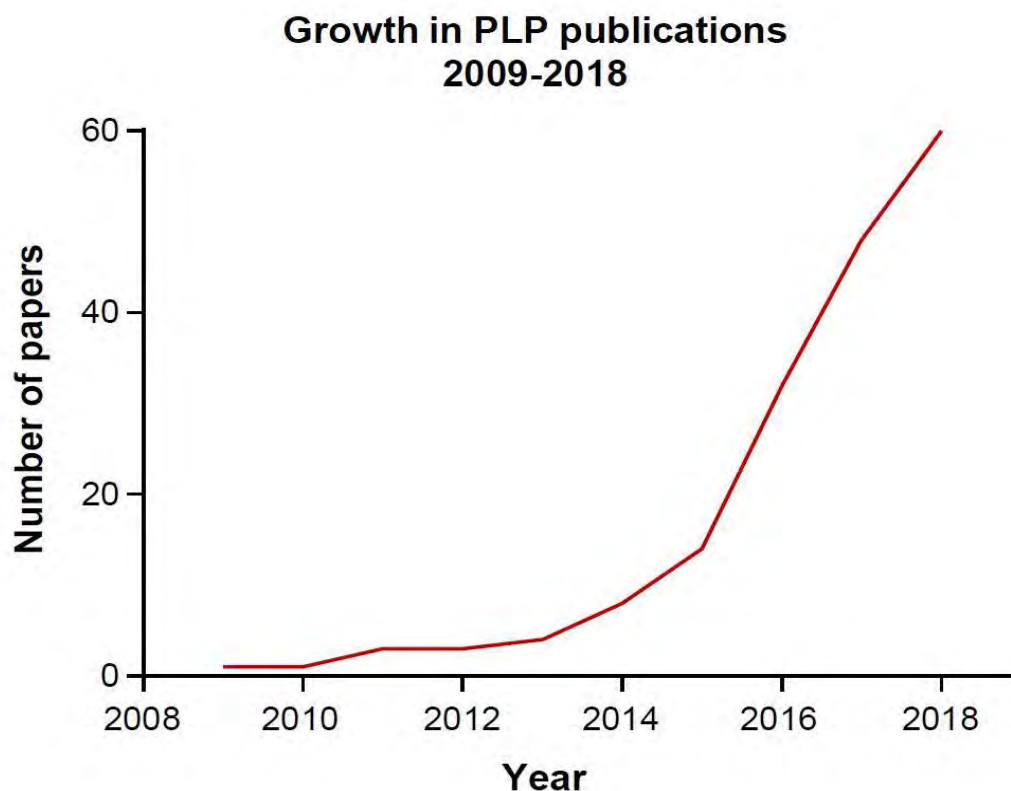


**Figure 1.8 Growth of publications describing membrane proteins purified using SMALP technology and its associated derivatives from 2009 to 2018 (Year-to-date)** The graph shows the total number of publications by the end of each year. Data was assembled by searching for [SMALP or DIBMA or styrene-maleic acid] and [membrane protein].

#### 1.4.4 Overview of membrane mimetics

##### Next-generation detergents

The use of head and tail detergents has been comprehensively discussed by many authors (Helenius and Simons, 1975; Moraes *et al.*, 2014; Seddon *et al.*, 2004) and detailed presentation of this material is outside the scope of this review. However, it is important to emphasize that detergents continue to be a vital tool in membrane biochemistry and an area for innovation. Over the years there have been attempts, some very successful, to create detergents that provide stability to membrane proteins [foscholine, lyso-lipids]. Most recently the maltose-neopentyl glycol detergents have produced promising results (Chae *et al.*, 2010).

##### Amphipols

Amphipathic polymers, or amphipols, were the first deliberate effort to move beyond detergents for membrane protein stabilization. Amphipols (APols) were created with the intent of stabilizing membrane proteins by binding tightly to hydrophobic portions of the protein and replacing the lipid bilayer (Etzkorn *et al.*, 2013; Park *et al.*, 2011; Scott *et al.*, 2013; Thomas *et al.*, 1994; Tribet *et al.*, 1996). Several iterations and functionalized versions have been reported that cover a wide variety of polar groups, bestowing a range of stabilizing properties (Bon *et al.*, 2014; Popot *et al.*, 2011; Scott *et al.*, 2013). The most widely-characterized APol, known as A8-35, is comprised of short-chain sodium

polyacrylates (~35 units) derivatized with octylamine and isopropylamine functional groups (Calabrese *et al.*, 2015; Giusti *et al.*, 2012; Popot *et al.*, 2011; Tribet *et al.*, 1996; Zoonens *et al.*, 2007; Zoonens and Popot, 2014a; Zoonens *et al.*, 2014). In some cases, it has been possible to use amphipols to support the refolding of membrane proteins to their native conformation, either to recover denatured protein from inclusion bodies within a cell or to assist in cell-free expression systems *in vitro* (Baneres *et al.*, 2011; Pocanschi *et al.*, 2006).

Despite stabilizing proteins, amphipols have not typically been used to solubilize membranes; rather, a traditional detergent is used to purify protein from the lipid bilayer, which is subsequently replaced with an amphipol (Zoonens *et al.*, 2014). Moreover, in the vast majority of cases where amphipols have been successful, the target protein has been prokaryotic in origin, and perhaps inherently more stable (Zoonens and Popot, 2014a).

### **Nanodiscs**

Nanodiscs are self-assembling lipid discs that are surrounded by an amphipathic helical polymer, known as the membrane scaffold protein (MSP). Similar to amphipols, nanodiscs rely on detergent purification for the removal of the target protein from its lipid bilayer. In this case, however, exogenous lipids are also added along with the MSP, while detergent molecules are simultaneously removed with the addition of adsorbent beads (Bayburt and Sligar, 2010; Denisov and Sligar, 2017). In its simplest form, a nanodisc consists

of phospholipids that form the nanodisc bilayer and an MSP, recombinant human apolipoprotein A-1 (ApoA1) that holds the raft together (Lee *et al.*, 2016a). The length of the scaffold protein dictates the nanodisc size and can be increased or decreased to accommodate the protein being stabilized. Evaluating different molar ratios of MSP to protein and lipid to MSP is necessary to determine the composition that best stabilizes each target protein, which can entail extensive screening (Denisov and Sligar, 2017; Mitra, 2013). One major advantage of this approach is the ability to regulate nanodisc size to ensure homogeneity. This is of particular concern when the intended goal is biophysical characterization or structural analysis of the material, where variable raft sizes could be a hindrance (Bayburt and Sligar, 2010; Lee *et al.*, 2016a). Both amphipols and nanodiscs have a good track record for compatibility with standard methods in biochemistry, biophysics and structural biology (Gao *et al.*, 2016; Hagn *et al.*, 2013; Huynh *et al.*, 2014).

### **Polymer-based lipid particles (PoLPs)**

The use of the styrene maleic acid (SMA) copolymer allows the direct isolation of proteins and their local lipids from the surrounding crude membrane. Isolation of transmembrane proteins using SMA creates monodispersed lipid disks of 10-11 nm in diameter containing a single molecule of the protein of interest, as well as its surrounding native lipid bilayer (Knowles *et al.*, 2009). This protein/lipid disc, which is held in place by the amphipathic SMA band, can be purified using affinity purification to ensure clean evaluation of the target protein

without the need for detergents. By capitalizing on the properties of SMA as an amphipathic copolymer capable of permeating a cell membrane, we can create SMA lipid particles (SMALPs) that contain an intact MP in its native environment, allowing the protein to stay in contact with both its natural lipid support-system and any interacting proteins.

#### **1.4.5 Latest applications of SMALPs**

##### **Use of SMALPs in high-resolution structure determination**

High-resolution structural information is a cornerstone of protein biochemistry. It is critical that new purification methods yield MP samples that facilitate structure determination. Therefore reports of atomic-resolution structures from X-ray crystallography and cryo-transmission electron microscopy (cryo-EM) are an essential validation of the SMALP method.

##### *Crystallography using LCP*

The first X-ray structure of an MP extracted and purified as a SMALP was reported by Broecker *et al.* (Broecker *et al.*, 2017). SMA-purified recombinant microbial rhodopsin (bR), a seven-transmembrane  $\alpha$ -helical MP, was crystallized using the lipidic cubic phase (LCP) method (van 't Hag *et al.*, 2016) resulting in a structure of 2.0Å resolution. This comparative study undertook the parallel LCP crystallization of both SMA- and detergent-purified bR. In the LCP method, the



MP spontaneously transfers from the SMALP or detergent micelle into the lipid *meso* phase, where crystallogenesis occurs. The two bR structures were nearly identical: the bR-SMALP was determined to a resolution of 2.0-Å and the detergent-purified bR resolved to 2.2-Å. This paper showed that high-resolution structural determination is possible for MPs purified using the SMALP methodology.

#### *High-resolution cryo-EM structures*

Despite success using the LCP method, most MPs have remained elusive to crystallography. To date, only the LCP method has been reported as a successful means for crystallizing an SMA-purified protein. The advent of the cryo-EM revolution, however, has provided a new path to high-quality, high-resolution structures of MPs (Zhang and Liu, 2018). Cryo-EM offers structural biologists a way to visualize MPs in several different orientations by suspending particles in vitreous ice prior to imaging. Recent advances in instrumentation have resulted in a sharp increase in the number of high-resolution MP structures deposited into the Protein Data Bank (PDB).

Following an early 23Å structure of the *Escherichia coli* multidrug transporter AcrB in SMALPs (Postis *et al.*, 2015), Parmar *et al.* recently published the first sub-nanometer resolution structure of a protein-SMALP (Parmar *et al.*, 2018). The resulting AcrB-SMALPs Cryo-EM map (Figure 1.9a and b) is consistent with high-resolution crystal structures of other EM-derived

maps for AcrB (Ababou and Koronakis, 2016; Murakami *et al.*, 2002). These studies demonstrated the suitability of the SMALP method for structural analysis of MPs. It is interesting to note that when preparing cryo-EM grids, the authors found it essential to blot the grids with ash-free filter paper low in metal ion content; its use proved critical to avoid destabilizing the AcrB-SMALPs, which are sensitive to divalent cations.

Very recently, Sun *et al.* (Sun *et al.*, 2018) showed that protein-SMALPs could be visualized at high resolution using cryo-EM when they published a 3.4 Å resolution structure of a protein-SMALP (Figure 1.9c and d). Alternative Complex III (ACIII) was isolated as a functional supercomplex with an aa3-type cytochrome c oxidase (cyt aa3) using 3:1 SMA. Collectively this represents a total mass of 464 kDa and 48-TM spanning  $\alpha$ -helices, the largest SMA-purified protein complex reported to-date. The final map of this complex revealed 11 lipid molecules adjacent to the protein and post-translational modifications (PTMs) that were previously indiscernible when traditional detergent purification methods were employed. This work highlights a significant advantage of SMA purification, which is the ability to gather information about the native protein complex, including endogenous lipids and associated binding partners - both soluble and membrane-bound - without the need for cross-linking (Komar *et al.*, 2016; Laursen *et al.*, 2013; Reading *et al.*, 2017).

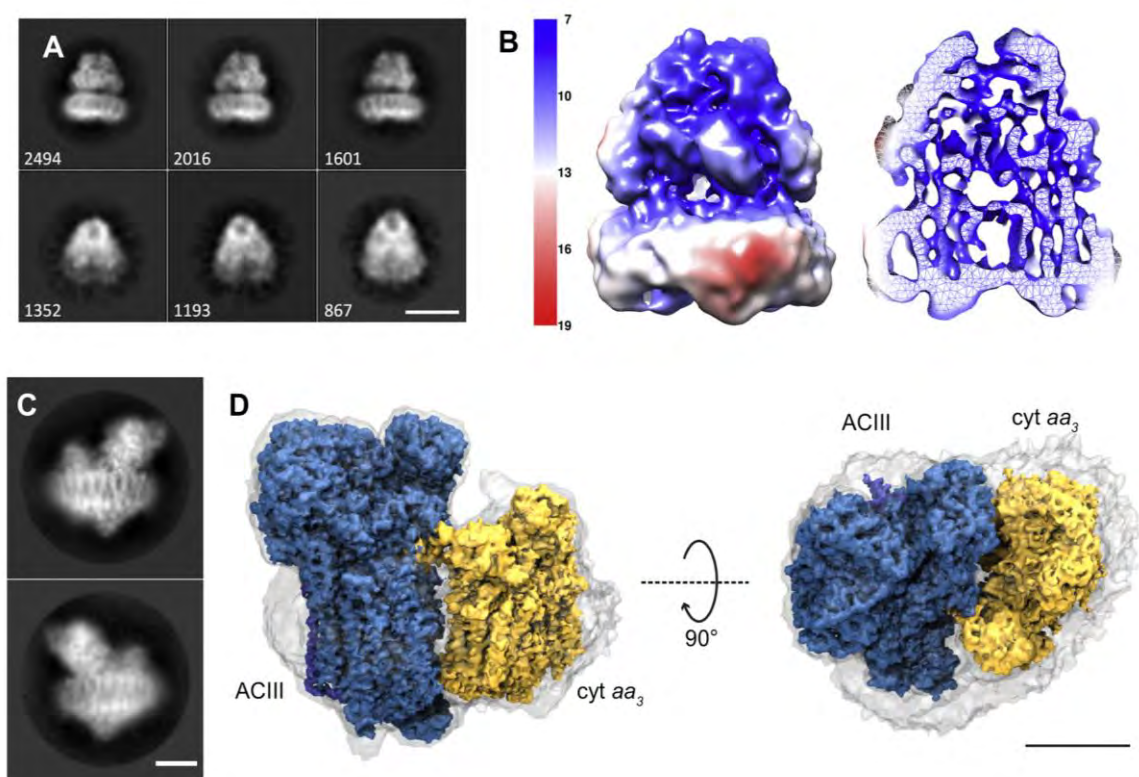


**Figure 1.9 Cryo-EM structures of two proteins in SMALPs** (a) AcrB-SMALP from *E.coli* (Parmar *et al.*, 2018) Representative 2D classes for the AcrB single particle cryo-EM dataset. Side views of AcrB-SMALP and high angle views shown on the top and bottom row, respectively. The corresponding particle number in each class is shown on the bottom left. The white scale bar represents 100 Å. (Parmar *et al.*, 2018) (b) The AcrB-SMALP 8.8 Å single particle reconstruction coloured by local resolution and shown as a surface (left) and slice through (right) (c) Two representative 2D class average images of the Alternative Complex III (ACIII) in a supercomplex with an aa<sub>3</sub>-type cytochrome c oxidase (cyt aa<sub>3</sub>) from *Flavobacterium johnsonia*, in a SMALP nanodisc (Laursen *et al.*, 2013). (d) Side (left) and top (right) views of the ACIII–cyt aa<sub>3</sub> supercomplex cryo-EM map. The transparent surface indicates the boundary of the nanodisc. Scale bars, 50 Å. (Sun *et al.*, 2018)

## Hydrogen-Deuterium Exchange-Mass Spectrometry

Another method of interrogating protein structure and dynamics is Hydrogen-Deuterium Exchange-Mass Spectrometry (HDX-MS), an approach historically challenging for analyzing hydrophobic MPs. HDX-MS, which measures the exchange rate of deuterium in place of the amine hydrogens along the polypeptide backbone, provides valuable insight into higher-order protein folding of solvent-accessible portions of the molecule. This is accomplished by incubating the protein of interest in deuterated buffer for set time intervals before quenching the reaction in low-pH buffer and immediately freezing the sample to prevent loss of deuterium atoms (referred to as “back-exchange”). Despite several advantages to applying HDX-MS to stable, monodisperse SMALPs as opposed to MPs indiscriminately surrounded by detergent micelles, it has remained a challenge, as exposure to quench buffer causes the sample to immediately and irreversibly aggregate due to the pH sensitivity of SMA. To overcome the hurdle, Reading *et al.* (Reading *et al.*, 2017) have outlined a protocol for HDX evaluation that is suitable for use with SMALPs. They prevented total protein aggregation during the quench step by including 0.1% DDM to the buffer, and avoided sample incompatibility issues with ESI-MS by filtering the sample through a pre-chilled 0.22  $\mu\text{m}$  spin filtration device following trypsin digestion to remove lipid molecules. This overcomes the aforementioned technical issue to provide another sample characterization method that is compatible with protein-SMALPs.

### Exploiting SMALPs for lipidomics work

Retention of local lipids is arguably the most unique aspect of SMALPs, as compared to other membrane mimetic systems. Lipids have been detected in SMALPs in several studies and lipid preferences for a number of proteins have been characterised for the first time using SMALPs (Smirnova *et al.*, 2011; Swainsbury *et al.*, 2018). A study of *Rhodobacter sphaeroides* proteins solubilized by SMA showed that they retained significant numbers of lipids (Dorr *et al.*, 2017). However, they also related the solubilization efficiency of *R. sphaeroides* membrane proteins to their local lipid environment. This finding supports a similar observation that some membrane regions display resistance to solubilization by SMA (Hall *et al.*, 2018). This highlights the fact that to use SMA to probe the lipidomics of MPs, we first need to develop a detailed understanding of the ability of SMA to solubilize proteins from different membrane types and regions. Similarly, the tendency of protein-SMALPs to retain, lose, gain or exchange lipids must be better understood or we risk misinterpreting data on lipid preferences of proteins (Barrera and Robinson, 2011; Cuevas Arenas *et al.*, 2017; Cuevas Arenas *et al.*, 2016; Grethen *et al.*, 2018). Nonetheless, it is clear that SMALPs provide a tool to address questions about the lipid preferences of MPs, which otherwise lack practical approaches.

### **Mass spectrometry of membrane proteins**

As a more general application, mass spectrometry (MS) is a powerful technique for the detection of both proteins and lipids. Obtaining intact masses of MPs and their complexes is challenging, as their hydrophobic regions are difficult to isolate and ionize (Laganowsky *et al.*, 2013). However, some methods have been reported for MS using membrane protein-detergent complexes (Gupta *et al.*, 2018; Stroud *et al.*, 2018), that may be adaptable to SMALPs. Significantly, such studies are also beginning to probe the lipids that associate with MPs; SMALPs are an excellent platform for such studies, since they isolate MPs along with their local lipids.

#### **1.4.6 Understanding and Developing the Polymer Family**

Fundamentals of the formation of SMALPs have been investigated largely using lipid-only discs (Barrera and Robinson, 2011; Cuevas Arenas *et al.*, 2017; Cuevas Arenas *et al.*, 2016; Grethen *et al.*, 2018). This has recently been thoroughly reviewed (Vargas *et al.*, 2015) and a couple of key points emerge. Firstly, SMA is an effective but mild solubilizer of model lipid bilayers (Hall *et al.*, 2018). However, SMALPs may be more dynamic than we initially assumed, and there is evidence that lipids exchange between discs (Barrera and Robinson, 2011; Cuevas Arenas *et al.*, 2016). Secondly, this work has also shown that the size of the discs can be, to some extent, manipulated by adjusting the ratio of

polymer to lipid during disc formation (Lee *et al.*, 2016b). This modification may allow us to accommodate larger proteins within SMALPs. However, it is important to reiterate that much of this work has been done using lipid-only SMALP discs, and their behavior may be altered by the presence of a membrane protein.

While the SMALP technology already has a strong track-record for MP purification it is not without limitations, principally its sensitivity to divalent cations (e.g.,  $Mg^{2+}$ ) and pH (SMA is insoluble below pH 6.5) (Oluwole *et al.*, 2017). These properties, which are the result of the negatively charged, outward-facing maleic acid moiety, complicate certain analyses such as  $MgCl_2$ -dependent ATPase assays.

Another challenge associated with this method has been the light-absorbing properties of SMA. Its styrene group absorbs at ~260 nm, which partially overlaps with UV-absorption by proteins. While purified protein-SMALPs contain only the SMA associated with each nanodisc, enough may be present to interfere with UV absorption and light-scattering assays (e.g., differential scanning fluorimetry, static light scattering and protein quantification).

### **Alternative and Functionalized Polymers**

The limitations of SMA have prompted the rapid discovery and development of additional disc-forming polymers. Both the hydrophilic and hydrophobic moieties of SMA can be varied to make new copolymers. In addition, the maleic acid side chains can be chemically altered to adjust their

properties, without sacrificing the ability of the polymers to form lipid discs. The properties of a selection of the new and alternative polymers are summarized in Table 1.2.

**Table 1.2 Selected alternative and functionalized amphipathic polymers, showing structures, size of nanodiscs, and tolerance to divalent cations**

	Styrene-Maleic Acid (SMA)	Diisobutylene Maleic Acid (DIBMA)	Styrene-Maleic Imide (SMI)	Styrene Maleimide Quaternary Ammonium (SMA-QA)
Chemical structure				
Optimum pH for nanodisc preparation	$\geq 6.5$	7.3, 8.4	5 - 7.8	2.5 - 10
Size of nanodiscs	10-13 nm	18 nm	6-11 nm	30 nm
Tolerance to divalent cations	5 mM	35 mM	> 100 mM	$\leq 200$ mM

To date there are limited publications describing the application of these new polymers to membrane proteins, and it will be interesting to see how this develops in the future.

#### *Diisobutylene maleic acid (DIBMA)*

Similar to SMA, DIBMA is a maleic acid-containing copolymer capable of solubilizing MPs into lipid discs known as DIBMALPs (Ravula *et al.*, 2018). In this



case, the hydrophobic region of the polymer consists of aliphatic di-isobutylene and therefore lacks the aromatic styrene moiety found in SMA. Hence, DIBMA is compatible with optical spectroscopy permitting routine characterization of the sample (Ravula *et al.*, 2018). Lipid exchange rate studies using FRET indicate that DIBMALPS may retain lipid bilayers better than SMALPs, which presents an exciting opportunity to investigate the lipids associated with different proteins (Cuevas Arenas *et al.*, 2016). Surprisingly, DIBMA is reported to be more tolerant to divalent cations than SMA (despite the presence of the maleic acid moiety), remaining soluble in up to 35mM CaCl<sub>2</sub> and >20 mM MgCl<sub>2</sub> for lipid-only DIBMA particles. Improved cation tolerance could be critical for functional characterization of proteins that rely on magnesium or calcium binding for their function. However it should be noted that the insensitivity to divalent cations has not yet been reported on DIBMALPs containing a membrane protein (Schmidt and Sturgis, 2018).

#### *Styrene maleic imide (SMI)*

Styrene maleic imide (SMI), a positively charged polymer comprised of alternating styrene and maleimide moieties, is also capable of solubilizing MPs into lipid discs of approximately 11 nm in diameter (Cuevas Arenas *et al.*, 2017; Cuevas Arenas *et al.*, 2016). As is the case with SMA, the presence of the styrene head group complicates analysis involving optical spectroscopy; however, unlike SMA, it can tolerate divalent cations at high concentrations, and its solubility range is pH 5 - 7.8. Biophysical characterizations of lipid-only SMI-

lipid particles indicate that its lipid content is low, but that SMI is capable of solubilizing proteins across a broad range of molecular weights (Cuevas Arenas *et al.*, 2017).

#### *Styrene maleimide quaternary ammonium (SMA-QA)*

Ravula *et al.* (2018) describes the synthesis of a pH-resistant form of SMA that is effective at solubilizing proteins into discs >20 nm in diameter, and within a pH range of 2.5 – 10: styrene maleimide quaternary ammonium (SMA-QA) (Lindhoud *et al.*, 2016). The resulting lipid discs exhibit “ultra-stability” even in the presence of divalent metal ions.

#### *Thiolated styrene-maleic acid (SMA-SH)*

Functionalization of SMA to include a thiol group has also been reported, resulting in a lipid-solubilizing derivative called SMA-SH (Hall *et al.*, 2018; Morrison *et al.*, 2016a). Using a fluorescent label attached to the SMA-SH, Förster resonance energy transfer (FRET) experiments have demonstrated that polymer, as well as lipids, can be rapidly exchanged between discs. This is another key insight into the dynamic nature of SMALPs (Morrison *et al.*, 2016b). The production of polymers that can be conjugated with a range of functional groups will also offer new possibilities for how protein-SMALPs can be studied (Morrison *et al.*, 2016a).

### 1.4.7 Perspectives

Head-and-tail detergents, MSPs, APols, SMA and other amphipathic polymers share many similarities. By some measures, SMA combines the best features of the other systems, but we are a long way from understanding both its full capabilities and its full limitations. The publication of high-resolution structural data from both crystallography and cryo-EM are an enormous milestone and provide a high-profile vindication of the SMALP method. Meanwhile, its proven utility in biophysical and functional work is growing as more publications appear. The next challenge is to build on the existing success to contribute further insight into membrane protein structure and function.

Because the capacity to extract the local lipid environment surrounding a protein is a unique aspect of SMALPs, it provides an opportunity to study the lipids associated with MPs. However, our understanding of the dynamics of SMALPs is still developing, and until we understand the fundamentals, we may struggle to interpret lipidomic data. On a similar note, reintegration of proteins from SMALPs into a bulk lipid bilayer would be a significant milestone and would open up the possibility of isolating proteins for transport assays.

In order to maximize the potential of SMALPs, there is a need to catalogue successes as well as failures with SMA (and similar polymers). Early successes have been dominated by more abundant bacterial proteins, arguably the lower-hanging fruit. As we turn to SMALPs to purify less abundant, and potentially less

stable, proteins, it is essential to document outcomes, both positive and negative, to deepen our understanding of the potential of this method.

Another consideration is how we can use SMALPs mostly effectively. The generic applicability of 2:1 SMA has frequently been discussed as an advantage of this method, but as more polymers are developed, we may be moving back towards the screening approach that has become *de rigueur* for detergents. Indeed, important advances have been reported using both the 3:1 and 2:1 S:M polymer variants and each may be appropriate for different proteins and studies. An alternative to screening would be to adopt a funnel approach, whereby the most widely applicable polymer (2:1 SMA) is tried first and others are used if needed for specific applications and proteins. Once again, extensive and honest cataloguing of results will increasingly allow patterns to emerge from the data that can guide these strategies.

Amongst the unknowns, it is critical to remember that SMA has already provided a generic, cost-effective and successful method for isolating a wide range of MPs, including several considered to be highly challenging (Logez *et al.*, 2016; van 't Hag *et al.*, 2016). While the fundamental chemistry of SMA presents certain challenges when it comes to biophysical and biochemical characterization of protein-SMALPs, the rapid accumulation of data and publications are indisputable proof of its utility.

As more lipid-disc forming polymers are discovered and synthesized, it may be useful to consider them as a family of polymer/lipid particles (PLPs), rather than just SMALPs. However, the remarkable ability of SMA to directly and efficiently solubilize and stabilize MPs bodes well for its ongoing potential to deepen our understanding of membrane proteins. As MP purification continues to evolve and the limits of our capabilities become apparent, we must address these limitations by continuing to develop new technologies and by using them judiciously.

## 1.5 Scope of Thesis

This thesis attempts to offer a multidimensional approach to studying the structural and biochemical properties of CFTR and GLUT1. It provides new evidence for the molecular mechanism of the CF-causing  $\Delta F508$  mutation and its second-site suppression by V510D, and evaluates the stabilizing effects of novel SSSM P1050R on  $\Delta F508$ -CFTR. Given that cystic fibrosis continues to be an area of high unmet medical need, a more thorough understanding of the effects of the  $\Delta F508$  mutation on CFTR conformational dynamics and how it leads to the molecular pathology of CF is of critical importance. However, several challenges exist with studying CFTR, a large membrane protein. For this reason, our team utilized molecular dynamics simulations to visualize full-length WT and  $\Delta F508$ -CFTR, and added suppressor mutations V510D and R1070W to  $\Delta F508$ -CFTR as a proof-of-concept for the MD simulations. From the four simulations generated, several testable hypotheses regarding  $\Delta F508$ -CFTR molecular pathology and the role of SSSMs within it were gleaned. Through mutational analysis on full-length CFTR and purified NBD1, I was able to support the validity of the predictions that were obtained, including the role of K564 in V510D second-site suppression, the occurrence of helical instability within TMD2 of  $\Delta F508$ -CFTR, and the stabilizing impact of novel SSSM P1050R when combined with NBD1 stabilizer V510D (Chapter II).

This thesis also explores the utility of styrene-maleic acid solubilization of both CFTR (Chapter III) and GLUT1 (Chapter IV) into lipid nanoparticles. By developing a protocol for CFTR solubilization using SMA, I was able to work toward evaluation of the protein's native structure without interference from potentially destabilizing detergents. This also allowed for the determination of the surrounding lipid content, which is an element of CFTR biology that has not yet been published, yet is critically important to our ability to study the structure and function of CFTR in its purified form. Furthermore, with the application of this non-denaturing solubilization protocol to GLUT1 protein purification in both HEK expression cells and primary erythrocytes, I was able to elucidate endogenous GLUT1 oligomerization in both systems, and identify protein interactions in erythrocytes without the need for cross-linking. This work represents the first time GLUT1's native oligomeric state in both an expression system and primary cells have been visualized with Native PAGE separation, and supports the use of SMA for native membrane protein complex characterization and purification.

## CHAPTER II: DETERMINING THE MOLECULAR MECHANISM OF SUPPRESSOR MUTATION V510D AND THE CONTRIBUTION OF HELICAL UNRAVELING TO THE $\Delta F508$ - CFTR DEFECT

### 2.1 Preface

Chapter II is a collaborative study that is in the final stages of manuscript preparation and will be submitted for publication within 2019.

❖ **Simon K.**, Nagarajan K, Mechin I, Duffy, C, Manavalan P, Altmann S, Majewski A, Foley J, Maderia M, Hilbert B, Batchelor J, Ziegler R, Kaczmarek S, Bajko J, Kothe M, Scheule R, Nair A, and Hurlbut G. Determining the Molecular Mechanism of Suppressor Mutation V510D and the Contribution of Helical Unraveling to the  $\Delta F508$ -CFTR Defect. *Manuscript in preparation*

This project was conceptualized by Greg Hurlbut and Ron Scheule. Tested hypothesis were based on homology models and molecular dynamics simulations by Partha Manavalan, Ingrid Mechin, Karthigeyan Nagarajan and Anil Nair. I contributed to the design of experiments and performed the cloning, western blotting and HRP trafficking assays for the V510D mechanism of action work. Stefan Kaczmarek and Jeff Bajko performed the electrophysiological evaluation of K564 mutational constructs. I performed NBD1 thermal shift assays with the help of Robin Ziegler using protein expressed and purified by Joe Foley. I created NBD1-V510D crystals with guidance from Michael Kothe. The crystal structure was solved by Brendan Hilbert and Joseph Batchelor. Caroline Duffy performed the Q1042, L1096 & P1050R mutation construct cloning and initial western blotting evaluation. Additional constructs for the P1050R work were made by me, Steve Altmann, Aliza Majewski and Matt Maderia, and I performed the additional P1050R western blot and HRP trafficking assays. I analyzed and interpreted all data with the exception of the crystal structure. I wrote the text and made the figures for this manuscript with contributions from Gregory Hurlbut, Ingrid Mechin, Partha Manavalan and Anil Nair.



## 2.2 Abstract

Cystic fibrosis (CF) results from mutations within the gene encoding the Cystic Fibrosis Transmembrane Conductance Regulator (CFTR), a transmembrane chloride channel found on the apical surface of epithelial cells. The most common CF-causing mutation results in a deletion of Phenylalanine 508 ( $\Delta$ F508-CFTR), a residue normally found within the NBD1 domain. Loss of F508 causes NBD1 to be less thermodynamically stable and prevents proper tertiary folding of CFTR. As a result, CFTR is not properly trafficked to the cell surface. Recently, progress has been made towards the development of small molecule “correctors” that can restore CFTR tertiary structure and stabilize the channel to overcome the instability of  $\Delta$ F508-CFTR. However, the resultant improvement in channel activity has been modest, and the need for potent correctors remains. To fully inform such efforts, a better understanding of the molecular pathology associated with  $\Delta$ F508-CFTR is required. Here we present a comprehensive study of the impact of F508 deletion on both full-length CFTR and purified NBD1. Through the use of homology modeling, molecular dynamics simulations, mutational analysis, biochemical, biophysical and functional characterization studies, we obtained insight into how the  $\Delta$ F508 mutation may lead to helical unraveling of TMs 10 and 11, and how suppressor mutations V510D and R1070W, as well as novel SSSMs identified in this work, may act to rescue  $\Delta$ F508-CFTR maturation and trafficking.

## 2.3 Introduction

Cystic Fibrosis (CF) is a genetic disease caused by mutations to the gene that encodes cystic fibrosis transmembrane conductance regulator (CFTR), a chloride channel found in the apical membrane of epithelial cells. Its basic topology consists of two transmembrane domains (TMD1 and TMD2), two nucleotide-binding domains (NBD1 and NBD2) and a unique regulatory (R) domain with multiple phosphorylation sites (Amaral and Kunzelmann, 2011; Chiaw *et al.*, 2011; Lewis *et al.*, 2010). CFTR gating is regulated by PKA-dependent phosphorylation of the R-domain, ATP-binding and dimerization of the cytoplasmic NBDs, resulting in an outward-facing, open conformation of the channel, facilitating passive transport down a concentration gradient (Dean *et al.*, 2001).

Roughly 70% of CF cases worldwide results from a deletion of F508 ( $\Delta$ F508-CFTR) within NBD1. Loss of this aromatic residue reduces NBD1 stability, lowering the unfolding transition temperature ( $T_m$ ) of purified NBD1 by 6–8°C, disrupting the interface between NBD1 and intracellular loop 4 (ICL4) of the second transmembrane domain (TMD2). Together, these defects diminish proper CFTR folding, apical trafficking, and channel function (Protasevich *et al.*, 2010). CFTR is instead retained in the endoplasmic reticulum and targeted for subsequent degradation (Lewis *et al.*, 2010; Rich *et al.*, 1990). While the impact of  $\Delta$ F508 on CFTR folding and stability has been known for some time (Cheng *et*

*al.*, 1990; Rich *et al.*, 1990), the mechanisms by which F508 loss destabilizes the channel have more recently been described (He *et al.*, 2014; Lewis *et al.*, 2010; Rich *et al.*, 1990).

Previously reported crystal structures and HDX analysis of both WT and  $\Delta$ F508-NBD1 have provided biochemical evidence that the loss of F508 does not impact NBD1 structure globally, but instead results in localized solvent exposure of the V510 loop (Atwell *et al.*, 2010; Lewis *et al.*, 2010; Thibodeau *et al.*, 2005). This result is consistent with *in silico* models of NBD1, which suggest the same localized impact at the V510 loop (Bisignano and Moran, 2010; Callebaut *et al.*, 2004; Zhenin *et al.*, 2015). Because a full-length structure of  $\Delta$ F508-hCFTR has not yet been published, much of what is known about the molecular interactions and structural defects at the NBD1:ICL4 interface that result from the  $\Delta$ F508 mutation is the product of molecular modeling. For example, such work has provided valuable insight into the local environment of the V510 loop, and its proximity to ICL4 as a consequence of the mutation (Mornon *et al.*, 2008; Serohijos *et al.*, 2008). CFTR homology modeling published by Kalid, *et al.* predicted that the loss of the large, aromatic ring structure of F508 leaves a hydrophobic cavity at the inter-domain interface of NBD1 and ICL4 (Kalid *et al.*, 2010).

A series of CFTR mutations have been identified, in part through patient genotyping, which significantly reduce the impact of  $\Delta$ F508 when these are

simultaneously present. Such CFTR second site suppressor mutations (SSSMs) result in improved CFTR trafficking and function, and a milder disease phenotype (Dörk T, 1991; Teem *et al.*, 2007). Among SSSMs, I539T, G550E, R553Q, and R555K are located within NBD1. These have been shown to increase the thermal stability of the domain, but do not reestablish the NBD1:ICL4 interface that is lost with  $\Delta F508$  (Chiaw *et al.*, 2011). However, when coupled with SSSMs that act as interface correctors between NBD1 and ICL4, a vast improvement can be seen in CFTR global assembly and channel function (Dörk T, 1991; Rabeh *et al.*, 2012a; Teem *et al.*, 2007). One such example, R1070W, may drive  $\Delta F508$  phenotype suppression by replacing the missing aromatic ring of F508 with a tryptophan at the ICL4 interface (Kalid *et al.*, 2010; Loo *et al.*, 2010). Another example, which was first identified during an attempt to create Cys-less CFTR (Wang *et al.*, 2007) and supported with homology modeling and biochemical characterization shortly thereafter, is V510D (Loo *et al.*, 2010; Mornon *et al.*, 2008), which is thought to restore the NBD1:ICL4 interface by creating a salt bridge with R1070 on ICL4. The half-life of  $\Delta F508/V510D$ -CFTR at the cell surface is reported to be similar to that of wild type CFTR, about 5-10 fold longer than the  $\Delta F508$  mutation alone (Loo *et al.*, 2010). In addition to correcting the NBD1:ICL4 interface, other possible interactions may be occurring within this  $\Delta F508/V510D$  CFTR double mutant that may be critical to our understanding of how such mutations act to suppress  $\Delta F508$ .

While it is well-established that suppressor mutations do have the ability to rescue  $\Delta F508$ -CFTR trafficking, the mechanism driving this rescue is only partially understood. In our objective to understand the effects of these mutations at the atomic level, we generated homology models of WT and  $\Delta F508$ -CFTR with and without SSSMs R1070W or V510D, and performed 1 microsecond molecular dynamics simulations for each of these systems. These simulations provided key insights into how the  $\Delta F508$  defect might impact CFTR structural integrity, both within NBD1 and of full-length CFTR overall (sans the regulatory domain), and identified possible residues - most notably K564 - that may play a critical role in the mechanism by which V510D both stabilizes NBD1 and improves  $\Delta F508$ -CFTR pathology.

This work was intended to accomplish three goals: i.) to validate a molecular model of  $\Delta F508$ -CFTR in the absence of a full-length structure, ii.) to gain insight into the effects of the  $\Delta F508$  mutation on CFTR conformational dynamics, and iii.) to determine how second-site suppressor mutations may influence such  $\Delta F508$ -CFTR conformational dynamics.

To accomplish this, we generated homology models of full-length wild-type and  $\Delta F508$ -CFTR +/- SSSMs V510D and R1070W, and performed MD simulations for each. With information acquired from these simulations, we developed several testable hypotheses regarding  $\Delta F508$  destabilization of full-length CFTR. By creating full-length WT and  $\Delta F508$ -CFTR constructs containing

certain SSSM or other point mutations, we gained new insights into how the V510D suppressor mutation has a corrective effect on  $\Delta F508$ . Moreover, by comparing the crystal structures of  $\Delta F508$ -NBD1 and  $\Delta F508/V510D$ -NBD1, we determined what structural changes and interactions resulted within NBD1, either at the V510 loop or other regions of  $\Delta F508$ -NBD1 that drive V510D stabilization of the soluble domain. In an effort to improve the stability of the TMD2 domain, we introduced charged residue substitutions along TM10 and TM11 with a view to create salt bridges within TMD2. We then evaluated the impact of these mutations on CFTR maturation and trafficking, both alone and in the context of additional mutations within NBD1 and ICL4. The experimental data (expression, trafficking and functional) obtained for these mutants support the hypothesis that a contributing factor of the  $\Delta F508$  defect may be the cause of helical instability within the second transmembrane domain.

## **2.4 Results**

### **2.4.1 CFTR homology model and molecular dynamics simulation**

Using homologous ABC transporter, Sav1866 (PDB code 2HYD) as a model, we generated novel CFTR models of wild-type and  $\Delta F508$ -CFTR (Figure 2.1) (Dawson and Locher, 2006). We replaced the NBDs of Sav1866 in the WT model with hCFTR NBD1 and NBD2 crystal structures (PDB IDs 2PZE and 3GD7 respectively), and the  $\Delta F508$ -NBD1 crystal structure (PDB ID 2PZF) into the  $\Delta F508$ -CFTR variant model (Atwell *et al.*, 2010; Lewis *et al.*, 2010). Relative

positioning of the NBDs was based on Sav1866 and NBD1 homodimer structures.

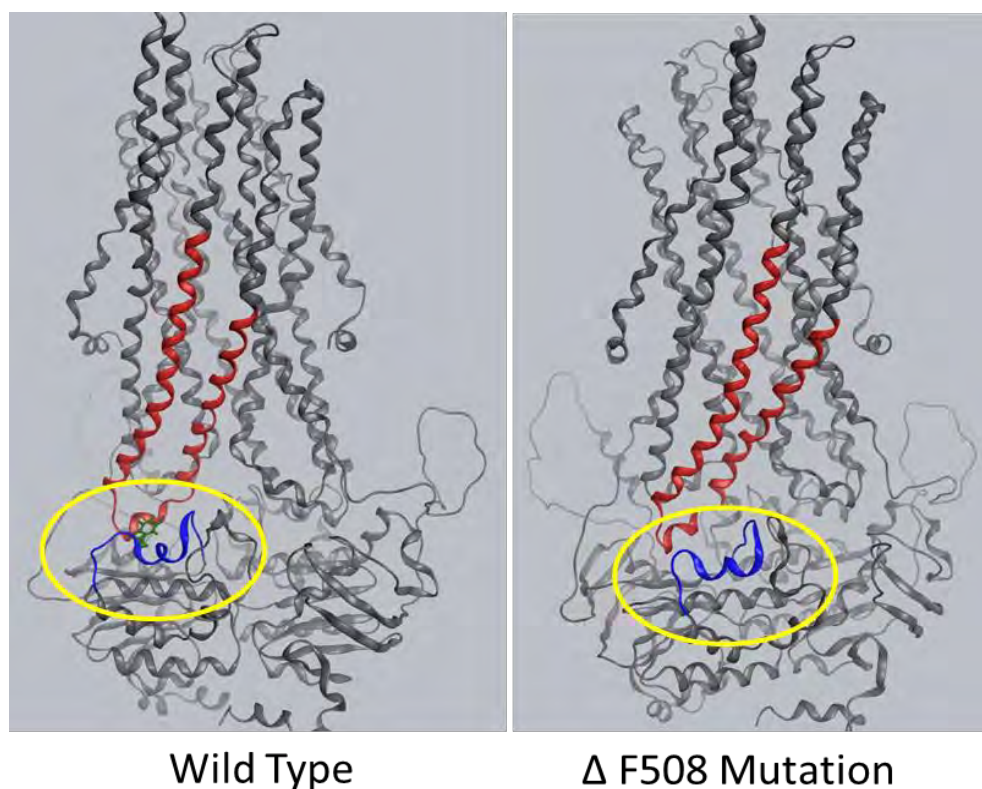


**Figure 2.1 CFTR homology models of full-length WT and  $\Delta$ F508 CFTR highlight differences at V510 loop.** Models were based on the crystal structure of SAV1866 in the outward facing conformation (PDB ID 2HYD). The Sav1866 NBD1 domain was replaced with hCFTR NBD1 crystal structure (PDB ID 2PZE) in the WT model, and the  $\Delta$ F508-NBD1 crystal structure (PDB ID 2PZF) was incorporated for the  $\Delta$ F508-CFTR variant models with V510D and R1070W mutations (not shown). Sav1866 NBD2 was replaced with the crystal structure of CFTR-NBD2 fused to maltose-binding protein (PDB ID 3GD7). A comparison of secondary structure that exists near the ICL4 loop reveals significant differences between the models. The blue loop/helix circled in yellow represents the V510 loop and flanking residues, including F508 in WT CFTR (left). This residue is absent in  $\Delta$ F508-CFTR (right), which causes the blue V510 loop to become more solvent-exposed, turning away from its normal interface with ICL4 (represented as the red helical structure).

To ensure accuracy of our models, we compared them to the recently published cryo-EM structures of outward-facing, open conformation CFTR, paying particular attention to NBD1, NBD2 and the intracellular loops (ICLs), as those regions of CFTR are the focus of this study. Structural alignment of those regions of our model and the experimentally-derived cryo-EM data (PDB ID 6MSM, (Zhang *et al.*, 2018b)) show high structural similarity. Alignment of NBD1 from our WT-CFTR model (based on NBD1 crystal structure PDB ID 2PZE) and the cryo-EM structure returned a root-mean-square deviation (RMSD) value of 1.139 Å. Alignment of NBD2 from our model (based on the CFTR-NBD2-maltose binding protein fusion complex crystal structure; PDB ID 3GD7) with the cryo-EM structure resulted in an RMSD value of 1.916 Å.

When we aligned our WT-CFTR homology model to the full-length cryo-EM structure of phosphorylated, outward-facing CFTR [PDB ID 6MSM, (Zhang *et al.*, 2018b)] we obtain an overall RMSD value for C-alpha atoms of 3.76Å (Figure 2.2). Table 2.1 provides RMSD values comparing our full-length WT-CFTR homology model and the CFTR cryo-EM structure.



**Table 2.1 RMSD values by domain for the full-length WT-CFTR homology model** when compared to the published full-length CFTR cryo-EM structure in the same open channel conformation [PDB ID 6MSM, (Zhang *et al.*, 2018b)]. Values were derived for both the intracellular loop (ICL) regions as well as the overall transmembrane helices (TMs) that comprise each ICL, and span from the cytoplasmic to extracellular side of the plasma membrane.

Region	Associated helices	Residues	RMSD (Å)	Panel in Figure 2.2
ICL1	TMs 2 & 3	162-182	1.513	A
TMs 2 & 3		125-215, includes ICL1	2.857	B
ICL2	TMs 4 & 5	261-284	1.056	C
TMs 4 & 5		225-320, includes ICL2	3.296	D
NBD1		387-646 ( $\Delta$ 405-436)	1.139	I
ICL3	TMs 8 & 9	951-974	1.330	E
TMs 8 & 9		911-1005, includes ICL3	2.890	F
ICL4	TMs 10 & 11	1060-1080	0.774	G
TMs 10 & 11		1020-1110, includes ICL4	1.709	H
NBD2		1193- 1427	1.916	J

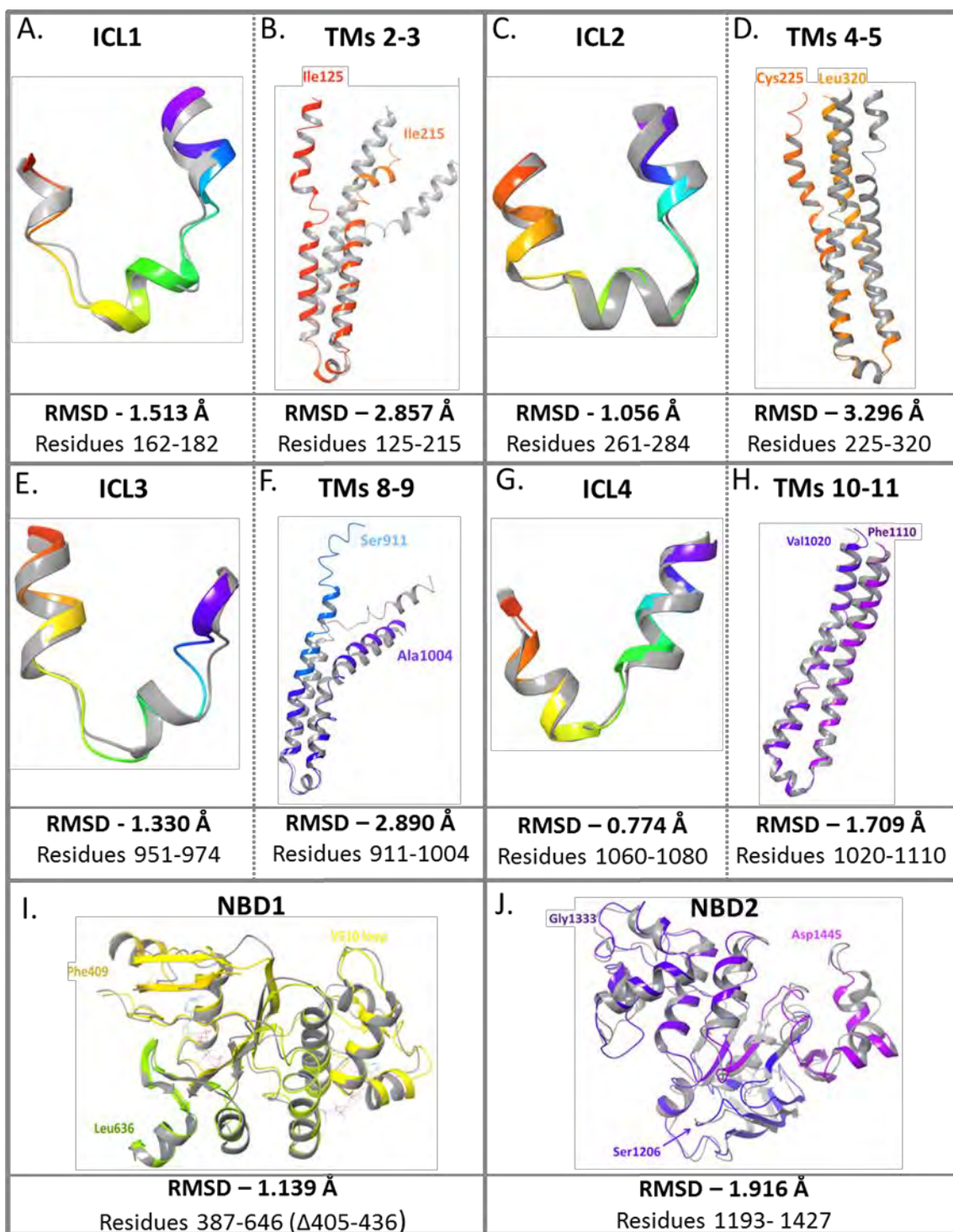


**Figure 2.2 Structural comparison and corresponding RMSD values of ICL and NBD regions for the human WT-hCFTR homology model (colored ribbon structures) and the published cryo-EM structure of hCFTR (grey ribbon structures, PDB ID: 6MSM) (Zhang *et al.*, 2018b).** Both structures represented in the figure are of CFTR in an outward-facing conformation. The figure highlights structural similarity between the two models for each intracellular loop (ICL) (panels A, C, E and G) displayed alongside the corresponding pair of transmembrane helices that comprise the ICL (B, D, F, and H, respectively), and an overall comparison of NBD1 (panel I) and NBD2 (panel J). Both NBDs display a high level of correlation between the model and cryo-EM structure, which is likely because the authors that published the cryo-EM structures used the same set of crystal structures to establish their models as were used in our homology model. Positioning in relation to the TMs would likely be slightly different, given that the model is based on Sav1866. Panels B, D and F highlight greater differences in TMs 3, 5 and 8, respectively, between the homology model and cryo-EM structure. In the model, the helices appear to be slightly straighter, while the cryo-EM model displays a helix-loop-helix structure for TMs 3 and 8. In all cases, the alignment appears different for one or both TMs that make up the pair. This may be due to the discrepancies in the channel pore size between Sav1866, which is larger to facilitate the passage of bigger molecules, and CFTR, which need only allow for the passage of ions. (Figure on previous page.)

Additional  $\Delta F508$ -CFTR variant models were generated by adding known SSSMs V510D and R1070W. Using these models, we built corresponding ~160,000 atom explicit membrane/explicit solvent systems to conduct MD simulations of 1 $\mu$ sec timeframe for each model (Figure 2.3).

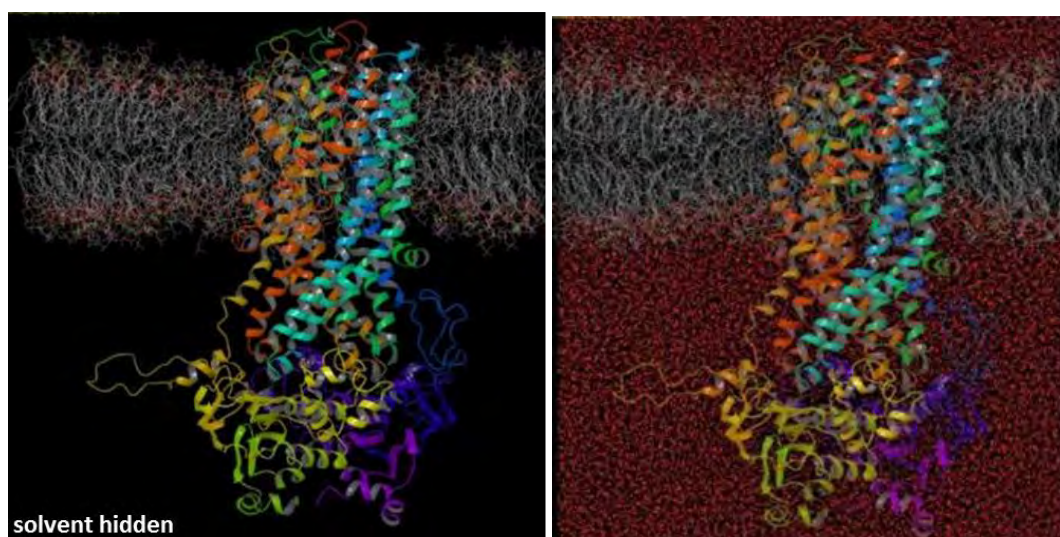


**Figure 2.3 CFTR MD simulation preparations.** A 160,000 atom system based on WT and  $\Delta F508$  CFTR models prepared for MD simulations. The system was soaked in TIP3 water model (red, in bottom image) and 1-palmitoyl-2-oleoyl-sn-glycero-3-phosphocholine (POPC) membrane (gray) was placed near residues in the MSD region.

### Quality Analysis for Molecular Dynamics Simulations

A quality analysis comparison was completed for the MD simulations (Figure 2.4). Macroscopic properties of the models that were evaluated during quality analysis confirmed a stable simulation was performed. All properties indicated an initial relaxation and eventual stabilizatio

## Analysis of Molecular Dynamics

Quality Analysis Comparison for WT,  $\Delta F508$ ,  
 $\Delta F508/V510D$  &  $\Delta F508/R1070W$  CFTR MD Simulations

Potential Energy (Kcal/mol)  
 Kinetic Energy (Kcal/mol)  
 Pressure (Bar)  
 Volume ( $\text{\AA}^3$ )  
 Temperature (K)

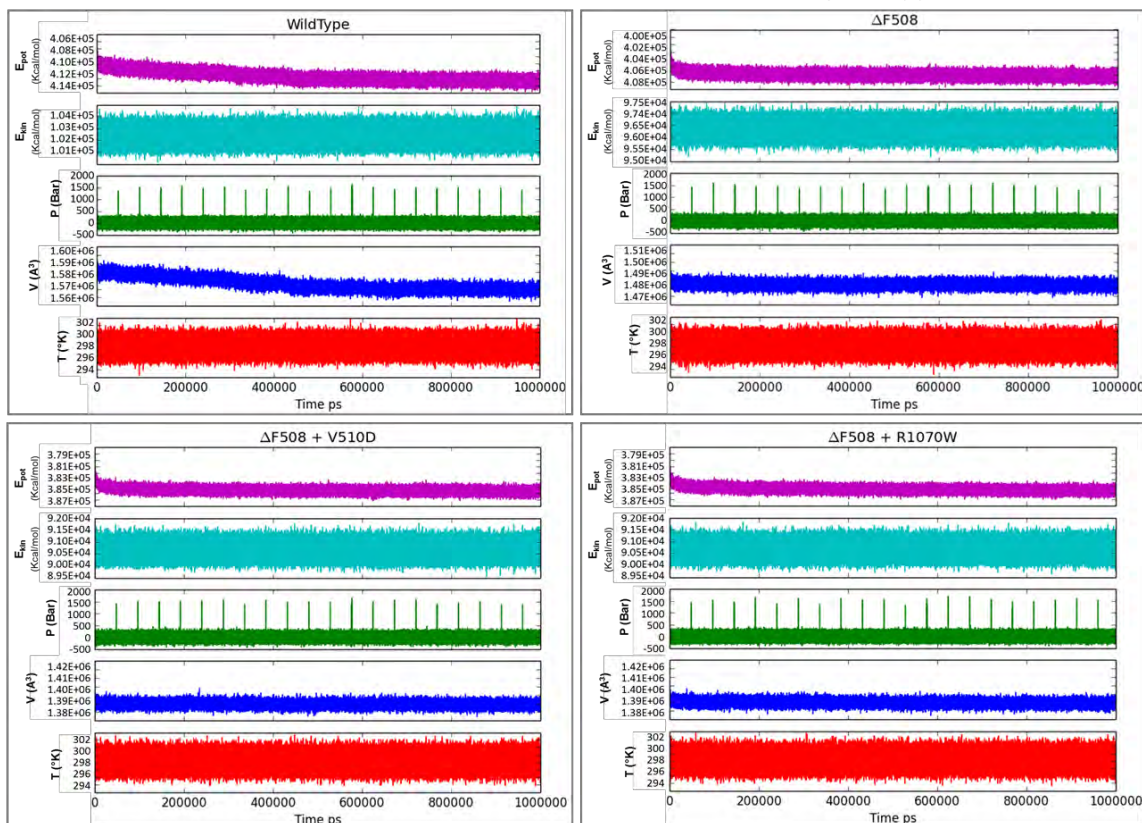


**Figure 2.4** Quality control analysis for Molecular Dynamics Simulations of WT,  $\Delta F508$ ,  $\Delta F508/V510D$  and  $\Delta F508/R1070W$  CFTR. Analysis of potential (purple) and kinetic (teal) energy, pressure (green), volume (blue) and temperature (red) all indicated an initial relaxation of the molecule. Eventually all parameters were stably maintained for the duration of the 1  $\mu$ s simulation.



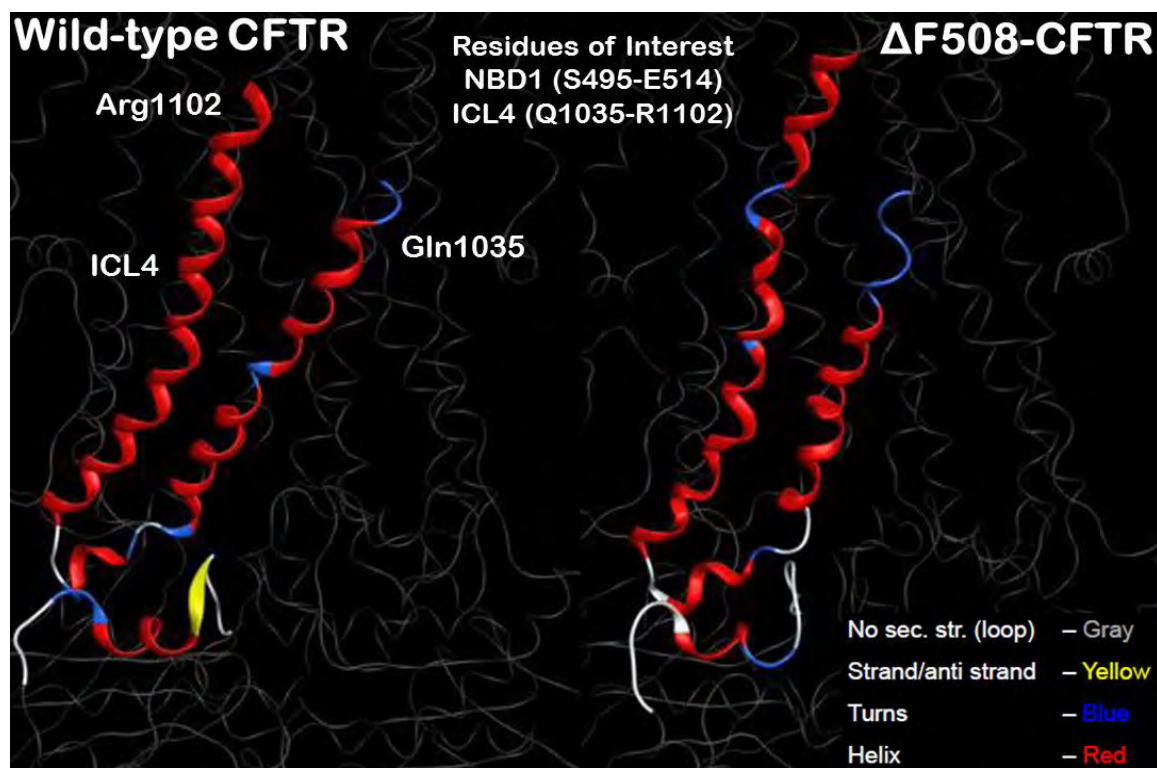


**Figure 2.5 CFTR residues of interest for MD simulation.** CFTR regions and corresponding residue numbers that were highlighted for differences in secondary structure throughout the course of the 1μsec MD simulation. Through the course of the MD simulation, the model was color-coded to signify a given secondary structure: Helix – red; strand/anti-strand – yellow; turns – blue; no secondary structure – grey.

While analyzing these MD simulations outcomes, we looked for specific and testable changes in secondary structure (Figures 2.5 and 2.6), solvent exposure, residue geometry, and the existence and conservation of salt bridges between selected residues in each of the models (Figure 2.8).

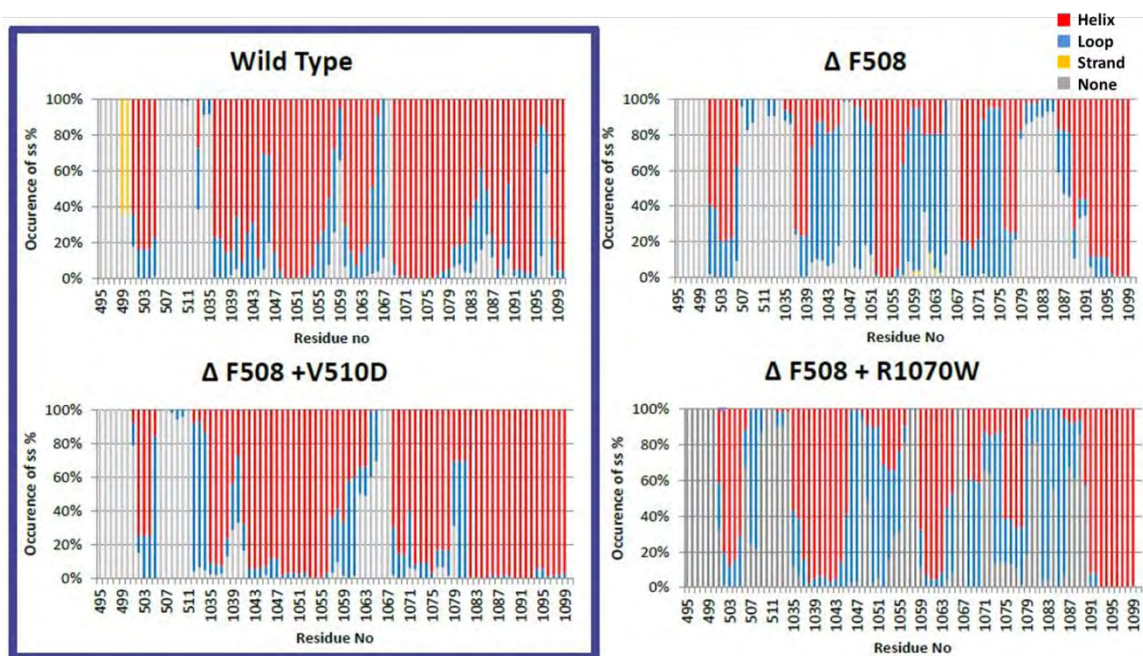


**Figure 2.6 % Occurrence of secondary structure changes was consistent with reported stability data for CFTR variants  $\Delta F508$ ,  $\Delta F508+V510D$  and  $\Delta F508 + R1070W$ .** A comparison of secondary structure classifications by percent occurrence for each residue of interest within the four CFTR homology models shows helical regions in red, loops in blue, strands in yellow and unstructured regions in grey. Significant changes were seen within TMD2 for  $\Delta F508$  and  $\Delta F508+R1070W$ , which are highlighted by the increased prevalence of unstructured regions (grey) from residues 1044 to 1095. When V510D is added to  $\Delta F508$ , helical structure appears to be maintained, as evidenced by a secondary structure profile more closely resembling WT (comparison of this is highlighted by the purple box to the left).

Overall, a comparison of the four (one each of the WT,  $\Delta F508$ ,  $\Delta F508+V510D$  and  $\Delta F508+R1070W$ ) 1 $\mu$ s MD simulations demonstrated a strong correlation between *in silico* protein stability and published experimental data such as secondary structure stability (WT  $\sim \Delta F508+V510D \gg \Delta F508+R1070W > \Delta F508$ ), and supported a proposed salt-bridge interaction between V510D and R1070 at the NBD1:ICL4 interface (Meng *et al.*, 2019; Meng *et al.*, 2017a). This work also supports previously made predictions regarding increased solvent exposure of the V510 loop in the V510D mutant (Mornon *et al.*, 2008).

### **Identification of V510D salt bridge interactions**

The analysis also offered several new insights concerning key residues within NBD1 that may play a role in V510D stabilization of  $\Delta F508$ -NBD1. For example, frequency analysis of intra- and inter-domain salt bridge possibilities for the MD run of  $\Delta F508/V510D$  model identified that 510D may interact with K564 and also, to a lesser extent, with R487 in NBD1 (Figure 2.7). This is in addition to its anticipated interaction with R1070 of the ICL4 loop. Potential salt bridges are retrieved (based on distance) for each charged residue from individual frames of the simulation. Residues with a high occurrence of interactions are analyzed further for the total number of salt bridge interactions that occur as a function of time and the residues involved in the detected salt bridge formation. See Figure 2.7 for analysis of salt bridge interactions with V510D within  $\Delta F508/V510D$ -NBD1.



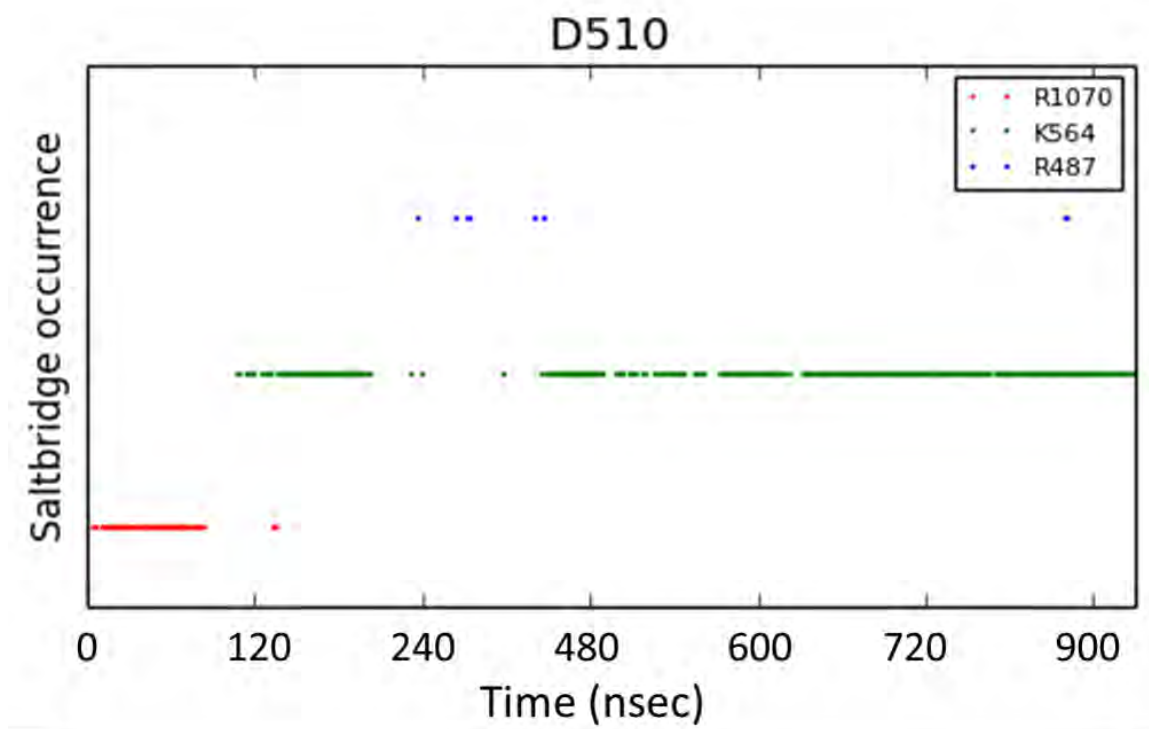


**Figure 2.7 Salt bridge interactions with V510D.** The prevalence of potential salt bridge interactions occurring between V510D and R1070 in the MD simulation model of  $\Delta F508/V510D$ -CFTR was evaluated. When the interactions made with V510D were displayed as a function of time (occurrences of individual residues interacting with D510 are spaced along the ordinate axis for clarity), the results suggest that R1070 and V510D form a salt bridge only during the initial phase of the model, and that V510D forms a more consistent interaction with K564, and very briefly with R487.

**Evidence of helical unraveling observed in  $\Delta F508$ -CFTR MD simulation**

An interesting observation from our MD simulations was the inherent instability of the TMD2 domain and a propensity to lose helical secondary structures of TM10 and TM11 as a consequence of  $\Delta F508$ . This significant structural change in helices 10 and 11 may contribute to the short half-life and dysfunction of  $\Delta F508$ -CFTR (Figures 2.8 and 2.9). Moreover, when we evaluated  $\Delta F508/V510D$ -CFTR using the same parameters, the model suggests stabilization and structural integrity is somewhat restored. However, our MD simulation results for  $\Delta F508/R1070W$ -CFTR suggest that the resulting helical stabilization is less than what was observed for the  $\Delta F508/V510D$ -CFTR.

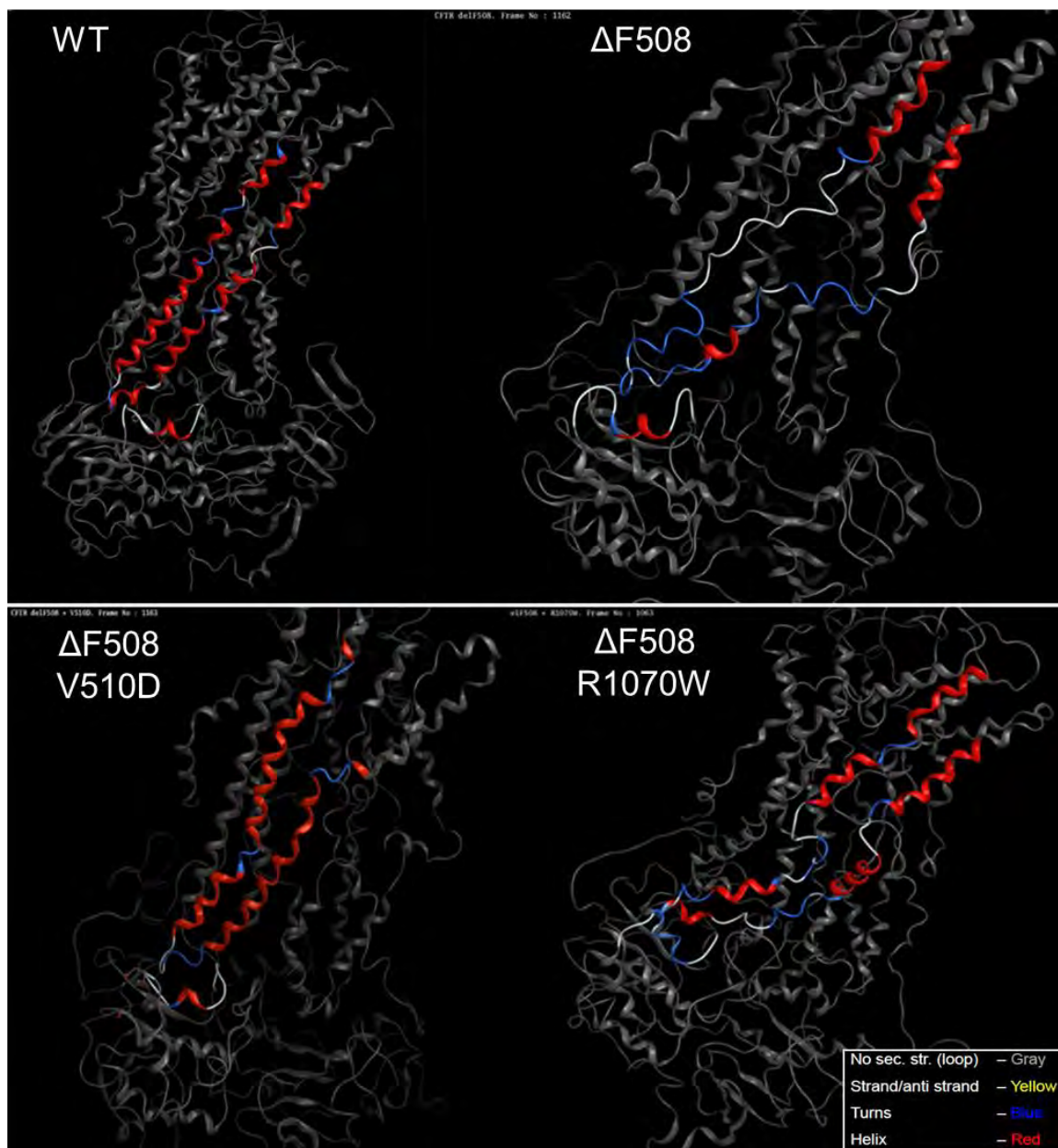


**Figure 2.8** Molecular dynamics simulations of WT,  $\Delta F508$ ,  $\Delta F508/V510D$  and  $\Delta F508/R1070W$  show evidence of helical unraveling along TMs 10 and 11, and at ICL4 which connects them. Still shots were taken of each of the four movies at the same point of progression in the simulation, highlighting the vast differences in helical stability across the four CFTR molecules.

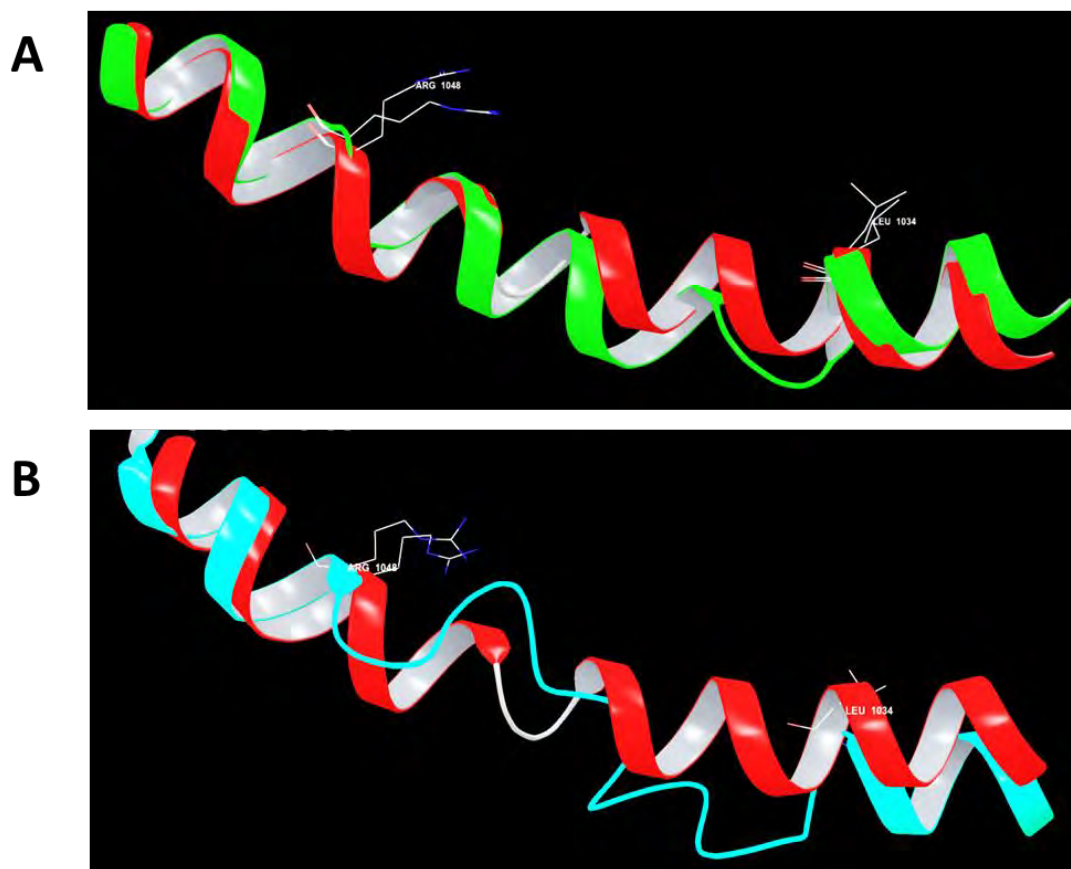


**Figure 2.9 Superposition of TM10 alpha helical region (residues 1028 – 1055) taken from the first (red) and last frame (green/teal) of MD simulations for WT (A) and  $\Delta F508$  (B) models of full-length CFTR. The simulation time between first and last frames is 1  $\mu$ sec. A.) MD simulation for WT-CFTR suggests that the alpha-helical conformation of TM10 does not change over the course of the simulation; however a slight adjustment in position may occur. RMS deviation between these two conformations is 1.551 Å. B.) A comparison of conformations for  $\Delta F508$ -CFTR TM10 region between the first frame (red helix) and last (cyan) highlights changes in conformation between residues 1034 and 1048, which is unwound and loses alpha helical conformation. RMS deviation between these two conformations is 2.375 Å.**

### 2.4.2 The role of K564 on V510D-mediated suppression on the $\Delta$ F508 trafficking defect

To validate the model's prediction of how V510D helps restore  $\Delta$ F508-CFTR folding and trafficking, we performed site-directed mutagenesis on full-length hCFTR to modify residues that appeared to create salt bridges with D510 (in addition to D510's possible salt bridge interaction with R1070), in the context of the  $\Delta$ F508/V510D-hCFTR *in silico* model. The two basic residues, K564 and R487, were replaced with alanine or serine residues in WT,  $\Delta$ F508-hCFTR, and  $\Delta$ F508/V510D-hCFTR expression constructs to test the impact of removing a positive charge in close proximity to D510, effectively eliminating a potential stabilizing interaction for the solvent-exposed V510 loop of  $\Delta$ F508-NBD1. A  $\Delta$ F508/V510K/K564D construct was also created to evaluate whether V510D rescue occurs if the K564/V510D salt bridge is maintained within NBD1 while the V510D:R1070 interaction at the NBD1:ICL4 interface is interrupted. We assessed the impact of each mutation on CFTR maturation and trafficking by transiently transfecting each construct into CF patient-derived submucosal gland epithelial cells (CFSME<sub>0</sub>) and comparing expression levels of mature, fully glycosylated CFTR ("C-band") and immature, ER-trapped CFTR ("B-band") detected 48 hours post-transfection. Results are reported as a ratio of C/B band (Figure 2.10).

We simultaneously created a second set of constructs with the same point mutations that contained an in-frame fusion of horseradish peroxidase (HRP) within CFTR's 4<sup>th</sup> extracellular loop which allows us to detect membrane-bound CFTR via an HRP-mediated signal. When CFTR variants traffic to the apical cell surface, the HRP tag is exposed on the outside of the plasma membrane, rendering it accessible to HRP substrate. To ensure the measured signal was the result of extracellular HRP localization, a qualification experiment was performed using Brefeldin A, a lactone antiviral that inhibits protein transport from the endoplasmic reticulum to the Golgi apparatus (Helms and Rothman, 1992). The addition of this compound to the cultured CFSME<sub>o</sub>- cells interrupted normal trafficking of the CFTR HRP reporter to the outer membrane, which translated to a reduction in extracellular HRP signal that was comparable to  $\Delta F508$ -CFTR. Relative CFTR surface localization can then be determined in live cells by measuring the resultant chemiluminescent signal (Phuan *et al.*, 2018; Phuan *et al.*, 2014). To ensure that samples in both the western blot and HRP trafficking assays were normalized for CFTR transfection efficiency, constructs were designed with a co-expressing soluble eGFP marker using the 2A bicistronic expression system (de Felipe, 2002; Minskaia and Ryan, 2013). This system ensures a 1:1 ratio of CFTR and GFP protein production.

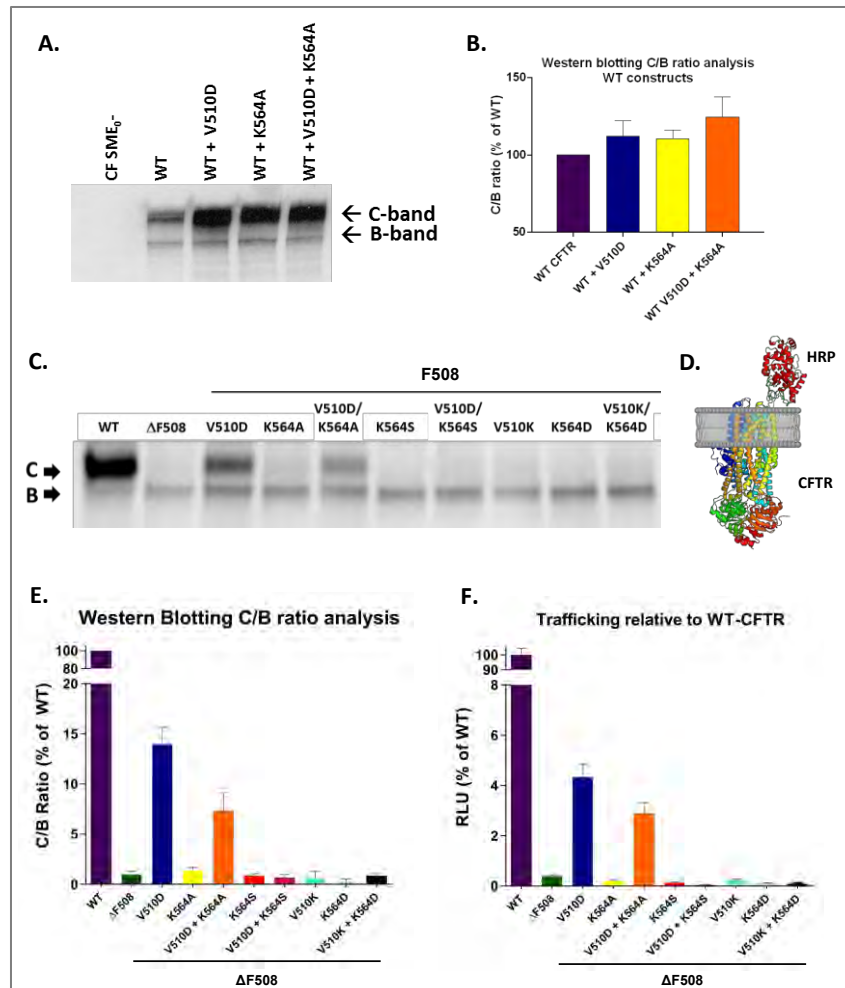


**Figure 2.10 Presence and position of residue K564 is key to V510D suppression of the  $\Delta$ F508 trafficking defect.** A & B. Immunoblotting analysis (A) and corresponding C/B ratio values (B) comparing WT-CFTR to WT constructs containing V510D and K564 mutations show no deleterious impact to CFTR maturation when mutations are added, and suggests an increase in detectable levels of mature CFTR. Panels C and E: immunoblotting analysis (C) and C/B ratio values (E) comparing WT and  $\Delta$ F508-CFTR to V510D and K564 mutants, showing partial CFTR rescue (as indicated by the increase in “C band”) when V510D is added to  $\Delta$ F508. This rescue effect is diminished when the K564A mutation is added to V510D. K564S and residue-swap mutations containing K564D and V510K completely eliminate CFTR trafficking. (D.) Cartoon of HRP-tagged CFTR molecule displaying the placement of an HRP tag on the fourth extracellular loop (ECL). F.) This HPR reporter molecule with mutations is used in the CFTR trafficking assay to measure trafficking of mutated CFTR. Results are displayed as RLU values relative to WT-CFTR.

Initial analysis was performed on WT-CFTR constructs containing the K564A mutation +/- V510D prior to evaluation on  $\Delta$ F508-CFTR to confirm that the K564 mutation had no deleterious effect on CFTR maturation. Immunoblotting for CFTR displayed no reduction in levels of fully-glycosylated CFTR when mutations were added and an increase in overall amounts of mature CFTR was detected. While some rescue of  $\Delta$ F508-CFTR is evident when V510D is present, (restoring trafficking to approximately 5-10% of WT levels), our data suggests that removal of charged residue K564 disrupts V510D rescue of the  $\Delta$ F508 trafficking defect. When K564 is mutated to an alanine on a  $\Delta$ F508/V510D background, roughly half of the rescue effect is preserved, suggesting that the impact of V510D rescue within NBD1 may rely on the presence of the lysine. Interestingly, when K564 is replaced with a serine, or when D510 and K564 are transposed, trafficking in both the HRP and western blot assays drops to  $\Delta$ F508 levels.

Additionally, we performed electrophysiology on these CFTR variants to more thoroughly understand the effect of the V510D mutations on the chloride channel's function as compared to WT and  $\Delta$ F508-CFTR, and what impact changing the positively charged residues at K564 and R487 to alanines would have on WT- and  $\Delta$ F508-CFTR maturation (Figure 2.11). For this experiment, fisher rat thyroid (FRT) cells were transfected with equal amounts of DNA expressing the K564A mutations, with and without V510D present. To ensure all signal measured could be attributed to CFTR, we first treated the cells with



benzamil to block the function of the  $\text{Na}^+$  channel ENaC, a major contributor to ion conductance in epithelial cells. We then treated the cells with forskolin to activate adenylyl cyclase and increase cAMP levels to maximize CFTR phosphorylation and its subsequent activation, as well as CFTR potentiator, Genistein. CFTR-specific inhibitor, CFTR-inh 172, was then added to confirm the increased signal was the result of CFTR activity. The maximal current after the addition of both Forskolin and CFTR potentiator Genistein ( $\text{FP}_{\text{max}}$ ) for each tested variant was then compared to WT and  $\Delta\text{F508}$ -CFTR. Data trends were similar to those of the HRP trafficking and western blot assays. K564S-containing constructs and residue-swap constructs were not evaluated in this assay, given the lack of CFTR trafficking seen. In addition, all tested CFTR variants with mutations that replaced R487 with amino acids of shorter side chain length, (e.g., R487A and R487S) led to a complete loss of trafficking (data not shown), and these were not investigated further.

Electrophysiological Evaluation of  $\Delta$ F508-CFTR mutants +/- V510D and K564A

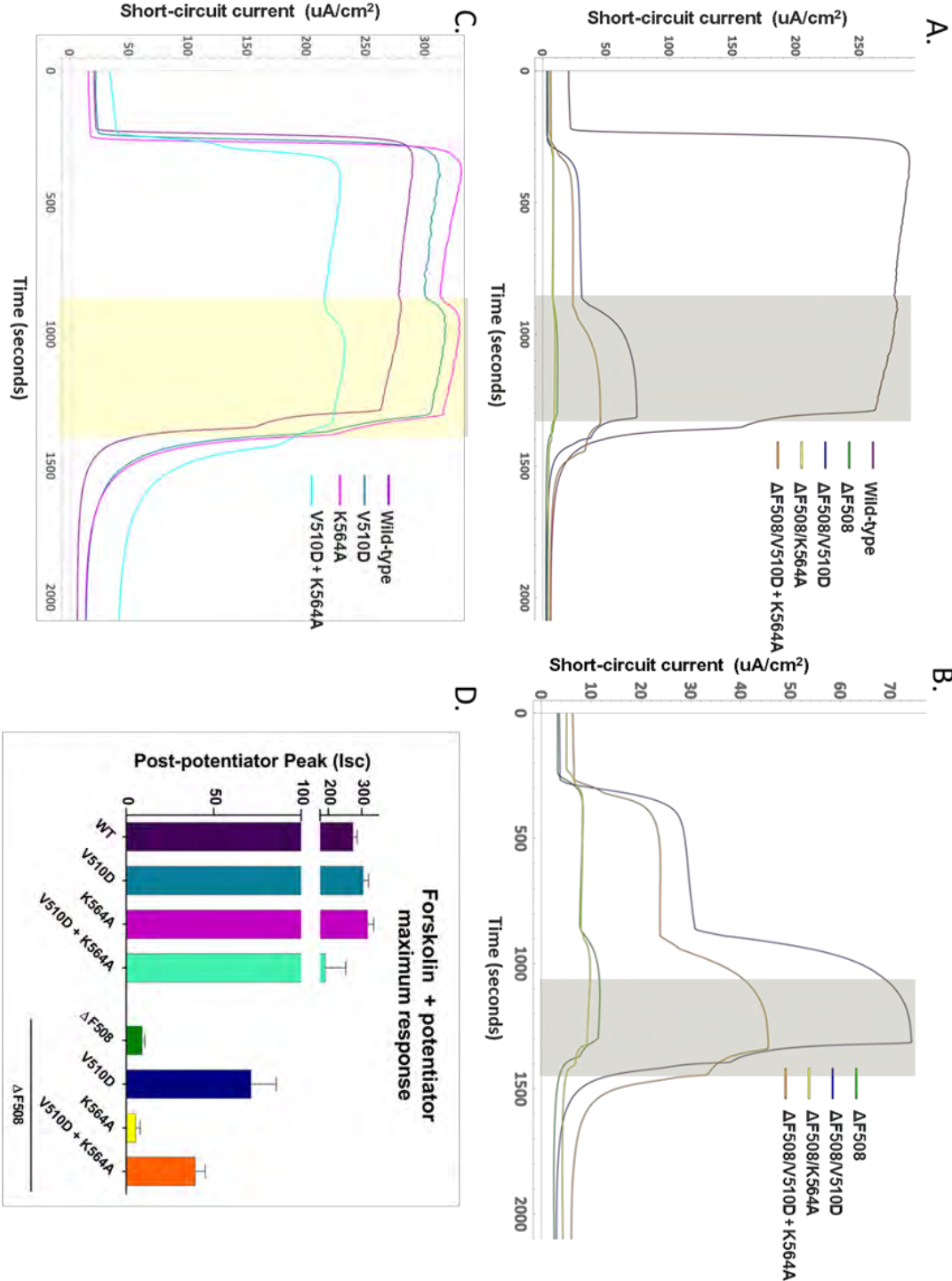


**Figure 2.11 Electrophysiological analyses of FRT cells expressing  $\Delta$ F508-containing CFTR mutants +/- V510D and K564A.** Fisher rat thyroid cells expressing mutated CFTR constructs were evaluated for channel conductance to determine how V510D impacts  $\Delta$ F508-CFTR function in the presence and absence of proximal residue K564A. Panel A shows current traces for CFTR mutants compared to wild-type. In panel B, the WT trace is removed to allow a more precise view of the current traces for cells expressing mutations on a  $\Delta$ F508 background. Data in panel C shows current traces for cells expressing CFTR mutants on a wild-type background. Panel D shows a quantitative comparison of all constructs displayed as peak forskolin + potentiator max response which is calculated by subtracting the post-inhibitor current from the peak forskolin + Genistein current (indicated by the highlighted region in each of the three trace panels). (Figure is seen on previous page.)

### 2.4.3 The impact of V510D on the structure and stability of NBD1

Given the inherent instability of NBD1 in its native form, much has been done to identify both point mutations and peptide deletions that improve yield and solubility of the purified protein (Aleksandrov *et al.*, 2010; Lewis *et al.*, 2010; Protasevich *et al.*, 2010; Rabeh *et al.*, 2012b). As described above, such NBD1 mutations include known CFTR SSSMs like G550E, R553Q, and R555K. NBD1-stabilizing modifications also include removal of NBD1's 37-residue regulatory insertion (RI, residues 402-438) with or without a further truncation of the majority of the 38-residue regulatory extension (RE, residues 638-676), either of which result in improved NBD1 thermostability as well as increased trafficking and half-life of full-length WT and  $\Delta$ F508 CFTR (Protasevich *et al.*, 2010). To that end, in an effort to better understand how the V510D suppressor mutation impacts

folding and stability of the NBD1 subdomain independent of ICL4, we performed a series of assays on purified  $\Delta$ RI- and  $\Delta$ RI/ $\Delta$ RE-NBD1 that included K564A/S mutations +/- V510D, and compared these to the  $\Delta$ F508 and WT versions.

### **Removal of K564 Decreases NBD1 Stability in the Presence and Absence of V510D**

To evaluate each NBD1 variant for changes in thermostability, we utilized two complimentary, label-free thermal shift assays. The first, differential static light scattering (DSLS), measures heat-induced changes in light scattering to determine a protein's aggregation temperature ( $T_{agg}$ ). The second, nano differential scanning fluorimetry (nanoDSF), records changes to the intrinsic tryptophan (and to a lesser extent, tyrosine) fluorescence profile with increasing temperatures as a measure of thermal protein denaturation. The temperature at which the denaturation transition occurs is defined as the inflection point of the fluorescent shift ( $T_m$ ).

Results from both assays show that the V510D suppressor mutation increases the  $\Delta$ F508-NBD1  $T_m$  by 2-3.5 °C (Figure 2.12). Mirroring results in the immunoblotting and HRP-trafficking assays for full-length CFTR variants, the K564A mutation minimizes the stabilizing effect of V510D on the  $\Delta$ F508 background, reducing its  $T_m$  by about 2 °C, which represents roughly 60% loss in V510D stabilization. Similarly, the K564S mutation eliminates the V510D rescue

effect, dropping both the melting and aggregation temperatures to below that of  $\Delta F508$ -NBD1. When compared to  $\Delta F508$  alone, K564S/V510D/ $\Delta F508$ -NBD1 has a  $\Delta T_m$  of  $-1.37 \pm 0.01$  °C ( $\Delta RI/\Delta RE$ ) and  $-1.68 \pm 0.025$  °C ( $\Delta RI$ ), and a  $\Delta T_{agg}$  of  $-1.6 \pm 0.20$  °C ( $\Delta RI/\Delta RE$ ) and  $-0.31 \pm 0.16$  °C ( $\Delta RI$ ).

Consistent with previously published data (Protasevich *et al.*, 2010), the addition of the  $\Delta RE$  truncation did not appear to contribute to NBD1 thermostability when compared to the  $\Delta RI$  removal alone in this set of assays, with the exception of the  $\Delta RI/\Delta F508/K564S$ -NBD1 protein in the nanoDSF assay, which exhibited a  $T_m$  of 2.1 °C lower than its  $\Delta RI/\Delta RE$  counterpart. Additionally, reported  $T_{agg}$  values for all mutations were an average of 3.6 °C or 3.9 °C higher for  $\Delta RI/\Delta RE$  or  $\Delta RI$  samples when compared to their  $T_m$  values, likely owing this difference to the distinct phase change between native, denatured and aggregated monomeric NBD1 protein previously reported by Protasevich *et al.* (Protasevich *et al.*, 2010).

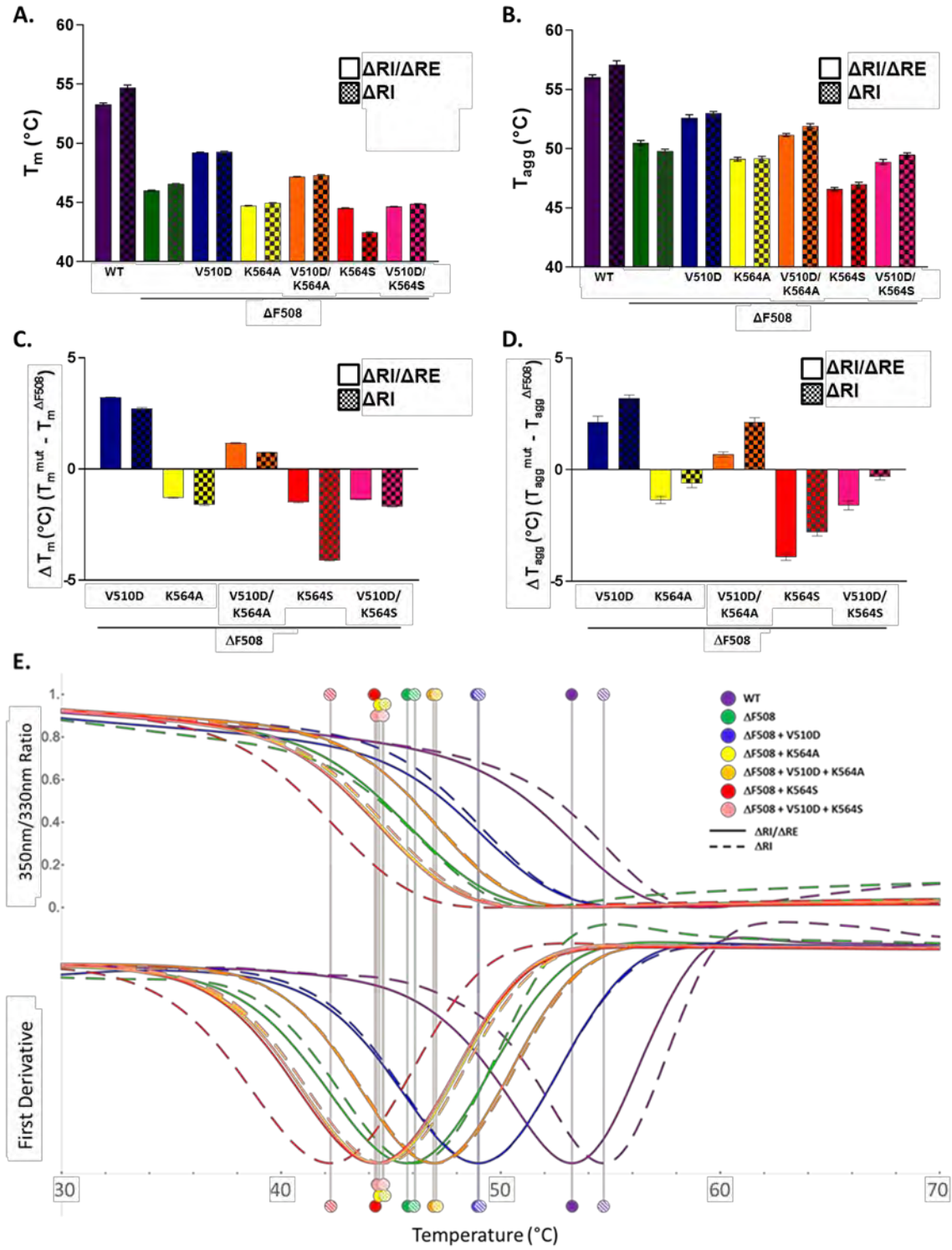


**Figure 2.12 Removal of K564 decreases NBD1 thermal stability in the presence and absence of V510D as indicated by DSLS and nanoDSF thermal shift assays.** Purified NBD1 protein ( $\Delta$ RI or  $\Delta$ RI/ $\Delta$ RE) was evaluated for changes in aggregation temperature ( $T_{agg}$ ) and melting temperature ( $T_m$ ). When point mutations K564A (yellow) and K564S (red) were made to  $\Delta$ F508-NBD1 (green), a reduction of both  $T_{agg}$  and  $T_m$  was seen, which was partially restored by the addition of V510D in all cases (as indicated by blue, orange and pink). The K564S mutation resulted in a net loss of both  $T_{agg}$  and  $T_m$  as compared to  $\Delta$ F508-NBD1, regardless of whether V510D was added. (Panels A/B) Overall  $T_m$  and  $T_{agg}$  (displayed as  $^{\circ}$ C) for NBD1 mutants; (C/D) changes in thermal stability ( $\Delta T_{agg}$  and  $\Delta T_m$ ) as compared to  $\Delta$ F508-NBD1; (E) Melting temperature curves for NBD1 mutants obtained by nano Differential Scanning Fluorimetry (nanoDSF). Curves are displayed as a ratio of fluorescent signals measured at 350 nm and 330 nm (top) and the first derivative of each (bottom), resulting in an inflection point indicating the  $T_m$  of each protein. Every effort was made to ensure protein was measured under parallel conditions and at equal concentrations. (Figure is seen on previous page.)

### **Structural analysis of $\Delta F508/V510D$ -NBD1 via crystallography**

While full-length CFTR trafficking and NBD1 stability data provided support for the key residues involved in V510D-mediated rescue of  $\Delta F508$ -CFTR, identifying the presence of the predicted salt bridge between K564 and V510D required a structural approach. To that end, we used crystallography to analyze changes in  $\Delta F508$ -NBD1 when V510D is present.

#### *The $\Delta F508$ NBD1/V510D Crystal Structure Confirms the D510 – K564 Salt Bridge*

To further investigate a possible interaction between the mutated aspartic acid residue at position 510 and K564 or R487 suggested by our molecular dynamics simulation, we determined the crystal structure of NBD1  $\Delta F508/V510D$ . As has been shown previously (Lewis *et al.*, 2010), deletion of F508 and the associated shortening of the adjoining loop results in a more solvent-exposed position for V510 (Figure 2.13). Introduction of the V510D mutation in the  $\Delta F508$  context results in a side chain rotation for D510 towards the main body of NBD1 and formation of a salt bridge with K564, whose side chain adopts an alternative rotamer from that observed in other CFTR NBD1 structures, where the amino moiety is hydrogen-bonded to the backbone carbonyl of I488. However, when V510D is present, K564 positions the residue side chain facing toward the aspartic acid, so as to create the salt bridge. There



are two molecules in the asymmetric unit in our crystal form. In one of them, we observe partial occupancy for both the original rotamer of K564, and the one that allows for K564-V510D salt bridge formation, while in the second molecule K564 exclusively adopts the new rotamer that allows for interaction with D510 (figure 2.13). No interaction appears to exist between R487 and V510D in our structure, and instead R487 is involved in a crystal contact (data not shown).

The observed interaction of the D510 side chain with K564 in the crystal structure supports the hypothesis from our molecular dynamics simulations that D510 predominantly interacts with residues in NBD1 to exert its stabilizing effect on CFTR. Interaction with K564 may stabilize the F508 loop, which in turn would be expected to increase productive folding of NBD1 and proper assembly of the full-length channel, a hypothesis that was consistent with corresponding *in vitro data*. The mutation also eliminates the exposed hydrophobic side chain of V510, further impacting NBD1 stability in a positive manner. Our structure of isolated NBD1 cannot rule out potential interactions of D510 with R1070, but given that we see a similar pattern of effects for the V510D and K564 mutants in the context of full-length CFTR and NBD1, it appears that the predominant effect of V510D is confined to NBD1. A cryo-EM structure of full-length dF508/V510D CFTR would be helpful to provide a more definitive conclusion regarding the role of the V510D mutation.

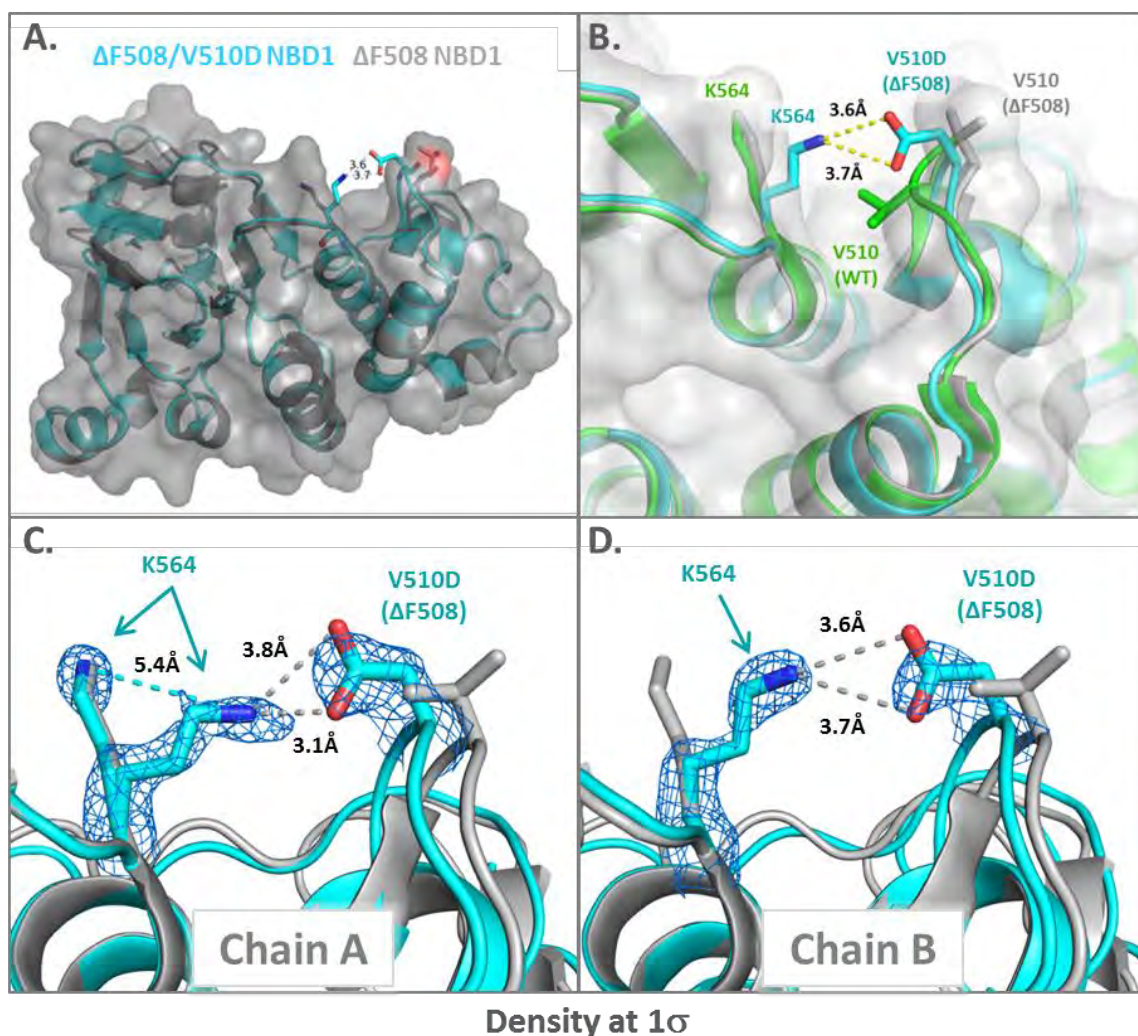


**Figure 2.13 The  $\Delta F508/V510D$  NBD1 crystal structure confirms the D510-K564 salt bridge.** Panel A. NBD1  $\Delta F508/V510D$  structure solved to 1.86 Å resolution (shown in blue) is aligned with  $\Delta F508$  NBD1 (gray). A clear salt bridge is formed between D510 and K564. Panel B shows local change in NBD1 structure at V510 loop (in grey) with the addition of the V510D mutation (blue). Wild-type NBD1 crystal structure shown in green for positional reference. Panel C/D K564 moves about 5.4 Å between the standard and V510D conformations. It appears to alternate from the standard rotamer to a new rotamer capable of creating a salt bridge with D510. In chain A (at left), K564 is mostly in the salt-bridge conformation and partially in the standard NBD1-1D conformation. In chain B (at right), K564 is fully in the salt-bridge conformation. Density looks better for the salt-bridge conformation, but there is a population in the standard conformation.

**Table 2.2  $\Delta$ F508/V510D-NBD1 structure determination/refinement statistics**

<b><math>\Delta</math>F508/V510D-NBD1 (<math>\Delta</math>RI/<math>\Delta</math>RE)</b>	
<b><i>Data Collection</i></b>	
Wavelength (Å)	0.979
Resolution range (Å)	42.77 - 1.857 (1.923 - 1.857)
Space group	P 2 <sub>1</sub> 2 <sub>1</sub> 2 <sub>1</sub>
<b><i>Unit cell dimensions</i></b>	
a, b, c (Å)	62.40, 81.66, 100.40
$\alpha$ , $\beta$ , $\gamma$	90°, 90°, 90°
Total reflections	1,254,648
Unique reflections	43,799 (4,112)
Multiplicity	6.0 (5.7)
Completeness (%)	99.47 (95.07)
Mean I/sigma(I)	9.2 (2.2)
Wilson B-factor	20.97
R-merge	0.124 (0.916)
R-meas	0.127 (>1.000)
R-pim	0.055 (0.410)
CC1/2, CC*	(0.741), (0.923)
<b><i>Refinement</i></b>	
Reflections used in refinement	43,791 (4,110)
Reflections used for R-free	2,116 (199)
R-work	0.1698 (0.2671)
R-free	0.2121 (0.3357)
Number of non-hydrogen atoms	3,966
Macromolecule atoms	3,470
Ligand atoms	64
Solvent atoms	432
Protein residues	442
RMS bonds (Å)	0.01
RMS angles (°)	1.45
Ramachandran favored (%)	97.94
Ramachandran allowed (%)	2.06
Ramachandran outliers (%)	0
Rotamer outliers (%)	0.52
Clashscore	4.81
Average B-factor	28.99
Macromolecules	28.11
Ligands	25.55
Solvent	36.53
Number of TLS groups	11

Parentheses denote value in outer shell

#### 2.4.4 Evaluation of Helical Unraveling

In an attempt to validate the helical unraveling predicted by the MD simulation of  $\Delta F508$ -hCFTR, and to better understand the impact  $\Delta F508$  may be having on TMD2, including whether NBD1 stabilization with and without ICL4 correction might lessen this impact, we created a series of constructs to introduce mutations along TMs 10 and 11, with the potential to stabilize helical structure. Using our structural models, we selected residues Q1042, P1050 and L1096, all within the region predicted to unravel, based on their likelihood to create salt bridges with existing residues in close proximity, and replaced each with charged residues in full-length WT,  $\Delta F508$ -hCFTR, and  $\Delta F508/V510D$ -hCFTR expression constructs. To ensure that the potential introduction of salt bridges along TMs 10 and 11 did not interrupt normal CFTR trafficking, we first tested the mutations on the WT-CFTR background, and saw no changes to normal CFTR maturation. We then evaluated mutations for their impact on  $\Delta F508$ - and  $\Delta F508/V510D$ -CFTR. No measurable increase in CFTR complex glycosylation and maturation was observed when the charged residue mutations were added to  $\Delta F508$ -CFTR, with the exception of the P1050R mutation. This effect is significantly augmented when V510D is added to  $\Delta F508$ -NBD1; an increase in fully-glycosylated CFTR was seen (albeit to varying degrees) with nearly all salt-bridge mutations when added to  $\Delta F508/V510D$ -CFTR. Based on this work, P1050R was identified as a potentially strong second-site suppressor

of  $\Delta F508$ -CFTR helical unraveling and was marked for further evaluation. Immunoblotting data of the initial evaluation panel for  $\Delta F508$  and  $\Delta F508/V510D$ -CFTR constructs is seen in Figure 2.14.

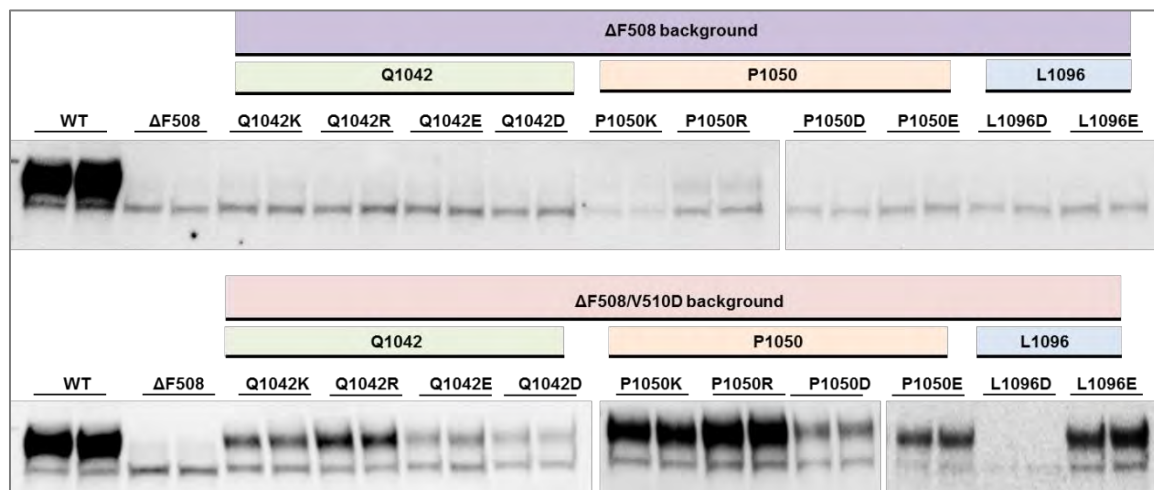


**Figure 2.14 Preliminary western blot analysis of helical stabilization mutations along TMs 10 and 11.** Initial analysis of  $\Delta F508$ -CFTR (panel A, samples included under purple rectangle) and  $\Delta F508/V510D$  CFTR (panel B, samples included under pink rectangle) expression when single point mutations were added along TMs 10 and 11 suggest that the addition of charged residues leads to an increase in  $\Delta F508/V510D$  maturation, indicated by the increase in “C band” intensity when samples are immunoblotted for CFTR. Samples were evaluated in duplicate, with an n of 3 for this set of constructs, and mutation sites are indicated by the green (Q1042), orange (P1050) or blue (L1096) rectangles.

This first round of mutation screening was repeated to include control construct  $\Delta F508/V510D$ -CFTR and was performed using plasmids that contained the bicistronic GFP internal transfection control which were absent in the original set of experiments



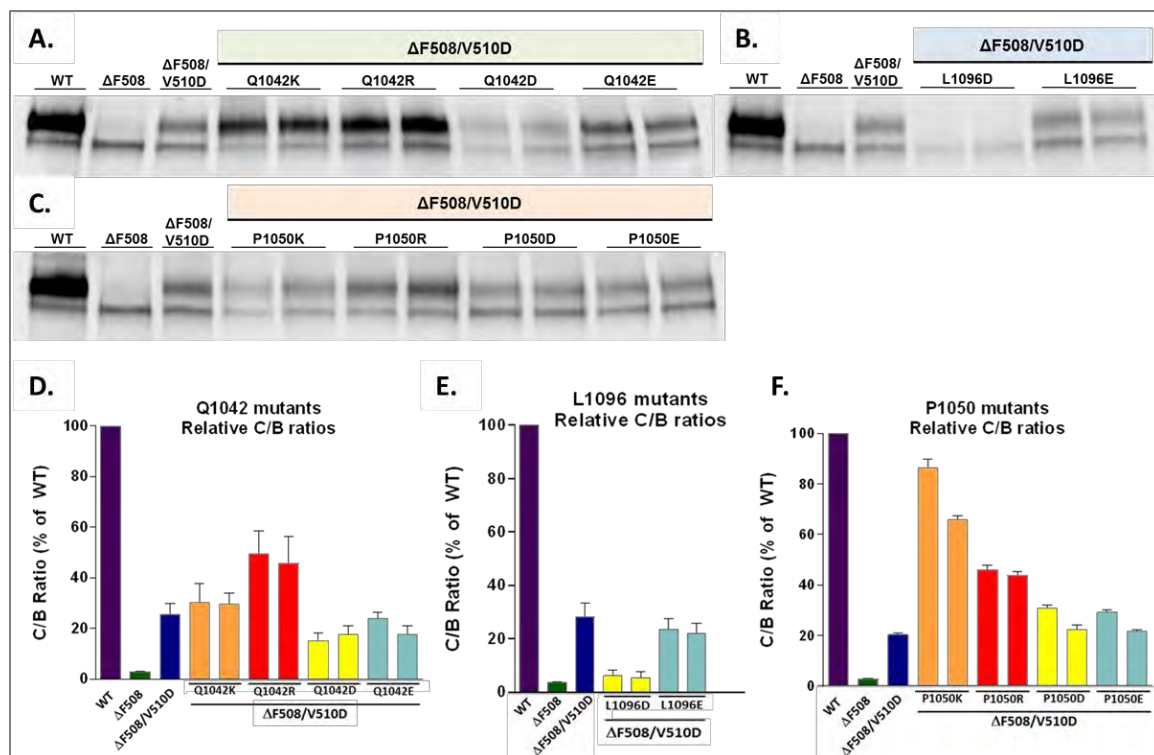


**Figure 2.15 Western blot and C/B ratio analysis of helical stabilization mutations along TMs 10 and 11.** Repeat analysis of  $\Delta F508/V510D$  CFTR expression with the addition of charged residue point mutations at Q1042 (A and D), L1096 (B and E) and P1050 (C and F) along TMs 10 and 11 confirm the stabilizing effect previously seen. Expression was normalized using a bicistronic GFP expression control. Similar to previous experiments, maturation is increased in nearly all cases when stabilizing mutations are added to  $\Delta F508/V510D$  CFTR as measured by an increase in fully-glycosylated CFTR. Again, P1050R was identified as a strong stabilizer of  $\Delta F508/V510D$  CFTR, as was Q1042R. A representative western blot from each mutation set is shown, with samples loaded onto the gel as biological replicates. This experiment was performed three times for this set of constructs. Mutation sites are indicated by the green (Q1042), orange (P1050) or blue (L1096) rectangles. Corresponding C/B ratio values reflect an n of 3 separate experiments for each mutational replicate. Bar graphs are colored based on the mutation made to a given residue in an effort to draw a comparison across experiments (orange: lysine; red: arginine; yellow: aspartic acid; teal: glutamic acid).

Overall, it appeared that the positively charged lysine and arginine residues were a more favorable fit than the negatively charged aspartic acid and glutamic acid residues, and that the slightly larger and more basic arginine resulted in the greatest level of CFTR maturation in all cases. Additionally, when such mutations were paired with V510D, a synergistic effect was seen on the levels of CFTR maturation when the double mutant was compared to either  $\Delta F508$ -CFTR or  $\Delta F508/V510D$ -CFTR alone. We observed that when the P1050R mutation was made to  $\Delta F508/V510D$ -CFTR it was capable of restoring trafficking better than V510D alone, and in a few instances, restored trafficking to near wild-type levels (Figure 2.15). This mutation was subsequently used for more in-depth analysis of helical stabilization. While P1050K had the highest C/B ratio via densitometry analysis, it produced slightly less CFTR overall. Significant increases were also noted in protein maturation when Q1042K or Q1042R was added to  $\Delta F508/V510D$ -CFTR, translating to a C/B ratio similar to that of P1050R (Figure 2.15, panels A and D). In only one instance, L1096D, did the mutation not act cooperatively with V510D to restore CFTR trafficking (Figure 2.15, panels B and E).

### **The role of V510D in P1050R-mediated helical rescue**

The V510D suppressor mutation is postulated to correct  $\Delta F508$ -CFTR dysfunction through partially-independent effects on the stability of both NBD1 and the ICL4-NBD1 interface. We sought to understand the extent to which V510D's cooperativity with helix stabilization was dependent on each

mechanism. To accomplish this, we first disrupted V510D's interaction with R1070 at the ICL4 interface by adding the R1070S mutation to  $\Delta F508/V510D$ -CFTR, both alone and in combination with TM10 salt-bridge mutation, P1050R.

As previously mentioned, when P1050R is added to  $\Delta F508$ -CFTR, a small improvement in CFTR maturation occurs that is approximately half that of the  $\Delta F508/V510D$  mutation alone (Figure 2.15). A synergistic increase in trafficking and maturation is measured when P1050R is combined with V510D, which restores the level of mature CFTR at the cell surface to ~80% of WT levels when analyzed by both western blotting (C to B ratio) and HRP trafficking assays (Figure 2.16). When the ICL4 interface is interrupted by the addition of R1070S, however, V510D-mediated rescue of  $\Delta F508$ -CFTR drops from approximately 15% to 5% of WT levels. A similarly modest rescue effect (~5% of WT) is seen when P1050R is added to  $\Delta F508/R1070S$ -CFTR; however, a synergistic effect is seen when both P1050R helical stabilization and V510D NBD1/ICL4 stabilization are added to  $\Delta F508/R1070S$ -CFTR, which improves trafficking to roughly half that of WT CFTR. To solely evaluate NBD1:ICL4 interface stabilization with and without P1050R, we assessed the impact of R1070W on  $\Delta F508$ -CFTR, and saw a very modest improvement in trafficking similar to V510D alone, as anticipated. When  $\Delta F508/R1070W/P1050R$  was evaluated, trafficking was restored to about half that of WT-CFTR, similar to the combination of V510D and R1070S with P1050R.



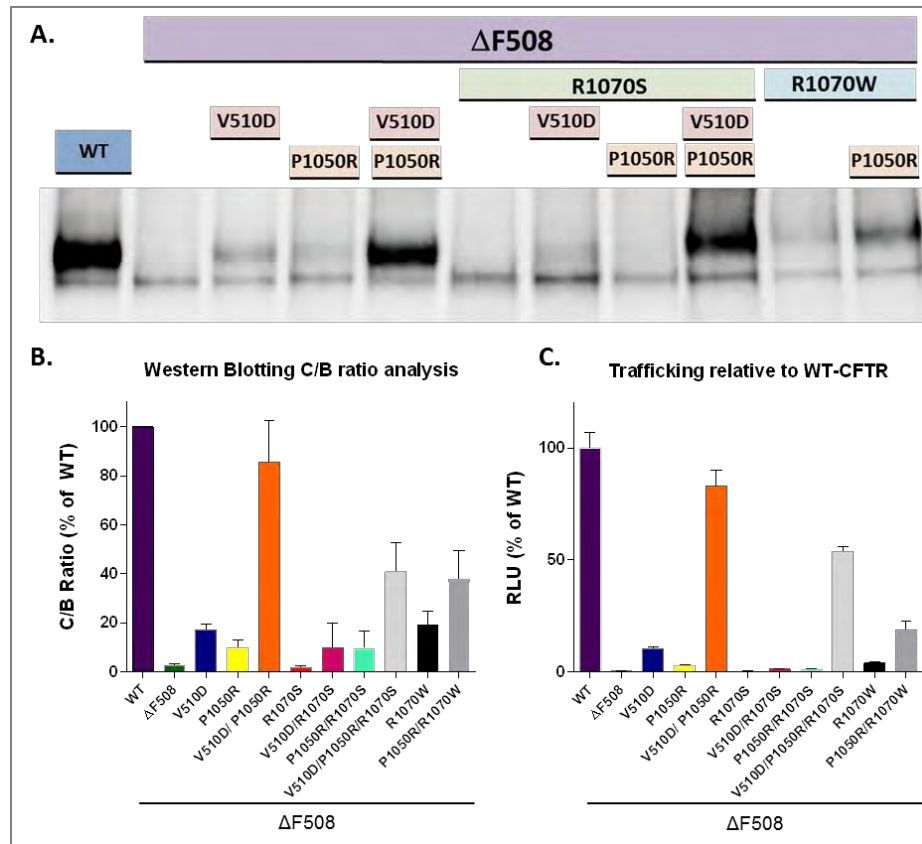


**Figure 2.16 NBD1 stabilization is critical for P1050R rescue of ICL4-stabilized  $\Delta$ F508-CFTR.** The impact of ICL4 and NBD1 stabilization on P1050R-mediated rescue of  $\Delta$ F508-CFTR was evaluated via western blotting (panel A; corresponding C/B ratio graph in panel B) and HRP trafficking (panel C). The addition of P1050R to  $\Delta$ F508-CFTR results in very modest improvements in CFTR maturation (yellow bar). However, when suppressor mutation V510D is paired with P1050R, the greatest impact on  $\Delta$ F508-CFTR maturation and trafficking is seen (orange) at about 80% of WT CFTR. When R1070S is then added to explore the impact of interrupting the NBD1:ICL4 interface, this level of CFTR maturation drops from ~80% to 50%. When R1070W is included to partially restore the ICL4 interface and V510D is removed, the impact on  $\Delta$ F508-CFTR is about half that of V510D, and the addition of P1050R to R1070W/ $\Delta$ F508-CFTR only improves this to roughly 25%, suggesting that NBD1 stabilization is critical to the P1050R rescue effect of  $\Delta$ F508-CFTR. For western blot,  $n=3$ ; for trafficking assay,  $n=6$  for each assay plate, with 3 replicate assays performed.

Next, we disrupted V510D-mediated NBD1 stability by again introducing K564A to remove the V510D salt-bridge interaction. Consistent with earlier results, V510D rescue of  $\Delta$ F508-CFTR is diminished by the replacement of a charged lysine residue at 564 with an alanine. However, when P1050R is added to  $\Delta$ F508/V510D/K564A-CFTR, a synergistic effect is again seen and trafficking is restored to approximately 40% of WT levels, despite the loss of K564 (Figure 2.17), supporting the hypothesis that V510D requires K564 for complete NBD1 stabilization, which is an essential component of  $\Delta$ F508-CFTR maturation and trafficking.

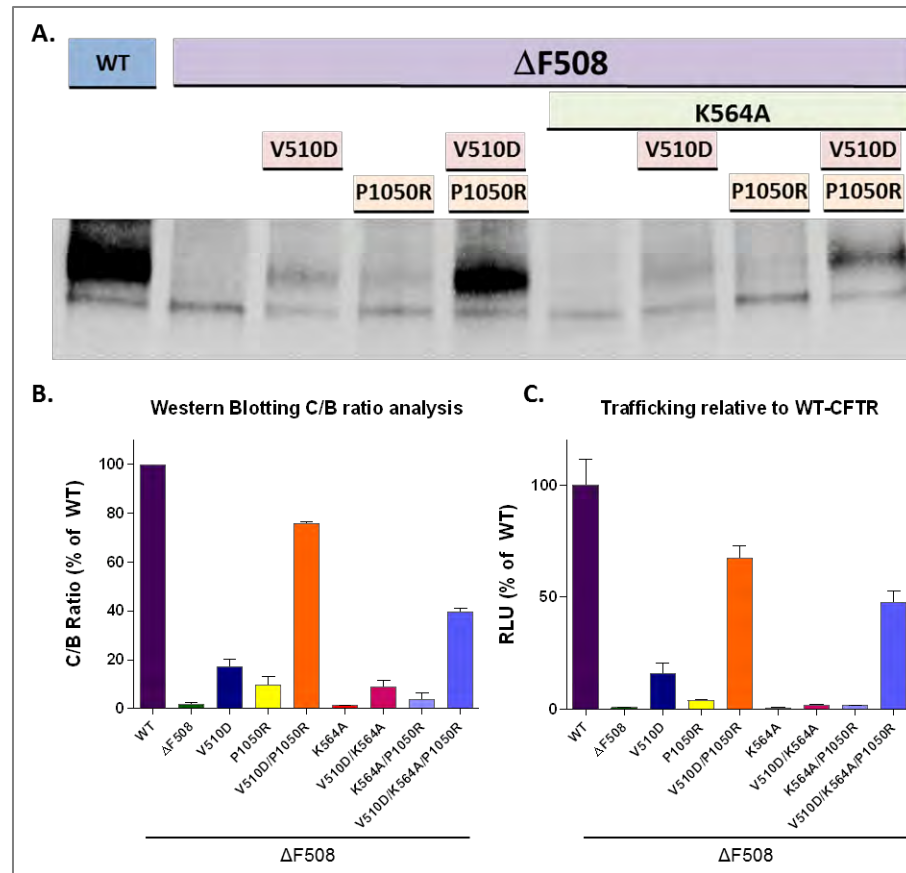


**Figure 2.17 NBD1 stabilization and K564/V510D interactions are critical for P1050R rescue of  $\Delta$ F508.** K564A leads to a 30-40% reduction in V510D/P1050R rescue of  $\Delta$ F508-CFTR as measured by immunoblotting and HRP trafficking assays, underscoring the importance of NBD1 stabilization on P1050R  $\Delta$ F508-CFTR rescue. For western blot,  $n=4$ ; for trafficking assay,  $n=8$  for each assay, with 3 replicate assays performed.

To understand whether the element of P1050R's mechanism that is NBD1-dependent required V510D specifically, we replaced V510D with alternate NBD1 stabilizing mutations F494N/Q637R (2S), or F494N/Q637R/F429S (3S) (Lewis *et al.*, 2004; Lewis *et al.*, 2010; Rabeh *et al.*, 2012a), which do not reside at the ICL4 interface. When the 2S or 3S mutations were added to  $\Delta$ F508-CFTR, a modest amount of rescue occurred via western blotting and HRP trafficking

(6.5% and 9.5% of WT, respectively, Figure 2.18). However, when the NBD1 stabilizing 2S or 3S mutations were coupled with P1050R, maturation and trafficking of the resulting protein improved synergistically, with  $\Delta F508/P1050R/2S$  reaching ~40% of WT and  $\Delta F508/P1050R/3S$  resulting in ~80% of WT trafficking levels.

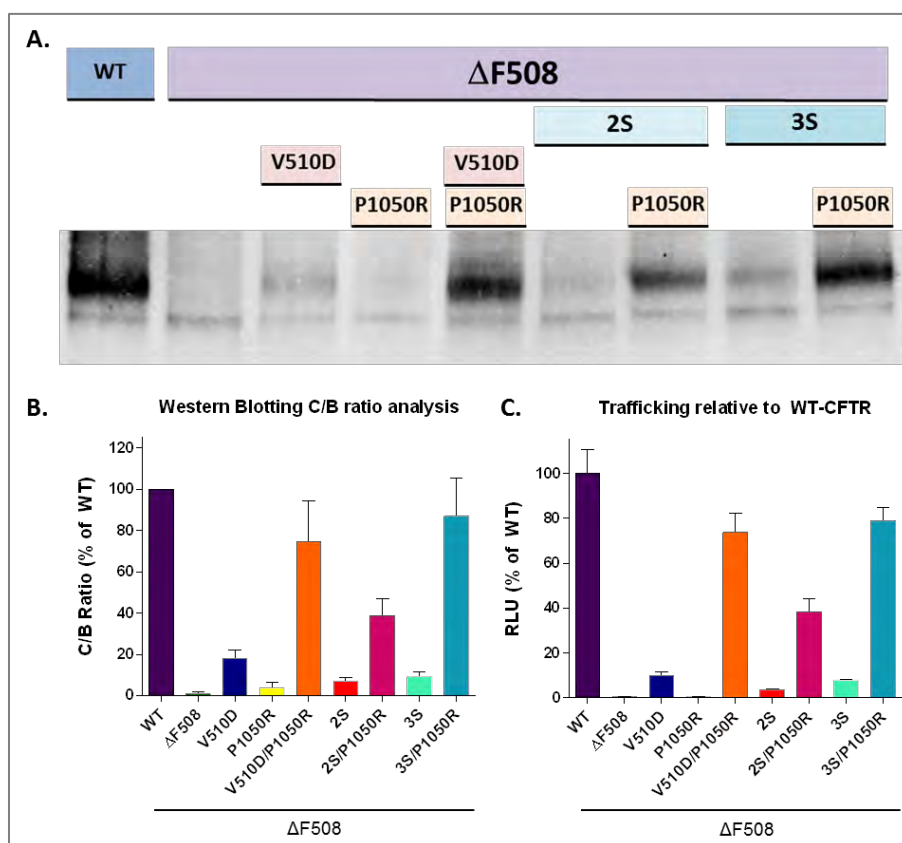


**Figure 2.18 The role of NBD1 stabilization on  $\Delta F508$ -CFTR rescue does not require dual correction by V510D when P1050R helical stabilization is added.** When the 2S or 3S mutations were added to  $\Delta F508$ -CFTR, improvements in trafficking of 6.5% and 9.5% of WT respectively were seen. However, when 2S or 3S mutations were coupled with ICL4 stabilizing mutation P1050R, maturation and trafficking significantly improved.  $\Delta F508/P1050R/2S$  resulted in ~40% of WT and  $\Delta F508/P1050R/3S$  in ~80% of WT trafficking levels. Western blot analysis and C/B ratios represent an n=4; for trafficking assay, n=8 for each assay, with 3 replicate assays performed.

## 2.5 Discussion

This work was intended to accomplish three goals: i.) to gain insight into the effects of the  $\Delta F508$  mutation on CFTR conformational dynamics, ii.) to determine how second-site suppressor mutations may influence these, and iii.) to validate a molecular model of  $\Delta F508$ -CFTR in the absence of a full-length structure.

Given the potential impact of structure-based drug design on the development of CF therapeutics, structural and biophysical properties of full-length CFTR continue to be of great importance. Recently, two high-resolution cryo-EM structures of hCFTR were published, providing “snapshots” of both inward- and outward-facing conformations, as well as new insight into CFTR channel gating and function (Liu *et al.*, 2017; Zhang *et al.*, 2018b). Ultimately, however, the native structure of  $\Delta F508$ -CFTR and a better understanding of the mutation’s impact on CFTR conformational dynamics would be invaluable, yet remains a significant challenge given the protein’s instability. And while a high-resolution structure of  $\Delta F508$ -CFTR with stabilizing mutations might provide important information, this stabilization may also mask key elements of the  $\Delta F508$  folding defect. *In silico* models and MD simulations may offer a complementary view of the protein and its intramolecular interactions, as well as a better understanding of the  $\Delta F508$  mutation’s impact on CFTR structure and how second-site suppressor mutations may influence this. With this in mind, we

generated novel CFTR models of wild-type and  $\Delta F508$ -CFTR (Figure 2.1) based on the crystal structure of the homologous ABC transporter, Sav1866 in the outward facing conformation (PDB code 2HYD) (Dawson and Locher, 2006), given its precedent as a model for CFTR structure (Dalton *et al.*, 2012; Mornon *et al.*, 2008; Serohijos *et al.*, 2008).

One aspect of the CFTR and Sav1866 structures that is notably different is the size of these proteins' extracellular pores, an observation that is highlighted by Zhang *et al.* (Zhang *et al.*, 2017) when comparing the structure of homologous protein, Sav1866 to phosphorylated zebrafish CFTR. In Sav1866, the channel opening that results from the separation of TM 4/6 and TM 10/12 is relatively large so as to accommodate drug-like substrates (Zhang *et al.*, 2017). In contrast, CFTR's extracellular pore is considerably smaller but is of sufficient size to provide a conduit for chloride ions. Because of this difference, several TM helices, which in our CFTR model were based on Sav1866, are rotated and displaced relative to the recently published CFTR cryo-EM structure. Notably, such differences are mostly limited to the extracellular side of CFTR's intramembrane region. Perhaps surprisingly, Sav1866 served as an appropriate template for CFTR's intracellular TMs, where substantial structural similarity is seen between the model and the solved structure (Figures 2.2 and 2.3). As described above, CFTR's NBD1 and NBD2 (Figures 2.2I and J), were modeled from crystal structures of the isolated domains. Both are very similar to the CFTR cryo-EM structure, including side chain orientations and, importantly, their

interactions with ICL regions. This similarity is not surprising, however, as the cryo-EM structures and our homology model incorporated the same NBD1 and NBD2 crystal structures as starting models for those domains.

While the results from our MD simulation represent only one random seed, the data provided a good starting point for hypothesis generation and subsequent experimental verification. However, multiple runs with different random seeds are needed for a comprehensive statistical analysis. With that said, the secondary structure (SS) analysis that resulted was in close agreement with previously reported experimental data for WT- and  $\Delta F508$ -CFTR stability with and without V510D or R1070W (Aleksandrov *et al.*, 2015; Krasnov *et al.*, 2008; Loo *et al.*, 2010; Meng *et al.*, 2017a). Our simulation also provided a solid platform for testable hypotheses regarding the impact of  $\Delta F508$  on TMD2 and critical interactions that support V510D suppression of  $\Delta F508$ , which we then successfully verified experimentally. For example, our models clearly show stronger conservation of  $\Delta F508$ -CFTR secondary structure with the addition of V510D compared to R1070W, an outcome previously predicted to be the result of V510D's dual stabilization of both the NBD1:ICL4 interface and NBD1 alone, as opposed to R1070W's primary role of interface correction (He *et al.*, 2013; Protasevich *et al.*, 2010).

By evaluating the impact of these mutations alone and with additional NBD1 stabilizers in full-length CFTR, and coupling this with structural and

stability data collected from solubilized  $\Delta F508/V510D$ -NBD1, we effectively supported the hypothesis that V510D plays a role in both interface correction and NBD1 stabilization, an outcome we observed in both WT and  $\Delta F508$ -CFTR. However, when the V510D mutation is made to WT CFTR, the result is a hyper-stabilized, yet less functional molecule, as significant increases are seen in trafficking, but activity is reduced when WT/V510D-CFTR is analyzed via electrophysiology (Figure 2.11). Given that no reduction in CFTR maturation, trafficking or function was seen when residue K564 was altered within the context of WT-CFTR, regardless of the presence of V510D, it is likely that in WT/V510D-CFTR, no interaction exists between D510 and K564 (Figures 2.10 and 2.11). Rather, D510's primary interaction becomes the salt-bridge with R1070, creating an interface that is too rigid, and may hinder the flexibility seen when the interface is mediated by F508. This level of interaction is not seen in  $\Delta F508$ -CFTR, however, likely due to the flexibility and solvent exposure of the V510 loop, which may make this interaction easier to disrupt.



### **2.5.1 Presence and position of residue K564 is key to V510D suppression of the $\Delta$ F508 trafficking defect**

In addition to providing support for V510D's dual role of ICL4 and NBD1 stabilization, we experimentally validated the salt-bridge interaction between K564 and V510D that was predicted from our MD simulation of  $\Delta$ F508/V510D-CFTR in several different ways. Quantitative data collected from CFTR immunoblotting (C/B band ratio), HRP-trafficking (Relative Fluorescence Units) and electrophysiology (FPmax values) experiments display highly correlative trends (Figures 2.7 and 2.8). In all cases, the addition of V510D results in modest rescue of CFTR trafficking (an average of ~5-10% of WT), which is diminished by half with the removal of K564's positive side chain. The validity of this 50% reduction is further supported by the positional likelihood of the K564-V510D salt bridge that is seen in the crystal structure. With regard to the near-total loss of trafficking that occurs in the case of K564S, (regardless of V510D), this may be attributed to perturbations that arise from the addition of a serine hydroxyl group at the tail-end of the  $\alpha$ -helix spanning residues 549-564 within NBD1. In such a conformation, it is energetically unfavorable for the hydroxyl group to lack an interaction and may compete with the peptide backbone for available hydrogen bonds, potentially destabilizing the domain and altering its conformation.

Another possible explanation for the inactivity of K564S is the potential creation of a phosphorylation site for Casein Kinase 2. The Ser phosphorylation motif for CK2 kinase is a critical acidic residue (preferably Asp) at position +3. Phosphorylation potential is enhanced further if it has additional acidic residues (again, preferably Asp) spanning from -2 to +7. Additionally, this requires the

absence of a proline or bulky hydrophobic side chain at  $n+1$ , or bulky hydrophobic doublets at  $+1$  and  $+2$ . All of these criteria are met in CFTR sequence 564 – 572, i.e. **K564(S)-D-A-D-L-Y-L-L-D**. Ser564 is at the C-terminal end of an  $\alpha$ -helix while the N-terminal end and the preceding loop have close interactions with ATP; a number of stabilizing residues are located in this region and hence any perturbation of this region may destabilize NBD1 and its interaction with ATP.

Despite the modest occurrence of an interaction that appeared between V510D and R487 in our salt bridge analysis performed for the  $\Delta F508/V510D$ -CFTR MD simulation, mutating the positively charged arginine residue at position 487 to an alanine does appear to significantly reduce trafficking and function of both WT- and  $\Delta F508$ -hCFTR (data not shown). This reduction in maturation may be due to the residue's potential role in ATP binding and hydrolysis, specifically transition state stabilization (Manavalan *et al.*, 1995). Indeed, no interaction is observed between D510 and R487 in our crystal structure. Rather, R487 is involved in a crystal contact in our crystal form and might therefore be unavailable for interaction with D510. If such an interaction were critical to V510D stabilization of  $\Delta F508$  NBD1, however, one might expect that as a result we would not be able to obtain the observed crystal form for the mutant. It is therefore probable that interaction with R487 is not a significant manifestation of the observed effects of the V510D mutation.

### **2.5.2 The occurrence and subsequent rescue of TMD2 helical unraveling in $\Delta F508$ -CFTR**

Our MD simulations data also provided insights into how TMD2 helical unraveling may be a key component of  $\Delta F508$ -CFTR destabilization, a prediction that has not previously been reported. It is suggested through our models that the  $\alpha$ -helical region of ICL4 spanning 1034 to 1050 (aa sequence ESEGRSP) is one of the most destabilized within  $\Delta F508$ -CFTR, likely owing to the presence of helix-breaking residues serine and proline, which make this region vulnerable to conformational perturbations. In WT-CFTR, when the NBD1:ICL4 interface and the  $\alpha$ -helical conformation of this region are intact, salt bridges exist between E1044 and K1041, and potentially with R1158 or K978 (from ICL2), which may help stabilize the loop. In  $\Delta F508$ -CFTR on the other hand, these salt bridges are broken, as E1044 and K1041 move away from each other, and L1040, which may normally create stabilizing interactions with L1091 and W0189 in TM11, becomes completely exposed. Based on this information, we hypothesized that the addition of polar residues at the intracellular side of helices 10 and 11 may produce stabilizing salt bridge interactions, effectively creating second-site suppressors of  $\Delta F508$ .

In order to determine which mutation sites would produce the most impactful stabilization, we referred to sequence and structural information for TMD1 for guidance, given the presumably greater stability that our model

suggests. Sequence comparison of the two TMDs shows a higher prevalence of charged residues within TMD1 (AA 66-431), which contains 19 Arg and 24 Lys, as well as 21 Glu and 9 Asp for a total of 43 positively charged and 30 negatively charged side chains. In comparison, TMD2 (AA845-1198) contains only 30 positively charged side chains (13 Arg and 17 Lys), and 19 negatively charged (9 Asp and 9 Glu). We did not take into account His residues in either case, as they are generally neutral. Based on this comparison, three residues were highlighted by our analysis as potential mutation sites: Q1042 and P1050, which are both on TM10 of ICL4, and L1096, which resides at the bilayer interface of TM11, with preference given to the former two based on their likelihood for success.

With the introduction of polar residues at these sites, patterns arose with which changes successfully increased the level of CFTR maturation and which had either no impact or a deleterious one. In all cases, polar residue insertions made no improvement to CFTR maturation and trafficking when added to  $\Delta F508$ -CFTR (Figure 2.12), which is unsurprising given the unstable nature of the protein overall, and if our model is any indication, the significant helical disorder that may be present. However, when the charged residue substitutions are paired with V510D, we see stabilizing trends emerge. Overall, a greater increase in CFTR trafficking was seen when replacements were made at Q1042 and P1050 with basic residues Arg and Lys, suggesting the possible interaction of either residue with E1046; however, a favorable position of the sidechains would be required, as the distance is too great for an interaction to occur

otherwise. The replacement of either Q1042 or P1050 with acidic residues Asp and Glu did not appear to improve trafficking more so than V510D alone, suggesting that the insertion of a negative charge, while not potentially destabilizing, provided no suppression of helical instability. This is in keeping with the “positive inside rule,” which states that positively charged residues (Arg and Lys) will frequently be located at the cytoplasmic edge of transmembrane helices, (Lew *et al.*, 2003; von Heijne, 1992), with the opposite being true for negatively charged residues (Baker *et al.*, 2017), a trend that is supported by extensive statistical observations for most MPs (Baeza-Delgado *et al.*, 2013; Baker *et al.*, 2017). The proposed utility of this “charged-residue flanking bias” (Baker *et al.*, 2017) is that positively charged amino acids bordering hydrophobic helices might be involved in TM orientation within the lipid bilayer (Lew *et al.*, 2003), as well as helix-helix interactions (Cosson and Bonifacino, 1992; Lew *et al.*, 2003; Smith *et al.*, 1996). With regard to L1096, we must consider that leucine is highly hydrophobic, and is known to play a critical role in both helical stabilization and TM helix-helix interactions (Baker *et al.*, 2017; Lew *et al.*, 2003; Zhao and London, 2006). Unsurprisingly, modifying this residue did not improve  $\Delta F508$ -CFTR trafficking as shown via western blot, and in the case of the L1096D mutation, abolished the V510D stabilizing effect.

### **Synergy between NBD1 stabilizing SSSMs and P1050R**

The impact of V510D on NBD1 and interface stabilization both contribute to its activity as an SSSM and its synergy with P1050R. Our studies with NBD1 stabilizing mutations help us understand the relative importance of these two effects. As described above, combinations of NBD1 stabilizing mutations F494N/Q637R (2S), or F494N/Q637R/F429S (3S) (Lewis *et al.*, 2004; Lewis *et al.*, 2010; Rabeh *et al.*, 2012a) both robustly synergize with P1050R to further rescue  $\Delta$ F508-CFTR maturation and trafficking in the absence of V510D. The 2S mutations, which together stabilize purified  $\Delta$ F508-NBD1 by  $\sim 2$  °C (He *et al.*, 2015) when combined with P1050R, rescue  $\Delta$ F508-CFTR maturation to approximately 40% of WT levels. A larger impact is seen in the presence of the 3S mutations, which together stabilize purified  $\Delta$ F508-NBD1 by 5.7 °C (Rabeh *et al.*, 2012a). Rescue of the  $\Delta$ F508-CFTR maturation and trafficking are highly similar when either 3S/P1050R or V510D/P1050R is present. In each case, rescue to levels >80% of WT was observed. It is noteworthy that the 2.5 to 3 °C increase in  $\Delta$ F508-NBD1 stability when V510D is present is far closer to that seen with 2S than 3S. The  $\Delta$ F508-CFTR rescue by V510D in the presence of P1050R is therefore greater than would be predicted from its impact on NBD1 stability alone. It is also noteworthy that R1070W/P1050R rescues  $\Delta$ F508-CFTR maturation to a similar level, 40% of WT, seen in the presence of 2S/P1050R. These levels of  $\Delta$ F508-CFTR rescue are roughly half those provided by P1050R in the presence of V510D, consistent with its dual activity. The findings are also

consistent with our studies of  $\Delta F508/R1070S/V510D$  CFTR, where, relative to  $\Delta F508/V510D$  CFTR, a significant reduction in apically localized CFTR and the band C/band B ratio are observed. Similar differences in relative rescue efficacies are seen for these mutations in the presence of P1050R.

It should be noted that while close correlation is generally seen between the HRP trafficking assay and C/B ratio values obtained by immunoblot densitometry, it is necessary to consider both values when interpreting the level of CFTR maturation. Although western blotting and increased C/B band ratio continue to be the canonical means of measuring increases in CFTR maturation, overall increases or reductions in CFTR protein expression are not reflected when reported as a ratio. The HRP-trafficking assay provides a much more quantitative measurement that is capable of discerning differences in relative levels of both overall and fully-glycosylated, apical surface CFTR.

Together, our findings further highlight the dual nature of V510D's SSSM mechanism. In addition, the data validate novel predictions derived from our *in silico* CFTR model and MD simulations. The data provide evidence that the impact of V510D and K564 have an additive effect on  $\Delta F508$ -CFTR rescue, which also supports the requirement of K564 for V510D stabilization. Central also among validated predictions are the previously undescribed impact of  $\Delta F508$  on the stability of TMD2 helices, the contribution of helical unravelling to  $\Delta F508$ -CFTR dysfunction, and the existence of novel SSSMs within TM10 that partially counteract this aspect of the  $\Delta F508$  defect. The data demonstrate that the novel

SSSM P1050R acts by a mechanism distinct from those of R1070W, V510D or NBD1 stabilizing mutations. Indeed, P1050R's synergy with interface and NBD1 stabilizing SSSM underscores the potential therapeutic value of small molecule  $\Delta F508$ -CFTR correctors that share its presumed mechanism of action, namely TM10 stabilization.



## 2.6 Materials and Methods

### Homology Modeling

Homology models of full-length WT,  $\Delta$ F508,  $\Delta$ F508/V510D and  $\Delta$ F508/R1070W CFTR were generated in Discovery Studio (BIOVIA, 2016) using the crystal structure of SAV1866 in the outward facing conformation (PDB code 2HYD) as a template. We replaced the SAV1866 NBD1 domain with the hCFTR NBD1 crystal structure (PDB code 2PZE), and made the appropriate corrections for all missing side chains and residue substitutions. Likewise, the  $\Delta$ F508-NBD1 crystal structure (PDB code 2PZF) was incorporated for the  $\Delta$ F508-CFTR variant models. For modeling NBD2, crystal structure of NBD2 fused to maltose-binding protein (PDB code 3GD7) was used as the template. Relative positioning of NBD1 and NBD2 were based on Sav1866 and NBD1 homodimer structures. The R-domain, which ranges from approximately 641-849, was not included in our model, as no homologous template was available for this domain. To create the  $\Delta$ F508 SSSM variants, stabilizing mutations V510D and R1070W were individually added to the  $\Delta$ F508-CFTR model, and any resulting steric hindrances were relieved by local energy minimization. All models were further refined using Maestro Protein Preparation Wizard (2016).

### Molecular Dynamics Simulations

We used the Desmond System Builder (Bowers *et al.*, 2006) to place a pre-defined lipid bilayer of 1-palmitoyl-2-oleoyl-sn-glycero-3-phosphocholine (POPC) using transmembrane boundaries reported in Uniprot for all homology models. Each system was solvated with a TIP3P (transferable intermolecular potential with 3 points) water model (Jorgensen 1983) and neutralized with chlorine counter ions. We also added Sodium Chloride at a concentration of 0.15 M, leading to roughly 160K atom systems. After equilibration, all simulations were carried out using the Desmond (GPU) simulation package from Schrödinger at a constant-temperature, constant-pressure ensemble (NPT) of 300 K and 1.01 Bar respectively for a time of 1  $\mu$ s and a frame-capture interval of 800 ps resulting in a total of 1,251 frames. Subsequent analyses were performed using Maestro (Maestro, 2016), Visual Molecular Dynamics (Humphrey *et al.*, 1996), MOE™: Molecular Operating Environment (CCG), and several modules that were developed in-house using Python, SVL and Perl scripting languages.

For each model, event analysis was completed to identify changes in secondary structure, residue surface area/volume/geometry, variation in residency time of chosen residues in select regions of the protein, and the presence or absence of salt bridges (Kabsch and Sander, 1983). Residues of interest for secondary structure analysis included neighboring regions S495-E514 within NBD1 and Q1035-R1102 at ICL4. Solvent accessibility calculations were performed using the Euclidean Distance Transform surface calculation method.

## **Construct generation and expression of full-length hCFTR mutants**

### **CFTR plasmid mutagenesis**

QuikChange Single and Multi-Site Directed Mutagenesis system (Agilent Technologies) was used to modify select residues located in NBD1 and along helices 10 and 11 in TMD2. Within NBD1, K564A/S and R487A/S mutations were made, and along TM10 and TM11, charged residues were introduced at Q1042, P1050 and L1096 in full-length WT,  $\Delta$ F508-hCFTR, and  $\Delta$ F508/V510D-hCFTR expression constructs. A second round of constructs was made to include suppressor mutations F494N, Q637R and F429S or R1070W alongside P1050R +/- V510D in  $\Delta$ F508-hCFTR. For some mutants, a duplicate set of mutated WT and  $\Delta$ F508-CFTR plasmids that express an HRP tag on ECL4 (between S902 and Y903) was created to evaluate trafficking (see Figure 2.9D.). All constructs contained a “self-cleaving” GFP transfection control, introduced by 2A-based bicistronic expression. In all cases, mutations were verified by Sanger sequencing.

### **CFSME<sub>0</sub>- cell culture**

CF patient-derived CFSME<sub>0</sub>- cells (kindly provided by Dr. Dieter C. Gruenert, UCSF) were maintained at 37 °C in Minimum Essential Medium with Earle's salts, supplemented with 10% (v/v) FBS, 2 mM L-glutamine and 1% (v/v) pen/strep on ECM-coated flasks (10 µg/mL human fibronectin, 30 µg/mL bovine collagen I, 0.1% BSA in LHC basal medium). For evaluation of CFTR trafficking,

cells were plated on collagen-coated plates (Corning BioCoat multiwall plates, Corning, Inc) and transiently transfected using FuGENE HD transfection reagent (Promega US, Madison, WI) according to the manufacturer's instructions.

### **Western blotting**

CFSME<sub>o</sub> cells were plated at 200,000 cells per well in a 6-well, collagen-coated plate and transfected with 3 µg plasmid DNA per well. After 48 hours, cells were washed twice with PBS and collected in cold lysis buffer (25 mM Tris-HCl pH 7.4, 150 mM NaCl, 1 mM EDTA, 1% NP-40 and 5% glycerol) supplemented with protease inhibitors (Roche Complete EDTA-free). Protein concentrations were determined by bicinchoninic acid assay (BCA protein assay kit, Pierce Thermo Fisher Scientific). Whole cell lysates were separated on 7.5% Criterion TGX 7.5% SDS-PAGE gels (Bio-Rad) and transferred to nitrocellulose membranes using a semi-dry transfer apparatus at 20 V for 10 minutes. Membranes were probed with anti-CFTR monoclonal antibody 570 (obtained from UNC Chapel Hill) at a 1:1000 dilution to determine CFTR protein expression and maturation of each mutant construct. Differences in trafficking were measured by comparing the ratio of "C" band to "B" band by densitometry.

### **HRP-Trafficking**

CFSME<sub>o</sub> cells were plated at 8,000 cells per well in 96-well collagen-coated plates and transiently transfected as described. After 48 hours, cell culture

media was removed, cells were washed with PBS, and Luminata Forte HRP substrate (EMD Millipore, Burlington, MA) was added to each well, and chemiluminescent signal of the HRP reporter on ECL4 was measured using an EnVISION plate reader.

To ensure that samples were being properly compared for expressed hCFTR in the HRP-trafficking and immunoblotting experiments, samples were normalized by eGFP expression based on RFU values of each sample lysate. For this, 20  $\mu$ L of lysate was added in triplicate to a 384-well white-walled plate (ProxiPlate-384 Plus, shallow-well microplate, PerkinElmer, Waltham, MA) and read on an EnVision plate reader (PerkinElmer) using excitation/emission wavelengths of 480/535 nm, and an anti-GFP antibody was used during immunoblotting. For the HRP trafficking assay, a semi-quantitative value (RLU) corresponding to the level of CFTR maturation was normalized to GFP expression.

## **NBD1 Analysis**

### **Protein Production**

Human CFTR NBD1 variants (residues 387–678 less 405–436 for  $\Delta$ RI or 405–436/647–678 for  $\Delta$ RI/ $\Delta$ RE, with and without selected mutations) were expressed in BL21 E.coli cells as N-terminal His<sub>10</sub>–Smt3 fusion proteins (Mossessova and Lima, 2000) using a pET24a-derived expression vector. Cultures were grown,

harvested and processed as previously described (Lewis 2005), and the protein was purified from the cell lysate using a nickel ion affinity column and a HiLoad 26/600 Superdex 200 column. The His10–Smt3 affinity tag was removed and the sample was again passed through a nickel ion affinity column and gel filtration column for further purification. The protein was concentrated and stored at -80 °C in buffer containing 50 mM Tris, 150 mM NaCl, 5 mM MgCl<sub>2</sub>, 12.5% w/v glycerol, 2 mM DTT, 2 mM ATP, pH 7.6. Final purity and concentration were determined by SDS-PAGE.

### **Differential Static Light Scattering (DSLS)**

Purified recombinant NBD1 was produced at Sanofi using previously described methods (Amaral and Kunzelmann, 2011; Schmidt *et al.*, 2011). Thermal stability of various NBD1 isoforms was evaluated by DSLS using the Harbinger Stargazer-384 instrument (Epiphyte Three, Toronto, Canada). NBD1 protein was diluted to 0.2 mg/ml in S200 buffer (50 mM Tris-HCl, 150 mM NaCl, 5 mM MgCl<sub>2</sub>, 2 mM ATP, 2 mM DTT, pH 7.6) containing 1% glycerol, and 10 µL of protein solution was aliquoted into wells of a 384-well low-volume optical plate (Corning Inc., Corning, New York), and 10 µL of mineral oil was then overlaid onto the protein solution. Once in the Stargazer instrument, the plate was heated from 25 °C to 70 °C at a rate of 1 °C/min to facilitate protein unfolding and aggregation. Throughout the experiment, visible light was shone on the protein from below, and images of the light diffraction pattern for each well were captured from above

the plate every 30 seconds. A linear regression curve was generated for each well, representing the increase in light scattering over time. By integrating the pixel intensity curve of each well, and plotting the total scattered light value against temperature, an inflection point representing the temperature of aggregation ( $T_{agg}$ ) was calculated for each sample.

### **Differential scanning fluorimetry (DSF)**

Nano differential scanning fluorimetry (nanoDSF) was performed to evaluate NBD1 thermal stability by measuring intrinsic tryptophan (and to a lesser extent, tyrosine) fluorescence as a measure of protein denaturation. Experiments were performed using the Prometheus NT.48 nanoDSF (NanoTemper Technologies, Germany). For this work, protein was diluted to 1 mg/mL in S200 buffer containing 1% glycerol. Approximately 10  $\mu$ L of each diluted sample was loaded into nanoDSF grade high-sensitivity capillaries (NanoTemper) in triplicate, and placed on the instrument's capillary loading tray. The instrument temperature gradient was set to increase from 20 °C to 95 °C at a rate of 0.5 °C/minute. Protein denaturation was detected at emission wavelengths of 330 and 350 nm, and a ratio of 350/330 was created for each time point collected. This ratio was then plotted against temperature, representing the transition from properly folded to fully denatured protein. The first derivative of the resulting sigmoidal curve was again plotted against temperature, with the extreme of the derivative curve displaying the melting temperature ( $T_m$ ) for each sample.

### **Crystal structure**

Crystallization: CFTR NBD1 V510D in buffer A was crystallized by mixing equal amounts of protein at 6 mg/mL with 0.1 M Tris pH 7.6, 28 % (w/v) polyethylene glycol 10,000. Crystallization reagents were from Hampton Research, Aliso Viejo, CA. Crystallization was induced by streak-seeding using crystals grown in 0.1 M HEPES, pH 7.5, 25% (w/v) polyethylene glycol 550 monomethylether, and plates incubated at 4 °C. Crystals grew over several days and were frozen by quick dip in reservoir solution supplemented with 25 % (w/v) ethylene glycol.

Data collection, processing, structure determination and refinement: Data were collected at the Advanced Photon Source (APS Argonne, IL) and processed using HKL2000 (Otwinowski and Minor, 1997). Molecular replacement was carried out using Phaser (McCoy *et al.*, 2007) of the CCP4 suite (Winn *et al.*, 2011). The structures were refined using Phenix (Adams *et al.*, 2010), followed by manual corrections in COOT (Emsley *et al.*, 2010). The structure was inspected and analyzed in COOT and PyMOL (2015).

### **Electrophysiology**

Transfected fisher rat thyroid (FRT) cells grown to confluence on transwell inserts were mounted in Ussing Chambers (Physiologic Instruments), bathed in symmetrical physiological saline (140 mM NaCl, 5 mM KCl, 2 mM CaCl<sub>2</sub>, 1 mM MgCl<sub>2</sub>, 10 mM HEPES, 10 mM Glucose, pH 7.4) and aerated. Benzamil (10 μM), forskolin (5 μM), ATP (10 μM), and CFTRinh-172 (20 μM) were added to either the apical and/or basolateral chambers. Transepithelial current (I<sub>sc</sub>),



conductance ( $G_t$ ), and voltage were measured using a multichannel voltage/current clamp VCCM8 system (Physiological Instruments) and recorded using the Acquire and Analyze 2.0 software (Physiological Instruments).

## **CHAPTER III: STYRENE-MALEIC ACID COPOLYMER EXTRACTION: A BREAKTHROUGH IN CFTR LIPID PARTICLE PURIFICATION AND STABILIZATION**

### **3.1 Preface**

Chapter III encompasses a collaborative effort toward CFTR-SMALP characterization and structural determination. A manuscript is being drafted that is focused on the characterization of the native lipid environment surrounding CFTR, and will include the characterization of CFTR-SMALPs.

Additional work pertaining to detergent purification and qualification of the SMA purification protocol were included for the purposes of context and completion.

- ❖ Simon K, Pollock N, Zhang B, Gordon E, He T, Maderia M, Dafforn T, and Hurlbut G, Identification of the native lipid environment surrounding CFTR using SMALP solubilization

I devised the concept of this project and have collected all data except that pertaining to the proteomics and lipidomics analysis, for which I did prepare the samples. I developed the protocol for SMA purification of CFTR with input from Naomi Pollock and Annuradha Jain with support from Greg Hurlbut. I performed the CFTR protein expression and purification with all polymers tested. Detergent purification was performed by Annuradha Jain, Bi Deng and me. I prepared all samples for proteomic and lipidomics evaluation, which were performed by Scott Shaffer and Bailin Zhang/Timothy He, respectively. I performed all TEM grid preparation and assay development with continued input and guidance from Gregory Hendricks and Lara Strittmatter. The Dafforn Lab and the Knowles Lab (University of Birmingham, UK) provided hydrolyzed SMA and SMI polymer for use in this work. Ashley Souza generated the cartoon schematic of CFTR-SMALPs seen in figure 3.5.

### 3.2 Abstract

Cystic fibrosis is the most common fatal genetic disease of people with European heritage. The disease is caused by mutations of the Cystic Fibrosis Transmembrane Conductance Regulator (CFTR) such as the destabilizing  $\Delta F508$  mutation, which leads to a near-total loss of CFTR channel function in 70% of CF cases worldwide. The development of methods to isolate and characterize full-length  $\Delta F508$ -CFTR would greatly aid in the discovery of drugs that restore the activity of this complex membrane protein (MP). Unfortunately, existing methods of MP production and purification typically yield only small amounts of unstable CFTR protein in detergent micelles. This has limited our ability to characterize CFTR biophysical and structural properties and interactions with potential therapeutic ligands. Recently, a new approach to membrane protein extraction using styrene-maleic acid (SMA) copolymer has emerged. Using SMA lipid particle (SMALP) technology, I have developed a method for solubilizing CFTR from cell membranes into monodisperse lipid disks without the use of detergents. The resulting CFTR-SMALPs contain a single molecule of stable, full-length CFTR and its surrounding native lipid bilayer. For this effort, I purified full-length wild-type human CFTR from HEK cell membranes, and analyzed the resulting material using native and SDS-PAGE, CFTR immunoblotting, and transmission electron microscopy (TEM) to ensure sample quality. Moreover, using mass spectrometry for protein and lipid analysis, I

characterized the CFTR-associated native lipid content of the CFTR-SMALPs from both the HEK expression cell line and the CF lung submucosal epithelial cell line, CFSME<sub>0</sub>-. This method and the preliminary applications outlined in this chapter lay the groundwork for full characterization of CFTR in its native state within the lipid bilayer, and may provide a path toward structural determination of full-length  $\Delta F508$ -CFTR.

### 3.3 Introduction

Cystic Fibrosis (CF) is a common, fatal genetic disease that currently impacts over 30,000 people in the United States, (70,000 worldwide) and is characterized by chronic pulmonary infections, pancreatic insufficiency and abnormally high sweat chloride levels. With a median predicted survival age of 47.7 years for patients born in 2016 (up from 41.2 in 2015), therapeutic improvements and a greater availability to lung transplantation have offered new hope to CF patients (CFF.org, 2018). Nonetheless, given the prevalence of comorbidities such as diabetes, liver failure, anxiety disorders and depression, CF remains an area of high unmet medical need (CFF.org, 2017). CF is caused by mutations in the Cystic Fibrosis Transmembrane Conductance Regulator (CFTR) gene, which encodes an epithelial chloride channel. Similar to other members of the ABC transporter family, CFTR comprises two transmembrane domains (TMD1 and TMD2) of 6  $\alpha$ -helices each and two cytoplasmic nucleotide binding domains (NBD1 and NBD2). Unlike other transporters, however, CFTR also contains a mostly unstructured regulatory (R) domain of about 200 amino acids that is thought to regulate channel activity through phosphorylation (Liu *et al.*, 2017; Zhang *et al.*, 2018b).

The most prevalent CF-causing mutation is a deletion of phenylalanine 508 ( $\Delta$ F508-CFTR), a residue within NBD1 that is thought to mediate the interaction between NBD1 and the fourth intracellular loop (ICL4) of TMD2.

Interruption of the NBD1:ICL4 interaction subsequently impacts CFTR tertiary structure, stability, and function (Lewis *et al.*, 2010; Rich *et al.*, 1990). This defect, which affects about 70% of CF patients worldwide, leads to a near-total loss of CFTR maturation and trafficking to the cell surface (Lukacs and Verkman, 2012; Thibodeau *et al.*, 2010). With the recent FDA approval of CFTR modulators designed to either increase chloride conductance (potentiators) or repair and stabilize misfolded CFTR (correctors), therapies for CF are now available to patients that target the root cause of the disease, rather than treat its symptoms (CFF.org, 2019b; Southern *et al.*, 2018). However the impact of such therapies has been relatively modest for many patients (Southern *et al.*, 2018), indicating that while these treatment options represents great progress, there is much work to be done.

To aid the discovery of drugs that restore the stability and activity of defective CFTR, better methods are needed to isolate and characterize full-length CFTR. Currently, the standard approaches for purifying membrane proteins (MPs) utilize detergents, such as n-Dodecyl  $\beta$ -D-maltoside (DDM), to solubilize the protein from cell membranes creating micelles around the hydrophobic regions of the protein (Chiaw *et al.*, 2011; Rosenberg *et al.*, 2004; Zhang *et al.*, 2018b). Although the resulting micelles stabilize the protein to some extent, they can often disrupt the protein's native structure and interfere with important molecular interactions with the lipid bilayer (Calabrese *et al.*, 2015). In fact, the reliance of detergent purification may be a significant barrier to

effective MP research, chiefly with regard to retaining the protein's stability and function during solubilization and reconstitution (Seddon *et al.*, 2004). This is particularly problematic for CFTR. Given its size and limited expression levels in cells, reconstitution with detergents will often yield only small amounts of unstable protein in the closed, dephosphorylated state. This limits the biophysical and structural characterization that can be undertaken, and hinders the study of interactions between full-length CFTR and potential therapeutic ligands.

One solution to the instability of purified human CFTR has been to study orthologues of the protein from different species (Aleksandrov *et al.*, 2010; Pollock *et al.*, 2015; Yang *et al.*, 2018). This has led to the identification of several key residues - often prolines - that appear in the sequence of orthologous CFTR from various animals, differ from the human sequence, and increase the thermal stability of the protein (Aleksandrov *et al.*, 2012). Inclusion of these residues in the human CFTR context has likewise enhanced the thermal stability of the human protein, and has allowed for the creation of stabilized versions of the protein that are more amenable to biochemical and biophysical characterization. In a similar way, hyper-stabilized versions of the NBDs of CFTR have been created in order to determine their structures at high resolution (Lewis *et al.*, 2010). Though these studies have provided vital information about the structure and function of human CFTR, a dilemma must also be acknowledged: until we know more about the subtleties of CFTR structure and function, we cannot discount the possibility that these mutations have structural and functional

consequences beyond our understanding. However, without making these changes it has been challenging to study the protein at all.

An alternative to artificially stabilizing membrane proteins is to provide them with a membrane mimetic that is more appropriate than conventional head-and-tail detergents. After all, membrane proteins do not function as isolated entities; rather, they rely on their surrounding lipid environment to provide stability and support (Bayburt and Sligar, 2010; Niesen *et al.*, 2017). There is evidence to suggest that membrane proteins and their endogenous lipid environment evolve to assume energetically-favorable conformations that support the protein's requisite function (Haines, 2001; Mulkidjanian *et al.*, 2009; Wilson and Lin, 1980). Altering this will directly impact the MPs structure, function, and energy state (Calabrese *et al.*, 2015), a consideration that must be taken into account when studying large MPs like CFTR in detergent micelles.

In an effort to address this limitation, much work has been done to develop effective methods that isolate MPs in small bilayer patches, *i.e.* in stable lipoprotein nanodiscs. One such approach involves replacing detergent micelles with exogenously added lipids to form self-assembling lipid disks of uniform size which are held in place by an amphipathic helical membrane scaffolding protein (MSP) (Bayburt and Sligar, 2010; Ritchie *et al.*, 2009). This method has been used to successfully stabilize maltose transporter MalFGK<sub>2</sub>, an ABC transporter similar to CFTR, but has not successfully been used to purify CFTR itself



(Alvarez *et al.*, 2010). While this method does offer a more stable option for the suspension of MPs, it still relies on the initial detergent purification of the protein. Using MSPs places the protein in a lipid environment, but without information about the lipid preferences of specific proteins, this environment is artificial and will not truly replicate the plasma membrane as experienced by the protein in question. Furthermore, this method does not circumvent the issue of an initial period of detergent destabilization of the target protein. Regardless, the best environment for a purified membrane protein is the endogenous lipid bilayer it is normally found in.

To that end, a number of publications have tried to reconstitute CFTR in exogenous lipids from a bottom up approach to determine the composition of lipids that provide the most stabilizing effect on the protein and may provide some insight into the native bilayer (Hildebrandt *et al.*, 2017). They are addressing a significant gap in the understanding of the overall structure and function of CFTR. Based on this previous analysis, we have initiated an evaluation of the lipid composition of the native bilayer surrounding CFTR.

In the last decade, a new approach to the extraction of IMPs has been described using styrene-maleic acid (SMA) copolymer (Knowles *et al.*, 2009; Lee *et al.*, 2016; Postis *et al.*, 2015). This method was developed to overcome the issues associated with detergent micelle purification of large proteins like GPCRs and ABC transporters. *In lieu* of separating out such a protein from its

surrounding lipid bilayer using detergents, this approach takes advantage of the amphipathic properties of SMA to nonspecifically solubilize MPs directly from the cell membrane thereby preserving the native lipid environment that supports the function of the protein (Knowles *et al.*, 2009). A recent publication on SMA purification showed that by combining the SMALP method with quantitative mass spectrometry, the lipid preferences of membrane proteins could be accurately determined.

With this technology, I have been able to purify monodisperse lipid disks containing a single molecule of full-length CFTR in its native environment, allowing the protein to stay in contact with its natural lipid support-system as well as any potential interactome proteins (Pankow *et al.*, 2015). For this effort, full-length human CFTR was isolated from Expi293 HEK cell membranes to ensure a native, fully glycosylated form of CFTR. Purified CFTR SMALPs were analyzed by SDS-PAGE silver stain, western blot, Native PAGE, mass spectrometry, transmission electron microscopy (TEM) and ultimately cryo-EM. Silver stain, western blot and mass spectrometry sample analysis confirm the isolation of high-purity CFTR. Negative stain EM of CFTR SMALPs shows monodisperse ~10 nm diameter particles resembling SMALPs containing Sav1866, a homologous bacterial transporter (Figure 3.5). With TEM analysis, I have also shown that CFTR-SMALPs can be stored at 4 °C for several days with minimal loss in sample quality, and that freeze/thaw cycles appear to have no impact on particle monodispersity. Moreover, because SMA purification does not

dissociate the surrounding native lipids surrounding MPs, I was able to solubilize CFTR-SMALPs from cystic fibrosis submucosal epithelial (CFSME) cells and determine the lipid composition that surrounds the protein, a finding not previously reported.

### 3.4 Results

My work on full-length hCFTR purification was first performed using detergent solubilization. Initial evaluation of different detergent purification protocols for CFTR involved solubilization with either 2% n-dodecyl- $\beta$ -D-maltopyranoside (DDM) with storage in 0.1% DDM, 1% decyl maltose neopentyl glycol (MNG-10) with storage in 0.03% 3 $\alpha$ -hydroxy-7 $\alpha$ ,12 $\alpha$ -di-((O- $\beta$ -D-maltosyl)-2-hydroxyethoxy)-cholane (FA-3), or 1% MNG-10 and 0.1% cholesteryl hemisuccinate (CHS) with storage in 0.05% FA-3 and 0.005% CHS. However, several attempts to characterize the stability and purity of both DDM- and MNG-10-solubilized CFTR, such as transmission electron microscopy of negatively stained particles (Figure 3.1) indicated that detergent-purified CFTR aggregated easily and did not respond well to freeze-thaws. In an effort to identify a more stable and robust way of purifying wild-type, and eventually mutant hCFTR in its native, mature form, I explored the utility and feasibility of styrene-maleic acid purification.

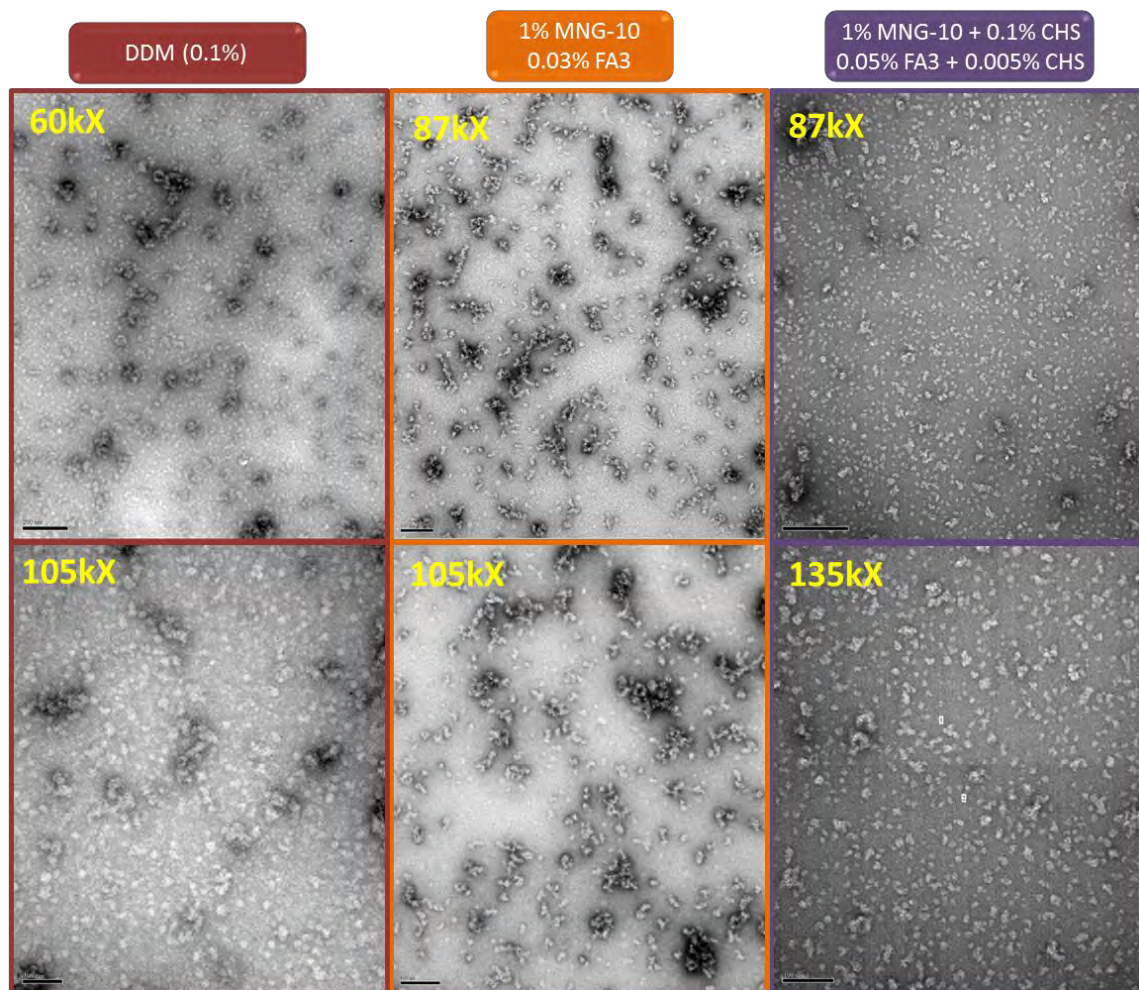


**Figure 3.1** TEM analysis of detergent-purified hCFTR at lower and higher magnifications. hCFTR was solubilized from insect cells using either DDM (left), MNG-10 (middle) or MNG-10 + CHS. Negative stain TEM analysis showed high levels of aggregation in all cases.

### 3.4.1 Expression of CFTR

Initial work toward developing this protocol was focused on determining the optimal cell type from which to solubilize full-length, wild-type human CFTR (WT-hCFTR) in order to obtain a fully native form of CFTR containing the two N-linked oligosaccharides present on ECL4. CFTR production was compared in Sf21 insect cells and Expi293 HEK cells. An equal number of cells were collected from each culture and analyzed for CFTR expression via immunoblotting with antibodies targeting the 10x-His or 3x-FLAG tags. Results for each western blot (seen in Figure 3.2) show stronger CFTR expression when Expi293 cells are transfected at 1 µg/mL of DNA using ExpiFectamine transfection reagent compared to baculoviral infection of Sf21 cells across a range of five viral dilutions.

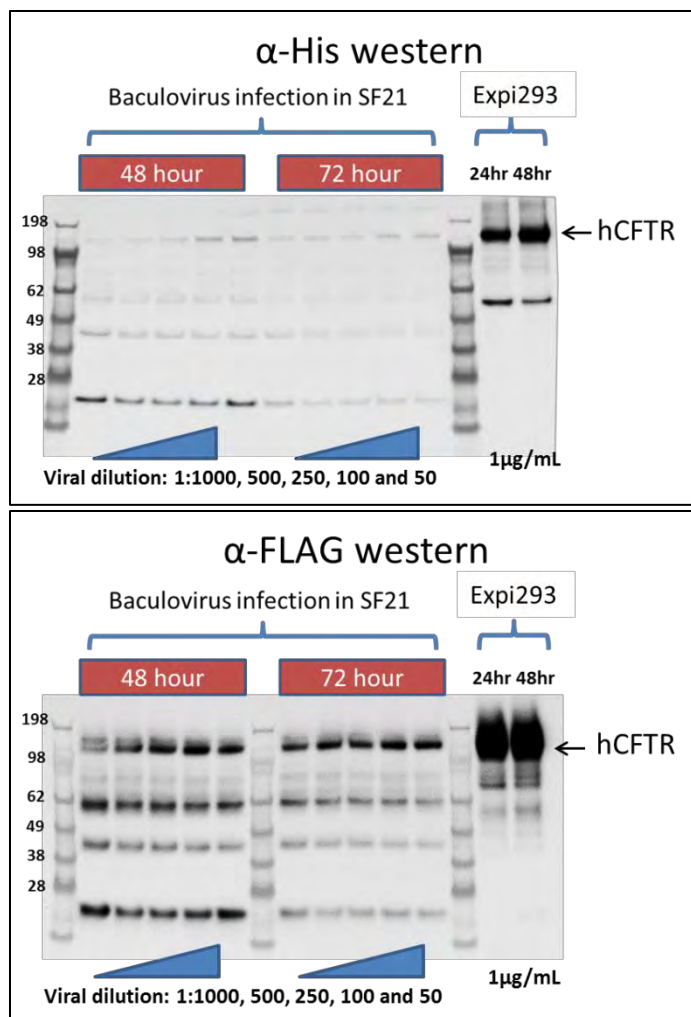


**Figure 3.2 Comparison of hCFTR expression levels in Sf21 insect cells and Expi293 HEK cells.** hCFTR expression is detected by immunoblotting with  $\alpha$ -His (top panel) or  $\alpha$ -FLAG Abs. Results indicate that expression of wild-type hCFTR is greater in cultured Expi293 HEK cells transfected at 1  $\mu$ g/mL of plasmid DNA after 24 or 48 hours compared to Sf21 insect cells that have been baculovirus-infected at viral dilutions ranging from 1:50 to 1:1,000 for 48 or 72 hours.

### 3.4.2 Encapsulation and purification of CFTR using Styrene Maleic Acid Co-Polymer (SMA)

In order to compare the effectiveness of SMA in encapsulation of CFTR from Expi293 and Sf21 cells, and its subsequent purification via an affinity tag, a preparation of crude membrane from each cell line was divided in half. CFTR was solubilised using SMA and purified using either the 3x-flag or 10x-his purification tags. Preliminary purification using SMA was performed in alignment with the existing detergent purification protocols; however, in all cases, CFTR was solubilized for two hours at 4 °C with a final concentration of 2.5% SMA in lieu of detergent. Additional changes included a reduction in  $Mg^{2+}$ /ATP concentration to 1 mM, and HisTrap affinity column elution performed by step gradient at 100 mM, 250 mM and 500 mM imidazole. Additionally, as with the reduction in  $Mg^{2+}$  divalent cation concentration, the pH of all buffers was raised to 7.8 to prevent aggregation of the SMA copolymer.

Expi293 HEK cells	Sf21 Insect cells
<ul style="list-style-type: none"> <li>• ExpiFectamine Transfection               <ul style="list-style-type: none"> <li>• 24 hrs</li> <li>• 48 hrs</li> </ul> </li> <li>• Purification tags               <ul style="list-style-type: none"> <li>• 10x-His</li> <li>• 3x-Flag</li> </ul> </li> </ul>	<ul style="list-style-type: none"> <li>• Baculovirus Infection               <ul style="list-style-type: none"> <li>• 5 Viral dilutions                   <ul style="list-style-type: none"> <li>• 48 hrs</li> <li>• 72 hrs</li> </ul> </li> </ul> </li> <li>• Purification tags               <ul style="list-style-type: none"> <li>• 10x-His</li> <li>• 3x-Flag</li> </ul> </li> </ul>

**Figure 3.3** Experimental parameters to evaluate CFTR production in Expi293 HEK cells and Sf21insect cells

Expi293 and Sf21 cells were then collected and each cell type sample was divided in half to be purified using either the 3x-flag or 10x-his purification tags. Preliminary purification using SMA was performed in alignment with the existing detergent purification protocols; however, in all cases, CFTR was solubilized for two hours at 4 °C with a final concentration of 2.5% SMA in lieu of detergent. Additional changes included a reduction in  $Mg^{2+}$ /ATP concentration to 1 mM, and HisTrap affinity column elution performed by step gradient at 100 mM, 250 mM and 500 mM imidazole. Additionally, as with the reduction in  $Mg^{2+}$  divalent cation concentration, the pH of all buffers was raised to 7.8 to prevent aggregation of the SMA copolymer. When all preps were compared, the CFTR purification from Expi293 cells using the 10x-His tag returned the best recovery and purity (Figure 3.4, panel A). CFTR appeared to be the majority species in several fractions when analyzed via silver stain SDS-PAGE analysis. When analyzed with TEM negative stain, micrographs showed monodisperse particles resembling SMA-purified homologous bacterial protein, Sav1866 (Figure 3.5).



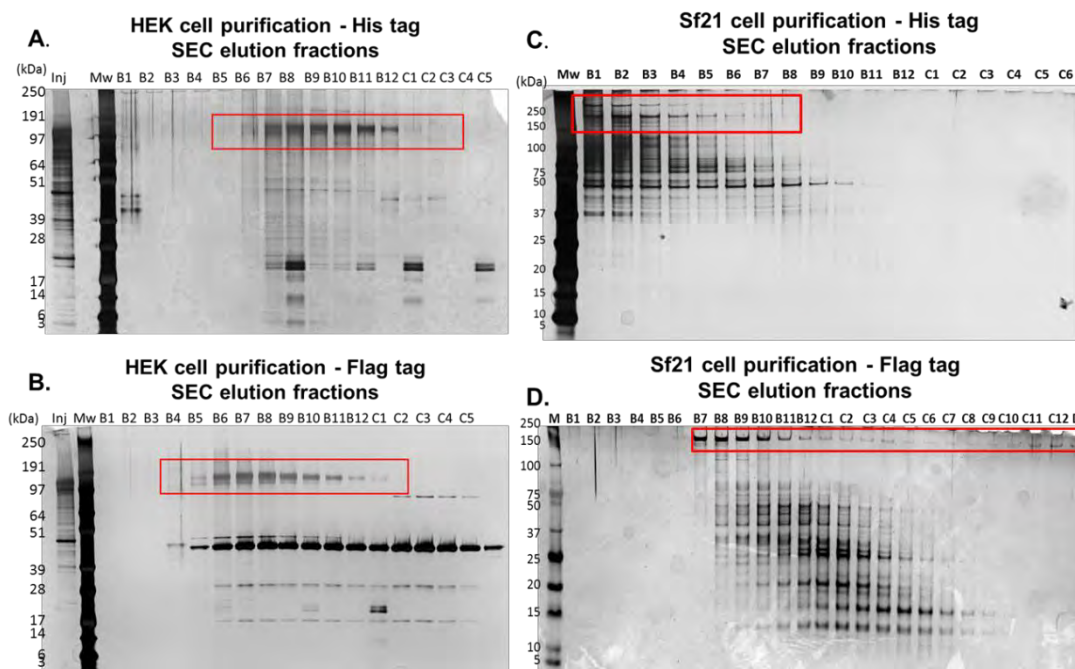


**Figure 3.4** SDS-PAGE silver stain analysis of size exclusion chromatography column elution fractions to evaluate HEK cell (A and B) and Sf21 cell (C and D) CFTR solubilization using SMA. A comparison of conditions identified HEK cell purification using a His-10x tag as the optimal combination for purification of hCFTR. Red boxes outline CFTR bands.

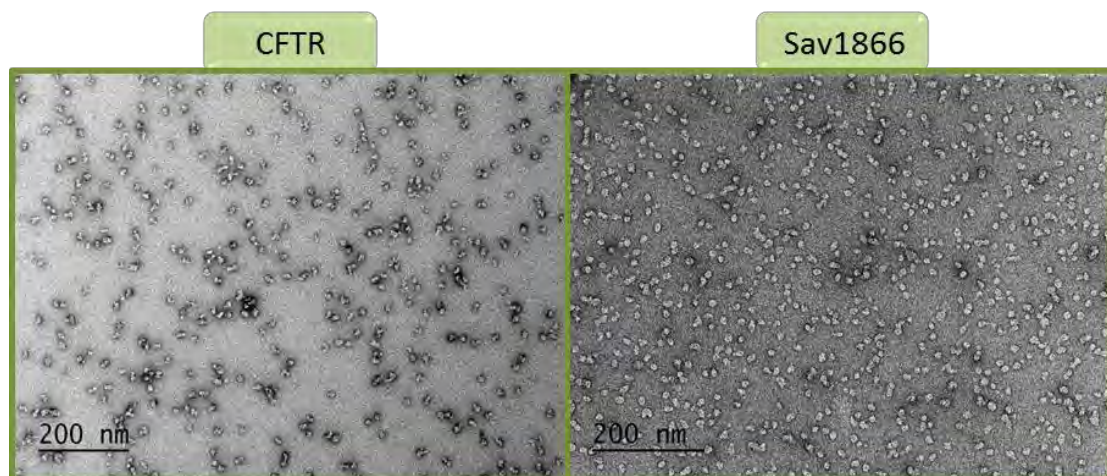


**Figure 3.5** TEM micrographs of CFTR and Sav1866 SMALPs. Particles of the two homologous proteins display similar morphology when negatively stained with 1% uranyl acetate staining solution and evaluated on a Tecnai Spirit 12 at 120 kV.

After this initial evaluation, parameters for hCFTR solubilization and purification from Expi293 HEK cells were established. A cartoon model of a single CFTR-SMALP is seen in Figure 3.6 and a schematic of the protocol is seen in Figure 3.7.

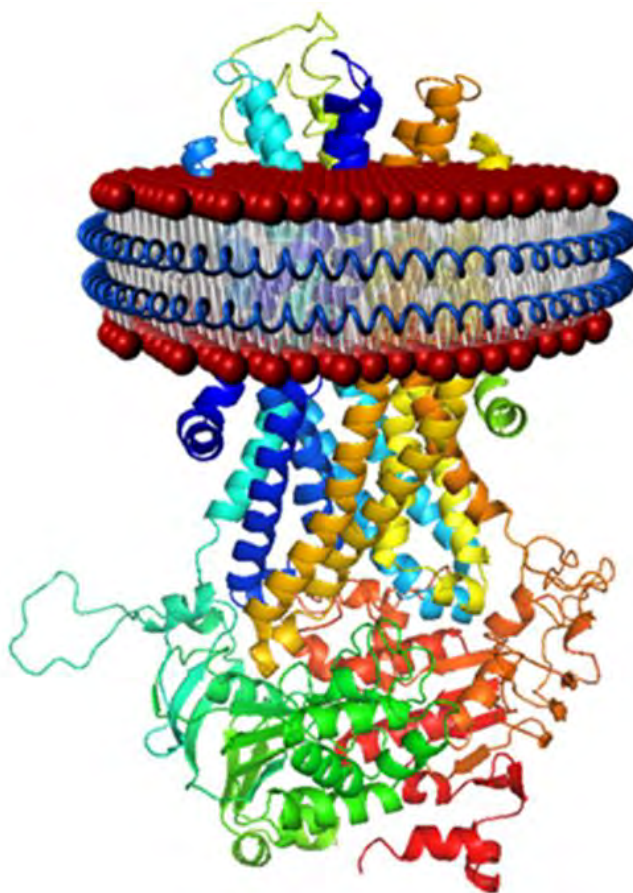


**Figure 3.6** Cartoon schematic of full-length hCFTR in a SMALP. ABC transporter CFTR can remain in its lipid bilayer while being held in place by an SMA copolymer (blue coil). Homology model of hCFTR was generated by Partha Manavalan; SMALP illustration produced by Ashley Souza.



**Figure 3.7 Schematic overview of the protocol for SMA purification of CFTR from mammalian cell membranes.**

Representative traces and SDS-PAGE gels of nickel affinity column elution fractions and size-exclusion column fractions are seen in Figures 3.8 and 3.9, respectively.

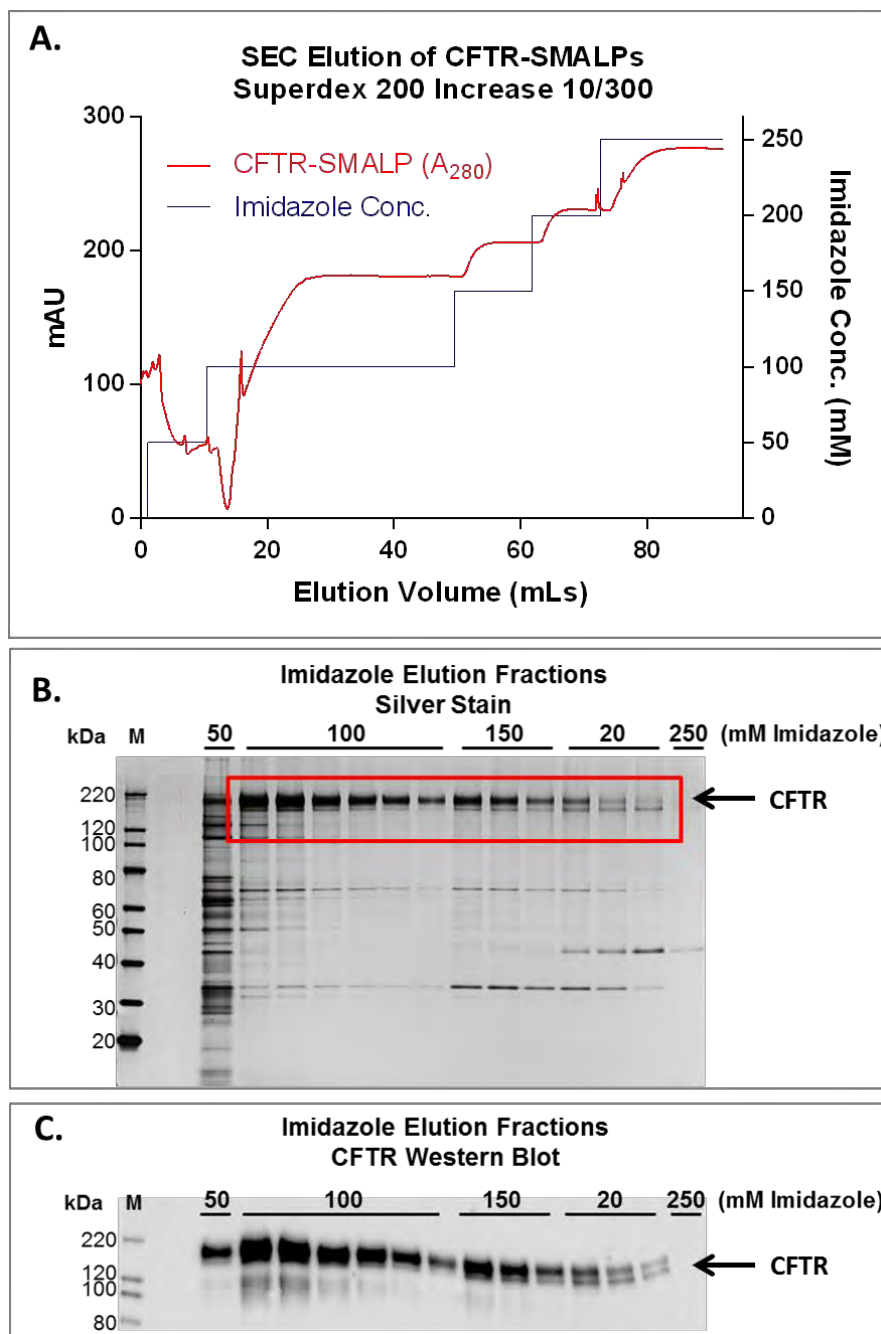


**Figure 3.8 SDS-PAGE Silver stain and western blot of eluted hCFTR.**

Fractions 13-30 show full-length hCFTR eluting with 100 and 250 mM imidazole concentrations. Western blot was probed with a monoclonal anti-hCFTR antibody targeting the C-terminus (AA 1370-1380). Each fraction is 2 mLs.

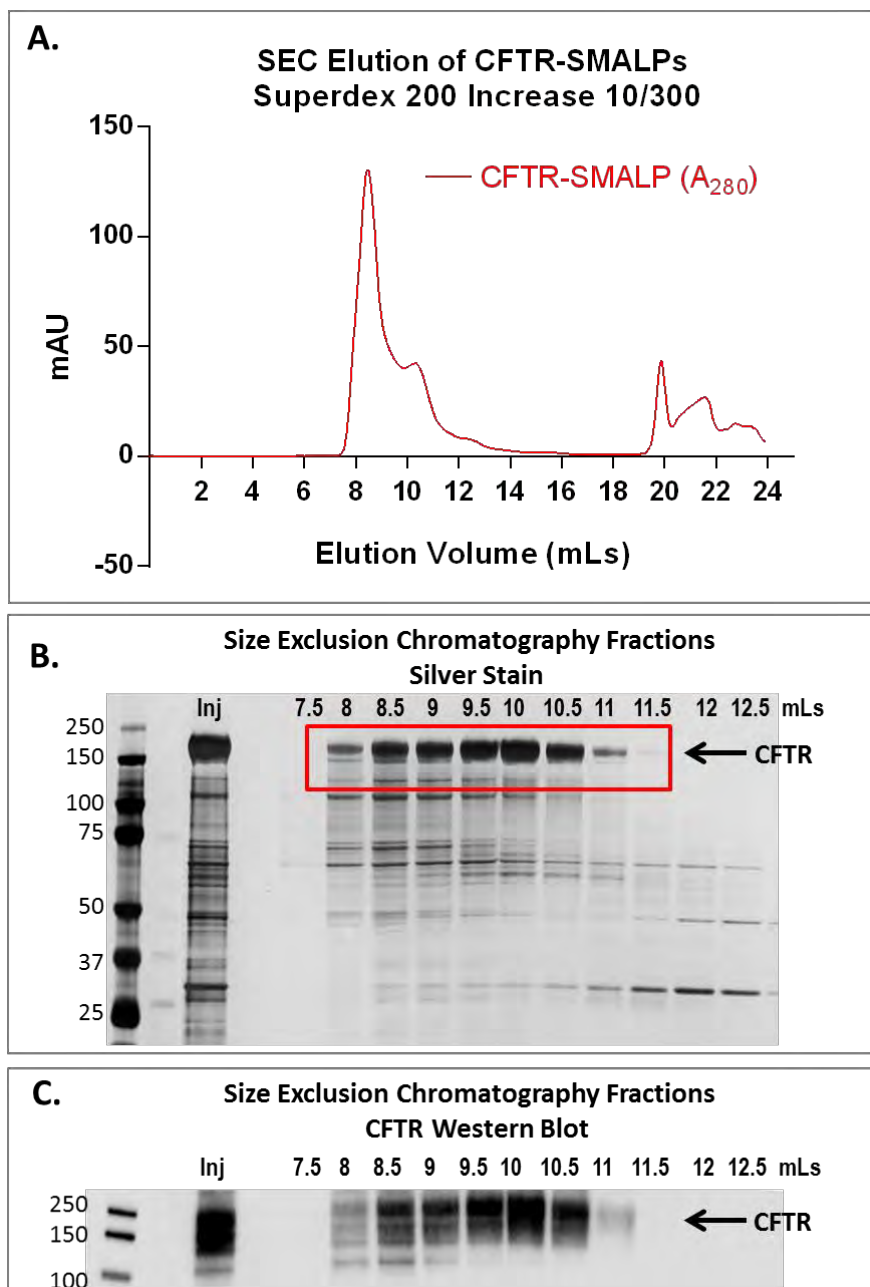


**Figure 3.9** SDS-PAGE Silver stain (top) and western blot (bottom) of SEC purified hCFTR. Fractions 20-27 contain full-length hCFTR, confirmed by western blotting. The low MW species (~10 kD) seen on the silver stain is the result of SMA that has separated from the hCFTR-SMALPs once separated on SDS-PAGE.



### Comparison of CFTR-SMALPs vs CFTR in detergent micelles

Once a working protocol for SMA purification of CFTR had been established, I performed a side-by-side comparison of the detergent-purified CFTR and CFTR-SMALPs to evaluate differences in particle homogeneity and stability. To prepare the purified CFTR, I solubilized hCFTR from transfected Expi293 cells with either 2% DDM or 2.5% SMA, and followed parallel affinity column and SEC gel filtration column procedures for each. The SEC purification chromatogram and corresponding silver stain of eluted SEC fractions for CFTR in DDM is seen below in Figure 3.10. A representative example of SMA purified CFTR fractions can be seen in Figure 3.9 on the previous page.

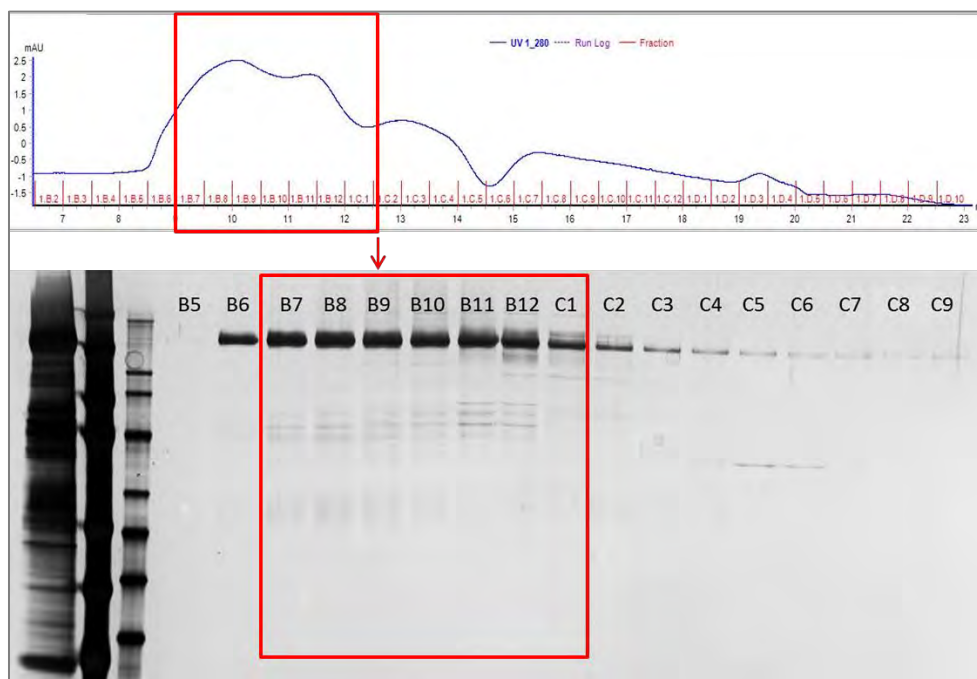


**Figure 3.10 SEC purification of detergent-purified CFTR.** Each eluted fraction is 0.5 mLs. Fractions B7-C1 were pooled for analysis; fraction B9 was used for TEM analysis.

Following SEC purification of both CFTR preps, a portion of each sample was snap-frozen and stored at -80°C for freeze/thaw evaluation using negative stain TEM analysis. Grids of both the fresh and frozen material were prepared with 1% uranyl acetate stain and grids were evaluated on an FEI Tecnai Spirit 12 for evidence of particle aggregation (Figure 3.11). CFTR-SMALPs appeared monodisperse and no aggregation was evident before or after freeze-thaw. The detergent preparation did appear to have some level of aggregates even when analyzed fresh, and was affected by the freeze-thaw cycle, however, as an increase in aggregation was seen in this sample.

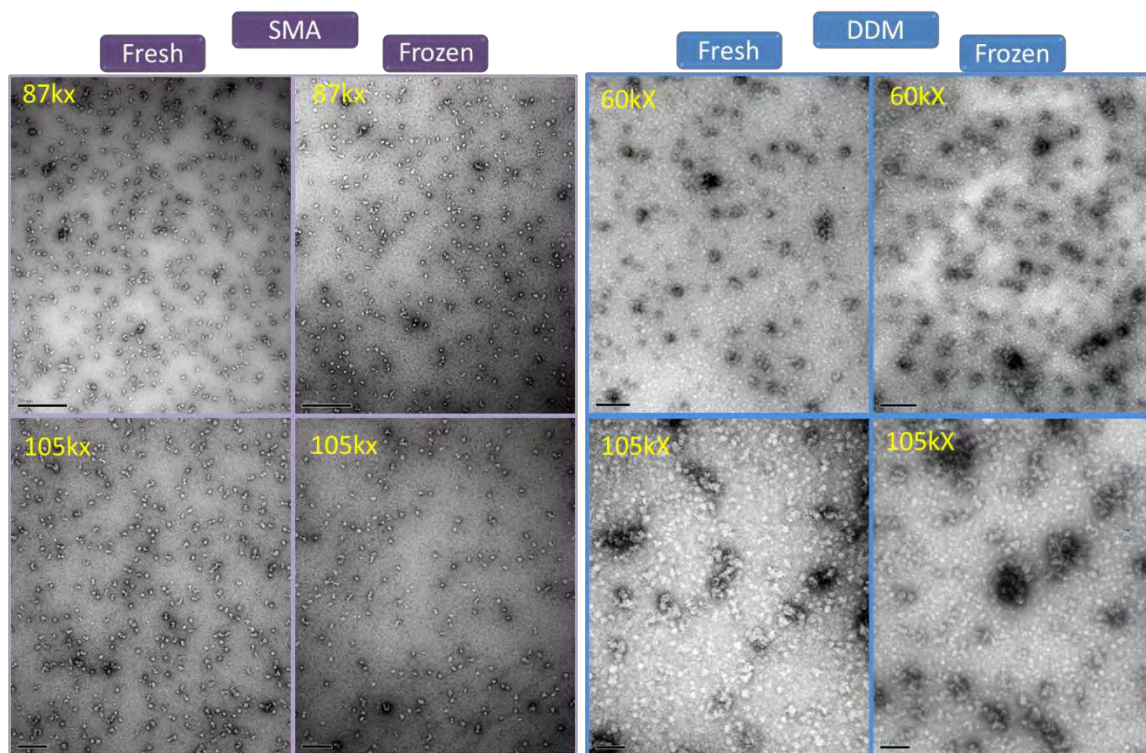


**Figure 3.11 EM Negative staining of purified CFTR in SMALPs or detergent micelles.** Full-length CFTR was purified from cell membranes using either 2.5% SMA copolymer or 2% n-dodecyl- $\beta$ -D-maltopyranoside (DDM). Negative stain TEM was performed on freshly-prepared material, as well as on material that had been snap-frozen and stored at  $-80^{\circ}\text{C}$  for 24 hours. Lower (top row) and higher (bottom row) magnifications are taken for each sample on the same grid. Samples analyzed using the FEI Tecnai Spirit 12 (120 keV). Negative staining: 1% Uranyl Acetate staining Carbon coated 400 mesh grids.



One observation that was surprising was the greater amount of lower molecular weight bands seen with SEC-purified CFTR-SMALPs compared to the detergent purified material immediately following column purification (Figures 3.9 and 3.10). I hypothesized that the bands visible with the CFTR-SMALP material when separated out on SDS-PAGE may be due to the inclusion of binding partners that were being purified out along with CFTR; interactions that would normally be interrupted by detergent purification. To evaluate sample purity and confirm the identity of the lower species seen with SDS-PAGE separation, I ran the CFTR-SMALP sample on a Native PAGE gel, which makes use of the negatively-charged maleic acid moiety that encircles the particles to migrate through a native Tris/Gly gradient gel. The gel was run in duplicate and one was transferred to a nitrocellulose blot for CFTR immunoblotting. The resulting banding pattern with both coomassie staining and anti-CFTR immunoblotting both showed a single major band (NativeMark MWM is an approximation and may not be reliable as a comparison of particle size), as well as a thinner band of a higher molecular weight, which may have been either aggregates of the CFTR-SMALPs or potentially two individual molecules that were co-purified in one long SMA polymer (See Figure 3.12).

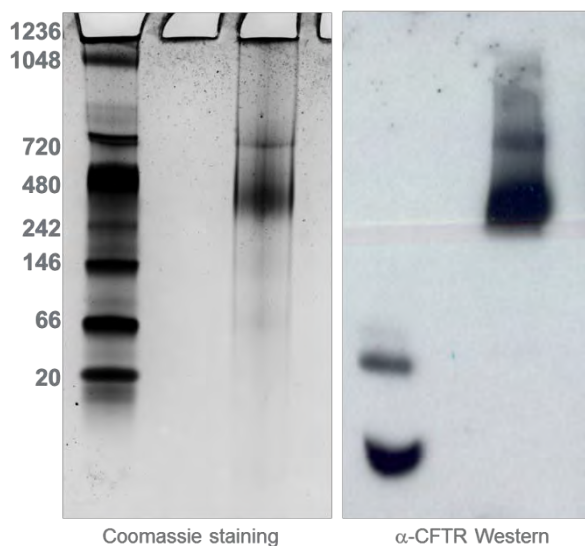


**Figure 3.12 Native PAGE analysis of CFTR-SMALPs** detected by coomassie staining (left) and anti-CFTR immunoblotting show migration of one major CFTR band and a slightly higher band which may be SMALPs that contain two molecules of CFTR co-purified into one lipid particle.

Samples were also prepared for proteomic analysis by separating the sample on a “short gel.” This separated the protein just far enough to distinguish three separate bands (seen in Figure 3.13). These bands were cut out of the gel and labeled as 1A, 1B and 1C, and were then sent for proteomic analysis. I compared the number of unique CFTR peptides detected to the total spectra collected for each gel fragment and determined that CFTR comprised 99.61% of the detected protein in band 1A, 94.77% in 1B and 67.36% in 1C. The remaining protein detected in 1C, which normally migrates to approximately 70 kDa, was folding chaperone HSP70, polyubiquitin and actin filaments, all of which are expected to bind to CFTR during the protein’s normal life cycle. Collectively, these data indicate that along with the CFTR, SMA co-extracts

associated proteins, which likely account for the smaller bands seen on SDS-PAGE. The band labeled 1B, which was 94.77% CFTR, is likely a small population of CFTR that has broken in half at the R-domain and migrated to about the 80-100kDa position on the gel. Both the N- and C-terminus were identified in the CFTR spectral pattern for that band.

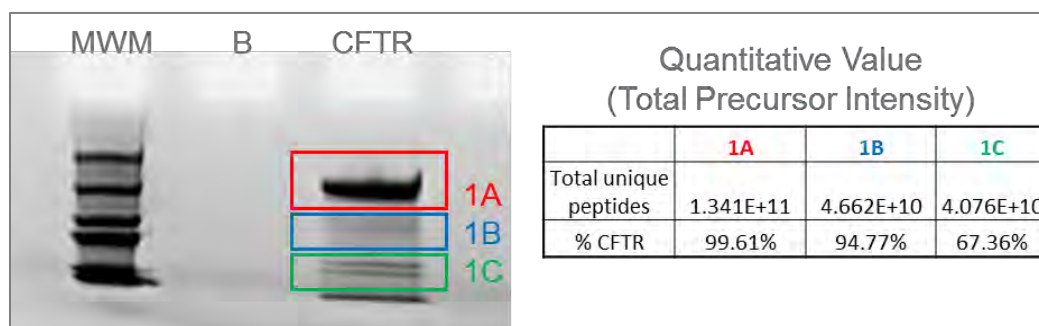


**Figure 3.13 Mass spectral analysis of SEC-purified CFTR-SMALPs shows high-purity CFTR protein.** On left, SEC fractions were pooled and separated out on a reducing 4-12% Bis-Tris “short gel” to separate out 3 sets of bands (1A, 1B and 1C) that correlated with bands of size 100kDa and higher (1A), 60-100kDa (1B) and 40-60kDa (1C). On right, percentage of total unique peptides identified as CFTR for each sample fraction. Keratin contaminants (common trace occurrences) and chymotrypsin peptides were removed from calculation.

### 3.4.3 Evaluation of alternative polymers for CFTR purification

Due to certain properties of SMA, particularly its sensitivity to divalent cations and the strong UV absorption of styrene, it can be challenging to perform certain quantitative assays on SMALPs such as ATPase activity and spectral analysis. In an effort to address these issues, alternative polymers have been developed that do not share the same incompatibilities. In the course of my work, I tested two of these polymers for their ability to solubilize CFTR from HEK293 membranes.

#### **Diisobutylene Maleic Acid (DIBMA)**

The first polymer tested, Diisobutylene/Maleic Acid Copolymer, or DIBMA, has replaced the styrene ring with diisobutylene, making it compatible with UV-based spectroscopy methods and, despite the presence of the maleic acid moiety, impervious to higher concentrations of  $\text{MgCl}_2$ . I purified CFTR on three occasions with DIBMA, which require an overnight incubation of the polymer with purified membranes when used at 4 °C. Each time I was able to obtain a reasonable amount of relatively pure material from the nickel column.

One issue inherent in the properties of DIBMA, however, is the reduction in particle stability that comes with removing the styrene head group, which is believed to intercalate stably into the lipid bilayer during traditional SMA purification. As a result, CFTR purified using DIBMA began to degrade after the

first 24 hours of the purification, and gel filtration had little impact on the overall purity of the prep.

Because I was unfamiliar with the solubilizing effect of DIBMA on Expi293 cell membranes, I prepared two separate solubilizing reactions. The initial 3 hour incubation with DIBMA returned very little CFTR in the imidazole elution fractions; however, after the 18 hour incubation with DIBMA at 4 °C, affinity column purification (seen below in Figure 3.14 top panel) showed a robust amount of CFTR eluting. Fractions containing CFTR were pooled and run over a gel filtration column for further purification; however, the resulting fractions returned sample that appeared less pure than that which was injected. The material was again concentrated and run over a clean SEC column a second time, and again purity did not improve, suggesting that the process of concentrating and gel filtration was unfavorable for the CFTR-DIBMALPs.

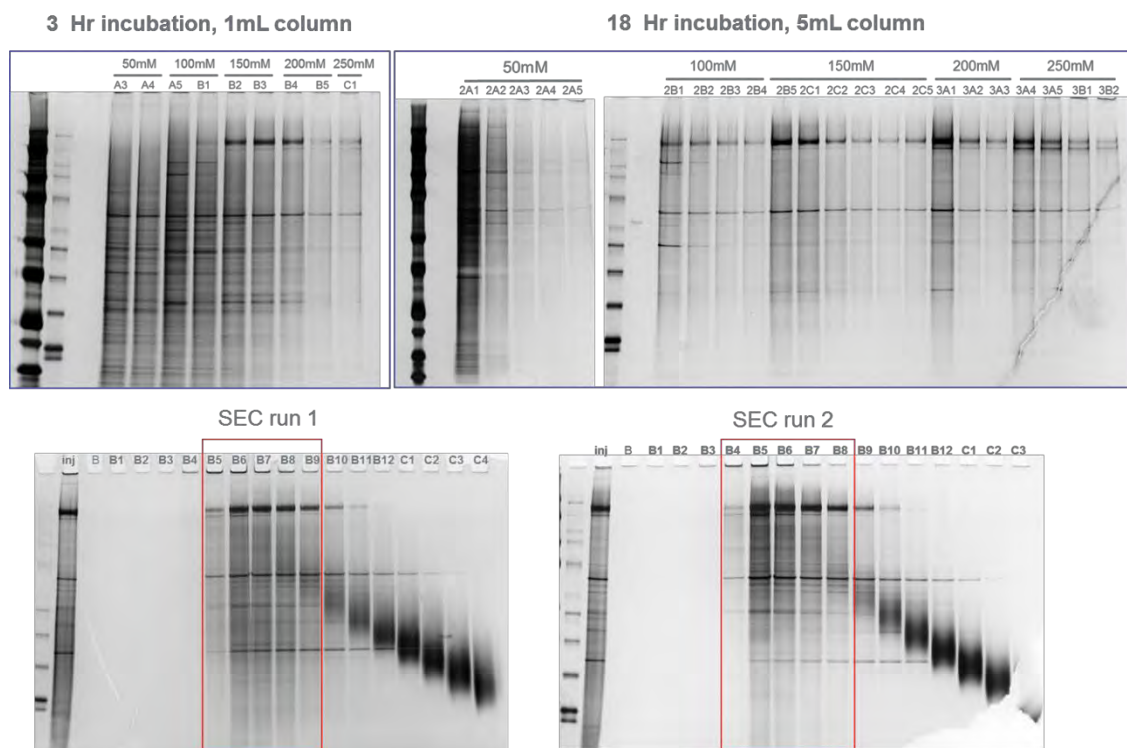


**Figure 3.14 Initial analysis of CFTR solubilization using DIBMA.** Silver stain analysis of imidazole-eluted affinity column fractions (top, imidazole concentrations indicated above each lane) collected after either 3- or 18-hour membrane incubation with DIBMA, and SEC gel filtration column fractions (bottom) from two SEC purification steps run concurrently. Because DIBMA lacks the styrene head group of SMA, it may require a longer incubation time for complete CFTR solubilization, and may be slightly more unstable as those made with SMA. Silver stain analysis of SEC fractions suggest that protein degradation may occur at significant levels when CFTR is purified using DIBMA. Fractions outlined in the red boxes are those containing CFTR purified with DIBMA that were collected as fractions of interest for further analysis.

In an attempt to stabilize the CFTR-DIBMALPs, I incorporated PKA phosphorylation and ATP- $\gamma$ -S to the preparation protocol, as I had done with

CFTR-SMALPs. Initial elution from the affinity purification column returned relatively pure material of good concentration (Figure 3.15).

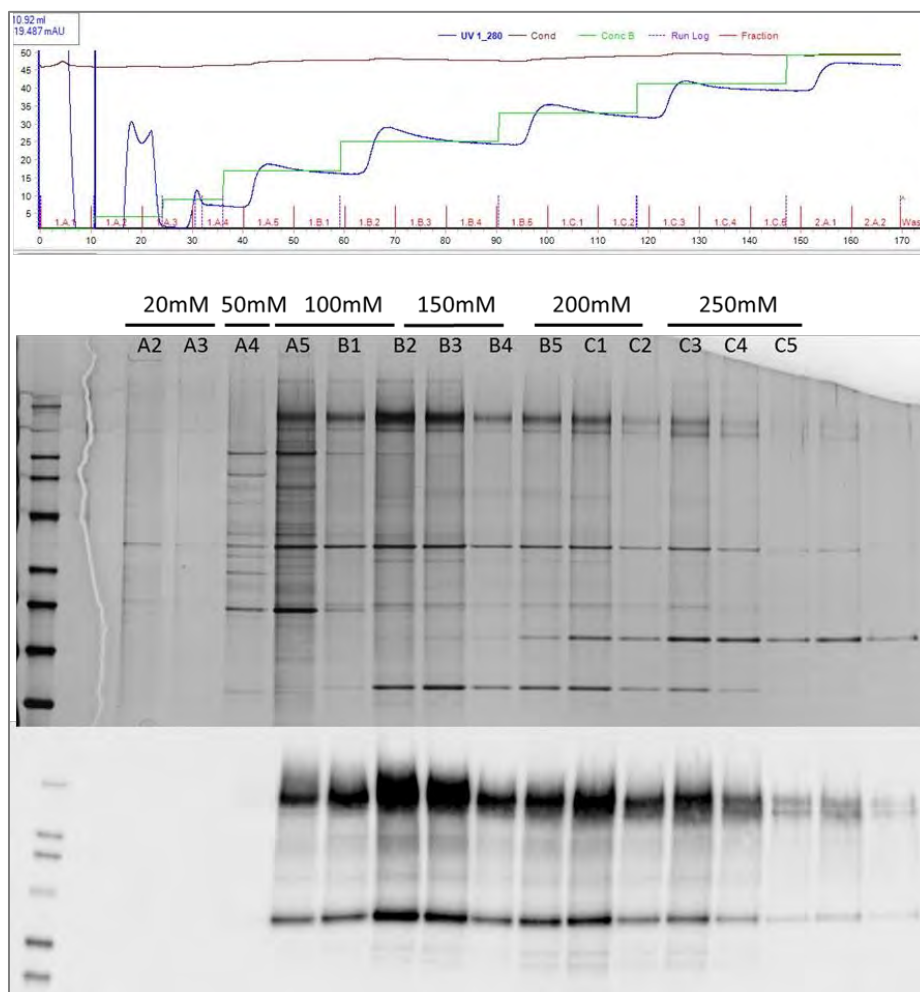


**Figure 3.15** Imidazole elution fractions for CFTR-DIBMALPs prior to phosphorylation treatment with PKA. Silver stain (top) and immunoblotting evaluation of imidazole elution fractions for CFTR-DIBMALPs shows a robust amount of CFTR of a reasonable purity after solubilization using DIBMA.

Following imidazole elution, the material was pooled, gently concentrated and added to a phosphorylation reaction. Because the material had been purified

with DIBMA, which is presumed to be insensitive to divalent cations, I used the recommended amount of 10 mM  $\text{MgCl}_2$  to facilitate the reaction, and followed the protocol that I had applied to CFTR-SMALPs. The reaction appeared to proceed normally, and no aggregation was apparent in the solution; however, results from the gel filtration SEC column suggested that no CFTR protein had successfully been passed through the column, and the only protein that did appear to elute was the remaining 43 kDa PKA that was used in the reaction prior to injection on the column.



**Figure 3.16 Fractional analysis of size-exclusion chromatography of PKA-treated CFTR-DIBMALPs** shows a total loss of CFTR after exposure to 10 mM  $\text{MgCl}_2$  during phosphorylation step.

When I inverted the column on the AKTA and flowed sodium hydroxide over it, the absorption trace revealed a significant amount of protein had been trapped at the start of the column. This was likely the result of a breakdown of the DIBMALP, perhaps due to the presence of magnesium, and the subsequent



CFTR unfolding and aggregation after disintegration of the nanodisc that held it in place.

### **Styrene co-maleimide (SMI)**

The second polymer evaluated was poly(styrene-co-maleimide) (SMI), a copolymer comprised of alternating styrene and dimethylaminopropylamine maleimide, which provides a solution to the challenges that the maleic acid moiety presents for users of SMA. Given the loss of the negatively charged maleic acid, which is thought to play a role in engaging the lipid head groups while hydrophobic styrene inserts into the lipid acyl tails, I incubated the membranes overnight with SMI to ensure good solubilization and cycled the solubilized CFTR-SMILPs over a 5 mL nickel column continuously overnight using an AKTA Pure and eluted the protein from the column the next morning. It was clear the column contained a significant amount of material, given the bright yellow color it accumulated. A higher than normal imidazole concentration of 500 mM was required to fully elute protein from the affinity column, as CFTR immunoblotting of the initial set of eluted fractions showed that 250 mM imidazole did not sufficiently remove CFTR from the nickel resin. Coomassie and silver stain analysis were performed on the full panel of eluted fractions which, unfortunately, suggested that the CFTR was a minor component of the elution. Given the challenges and inefficiency seen with purifying lipid particle samples using gel filtration columns, I decided not to pursue the SMI purification method any further.

### 3.4.4 Lipid evaluation of CFTR-SMALPs

As discussed previously, there is great utility in understanding the native lipid environment of a membrane protein. Not only does this information provide important structural information regarding the surrounding charge and lateral pressure on the molecule, it also offers valuable information that can be incorporated into purification protocols for functional analysis. As was mentioned earlier, the limitations inherent in SMA purification impede many types of structural analysis; a design flaw that could easily be circumvented by employing a more structurally benign polymer. At the same time, a significant advantage of SMA is its strong solubilizing capabilities and its compatibility with a number of different cell types. Ideally, we could harness the extensive solubilizing capability of SMA initially, and then replace this polymer with one that is better suited for the downstream analysis intended; however, this approach relies on a precisely-timed approach and a supporting network that won't allow CFTR to unfold and aggregate in the process, preferably without the use of detergent. So if we know which lipids endogenously surround CFTR, we can parlay this information into an exogenously-added lipid bilayer for CFTR lipid particle stabilization.

For lipidomics evaluation of CFTR-SMALPs, I first created a CFTR-SMALP sample from Expi293 expression cells as a proof-of-concept, and then solubilized CFTR from the more physiologically-relevant CFSME<sub>0</sub>- cells. Both

samples were analyzed for lipid content of SMALPS as well as total membrane fraction, and proteomics.

### **CFTR lipid composition in Expi293 expression cells as proof-of-concept**

For initial attempts, and to create a set of control samples, I first transfected Expi293 cells with hCFTR plasmid and solubilized CFTR with SMA. This provided an abundant sample that could be used to validate the experimental approach and ensure differences in lipid composition could be detected between total membrane and SMALPed CFTR. Sample set and rationale for each is outlined below.

#### ❖ *hCFTR-SMALPs* solubilized from the Expi293 human expression cell line.

This cell line is used as a means of producing a large amount of protein for solubilization and purification, but is not reflective of the native environment of hCFTR. For CFTR expression in this cell line, a cationic lipid-based transfection reagent was used. This may impact the overall lipid content. CFTR-SMALPs were purified using a nickel column and size exclusion chromatography

#### ❖ *Expi293-SMALPs* solubilized from a NON-TRANSFECTED batch of Expi293 cell membranes. This sample represents a total population of purified membrane proteins and lipids from the Expi293 cells solubilized using SMA. To create this sample, Expi293 cell membranes were incubated with SMA for two hours at 4 °C per the standard protocol, at which point the solubilized

suspension was spun down at 100,000 xg for 1 hr to remove large membrane fragments. The resulting supernatant contained nonspecifically-purified SMALPs. Because the final ultracentrifugation step would not pellet individual lipid molecules that would be detected in the lipidomics analysis, I ran both the hCFTR-SMALPs and Expi293-SMALPs on a Native PAGE gel. This allowed for PAGE purification of the Expi293-SMALPs which had not undergone column purification. When run on the Native PAGE gel, the Expi293-SMALPs separated into 3 distinct bands, which were cut out of the gel. The sample containing CFTR-SMALPs was also run on the Native PAGE gel and resolved to one band, which was also cut out of the gel and provided for both proteomics and lipidomics analysis. In addition to gel fragments, all samples were sent for analysis in SEC buffer. Each sample was analyzed by MS/MS with gating set to isolate members of different lipid classes. We compared profiles from 4 lipid classes in particular, shown in the table below.

**Table 3.1 Summary of the four classes of lipids analyzed in detail from Expi-293-generated samples**, as well as the MS/MS transition that was used to gate for each class of lipids.

Abbreviation	Lipid Class	MS/MS Transition
PC	Phosphatidylcholine	Precursor ion scanning (PIS) of 184.1
PE	Phosphatidylethanolamine	Neutral loss of 141
PS	Phosphatidylserine	Neutral loss of 185
PA	Phosphatidic Acid	Neutral loss of 115, NH <sub>4</sub> <sup>+</sup> Adducts
PI	Phosphatidylinositol	Neutral loss of 277, NH <sub>4</sub> <sup>+</sup> Adducts
PG	Phosphatidylglycerol	Neutral loss of 189, NH <sub>4</sub> <sup>+</sup> Adducts
CER	Ceramide	PIS of 284.4, , NH <sub>4</sub> <sup>+</sup> Adducts
CE	Cholesteryl Ester	PIS of 369.1, NH <sub>4</sub> <sup>+</sup> Adducts

We first compared the lipid profiles for total Expi293 membrane and Expi293-SMALPs and found no significant differences in detection patterns apparent between them. This suggests that no solubilization bias for certain lipid classes exists for this human HEK-cell derived cell type. We then looked for differences between CFTR-SMALPs, Expi293 SMALPs and total Expi293 membrane. Results suggest that no significant differences in the prevalence of lipid classes exist between the Expi293-SMALPs and total Expi293 membrane sample, which are primarily made up of phosphatidylcholine (PC) and to a lesser degree, phosphatidylethanolamine (PE), with smaller fractions of each of the remaining classes detected. The lipid content breakdown for CFTR-SMALPS indicates that while PC also makes up the majority of lipids in the CFTR-SMALP particles, it only represents 50%, as opposed to the roughly 75% seen with the other two samples. Further, levels of phosphatidylserine (PS, mainly subclass PS-28:0) and Phosphatidylethanolamine (PE) (mainly PE - 32:1, 32:2, 34:2) lipids detected did increase significantly with the CFTR-SMALP nanodiscs. A breakdown of lipid content for Expi293-based samples can be seen in Figure 3.17.

With this data, we feel confident concluding that there is a distinct preference demonstrated for CFTR lipidic association when compared to general association profiles of SMALPs and total Expi293 membrane fraction. This work in Expi293 expression cells served as proof-of-concept.

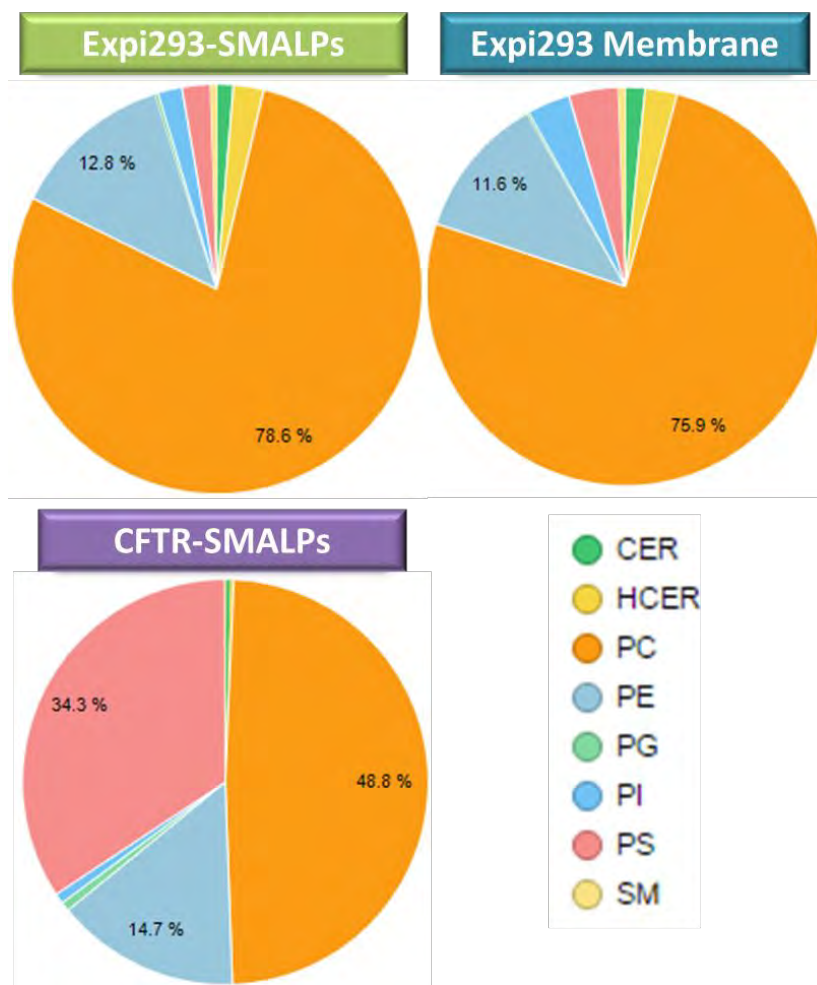


**Figure 3.17 Lipid profiles comparing the content of Expi293-SMALPs, Expi293 membranes and CFTR-SMALPs** are displayed as the percent of each class that was detected for a given sample. Data suggest no significant differences in the prevalence of lipid classes exist between the Expi293-SMALPs and total Expi293 membrane sample, which is roughly 76% phosphatidylcholine (PC), 12% phosphatidylethanolamine (PE), and smaller fractions of each of the 6 remaining classes queried. This result indicates that no lipid bias exists upon SMA insertion and solubilization of Expi293 cells. The lipid content breakdown for CFTR-SMALPS again highlight the major components as PC and PE, although PC only represents 50%, as opposed to the roughly 75% seen with the other two samples.

To ensure that we could draw conclusions about the particle content of each sample, proteomic analysis was performed on each sample tested. For all non-CFTR SMALP samples, no detectable CFTR was measured. In samples that contained CFTR-SMALPs, either in solution or in Native PAGE gel fragments, CFTR was the most abundant species. Of note, a series of peptides that was detected was for the microtubule-associated protein, kinectin (KTN1), which is normally found anchored to the endoplasmic reticulum, and could indicate that a subset of our CFTR-SMALP population is being isolated from ER membranes.

### **CFTR lipid composition in physiologically-relevant CFSME<sub>0</sub>- cells**

Once the Expi293 samples were analyzed to determine assay parameters, the hCFTR-SMALPs in the cystic fibrosis cell line, CF submucosal gland epithelial cells (CFSME<sub>0</sub>-), were analyzed.

- ❖ **hCFTR-SMALPs** solubilized from human CFSME<sub>0</sub>- cells. This cell line represents a human lung tissue that normally contains trace amounts of CFTR. Cells were transiently transfected with the hCFTR plasmid via electroporation, and were seeded on collagen-coated plates for 48 hours post-transfection.
- ❖ **GFP-SMALPs (Sham control)** This sample represent SMALPs isolated from cells that were electroporated with a plasmid for soluble eGFP expression. This treatment group was used as a control for CFSME<sub>0</sub>- cell membrane SMALP solubilization after electroporation.
- ❖ **CFSME<sub>0</sub>- total membrane (untreated negative control)** – This sample is the untransfected CFSME<sub>0</sub>- membrane fraction, and was included to determine whether SMA preferentially targets certain lipids.
- ❖ **CFTR-transfected CFSME<sub>0</sub>- total membrane** – This sample will be analyzed to determine whether the expression of hCFTR alters the total cell lipid composition overall.



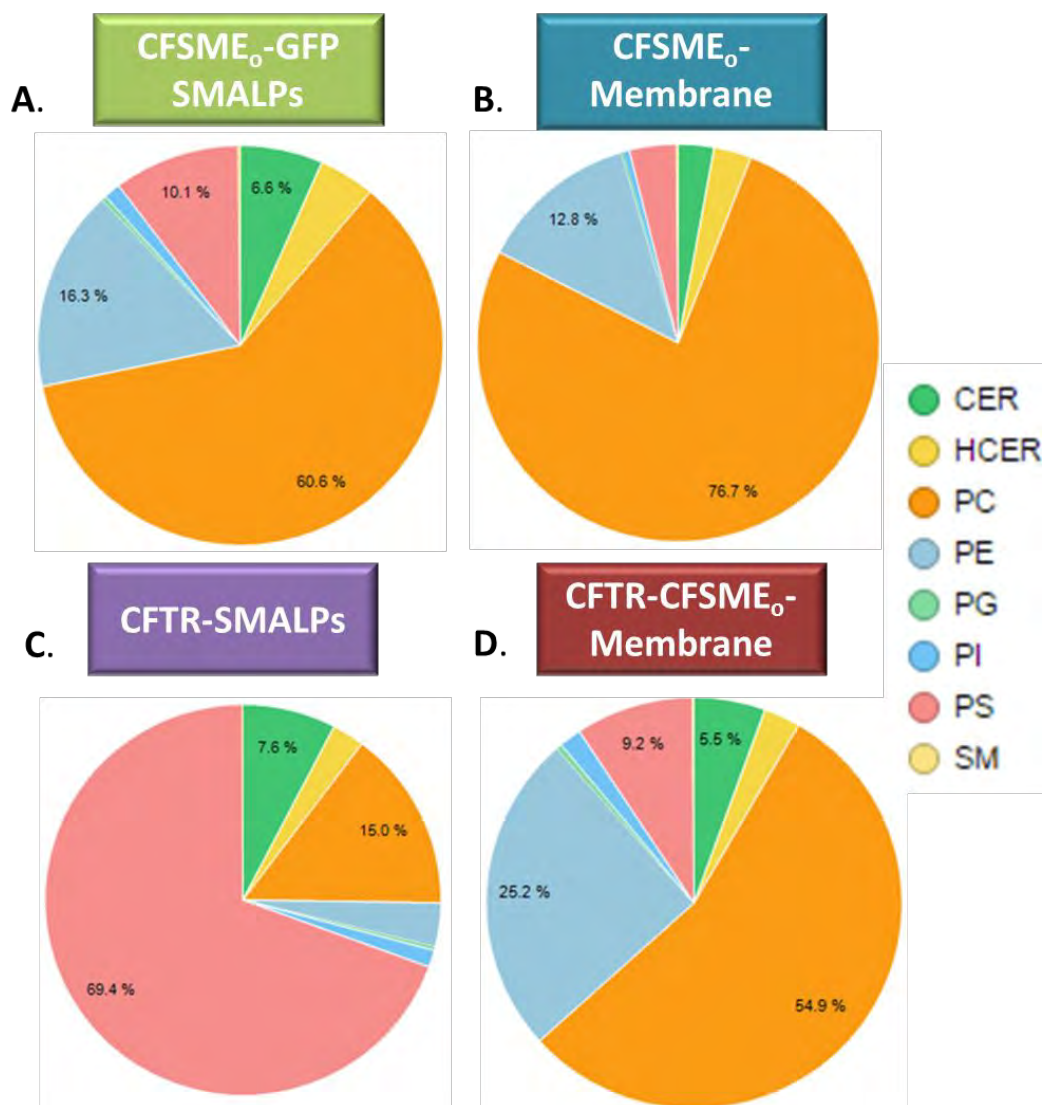


**Figure 3.18 Lipid profiles comparing the content of GFP-transfected CFSME<sub>0</sub>- SMALPs (A), CFSME<sub>0</sub>-total membrane (B), CFTR-SMALPs (C) and CFTR-containing CFSME<sub>0</sub>- membranes.** Results are given as % of each class that was detected for a given sample. The data show some minor differences in the prevalence of lipid classes exist between the CFSME<sub>0</sub>-SMALPs, total CFSME<sub>0</sub>-membrane sample and CFTR-CFSME<sub>0</sub>- membrane sample, which is between 55-75% phosphatidylcholine (PC), 12 -25% phosphatidylethanolamine (PE), and 5-10% PS. The lipid content breakdown for CFSME<sub>0</sub>- CFTR-SMALPS contains a significantly larger component of PS lipids and a reduced level of PC lipids. Of note, the amount of PE lipids was also much lower in the CFTR-SMALP sample.

Preliminary data from CFSME<sub>0</sub>- lipid analysis suggests that similar to Expi293 samples, the major components of the two non-CFTR containing samples were PE and PC lipids. The sample of CFTR-transfected, whole-membrane prep also had majority fractions of PE and PC lipids; however, there was significantly less PC, and a greater quantity of PE. When CFTR-transfected CFSME<sub>0</sub>- membrane were SMALPed and the sample was enriched for CFTR using affinity purification, the level of PC lipids detected in the CFTR-SMALP samples diminished greatly, and there was a significant increase seen in levels of PS (mainly PS-28:0) for the sample. Overall, it appears that CFTR may have a preference for phosphatidylserine, with the main contributor to this differential across samples being PS subclass (14:0/14:0)-H, which occurs in much higher prevalence in CFTR-SMALPs from both cell lines as compared to other subclasses of PS as well as other lipid classes overall. This may not be surprising, however, when we consider the main subclasses that contribute to PE prevalence in Expi293 CFTR-SMALPs. They, too, have at least one fully saturated lipid chain - PE (16:0/16:1)-H and PE (16:0/18:1)-H, for example. In addition to the lipid classes quantified above, significant enrichment of cholesterol esters was detected in CFTR-SMALP samples.

To confirm CFTR specificity of the lipid classes found in the CFTR-SMALPs, it would be important to evaluate the content of SMALPs containing other purified MPs of different classes (transporter, channel and pore, for example) that containing different numbers of TMs. A correlation may exist

between size of the protein (i.e., number of TMs) and the relative percentage of unsaturated lipid classes that tend to pack more tightly around proteins in the lipid bilayer. While this data represents a very solid first trial, the experiment will be repeated to confirm the results. A side-by-side comparison of the Expi-293 and CFSMEo- data is seen in Figure 3.19.

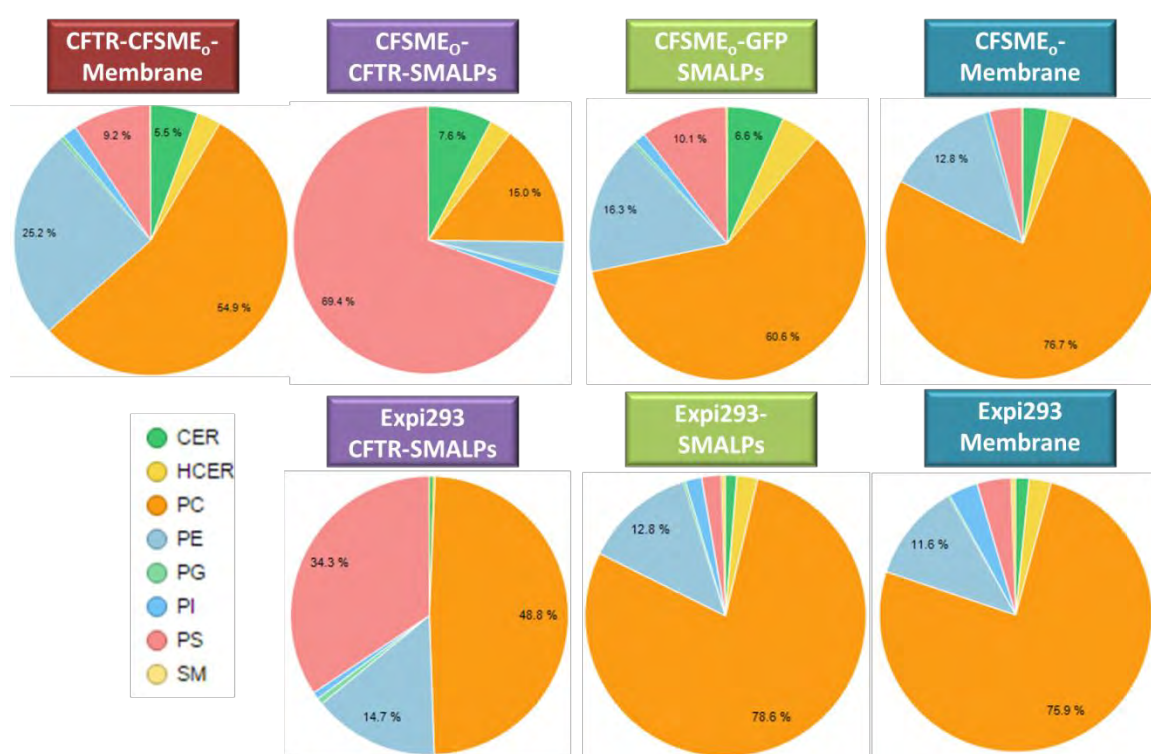


**Figure 3.19 Comparison of lipidomics data for two cell lines, CFSMEo-lung cells (top row) and Expi293 expression cells (bottom row).** For comparison purposes in this discussion, this Figure displays a different alignment and consolidation of data that appears in Figures 3.17 and 3.18. Sample type (L to R: CFTR-containing total membrane, CFTR-SMALPs, total membrane SMALPs and total untreated cell membrane) is separated by column to allow for comparison between the two cell types. The data suggests a strong prevalence for CFTR to reside in an environment that is enriched with phosphatidylserine, which contains long, saturated acyl chains and may provide a more static environment for CFTR.

### 3.5 DISCUSSION

The expression and purification of human CFTR has been an active area of research since the gene was first sequenced in 1989 (Riordan *et al.*, 1989a). Developing a detailed understanding of the structure and function of CFTR has been, and will continue to be, a critical undertaking in the pursuit of novel and effective therapies to mitigate and to prevent the devastating effects of the loss-of-function mutations that cause cystic fibrosis. Recent years have brought important developments in this area. Novel small-molecule drugs that directly target mutant CFTR (Birket *et al.*, 2016; Mijnders *et al.*, 2017; Ren *et al.*, 2013) are now available. More recently high-resolution structures of several CFTR molecules have been published giving new insight into its function (Liu *et al.*, 2017; Zhang and Chen, 2016; Zhang *et al.*, 2018b). However many gaps remain in our understanding of this protein and how it can be targeted to develop more effective therapies.

One major challenge that remains is producing adequate amounts of human CFTR to enable functional and structural studies. Significant effort has been expended to generate stabilized versions of human CFTR that incorporate polymorphisms from other species and allow stable purified protein to be generated (Hildebrandt *et al.*, 2014; Lewis *et al.*, 2004; Lewis *et al.*, 2010; Rabeh *et al.*, 2012a; Sharma *et al.*, 1990; Wang *et al.*, 2007). Similar efforts have been used to thermally stabilize G-protein coupled receptors (GPCRs), which has

been a pre-requisite to the generation of high-resolution structures (Heydenreich *et al.*, 2015; Vaidehi *et al.*, 2016).

Detergent purification of a large transmembrane protein like CFTR is also challenging from a stability perspective. After initial work was done to purify CFTR in several combinations of detergents for solubilization and storage, I considered lipoprotein nanodisc technology (Bayburt and Sligar, 2010; Ritchie *et al.*, 2009) to isolate and stabilize individual molecules of CFTR. In its most basic form, a nanodisc comprises a single phospholipid or a mixture of two phospholipids that combine to form the nanodisc bilayer. Recombinant human apolipoprotein A-1 acts as the Membrane Scaffold Protein (MSP) that holds the raft together, securing the lipids in place. The length of the scaffold protein dictates the nanodisc size, which can be increased or decreased to accommodate the protein that is being stabilized. However, this protocol requires initial purification of the MP into detergent micelles, which is then replaced with exogenous lipids, thus introducing the primary limitations associated with detergent purification of CFTR. Success of this protocol relies on a robust sample of detergent-purified starting material which is stable enough to withstand lipid exchange, preferably into a mixture of the MP's endogenous lipid environment. However, given the challenges associated with detergent purification of CFTR, starting material would be relatively unstable and of low abundance, and selecting the appropriate lipid mixture for creating the nanodisc would require

extensive qualification, as the endogenous lipid composition had not yet been determined.

In this study we show that true wild-type CFTR can be expressed at sufficient levels in suspension HEK cells to allow for robust purification; and that, when solubilized using styrene-maleic acid copolymers, this protein is stable for a variety of structural and functional characterizations. By encapsulating CFTR in an SMA-lipid particle (SMALP), which incorporates lipids from the bilayer, we have provided the first direct evidence of the lipid preferences of CFTR. This lipidomics data from HEK-cell expressed CFTR indicates that negatively charged phosphatidylserine (PS) associates with CFTR at levels beyond its abundance in the HEK cell membranes (Figure 3.17). Our data supports previous findings in which supplementation of detergent-purified CFTR with different lipids was evaluated for changes in ATPase activity. The addition of PS to the purified protein improved its functional stability and ATPase activity levels by six-fold (Hildebrandt *et al.*, 2017).

Another publication evaluated the impact of CFTR depletion on the overall fatty acid composition of intestinal Caco 2/15 cells (Mailhot *et al.*, 2010). This work provided evidence that CFTR is involved in overall FA homeostasis, and that CFTR knock-down results in a statistically-significant increase in levels of myristic (14:0) and palmitic (16:0) FA, which are both saturated, long-chain lipids with a single carbon backbone. This data simultaneously displayed a

significant downregulation of longer acyl-chain saturated FAs ( $P < 0.05$ ) (Mailhot *et al.*, 2010). Additionally, when de novo synthesis of lipids was evaluated for a period of 12 days in the presence of [ $^{14}\text{C}$ ]-acetate for 24 h, and lipids were extracted from the cells and cell culture medium and evaluated for lipid content, the levels of triglycerides (TG), phospholipids (PL) and cholesteryl ester (CE) saw only a slight reduction in-total when total cells were probed. However, the levels of TG, PL and CE detected in the spent medium of CFTR knockdown cells was significantly higher compared to mock-treated cells, including a nearly four-fold increase in the levels of cholesteryl esters and a 5 to 7-fold increase in the larger, more robust triglycerides (Mailhot *et al.*, 2010). This collection of published data, coupled with our data showing remarkably similar lipid profiles for CFTR-SMALPs from CF-patient derived CFSME cells and HEK expression cells, nicely supports our hypothesis that CFTR likely regulates its local lipid environment for selected stabilization.

Moreover, our studies showed that CFTR-SMALPs were enriched with cholesterol compared to the average bilayer composition. The importance of cholesterol for the function of human ABC proteins, and specifically of CFTR, has been demonstrated in many publications (Abu-Arish *et al.*, 2015; Fang *et al.*, 2010; Hirayama *et al.*, 2013; Modok *et al.*, 2004; Rothnie *et al.*, 2001). These studies highlight the role of cholesterol in CFTR-expressing cells such as function and translocation (Lu *et al.*, 2019) and CFTR spatial confinement (Abu-Arish *et al.*, 2015), and draws correlations between the level of cholesterol and CFTR

gene expression in CF lung cells (Fang *et al.*, 2010; White *et al.*, 2007). Further, cholesterol may help prevent permeability of sodium ions across the membrane local to CFTR, an important factor for effective chloride transport through CFTR (Haines, 2001).

The importance of determining the local lipid environment for CFTR could be wide-reaching and help provide insight on function and structure, but also best practices for purification of CFTR. Several recent publications pertaining to the purification and characterization of CFTR have utilized the non-ionic detergent, digitonin (Liu *et al.*, 2017; Zhang and Chen, 2016; Zhang *et al.*, 2018b), which selectively permeabilizes the plasma membrane (as opposed to organelle membranes), likely due to its affinity for cholesterol (Zhong *et al.*, 2010). This approach likely disrupts the normal lateral positioning of the protein and will certainly impact function, and should be carefully considered when deciding experimental approach.

A preference for residence within a Liquid-Ordered Phase (lo), which is characterized by highly ordered acyl chain packing, tends to be favorable for larger membrane proteins like CFTR, particularly one that requires measured control of its orientation and channel gating. The prevalence of long, saturated acyl chains and glycosphingolipids provide a higher order of structure to the lipid bilayer and offer more stability to the protein within them. Indeed, it may be a requirement of CFTR to reside within an area of reduced lateral motion and a



certain lateral pressure profile ( $\Omega(z)$ ), a value that describes the lateral force or pressure exerted by the lipid bilayer on the protein residing in it (Battle *et al.*, 2015; Cantor, 1999). In this case, the lipid classes and specific subclasses that are seen to be enriched in CFTR lipid particles, primarily phosphatidylserines, support the need for CFTR to have an ordered and more compact environment.

As alluded to in the results section, there are limitations to working with SMA that are due to the ring shape of the styrene head group. While this moiety provides stability by intercalating into the lipid chains, it also interferes with absorption studies, emits a fluorescent signal, and may lead to a hyper-stabilized particle that is unable to be analyzed in assays such as nanoDSF thermal unfolding and aggregation assays with any meaningful interpretation of the output. Additionally, attachment of CFTR-SMALPs to a chip for surface plasmon resonance (SPR) was not detected, likely owing to the negatively-charged maleic acid moiety that encircles the particles that may create repulsion with the negatively charged chip surface.

With all of this considered, the application of styrene-maleic acid purification to the study of CFTR offers a new and exciting opportunity to capture this important and challenging protein in its native state, and opens the door to more complete and relevant approaches to CF drug discovery.

### **3.6 Materials and Methods**

#### **Protein expression and purification**

##### **Expi293 hCFTR transfection**

Expi293F cells (cGMP banked, Cat# 100044202) were seeded in 1 liter Erlenmeyer vented cap flasks at a density of  $2 \times 10^6$  viable cells (vc) per mL with a final seeding volume of 250 mL in Expi293 Expression Medium (Gibco Cat# A1435101). Cells were then transfected using the ExpiFectamine 293 Transfection Kit (Cat# A14524) as follows. A total of 200  $\mu$ g of hCFTR expression plasmid DNA were added to 5 mL of OptiMEM medium (Cat# 31985070) and 540  $\mu$ L of ExpiFectamine to a second 5 mL volume of OptiMEM. The two solutions were mixed and cells placed in a 37 °C incubator. Approximately 16-18 hours post-transfection, enhancers 1 and 2 were added from the ExpiFectamine reagent kit. Cell viability and density were checked 48 hours post-transfection and cells below 95% viability were collected. Otherwise, cells were collected 72 hours post-transfection by centrifugation at 1850 xg for 10 minutes, washed with cold PBS + protease inhibitors, then pelleted again. Pellets were then weighed and flash-frozen.

**Styrene maleic acid solubilization of hCFTR from Expi293F cells**

This protocol is scaled for purification of hCFTR-His10 from a 6 L culture of transfected Expi293F HEK cells. All steps were performed in a 4 °C cold room or on ice.

*Lysis*

Fresh lysis solution was prepared by adding EDTA-free protease inhibitor tablets to 200 mL of lysis buffer (50 mM Tris, 500 mM NaCl, 1 mM ATP, 1 mM MgCl<sub>2</sub>, pH 7.8; for Cryo-EM use ATP- $\gamma$ S). Cells were harvested from culture by centrifugation at 2620 xg for 10 minutes or frozen cell pellets were thawed on ice. In both cases the weight of cell pellet were measured and the cell pellets were resuspended in 4 mL of lysis buffer per gram of cell weight. Resuspended cells were lysed using a C3 cell press by passing cells twice at a pressure of 10,000 psi. Lysed cells were pelleted (2,000 xg, 30 min). Supernatants were decanted into new tubes and ultracentrifuged for one hour at 100,000 xg to pellet membranes. After the final centrifugation membrane pellets were retained and weighed, and the supernatant was discarded.

*Solubilization*

SMA2000P (Cray Valley) was prepared according to the protocol reported by Lee *et al* (2016). To prepare a solubilisation buffer SMA was dissolved in Solubilization buffer (20 mM Tris, 500 mM NaCl, 1 mM MgCl<sub>2</sub>, 10% glycerol, 1 mM ATP, pH 7.8) to a final concentration of 5 % (w/v), and a total of 12.5 mL per

1 g of membrane pellet. Membranes were resuspended using 4 mL of lysis buffer per 1 g of initial cell weight<sub>[PN1]</sub>. Membranes were fully resuspended using a 15 mL glass Dounce homogenizer (10 cycles per 15 mL volume). Homogenized membranes were transferred to a chilled 50 mL conical tube and an equal volume of the 5 % SMA solution was added to give a final SMA concentration of 2.5 % (w/v). The samples was incubated for 2 h with gentle rocking in a cold room then transferred into chilled 50 mL ultracentrifuge tubes and ultracentrifuged (100,000  $\times g$ , 1 h, 4 °C). The supernatant containing SMA-solubilized membranes was collected and the pellet was discarded.

SMA2000P (Cray Valley) was prepared according to the protocol reported by Lee *et al* (2016). To prepare a solubilization buffer SMA was dissolved in solubilization buffer (20 mM Tris, 500 mM NaCl, 1 mM MgCl<sub>2</sub>, 10% glycerol, 1 mM ATP, pH 7.8) to a final concentration of 5% (w/v), and a total of 12.5 mL per 1 g of membrane pellet. Membranes were fully resuspended using a 15 mL glass Dounce homogenizer (10 cycles per 15 mL volume). Homogenized membranes were transferred to a chilled 50 mL conical tube and an equal volume of the 5 % SMA solution was added to give a final SMA concentration of 2.5 % (w/v). The samples was incubated for 2 h with gentle rocking in a cold room then transferred into chilled 50 mL ultracentrifuge tubes and ultracentrifuged (100,000  $\times g$ , 1 h, 4 °C). The supernatant containing SMA-solubilized membranes was collected and the pellet was discarded.

### *Purification*

SMA-solubilized material was filtered through a 70  $\mu$ m nylon cell strainer (Falcon, Cat# 21008-952) into a 125 mL flask. A 5 mL Ni-Sepharose His-Trap HP or FF column (GE Healthcare, Cat# 17-5247-01) was attached to a peristaltic pump in the cold room. The column was washed with 2 column volumes (CV) water followed by 2 CV of buffer S at a flow rate of 1 mL/min. The SMALP-containing supernatant was circulated across the column at 1 mL/min for 16 h. The His-Trap column was attached to an AKTA input line washed with 15 CV of solubilization buffer. Protein was eluted from the column using step-wise imidazole gradient over a total volume of 50 CVs (20 CVs 0 mM, 20 CVs 10 mM, 10 CVs 50 mM, 16 CVs 100 mM, 10 CVs 250 mM) in a base of buffer S. Fractions of 2 mL were collected throughout. Samples were prepared from each fraction to run a silver stained gel to determine which fractions contain hCFTR SMALPs and pool them. Pooled fractions containing CFTR were dialyzed overnight in 4L of fresh buffer S using a 30 kDa MWCO dialysis membrane in an effort to remove imidazole. The dialyzed sample was concentrated to a final volume of 350  $\mu$ L for SEC purification (30 kDa MWCO Amicon Ultra-15 centrifugal filtration cartridges, Millipore).

### *Size Exclusion Chromatography (SEC)*

Concentrated CFTR was further purified by SEC using a Superdex 200 10/300 column in SEC buffer (20 mM Tris, 150 mM NaCl, 1 mM MgCl<sub>2</sub>, and 1 mM ATP,

pH 7.8) at a flow rate of 0.5 mL/min. Protein was collected in 0.5 mL fractions for silver stain and western blot analysis.

### **Insect Cell (Sf9 / Sf21) Transfection**

Cells were maintained in Sf900 IITM SFM (Gibco Cat# 10902-088) at >95 % viable and at a passage number below 25 for use in transfection. Two 1 L cultures were seeded at  $1 \times 10^6$  vc/mL in 3 L vented shake flasks. Each culture was infected with an appropriate dilution of WT hCFTR 3xFlag/10xHis viral stock. Viral stock dilutions depend on viral titer, and were determined by western blot analysis for each stock (1:5000, 1:1000, 1:500, 1:100, 1:20 dilutions typically tested in small-scale 50ml Sf9 cultures). Following infection, cultures were placed in a 27 °C incubator, shaking at 120 rpm for 72 hours.

### **Detergent solubilization of hCFTR from Sf9/Sf21 cells**

#### *Lysis*

Fresh lysis solution was prepared by adding protease inhibitor stocks (1000x) to 50 mM Tris, 500 mM NaCl, 2 mM ATP pH 7.5). Cells were harvested by centrifuging at 2,620 xg for ten minutes. Supernatants were decanted into new tubes and the cell pellet was resuspended in lysis buffer at a ratio of 4mL buffer per gram cell weight. Cells were lysed using a Branson Digital Sonifier at 30% intensity, running at alternating on/off intervals of 1 second for a total of one minute 'on' time. Lysates were transferred to 70 mL ultracentrifuge tubes and centrifuged at 12,000 xg for 30 minutes. Supernatants were transferred to new

tubes and ultracentrifuged for one hour at 100,000  $\times g$  to pellet membranes. After the final centrifugation membrane pellets were retained and weighed, and the supernatant was discarded.

### *Solubilization*

Pelleted cell membranes were resuspended in solubilization buffer (20 mM Tris, 500 mM NaCl, 2 mM MgCl<sub>2</sub>, 2% n-dodecyl-beta-D-maltopyranoside (DDM), 20% glycerol, 2 mM ATP, pH 7.4) at 4 mL per gram initial cell weight and homogenized using a 15 mL glass Dounce homogenizer. The homogenized sample was then transferred to ultracentrifuge tubes and centrifuge at 100,000  $\times g$  for 1 hour. Supernatant containing detergent-solubilized CFTR was collected and the remaining membrane pellet was discarded.

### *Purification*

A 4 mL resin bed (anti-FLAG M2 affinity resin, Sigma Cat# A2220) was poured in a BioRad Econo-Pac column (Cat# 732-1010EDU) and rinsed with 3 CV Flag buffer (20 mM Tris, 150 mM NaCl, 2 mM MgCl<sub>2</sub>, 0.1% DDM, 20% glycerol, 2 mM ATP, pH 7.4) to remove excess resin solution, and was washed with 3 CV Flag clean buffer (100 mM glycine HCl, pH 3.5). The resin was equilibrated with 5 CV Flag buffer, subsequently added to the bottle of detergent-solubilized hCFTR/3xFLAG/10xHis membranes, and incubated for 1 hour with rotation. After incubation, the solubilized sample was centrifuged at 300  $\times g$  for 5 minutes, the supernatant was poured off and the resin was loaded back onto the column

and wash with 20 CV Flag buffer. The column was capped to prevent solvent flow and 5 CV of Flag elution buffer (20 mM Tris, 150 mM NaCl, 2 mM MgCl<sub>2</sub>, 0.1% DDM, 20% glycerol, 2 mM ATP, pH 7.4, 750 µg/mL 3xFLAG peptide) was added. Remove The resin/buffer slurry was removed and placed into a 250 mL roller bottle and incubate overnight with rotation. Following incubation, elution slurry was loaded into a fresh column and the CFTR-containing eluate was collected, concentrated and buffer-exchanged into Flag buffer using a 100,000 MWCO Amicon Ultra-15 centrifugal filtration cartridge (Millipore Cat# UFC910024) to a final volume of 0.5-1 mL. Protein was snap frozen and stored at -80°C for future use.

## **Polymer preparation**

### **Diisobutylene Maleic Acid (DIBMA) polymer**

To prepare DIBMA polymer for use, 3 mL of DIBMA (Sokalan CP9 in alkaline solution) was dialyzed in a 5 mL microdialysis capsule using a 3.5 MWCO dialysis membrane for 16 hours against 1 L target buffer (e.g. 50 mM Tris, 200 mM NaCl, pH 7.4). After four hours, buffer was changed and material was dialyzed again overnight. Dialyzed DIBMA stock was filtered through a 0.22 µm syringe filter. DIBMA concentration was determined by refractometry using a refractive index increment of  $dn/dc = 1.346 \text{ M}^{-1}$ , where  $c$  is the DIBMA concentration based on the number average molecular weight ( $M_n$ ) of DIBMA.



## **CFTR Expression Cell Lines**

### **CFSMEo<sup>-</sup>**

CF patient-derived CFSMEo<sup>-</sup> cells (obtained from Dr. Dieter C. Gruenert, UCSF) were maintained at 37°C in Minimum Essential Medium with Earle's salts, supplemented with 10% (v/v) FBS, 2mM L-glutamine and 1% (v/v) pen/strep on ECM-coated flasks (10ug/mL human fibronectin, 30ug/mL bovine collagen I, 0.1% BSA in LHC basal medium).

### **Expi293F™ suspension cell line:**

Expi293F Cells are derived from the human 293 cell line, and are intended for use with the Expi293 Expression System. Cells were grown in suspension culture at an average density of  $0.5\text{--}2 \times 10^6$  c/mL, however they can be cultured at up to  $1 \times 10^7$  c/mL with impact on viability. They were maintained in Expi293 Expression Medium. Transient CFTR expression was facilitated with the cationic lipid-based ExpiFectamine™ 293 transfection reagent.

### **Electroporation**

CFSMEo<sup>-</sup> cells were lifted from culture dishes by adding 7mLs of PET™: Cell Dissociation Formula (Athena Enzyme Systems, Baltimore, MD) and incubating the flask at 37 °C for 5 minutes or until cells had lifted off the dish. Cells were then resuspended in an equal volume of MEM complete medium and centrifuged at 1000 rpm for 5 minutes rinsed in 5 mL MaxCyte Electroporation buffer and repellet by centrifuging at 1000 rpm for 5 minutes. The pellet was then

resuspended in electroporation buffer at a concentration of  $2.5 \times 10^7$  viable cells per mL. To this cell suspension, an appropriate amount of plasmid DNA was added for a final concentration of 100  $\mu\text{g/mL}$ . The cell/DNA mixture was then loaded into an appropriately-sized electroporation cuvette. OC100 cuvettes hold 100  $\mu\text{L}$  and OC400 cuvettes hold 200- 400  $\mu\text{L}$ . The cuvette was then inserted into the MaxCyte STX machine and electroporated with MaxCyte CFBE system protocol. Following electroporation, the cells were collected from the cartridge and 1/10 volume of DNase (2000 Kunitz units/mL) was added to the transfected cells, which were subsequently transferred to a 6-well plate and incubated at 37 °C for 20 minutes to allow cells to recover. Following this, 5 mL media was added to each well and cells were collected in a 15 mL conical tube and spun down at 1000 rpm for 5 minutes. Cells were resuspended in 5 mL of media, counted, and plated as needed.

### **SMALP SDS-PAGE Protocol**

Imidazole-eluted or SEC column-eluted fractions containing CFTR-SMALPs were separated on NuPAGE™ 4-12% Bis-Tris Protein gels (ThermoFisher) and transferred to nitrocellulose membranes using an iBlot™ semi-dry transfer apparatus at 20 V for 10 minutes. Membranes were probed with anti-CFTR monoclonal antibody 570 (obtained from UNC Chapel Hill) at a 1:1000 dilution to determine CFTR protein expression in each eluted fraction. For SDS-PAGE: NuPAGE LDS sample buffer (Invitrogen), Molecular weight markers: MagicMark™ XP Western Protein Standard 20-220 kDa (Invitrogen Cat#

LC5602) and Precision Plus Protein™ Kaleidoscope™ Prestained Protein Standard 10-250 kDa (BioRad Cat# 1610375) were used.

### **Calf intestinal alkaline phosphatase (CIP) treatment**

Purified CFTR was added to 200  $\mu$ L reaction buffer (100 mM NaCl, 50 mM Tris-HCl, 1 mM MgCl<sub>2</sub>, 1 mM dithiothreitol (DTT), pH to 7.9) and CIP (20 units) was added. The mixture was incubated for 1 hr at 20 °C to allow the reaction to proceed.

## **Electron Microscopy**

### **Negative stain TEM**

Carbon-coated 400 mesh grids (Electron Microscopy Sciences, Hatfield, PA), were glow discharged for 45 seconds at 0.2 mBar and 20 mA using a PELCO easiGlow™ Glow Discharge Cleaning System (Ted Pella, Inc, Redding, CA). A single 8  $\mu$ L drop of protein was added to the grid and left on for 30 seconds, then wicked away with filter paper, leaving behind bound particles. In cases where sample concentration was low, the sample was fixed with a 2% glutaraldehyde solution prior to staining with a 1% (w/v) uranyl acetate solution.

## CHAPTER IV: CAPTURING THE PHYSIOLOGICAL COMPLEXES OF GLUT1 FROM RBCS: SMALP SOLUBILIZATION

### 4.1 Preface

Chapter IV is a collaboration that I devised with Andrew Simon in an effort to use my thesis work to answer questions that arose with his. A portion of the study design was based on experiments proposed by our thesis mentor, Anthony Carruthers.

- ❖ **Simon KS**, Pollock NL, Simon AH, Maderia M, Hurlbut GD, Carruthers A. Capturing the physiological complexes of GLUT1 from RBCs: SMALP solubilization. *Manuscript in preparation*

During the course of this study, work was also performed that contributed to a manuscript on the development and use of Native PAGE separation of SMALPs. This manuscript is currently in press.

- ❖ Pollock NL, Rai M, Parmar M, **Simon KS**, *et al* (in press). SMA-PAGE: A new method to examine complexes of membrane proteins using SMALP nano-encapsulation and native gel electrophoresis. *BBA Biomembranes*

Experimental design for this manuscript was completed by Andrew Simon and me, with input from Naomi Pollock and Anthony Carruthers. The protocol for GLUT1 purification was modified from the CFTR purification protocol, with input from AS and Naomi Pollock. I performed the GLUT1 protein expression and purification in HEK cells, and performed the downstream analysis with support from NP. AS provided and executed the protocol for RBC ghost generation used in erythrocyte SMALP experiments. NP and I prepared all samples for proteomic evaluation, which was performed by Scott Shaffer. I performed all TEM grid preparation and microscopy on the FEI Tecnai Spirit TEM. AS and Lara Strittmatter obtained SEM images of erythrocyte ghosts. The Dafforn Lab and the Knowles Lab (University of Birmingham, UK) provided hydrolyzed SMA polymer for use in this work. Ashley Souza generated the cartoon schematic of GLUT1-SMALPs seen in Figure 4.3. I have analyzed the data with input from AS, NP and TC, and have written the text and prepared all Figures for this manuscript.

## 4.2 Abstract

GLUT1, expressed in high abundance on the surface of erythrocytes, and at lower levels in many other cell types, is implicated in several diseases including GLUT1 deficiency syndrome, cancer and diabetes. However, much is still unknown about the oligomeric structure and kinetic function of the protein. Published crystal structures of detergent-purified GLUT1 display a monomer comprising 12-transmembrane helices in the closed conformation. Biochemical studies, on the other hand, demonstrate that GLUT1 exists as a multimer in both erythrocytes and transfected cell lines. This oligomerization may explain cooperative interactions between exofacial and endofacial glucose binding sites in cells. The recent development of styrene/maleic acid lipid particles (SMALPs) as an alternative to detergent purification of integral membrane proteins (IMPs) offers a valuable tool for structural and functional analysis of, as well as drug discovery efforts focused on, proteins like GPCRs and ABC transporters. In lieu of separating out such a protein from its surrounding lipid bilayer and associated proteins using detergents, this method takes advantage of the amphipathic properties of SMA to extract IMPs directly from the membrane. The result is a monodisperse solution of stable protein surrounded by its native lipids, held in place by an SMA copolymer band. We have recently applied this method to the purification of the facilitated glucose transporter GLUT1 (SLC2A1) in an effort to better characterize its structure, function, and potential ligand interactions. By

utilizing SMA, it is possible to extract the protein in its native, multimeric state, allowing for a better understanding of the endogenous structure of GLUT1, both in erythrocytes and HEK cells, as well as of potential mechanisms that may regulate oligomerization and kinetic activity.

For this effort, full-length human GLUT1 was isolated from Expi293 HEK cell membranes, and GLUT1/SMALPs were purified using a sepharose affinity column and SEC separation. Purified GLUT1/SMALPs were analyzed by SDS-PAGE silver stain, western blot, and transmission electron microscopy (TEM). MPs from RBCs were also solubilized using SMA, resulting in a heterogeneous solution of GLUT1, Band 3 (SLC4A1), equilibrative nucleotide transporter-1 (ENT1), monocarboxylate and several other associated proteins from the ankyrin and actin junctional complexes. This work was able to show a clear delineation between monomeric, dimeric, and tetrameric GLUT1 oligomers, each extracted directly from the RBC membrane. Additionally, this marks the first use of SMA to successfully isolate membrane proteins and their associated complexes from the membranes of a primary cell, highlighting the great potential for studying intact membrane complexes from their native environments.

### 4.3 Introduction

Glucose is the preferred metabolic substrate of most cells in the human body and a central component of energy homeostasis across all its tissues. In fact, an adult body might utilize as much as 300 g of glucose per day with the majority of this being consumed by the brain (Richter, 2010). Supporting this rate of consumption requires blood glucose concentrations to stay high, between 4-12 mM (Wright, 2009). This state is maintained through the combination of diet and internally regulated storage and mobilization by tissues such as liver and skeletal muscle (Wasserman, 2009). The importance of glucose in the human physiology is paralleled in countless other species, a phenomenon underscored by the highly conserved natures of glycolytic enzymes found in organisms across taxa, both modern and ancient (Romano and Conway, 1996). Considering this breadth of utility across the evolutionary landscape, it is not surprising to find glucose at the nexus of multiple anabolic and catabolic pathways. This dependence on glucose highlights the importance of connecting its supply with its demand. On its own, glucose is largely incapable of crossing the plasma membrane that partitions the cell from its surroundings (Wood and Morgan, 1969). Specialized transmembrane enzymes are needed to facilitate the transport of glucose from one side to the other. There are several families of proteins that can catalyze this action (Pao *et al.*, 1998), but of highest

prevalence, and of particular relevance to this work, are the glucose transporters (GLUTs) (Jones *et al.*, 2000a; Stein, 1986).

In humans, the first member of the glucose transporter family, GLUT1, is expressed nearly ubiquitously throughout the body, though not always as the predominant sugar transporter in every cell type. It is the most prevalent transporter in blood-tissue barriers, certain cell types in the brain (such as astrocytes), cardiac smooth muscle, and red blood cells (RBCs) (Harik *et al.*, 1990; Mann *et al.*, 2003; Takata *et al.*, 1990). The study of GLUT1 function is the central historical strand of research into facilitated diffusion, both as a basic physiological phenomenon and enzymatic modality. Further, this research was greatly aided by the use of the erythrocyte as a model environment for investigation of glucose transport phenomena. A century ago, the first evidence of enzymatic catalysis playing a role in permeability of the human red blood cell to glucose was unknowingly being characterized as rates of translocation were found to be proportional to extracellular glucose concentrations (Ege, 1919). This trend in permeability was later characterized in greater detail (Bang and Orskov, 1937), though the possibility of simple diffusion wasn't ruled out until glucose exchange was shown to be inhibited by treatment with mercuric cyanide (Wilbrandt *et al.*, 1947). The use of the term "carrier" was later suggested (LeFevre, 1948) and the mechanism was theorized in specific detail several years after (Widdas, 1952). The high content of GLUT1 in human erythrocyte membranes facilitated the isolation and resuspension of the transporter in



liposomes, a feat which marked a great step forward in the isolated study of secondary active transporters (Hinkle *et al.*, 1976; Kasahara and Hinkle, 1977). The following decades saw great advances in the understanding of GLUT1 and the methodologies used to study it (Baldwin, 1992, 1993; Baldwin *et al.*, 1995; Cura and Carruthers, 2012; Mueckler and Thorens, 2013; Thorens and Mueckler, 2010). The use of erythrocytes as a prototype for studying solute transport laid the groundwork for their continued use to study the mechanisms and kinetics of glucose transport to this day. Revelations about the complexities of GLUT1 function and regulation have been linked to combinations of substrate binding as well as intra- and intermolecular interactions within and between enzyme subunits. Understanding these phenomena in greater detail will require further characterization of the structural basis for GLUT1 behavior and dynamics.

Recent crystallographic characterization of human GLUT family members has provided valuable insights into the structural conformations of the monomeric transporter. These studies have successfully isolated and characterized hGLUT1 and hGLUT3 in various conformations with and without bound substrates and inhibitors (Deng *et al.*, 2015; Deng *et al.*, 2014; Kapoor *et al.*, 2016) (PDB 5C65). When considered on its own, in isolation from other salient evidence, the data collected from these works allowed for the construction of a theoretical mechanism of the GLUT1 transport cycle. The culmination of this analysis is the proposal that GLUT1 functions as a monomer and facilitates transport as an alternating access carrier (Yan, 2017). The aforementioned model is founded on

one proposed previously to describe, in general, the action of carriers in the MFS superfamily whereby conformational changes reorient transmembrane helical bundles to allow for diffusion between an interior volume of the carrier and the intra- or extracellular solvent (Jardetzky, 1966). There is compelling evidence within the crystallographic work that the fundamental mechanisms of the GLUT1, GLUT3, and GLUT5 transporters are congruent with this model. The structural evidence reveals distinct molecular conformations progressing from unbound outward-open (Nomura *et al.*, 2015a) to substrate-bound outward-open (Deng *et al.*, 2015) to substrate-bound outward-occluded (Deng *et al.*, 2015) to substrate-bound inward-open (Deng *et al.*, 2014; Kapoor *et al.*, 2016) to unbound inward-open (Nomura *et al.*, 2015b). While these observations confirm the fundamental structural dynamics which facilitate the substrate translocating activity of the GLUTs, and GLUT1 in particular, they do not provide comprehensive elucidation of their catalytic landscape. In fact, there is overwhelming documentation of highly nuanced coordination and regulation of GLUT1 as both a monomer and a multimer. There is a wealth of biochemical and kinetic data which is incompatible with a simple alternating access carrier model and instead, strongly demonstrates that GLUT1 exists as a monomer, dimer, or tetramer. These statements are not intended to discredit the conclusions derived from the structural analysis of the enzyme, but rather to emphasize that they merely provide the foundation for further elaboration of the structural basis for the complex behaviors already being characterized by other methodologies.

Biochemical characterization of GLUT1 quaternary structure suggests that it can be found in one of three oligomeric states: monomeric, dimeric, or tetrameric. Size exclusion chromatography experiments using detergent-solubilized, purified GLUT1 have been used to show the enzyme as a monomer (Lundahl *et al.*, 1991) as well as dimer or tetramer (Hebert and Carruthers, 1991; Hebert and Carruthers, 1992). The higher order oligomers have been shown to be sensitive to reducing agents such as dithiothreitol (DTT). Detergent solubilization of GLUT1 in the presence or absence of DTT shows the dimer or tetramer to be the predominant form, respectively. This has been demonstrated by size exclusion chromatography (Hebert and Carruthers, 1992; Zottola *et al.*, 1995), freeze-fracture electron microscopy (Graybill *et al.*, 2006; Hinkle *et al.*, 1976), and dynamic light scattering (Graybill *et al.*, 2006). Transmembrane (TM) domain swapping between GLUT1 and GLUT3 to create chimeric proteins has revealed the sequence-specificity of tetramerization in GLUT1. GLUT3 exists primarily as a dimer while GLUT1 presents as a mixture of dimers and tetramers. However, the GLUT1 chimera with the TM9 from GLUT3 shifts to presenting as a dimer while GLUT3 containing GLUT1 TM9 shows evidence of tetramerization (De Zutter *et al.*, 2013).

Studies of the ligand and inhibitor-binding capacities of endogenously expressed, exogenously expressed, and purified GLUT1 protein have generated evidence supporting the theories of its conformational function and quaternary structure. Early analysis of purified GLUT1 showed that binding of exofacial and

endofacial inhibitors was mutually exclusive, lending credence to the idea that GLUT1 alternately, and exclusively, presents intra- and extracellular ligand binding sites (Baker and Naftalin, 1979; Gorga and Lienhard, 1981). The GLUT1 inhibitor cytochalasin B (CCB) binds to the intracellular face of the enzyme where it competes with substrate for access to the binding site (Basketter and Widdas, 1978). Incubation of purified tetrameric and dimeric GLUT1 with saturating concentrations of CCB show binding stoichiometries of 0.5 and 1.0 mol of CCB per mol GLUT1, respectively (Hebert and Carruthers, 1992). This supported the idea that GLUT1 tetramers present equimolar inward-facing and outward-facing binding sites in obligate anti-parallel conformations while subunits of the GLUT1 dimer do not restrain each other in this manner (Hebert and Carruthers, 1991). There is also significant kinetic data supporting the oligomerization of GLUT1 subunits and suggests complex allosteric regulations imposed by these interactions. Both *cis*- and *trans*-allostery can be demonstrated using exo- and endofacial inhibitors at concentrations far below their respective  $K_i$ 's. The phenomenon of *cis*-allostery is observed when non-substrate binding affects the kinetics of substrate-enzyme interactions on the same side as its binding, while *trans*-allostery is observed when non-substrate binding effects substrate binding on the opposite side of the enzyme. Exofacial *cis*-allostery is observed when maltose, a non-transportable disaccharide which competes with glucose for binding to the outward-open conformation, is used at very low concentration. Under these conditions, the uptake rate of glucose by GLUT1 is accelerated

rather than inhibited (Hamill *et al.*, 1999). Endofacial *cis*-allostery is observed in a similar manner using CCB or forskolin (Cloherty *et al.*, 2001; Robichaud *et al.*, 2011). *Trans*-allostery can be observed when an intracellular inhibitor (e.g., CCB or forskolin) enhances the uptake of extracellular sugars (Cloherty *et al.*, 2001). More recently, analysis of both the GLUT1 crystal structure and homology modeling revealed glutamine 282 to be an important residue in the binding of transporter substrates. By combining this mutation with the substitution of TM9 from GLUT3, kinetic analysis of *cis*- and *trans*-allostery showed that *cis*-allostery depends on glutamine 282 while *trans*-allostery depends on TM9. This means that *cis*-allostery is a function of intramolecular interactions while *trans*-allostery is dependent on oligomeric structure (Lloyd *et al.*, 2017). Together, these studies demonstrate that the structural and conformational basis for GLUT1 function is homologous with the simple alternating access model. That is, each GLUT1 monomeric subunit acts as a functional alternating access carrier. However, GLUT1 oligomerization gives rise to more complex allosteric behaviors.

Another notable observation pertaining to the GLUT1 structure/function relationship is the difference in glucose transport that exists between ATP- and AMP-containing RBC ghosts. The overall topology of RBC ghosts is impacted by the presence or absence of ATP upon resealing, resulting in either a traditional diskocyte form (+ATP) or a spiky, more spherical shape known as an echinocyte (-ATP) (Figure 4.1). There is biochemical evidence that glucose transport regulation may involve ATP-dependent conformational changes (Blodgett *et al.*,

2007), as evidenced by GLUT1's protection against tryptic digest across multiple domains when ATP is present. This finding, coupled with measured differences in glucose transport kinetics for the two RBC ghost morphologies, suggests that ATP may play a regulatory role in GLUT1 allostery and enzyme kinetics.

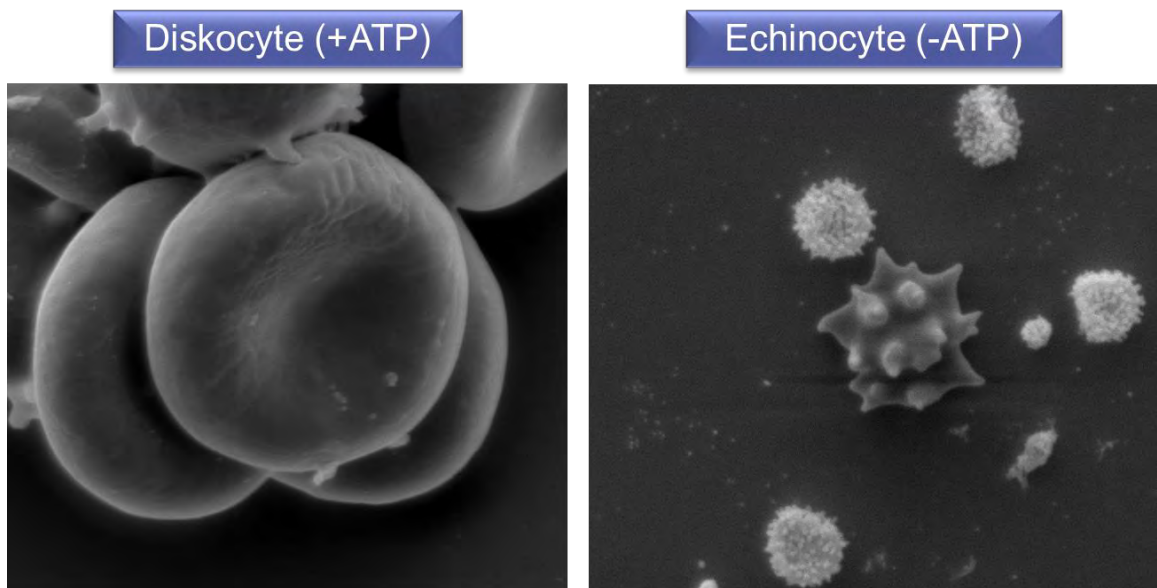


**Figure 4.1** The morphology of resealed red blood cell ghosts is impacted by the presence or absence of ATP. When RBC ghosts are resealed to contain ATP, they take on a diskocyte shape (left), however if ATP is excluded or ADP/AMP is added, the cells reform into echinocytes when resealed (right). Magnification is 34,982x (left) and 5000x (right).

There is considerable value in understanding how GLUT1 conformational changes may occur in the presence of ATP, and how GLUT1 interacts with (and may rely on) other erythrocyte MPs for oligomerization and transport. Of course, as is true for many transmembrane channels and carriers, there would be a clear

advantage to studying a more physiologically-relevant structural model than one whose environment is disrupted by the use of detergents for solubilization, as with the current high resolution structure of GLUT1.

The recent development of styrene/maleic acid lipid particles (SMALPs) as an alternative to detergent purification of integral membrane proteins (IMPs) offers a valuable tool for structural and functional analysis of, as well as drug discovery efforts focused on, proteins like GPCRs and ABC transporters. In lieu of separating out such a protein from its surrounding lipid bilayer and associated proteins using detergents, this method takes advantage of the amphipathic properties of SMA to extract IMPs directly from the membrane. The result is a monodisperse solution of stable protein surrounded by its native lipids, held in place by an SMA copolymer band. We have recently applied this method to the purification of GLUT1 in an effort to better characterize its structure, function, and potential ligand interactions. By utilizing SMA, it is possible to extract the protein in its native, multimeric state, allowing for a better understanding of the endogenous structure of GLUT1, both in erythrocytes and HEK cells, as well as of potential mechanisms that may regulate oligomerization and kinetic activity.

For this effort, full-length human GLUT1 was isolated from Expi293 HEK cell membranes, and GLUT1/SMALPs were purified using a sepharose affinity column and SEC separation. Purified GLUT1/SMALPs were analyzed by SDS-PAGE silver stain, western blot, and transmission electron microscopy (TEM).

MPs from RBCs were also solubilized using SMA, resulting in a heterogeneous solution of complexes containing GLUT1, Band 3 (SLC4A1), Equilibrative Nucleotide Transporter-1 (ENT1) and Monocarboxylate Transporter 1 (MCT1), among other erythrocyte MPs. These experiments were able to confirm several hypotheses about basic GLUT1 quaternary structures that had been, until now, never directly observed. These results clearly demonstrated that GLUT1 oligomersexists naturally in the RBC membrane as monomers, dimers, and tetramers. This is important to the study of GLUT1 transport mechanism as several kinetic theories rely on the existence of these multimers in order to explain some of the more complicated transport phenomena previously observed.



## 4.4 Results

### 4.4.1 SMA solubilization and purification of GLUT1 oligomers from Expi293F™ expression cells

Initial GLUT1 solubilization and purification was performed using the Expi293 cells as a proof-of-concept. I based the starting protocol on my work purifying CFTR-SMALPs, with little modification made. A schematic of the protocol is seen in Figure 4.2. The result of this treatment should be the isolation of GLUT1, GLUT1 oligomers, and their associated proteins as integral proteins within SMA-solubilized membrane discs. An example of one such disc is shown in Figure 4.3.

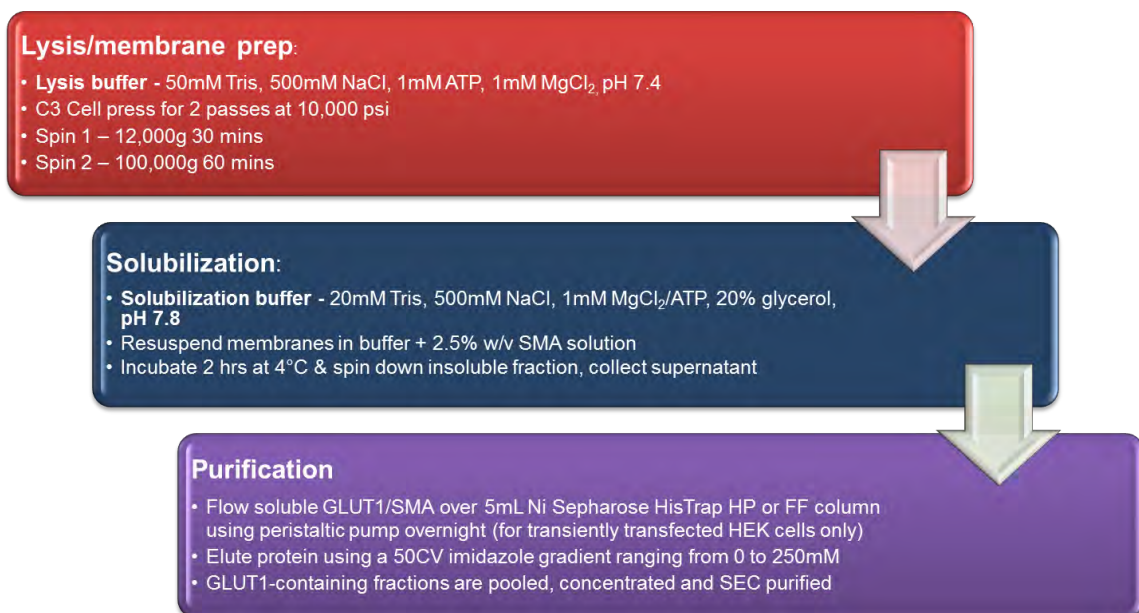


**Figure 4.2 Overview of the protocol for SMA purification of hGLUT1 from Expi293 cell membranes**

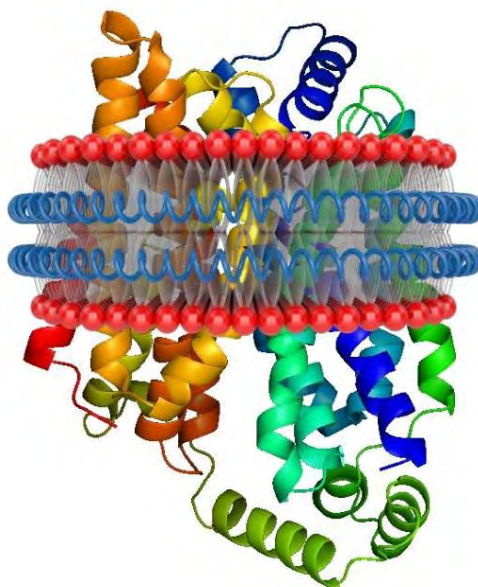


**Figure 4.3 Cartoon schematic of full-length, monomeric GLUT1 in a SMALP.** Glucose transporter GLUT1 can remain in its lipid bilayer while being held in place by an SMA copolymer (blue coil). Crystal structure of monomeric GLUT1 was generated by Deng, *et al.* (Deng *et al.*, 2014). SMALP illustration was produced by Ashley Souza.

As outlined previously for CFTR, Expi293 cells are grown at  $2.0 \times 10^6$  vc/mL under the following conditions: 37 °C, 8% CO<sub>2</sub>, 80% humidity in a rotating platform incubator set to 125 rpm. Cells are transfected with 1 µg/mL of 10x-His-tagged hGLUT1 plasmid DNA and grown for ~48 hours or until viability drops to 90%, at which point the cells are collected using traditional centrifugation methods. Cell pellets are washed with cold PBS containing protease inhibitors, pelleted, and snap-frozen for future use. To prepare the membrane fraction for hGLUT1 solubilization, cells are lysed using a C3 cell press for two passes at 10,000 PSI. The resulting cell lysate is then spun down at 12,000 xg for 30 mins

to remove large cell debris, and the supernatant containing the membrane fraction is spun at 100,000 xg for 1 hour. Membranes are then resuspended into solubilization buffer using a Dounce homogenizer, and an equal volume of 5% SMA polymer resuspended in the same buffer is added to the suspension for a final polymer concentration of 2.5% w/v. SMA solubilization is carried for 2 hours at 4 °C with end-over-end rotation of the solution. After two hours, the suspension is again spun at 100,000 xg for an hour, and the supernatant containing C-terminal 10xHis tagged GLUT1-SMALPs is collected and captured on a Ni-Sepharose HP column by continuous flow over the column for about 18 hours. The following day the column undergoes extensive washing, and GLUT1-SMALPs are eluted with increasing amounts of imidazole. Fractions that are eluted with 100 and 250 mM imidazole are pooled and concentrated to facilitate injection into a size-exclusion column for further purification. At both the imidazole elution and SEC column elution steps, fractions are collected and analyzed via SDS-PAGE silver stain and western blotting for hGLUT1 (Figure 4.4).

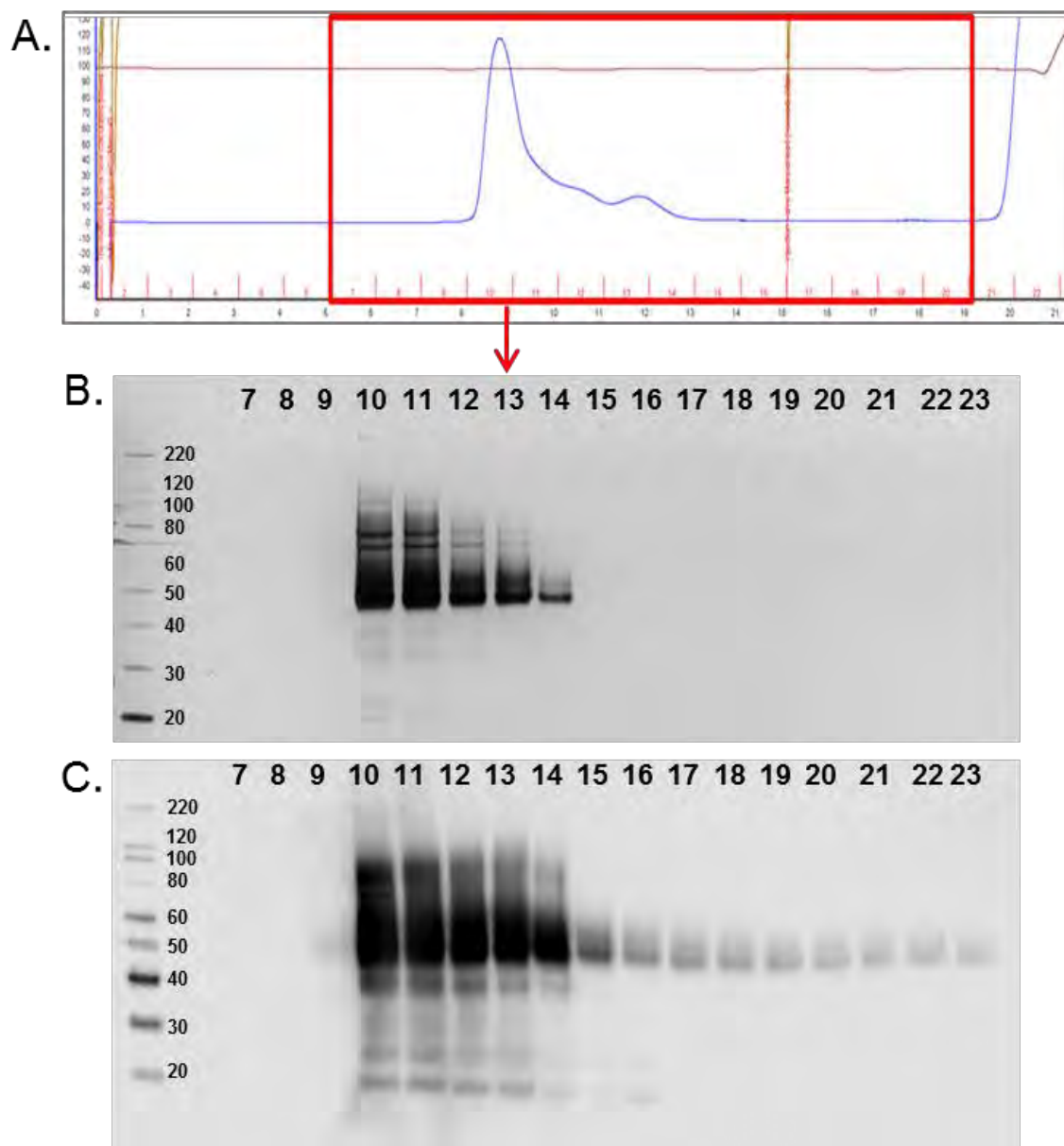


**Figure 4.4 SEC chromatogram of hGLUT1-SMALP purification and fractionation (A), SDS-PAGE Silver stain gel (B) and western blot (C) of SEC purified hGLUT1.** Fractions 10-14 contain full-length GLUT1, confirmed by western blotting. For immunoblotting of GLUT1, EMD-Millipore anti-GLUT1 rabbit polyclonal antibody was used at 1:1000.

#### **4.4.2 GLUT1 oligomerization detection using Native PAGE**

After fractions were separated on the reducing SDS-PAGE gel, they were separated out using the Native PAGE protocol suitable for separation of SMALPs. When GLUT1-SMALPs were loaded onto the gel intact, material in fractions 11-14 separated into three distinct sizes. It appears that the material in fraction 10 and some of fraction 11 may have been aggregated and did not run properly through the gel, as evidenced by the lack of signal in those lanes on the western blot. Additionally, there is a higher molecular weight species above the tetramer bands. While it is possible this indicates an even higher oligomeric state for GLUT1, it would have to be associated in such a way as to completely mask the epitope for the antibody used in the Western blot. Additionally, the band has much sharper boundaries than usually observed in GLUT1 blots due to the highly variable glycosylation patterns that often cause GLUT1 to run in a more diffuse manner.

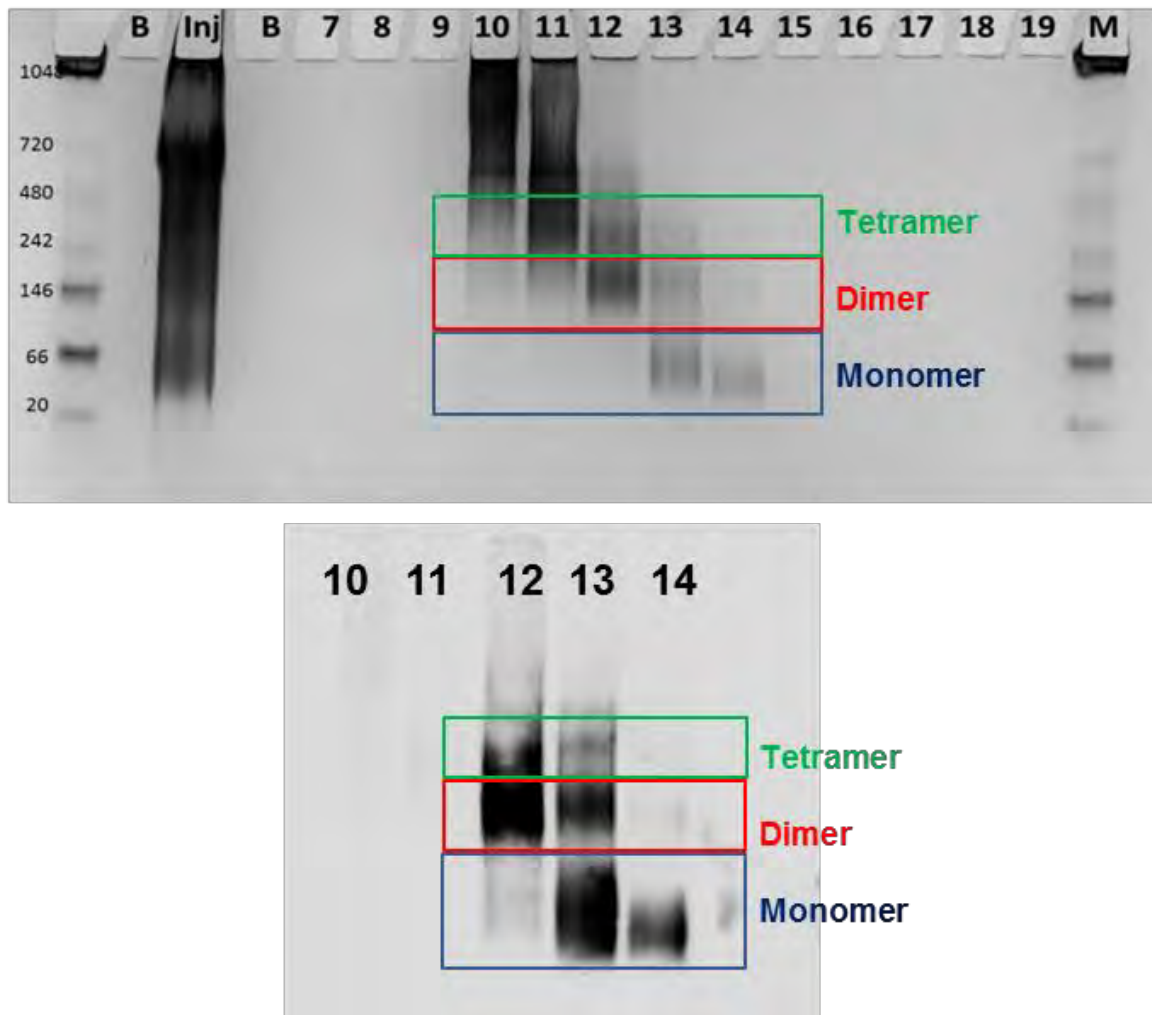


**Figure 4.5 Native PAGE Silver stain (top) and western blot (bottom) of SEC purified GLUT1 fractions.** Protein from SEC fractions 10-14 appear to separate on a Native PAGE gel into 3 potential oligomerization states. This protein is confirmed as GLUT1 through immunoblotting.

Negative stain TEM analysis of each fraction was performed, and showed monodisperse lipid discs of somewhat variable size. The diameters range from ~10 nm to ~14 nm when measured. A micrograph of fraction 13 can be seen in Figure 4.6.



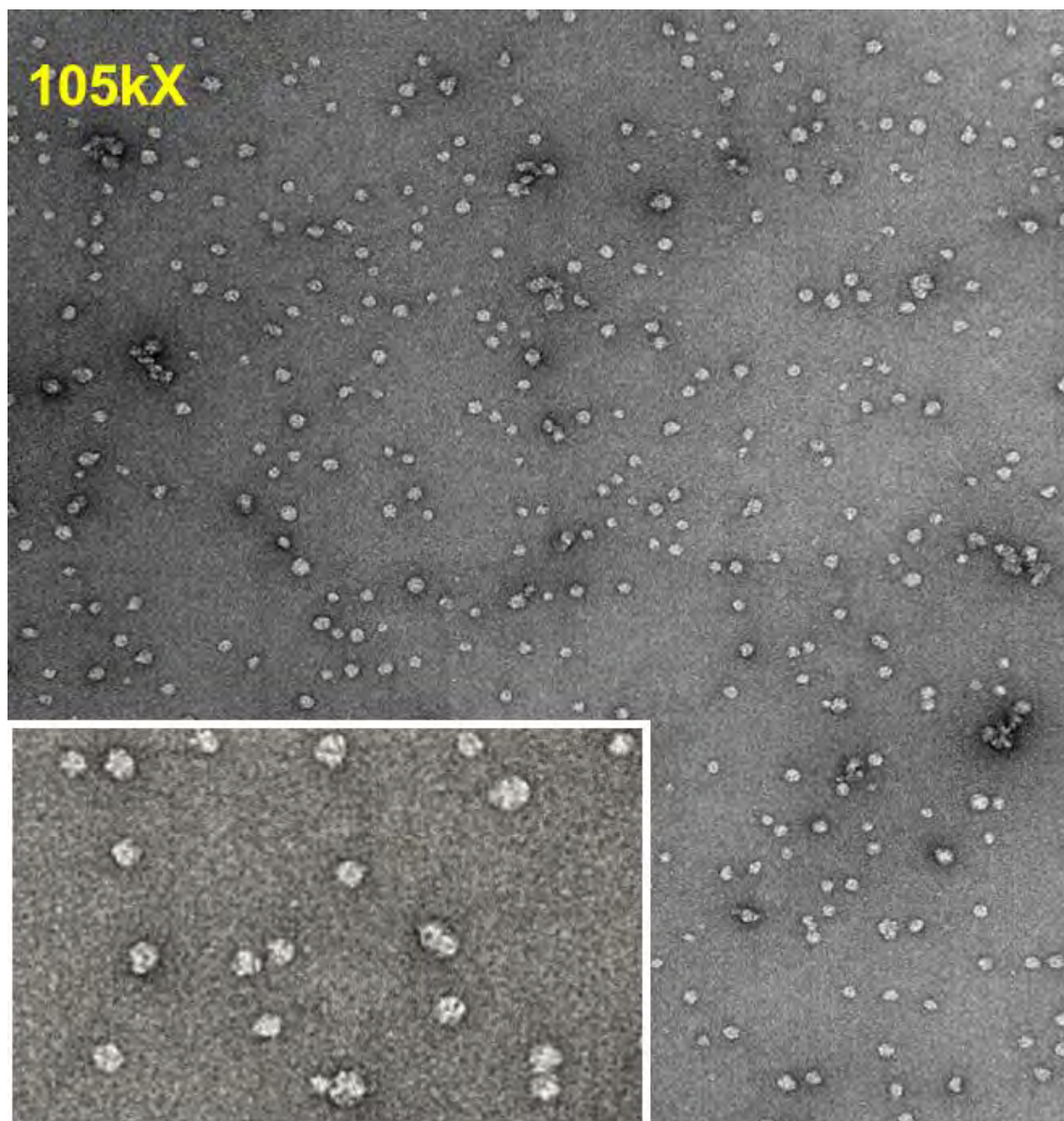


**Figure 4.6** TEM analysis of hGLUT1-SMALPs, fraction 13. Samples were stained with 1% uranyl acetate and analyzed using an FEI Tecnai Spirit 12 (120kV). The enlargement is included to show the slight variation in particle diameter.

Proteomic analysis of fractions 10-14 via mass spectrometry definitively shows GLUT1 (SLC2A1) in all samples and high levels of Hsp70 (HSPA1B) in each fraction.

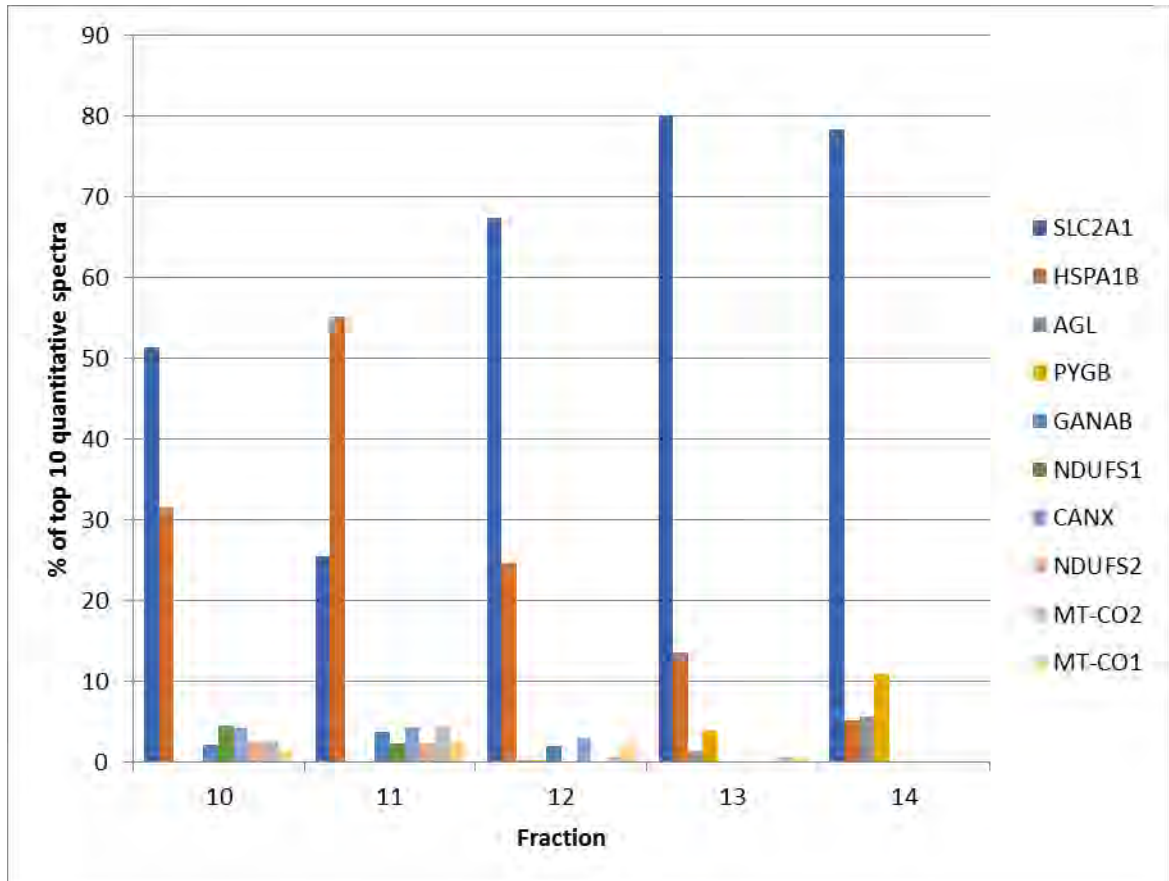


**Figure 4.7 Quantitative comparison of the top ten most prevalent proteins in GLUT1-SMALP fractions** (the top 10 protein represent 50% (10), 68.8% (11), 81.3% (12), 93.75% (13) and 92.5% (14) of each fraction. In all except fraction 11, GLUT1 comprises the majority of detected proteins with Hsp70 in high abundance as well.



The hGLUT1-SMALP purification from Expi293 cells has been repeated several times, and in all cases, the same three-tiered separation is seen when fractions are separated out under Native PAGE conditions (Figure 4.8).

**Fraction B6 B7 B8 B9 B10 B11 B12 C1 C2 C3**

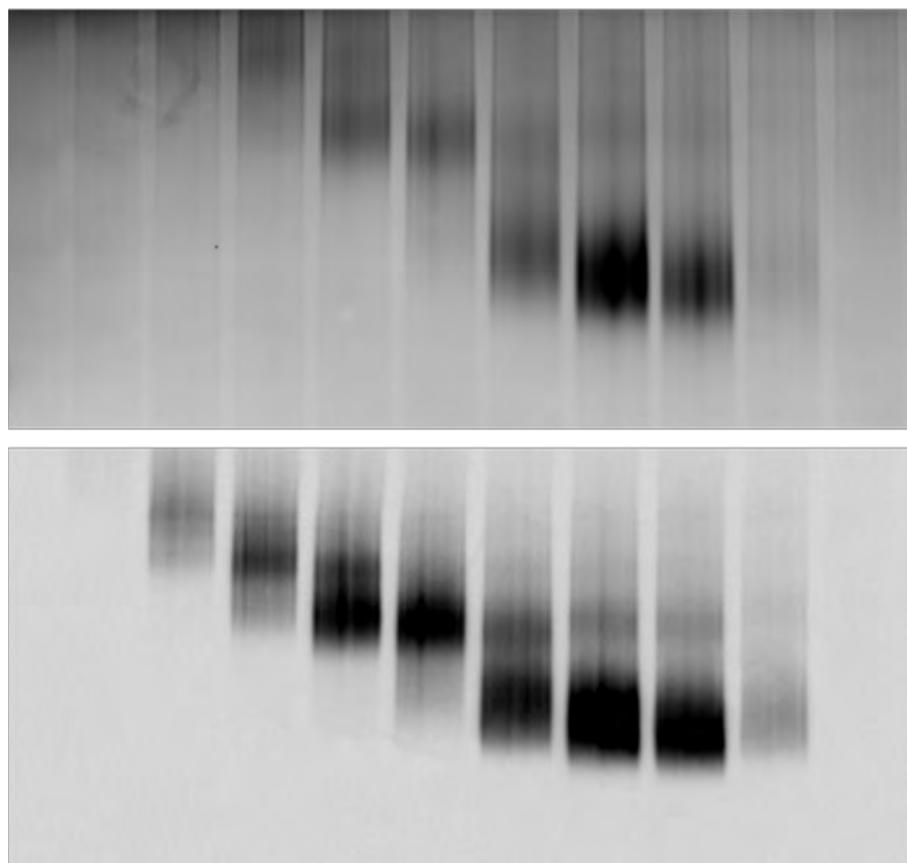


**Figure 4.8 Native PAGE Silver stain (top) and western blot (bottom) of SEC purified GLUT1 fractions.** The purified GLUT1 protein fractions display three distinct native sizes when separated out under non-denaturing conditions. The majority of the protein appears to elute in later fractions B11-C1, most of which migrates as monomeric GLUT1. Fractions B9 and B10 appear to consist mostly of dimeric GLUT1, and B8 and B9 contain tetrameric GLUT1. B7 is likely aggregated protein that did not migrate properly through the gel.

#### **4.4.3 SMA solubilization and purification of untagged GLUT1 oligomers from erythrocyte membranes**

Once GLUT1 purification from Expi293 cells using SMA had been characterized, we applied this method to erythrocyte membranes. When purifying GLUT1 from RBC membranes, a non-specific collection of membrane proteins and associated binding partners was collected due to lack of an affinity tag. However this provided the opportunity to look for associations with GLUT1 and understand its native state with regard to erythrocyte complexes.

For this work, red blood cells were collected fresh and membranes were thoroughly washed to remove all traces of iron (a divalent cation) which could potentially interfere with SMA solubilization. Similar to the Expi293 protocol, SMA was added to the membrane prep at a final concentration of 2.5%. One observation that I noted was the significantly different rates of solubilization between RBC ghosts (images of pellets) and Expi293 HEK cell membranes. While the HEK cell membranes require a minimum of two hours to solubilize, the solution containing RBC membranes clarified within 120 seconds of SMA addition, symbolizing near complete solubilization of the membranes. The resulting pellet after ultracentrifugation was perfectly clear, suggesting that all that remained was the cytoskeleton (Figure 4.9 and Figure 4.10).

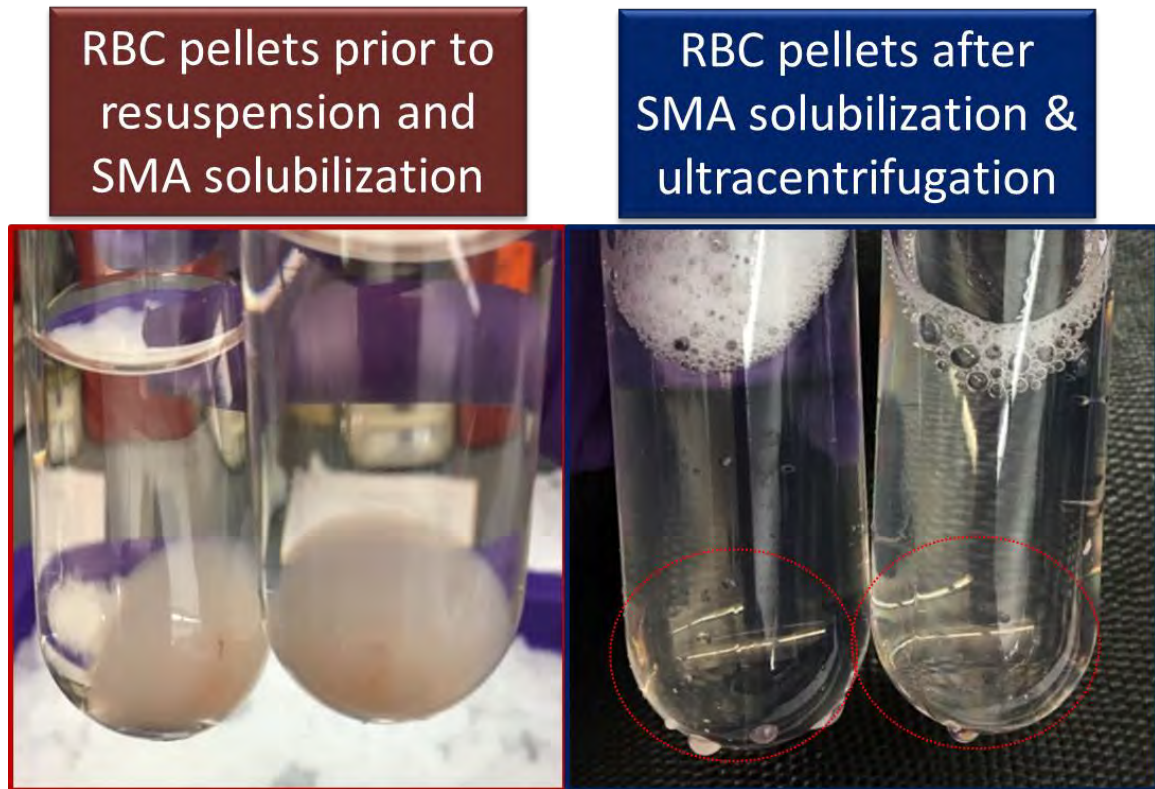


**Figure 4.9 RBC membrane pellets before and after SMA solubilization.** Prior to solubilization (left), RBC membrane pellets appear opaque. Pellets are resuspended in 2.5% SMA and within 60 seconds the solution has completely clarified, indicating membrane solubilization. After a 1 hour ultracentrifugation, the remaining pellets appear glassy, and are likely comprised of the cytoskeletal remains that are visible in SEM micrographs after RBC treatment with SMA.

In the hopes of visualizing this process, we performed scanning electron microscopy (SEM) on both unsealed and sealed RBC ghosts to determine whether the solubilization rate was dependent upon access to both sides of the membrane (i.e., whether it was a reflection of the different compositions of the erythrocyte phospholipid bilayer). The outer membrane leaflet of an erythrocyte contains uncharged, choline containing lipids while the inner leaflet primarily

consists of charged phospholipids. What we observed is that whole cell membranes and membrane fractions (or in this case, unsealed ghosts) both appear to solubilize with the same rapid pace, leaving behind the cytoskeletal infrastructure of the cell (Figure 4.10). This was observed in RBC ghosts resealed with either AMP (Figure 4.11) or ATP (Figure 4.12) with extensive membrane solubilization seen within 30 seconds in both cases. Additionally, we observed differences in the physical changes to RBC ghost membranes during solubilization done using SMA versus those done using Triton. When SMA is the solubilizing agent, membranes in the process of transitioning into the soluble fraction appear textured in a granular pattern while those in the presence of Triton show twisting invaginations of the membrane (Figure 4.12). Neither the cause nor consequence of this difference is characterized further in this work, but does suggest a fundamental difference in the processes employed by each chemical.

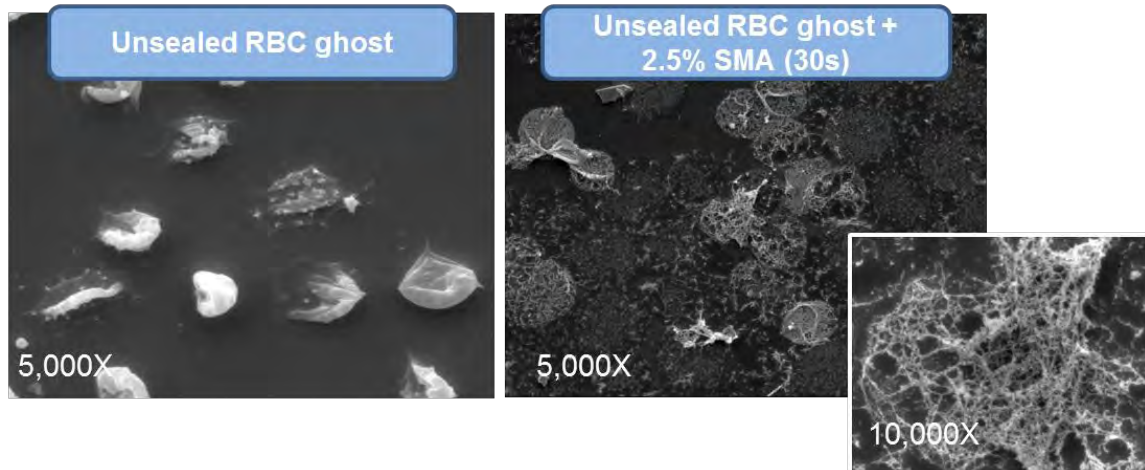


**Figure 4.10** Unsealed RBC ghosts untreated (left) and treated with 2.5% SMA solution for 30 seconds (right). A magnified view of the right panel can be seen at 10,000x magnification. After membranes are incubated with SMA, only cytoskeleton remains, highlighting the rapid nature of SMA solubilization of erythrocyte membranes. Samples are fixed with 2.5% glutaraldehyde solution before evaluation using SEM.

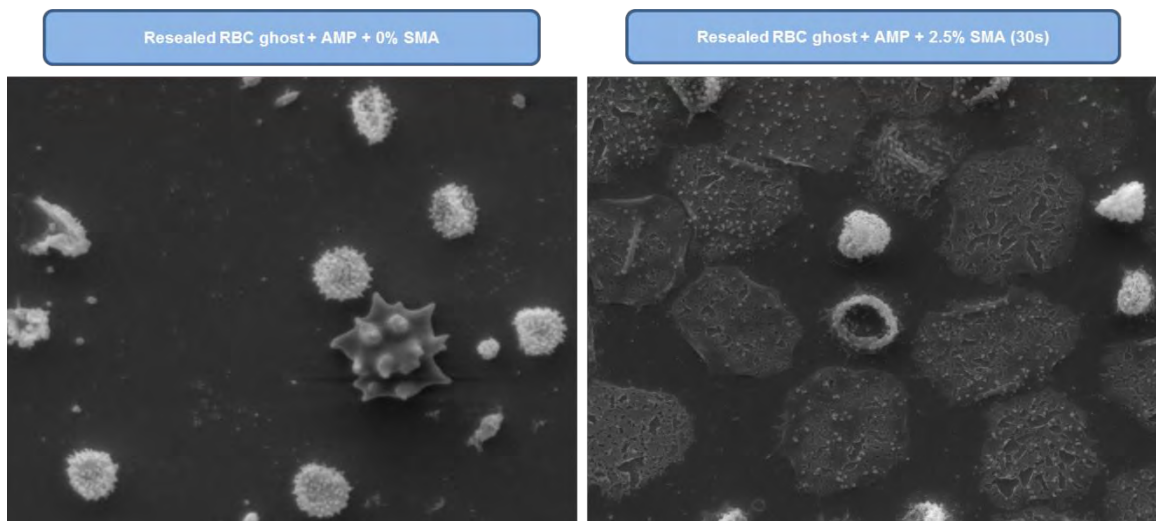


**Figure 4.11** AMP-containing resealed RBC ghosts in the echinocyte morphology, untreated (left) and treated with 2.5% SMA solution for 30 seconds (right). NO differences are seen between solubilization of diskocyte and echinocyte solubilization rates when SMA is added at 2.5% w/v. Samples are fixed with 2.5% glutaraldehyde solution before evaluation using SEM. Magnification is 5000x in both panels.

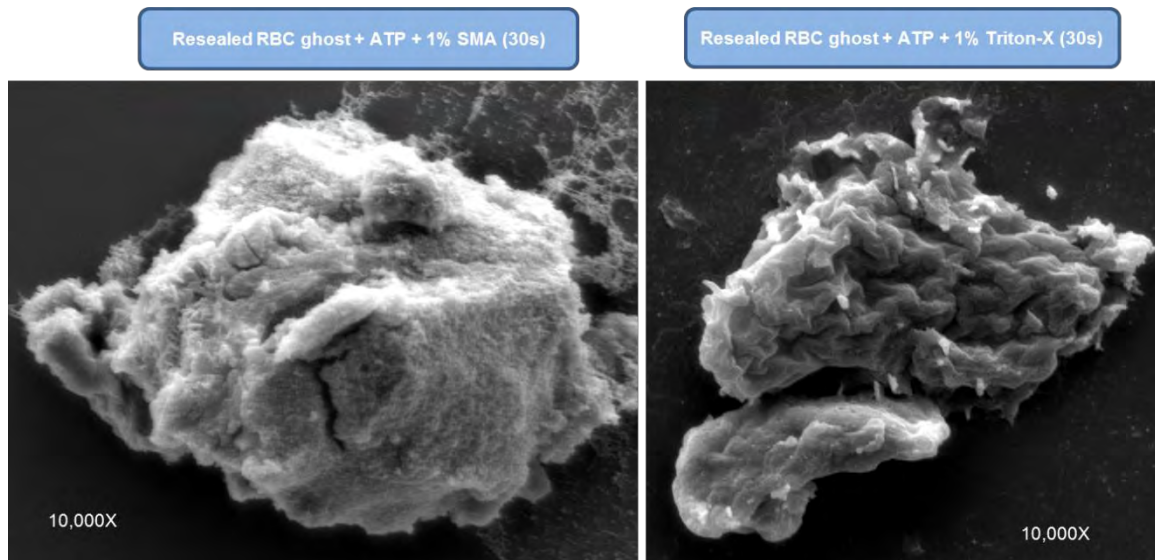


**Figure 4.12** Resealed RBC ghost + ATP treated with 1% SMA for 30 second (left) and treated with 1% Triton-X for 30 seconds (right). To ensure the pattern of membrane solubilization was the result of SMA addition, control samples were evaluated after treatment with 1% Triton-X for 30 seconds. Samples are fixed with 2.5% glutaraldehyde solution before evaluation using SEM.

Once the kinetics of erythrocyte solubilization had been determined, we performed an experiment to determine whether SMA solubilization could be used as a means for detecting differences in GLUT1 and Band3 oligomerization in RBCs as a reflection of cytoskeletal dynamics using known actin modulators.

Extensive cross-linking data has shown that in erythrocytes, GLUT1 associates with other transmembrane glycoproteins such as anion exchanger Band 3, glycophorin-C, structural maintenance protein 4.1, (Rungaldier *et al.*, 2013; Takakuwa, 2000; Takakuwa and Manno, 1996) and aquaporin, to name only a few. These proteins are largely reliant on erythrocyte cytoskeletal and

support proteins such as stomatin and actin to maintain such heteromultimeric complexes. By modulating actin filament formation and degradation, we hoped to utilize the native solubilizing properties of SMA to capture changes in protein associations as a function of actin remodeling. To effect this change, the following compounds were used:

- i. Latrunculin-A – destabilizes and depolymerizes dynamic actin filaments by binding to and sequestering monomers
- ii. Jasplakinolide – stabilizes dynamic actin filaments

Cells were incubated at 37 °C for four hours with Latrunculin A (5 µM), Jasplakinolide (2.5 µM) or ATP + DMSO as a control, after which time the cells were spun down, lysed, and washed extensively to remove all hemoglobin so as to avoid disruption of SMA solubilization with the presence of  $\text{Fe}^{2+}$ , a divalent cation. Of note, it was more challenging to lyse the red blood cells that had been treated with Jasplakinolide, and more extensive washing was required before the membrane pellet appeared sufficiently clear to begin solubilization.

Membrane fractions were treated with 2.5% SMA w/v and incubated at RT for about 30 minutes (complete clarity of the solution again occurred within minutes), and the suspension was ultra-centrifuged for one hour to remove excess membrane fraction and cytoskeleton. Each sample was then concentrated and spun down at 10,000 xg for 10 minutes to remove any aggregation that formed during concentration. The supernatant was then



separated over a size exclusion column and fractions were collected for analysis (Figure 4.13).

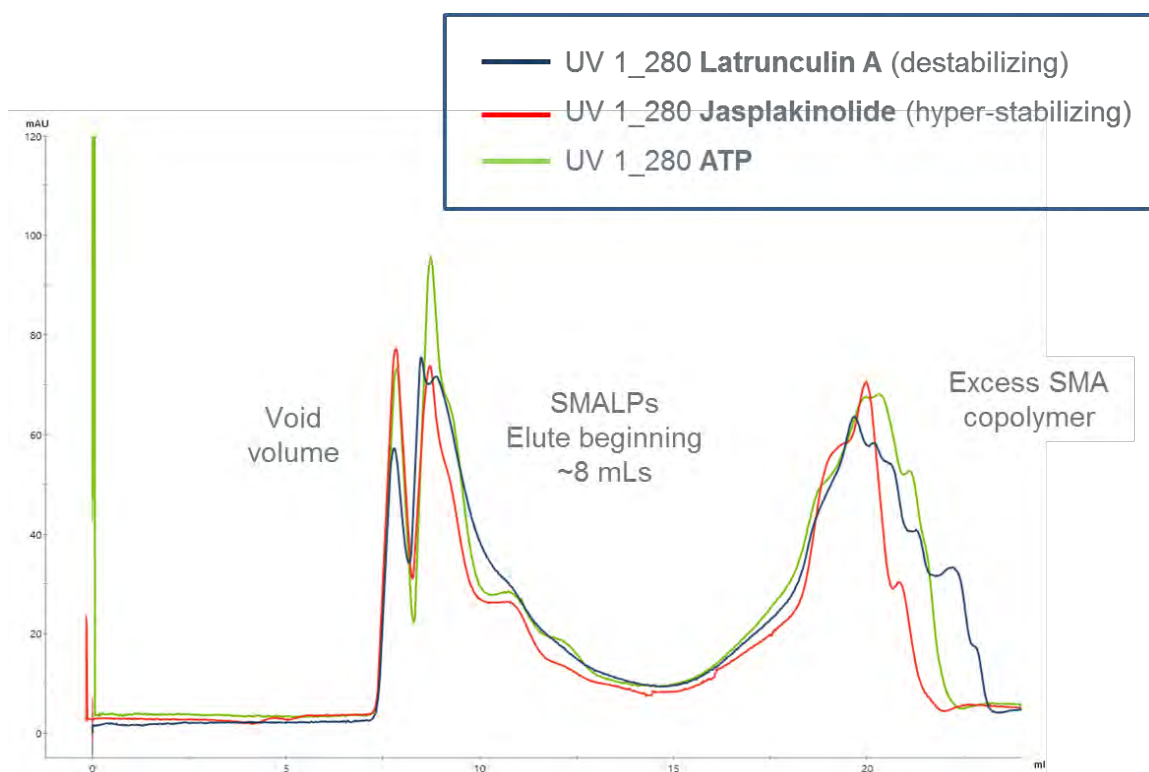


**Figure 4.13 SEC traces show potential differences in elution profile of RBC SMALPS after treatment with actin modulators.** Whole RBCs were incubated with actin modulators Latrunculin A or Jasplakinolide, or with ATP. Membranes were then subject to solubilization with 2.5% SMA and the resulting solubilized proteins were separated out on size exclusion chromatography. The profile for the control group (green line) shows a major elution peak at about 9.5 mLs. When cells are treated with actin stabilizer Jasplakinolide (red line), which is expected to increase protein complex size at the membrane, the elution of higher MW species occurs earlier, and a slightly larger peak is seen at 9 mLs. When cells are treated with actin destabilizer, Latrunculin A (blue line) the membrane protein complexes elute slightly later, suggesting the presence of smaller, potentially destabilized protein complexes.



To evaluate changes in membrane protein complex oligomerization due to actin remodeling, elution patterns of GLUT1 and Band 3/Anion exchanger 1 (SLC4A1) were evaluated by immunoblotting after Native PAGE separation.

Changes in BAND3 and GLUT1 immunoblotting profile suggest that an impact was made on membrane protein complex oligomerization due to treatment with actin remodeling agents (Figure 4.14). When Native PAGE gels of each sample were run and immunoblotting was performed for GLUT1 and Band3, earlier fractions showed more substantial levels of Band3 expression, whereas GLUT1 appeared to elute in the second half of the fractions, and banding pattern was distributed between two tiers of separation. However, after Latrunculin-A treatment, both Band3 and GLUT1 bands appear to elute both earlier and later than the untreated sample. Additionally, they migrate lower on the Native PAGE gel, suggesting that some level of dissociation had occurred in the associated complex. In contrast, the addition of actin hyper-stabilizing agent, Jasplakinolide, appeared to cause an increase in the size of banding patterns associated with GLUT1 and Band3, potentially causing an increase in the level of heteromultimeric complexes that were solubilized with SMA. Aquaporin and Equilibrative Nucleoside Transporter-1 (ENT1) were also detected in these samples; however, no major changes were seen to their relative location on the blot (data not shown). Interestingly, when these samples are run on a reducing SDS-PAGE gel, the three sizes of GLUT1 as well as distinctions between banding patterns in each treatment group are no longer observed. This is likely

because the SDS treatment disrupts protein-protein interactions and dissociates the SMALP structures so that differences in quaternary structure, both normal and pharmacologically-induced, are homogenized and no longer resolvable.

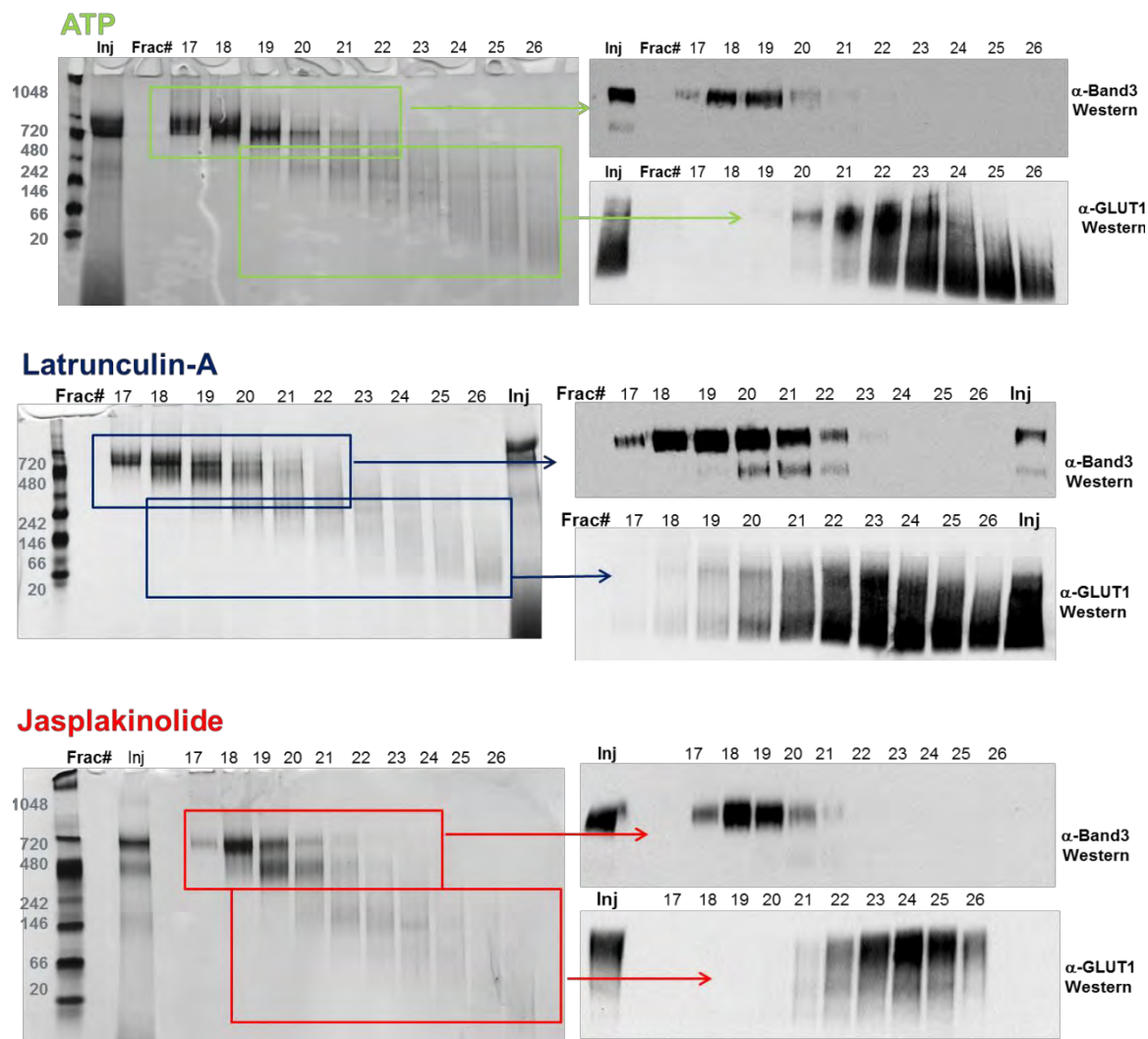


**Figure 4.14 SMA extraction of RBC membrane proteins** after four-hour whole-cell treatment with Latrunculin A (5  $\mu$ M) and Jasplakinolide (2.5  $\mu$ M) was performed. Thoroughly washed membranes underwent SMA solubilization, and the material was purified on a *Superdex 200 increase 10/300 SEC* column. The resulting fractions were evaluated using SDS-PAGE (data not shown) and Native PAGE. Differences in GLUT1 and Band3 oligomerization could be seen with silver stain and western blotting; however, no differences were seen between treatment groups when the fractions were run on a reducing SDS-PAGE gel and oligomers were dissociated prior to separation.

## 4.5 Discussion

Using SMA, we have developed a method for isolating highly enriched, monodisperse and stable GLUT1 from mammalian cells, both cultured and primary. By first developing the protocol for GLUT1 purification from a human expression cell line, I was able to demonstrate the ability to isolate the protein in different oligomeric states and separate out the three distinct forms (monomer, dimer and tetramer) using Native PAGE separation. We believe this is the first evidence of oligomeric GLUT1 that has successfully been separated out using PAGE. Purified GLUT1 from HEK cells provided great utility as a first-pass proof-of-concept for GLUT1 oligomeric solubilization, and may provide opportunities to evaluate small molecule ligand binding to the protein in its different oligomeric states.

I then adapted the protocol for GLUT1 isolation and purification to red blood cell membranes for the total solubilization of RBC membrane proteins. Our initial observation was that the lipid content of RBCs makes them particularly amenable to SMA solubilization, as complete disintegration of the lipid bilayer occurs within 30 to 60 seconds (as seen in SEM images) after resuspension in a 2.5% w/v SMA solution. Because the proteins being solubilized are not expressed with an affinity tag, it was necessary to separate out the different elements using gel filtration over a Superdex 200 increase 10/300 SEC column. By collecting each eluting fraction and analyzing on a

Native PAGE gel, it was possible to identify the presence of several MPs that co-eluted with GLUT1, including several members of both the Ankyrin complex and the Actin Junctional complex (Lux, 2016).

In addition to confirming information about GLUT1 and its associated proteins in erythrocyte membranes, this approach offers a means of obtaining large amounts of MPs for use in drug discovery studies such as the aforementioned ligand binding studies. Because proteins like GLUT1 and Band 3 exist in very high quantities within the lipid bilayer of erythrocytes, there is an opportunity to purify much more protein with much less expense of both time and money. Of course, this protein would lack affinity tags so the preparation step of gel filtration SEC would require some level of qualification before you would arrive at a sample you could characterize reliably.

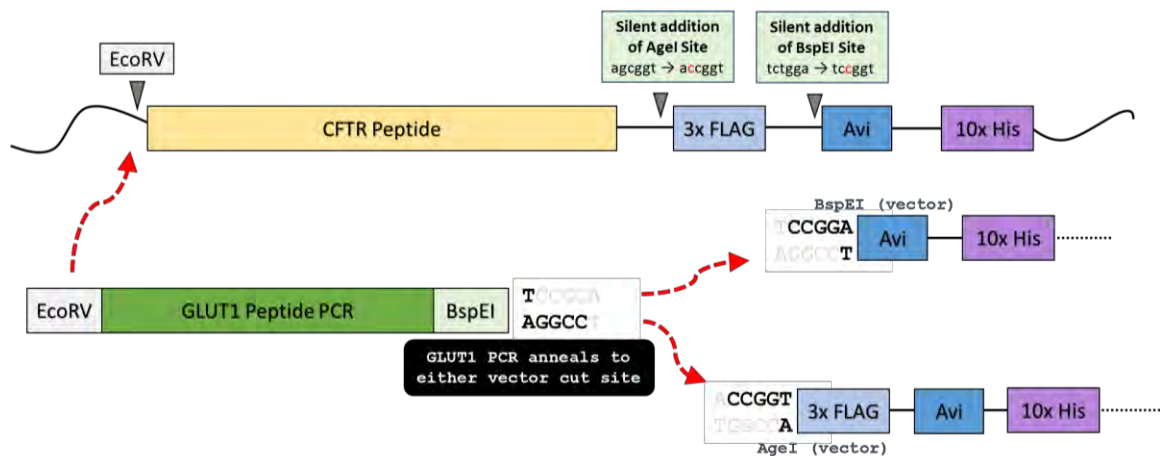
Lastly, the work outlined in this chapter represents the great potential for SMALPing more complex primary human tissue. This provides a means of obtaining mutant proteins expressed in low abundance, a resource that could prove very valuable to rare disease drug discovery efforts.

## 4.6 Materials and Methods

### Protein expression and purification

#### *Cloning of GLUT1 expression cassette*

To develop the human GLUT1 expression plasmid for transiently transfecting Expi293 cells, we used the WT-hCFTR plasmid containing FLAG, 10xHis and Avi-purification tags as a parent construct. Because no restriction sites were available to remove the CFTR peptide sequence from the C-terminal series of tags, two silent mutations were added to create cut sites upstream of FLAG and Avi. Silent addition of AgeI site (agcggg → accggg). Silent addition of BspEI Site (tctgga → tccggg). Because the overhanging ends of BspEI and AgeI are compatible, either site can be used to clone in the GLUT1 peptide from PCR primers with added EcoRV and BspEI sequences.



***Expi293 hGLUT1 transfection***

Expi293F cells (cGMP banked, Cat# 100044202) were seeded in 1 liter Erlenmeyer vented cap flasks at a density of 2e6 viable cells (vc) per mL with a final seeding volume of 250 mL in Expi293 Expression Medium (Gibco Cat# A1435101). Cells were then transfected using the ExpiFectamine 293 Transfection Kit (Cat# A14524) as follows. A total of 200 µg of hGLUT1 expression plasmid DNA was added to 5 mL of OptiMEM medium (Cat# 31985070) and 540 µL of ExpiFectamine to a second 5 mL volume of OptiMEM. The two solutions were mixed and cells placed in a 37 °C incubator. Approximately 16-18 hours post-transfection, enhancers 1 and 2 were added from the ExpiFectamine reagent kit. Viability and density of cells were checked 48 hours post-transfection and cells that had fallen below 95%, viability were collected. Otherwise, cells were collected 72 hours post-transfection by centrifugation at 1850 xg for 10 minutes, washed with cold PBS + protease inhibitors, then pelleted again. Pellets were then weighed and flash-frozen.

**Styrene maleic acid solubilization of hGLUT1 from Expi293F cells**

This protocol was scaled for purification of hGLUT1-His10 from a 6L culture of transfected Expi293F HEK cells. All steps were performed in a 4 °C cold room or on ice.

### *Lysis*

Fresh lysis solution was prepared by adding EDTA-free protease inhibitor tablets to 200 mL of resuspension buffer (50 mM Tris, 500 mM NaCl, pH 7.8). Cells were harvested from culture by centrifugation at 2620 xg for 10 minutes or frozen cell pellets were thawed on ice. In both cases the weight of cell pellets were measured and the cell pellets were resuspended in 4 mL of lysis buffer per gram of cell weight. Resuspended cells were lysed using a C3 cell press by passing cells twice at a pressure of 10,000 psi. Lysed cells were centrifuged (12,000 xg, 30 min). Supernatants were decanted into new tubes and ultracentrifuged for one hour at 100,000 xg to pellet membranes. After the final centrifugation, hGLUT1-containing membrane pellets were retained and weighed, and the supernatant was discarded.

### *Solubilization*

SMA2000P (Cray Valley) was prepared according to the protocol reported by Lee *et al* (2016). To prepare a solubilization solution, SMA was dissolved in buffer (20 mM Tris, 500 mM NaCl, 1 mM MgCl<sub>2</sub>, 10% glycerol, 1 mM ATP, pH 7.8) to a final concentration of 5% (w/v), and a total of 12.5 mL per 1 g of membrane pellet. Membranes were fully resuspended using a 15 mL glass Dounce homogenizer (10 cycles per 15 mL volume). Homogenized membranes were transferred to a chilled 50 mL conical tube and an equal volume of the 5% SMA solution was added to give a final SMA concentration of 2.5 % (w/v).



Resuspended membranes were incubated for 2 h with gentle rocking in a cold room then transferred into chilled 50 mL ultracentrifuge tubes and ultracentrifuged (100,000  $\times g$ , 1 h, 4 °C). The supernatant containing SMA-solubilized membranes was collected and the pellet was discarded.

### *Purification*

SMA-solubilized material was filtered through a 70  $\mu m$  nylon cell strainer (Falcon, Cat# 21008-952) into a 125 mL flask. A 5 mL Ni-Sepharose His-Trap HP or FF column (GE Healthcare, Cat# 17-5247-01) was attached to a peristaltic pump in the cold room. The column was washed with 2 column volumes (CV) water followed by 2 CV of solubilization buffer at a flow rate of 1 mL/min. The SMALP-containing supernatant was circulated across the column at 1 mL/min for 16h using a recirculating loop of tubing on an ÄKTA pure chromatography system (GE Healthcare Life Sciences). The column was washed with 15 CV of solubilization buffer. Protein was eluted from the column using step-wise imidazole gradient over a total volume of 50 CVs (20 CVs 0 mM, 20 CVs 10 mM, 10 CVs 50 mM, 16 CVs 100 mM, 10 CVs 250 mM) in a base of solubilization buffer. Fractions of 2 mL were collected throughout. Fractions were analyzed on SDS-PAGE silver stain gel and anti-GLUT1 western blot and those containing hGLUT1-SMALPs were pooled and dialyzed to remove imidazole. The dialyzed sample was concentrated to a final volume of 350  $\mu L$  for SEC purification (30kDa MWCO Amicon Ultra-15 centrifugal filtration cartridges, Millipore).

### *Size Exclusion Chromatography (SEC)*

Concentrated hGLUT1 was further purified by SEC using a Superdex 200 10/300 column in SEC buffer (20 mM Tris, 150 mM NaCl, 1mM TCEP, 1 mM MgCl<sub>2</sub>, 1 mM ATP, pH 7.8) at a flow rate of 0.5 mL/min. Protein was collected in 0.5 mL fractions for silver stain and western blot analysis.

### **Erythrocyte membrane complex purification**

Whole blood was obtained from healthy human donors (Biological Specialty Corp, Cat# 100-17). All steps were performed on ice or at 4 °C unless otherwise specified.

To thoroughly wash the erythrocytes, one unit of blood (~500 mL) was combined with three volumes of ice-cold kaline (150 mM KCl, 5 mM HEPES, 0.5 mM EDTA, pH 7.4). Cells were centrifuged for 10 minutes at 3000 xg and 4 °C. Supernatant was carefully removed and the pellet was resuspended in 10 mL of ice-cold kaline buffer and the sample was divided in half.

Fresh lysis solution was prepared by adding EDTA-free protease inhibitor tablets into 200 mL 10 mM Tris, 150 mM NaCl, 1 mM MgCl<sub>2</sub>, 1 mM ATP, pH 8.0. Cells were centrifuged for 10 minutes at 3000 xg and 4 °C. Supernatant was carefully decanted and the pellet was resuspended in 4 mL of lysis buffer per gram of cell pellet weight. Resuspended cells were incubated on ice for 60 minutes. Lysates

were then transferred to 40 mL Oak Ridge ultracentrifuge tubes (Thermo Scientific, Cat# 3138-0050) and centrifuged at 12,000 xg for 30 minutes. The supernatant containing erythrocyte membranes were transferred into new tubes and centrifuged at 100,000 xg for 60 minutes to pellet membranes. Supernatants were discarded. A 5% w/v SMA solution was freshly prepared in solubilization buffer (20 mM Tris, 500 mM NaCl, 1 mM MgCl<sub>2</sub>, 1 mM ATP, 10% glycerol, pH 7.8). The pelleted cell membranes were resuspended in 4 mL solubilization buffer per gram of original cell pellet, and membranes were homogenized using a 15 mL glass Dounce homogenizer. The homogenized membrane preparation was transferred to a clean, pre-chilled 50 mL conical tube and an equal volume of 5% SMA solution was added for a final suspension of 2.5% SMA. Erythrocyte membranes were incubated in the SMA solution for approximately 10 minutes, after which time the solution was ultracentrifuged at 100,000 xg for 60 minutes. Supernatant containing SMA-solubilized GLUT1 SMALPs was collected and the pellet was discarded. Solubilized GLUT1 SMALPs were filtered through a 70 µm nylon cell strainer (Falcon, Cat# 21008-952). The filtered sample was dialyzed overnight using a Slide-a-lyzer™ dialysis cartridge with a 30 kD MWCO overnight against dialysis buffer (20 mM Tris, 500 mM NaCl, 1 mM MgCl<sub>2</sub>, 1 mM ATP, 10% glycerol, pH 7.8). Samples were removed from the dialysis cartridges and concentrate using 10,000 MWCO Amicon Ultra-15 centrifuge cartridges (Millipore, Cat# UFC910024) to a final volume of 350 µL for size exclusion chromatography. Size exclusion chromatography was conducted using a

Superdex 200 10/300 SEC column on an AKTA device with a flow rate of 0.5 mL per minute, delta pressure of 3 MPa, and pre-column pressure of 5 MPa. Eluted 1.0 mL fractions were collected for silver stain and western blot analysis.

### **SMALP SDS-PAGE protocol**

Imidazole-eluted or SEC column-eluted fractions containing GLUT1-SMALPs were separated on NuPAGE™ 4-12% Bis-Tris Protein gels (ThermoFisher) and transferred to nitrocellulose membranes using an iBlot™ semi-dry transfer apparatus at 20 V for 10 minutes. Membranes were probed with anti-GLUT1 monoclonal antibody (Millipore) at a 1:1000 dilution to determine GLUT1 protein expression in each eluted fraction. For SDS-PAGE: NuPAGE LDS sample buffer (Invitrogen); Molecular weight markers: MagicMark™ XP Western Protein Standard 20-220 kDa (Invitrogen Cat# LC5602) and Precision Plus Protein™ Kaleidoscope™ Prestained Protein Standard 10-250 kDa (BioRad Cat# 1610375) were used.

### **Mass Spectrometry for proteomic analysis**

#### *In-gel Digestion and LC-MS/MS Analysis*

The purified sample was run under either reducing conditions on an SDS-PAGE gel for 5 min or native conditions on a Tris-Glycine gel for 1 hour (wherein SMALP particles travel through the gel intact) to separate proteins from lower molecular weight contaminants. After which time, the entire protein region of the gel was excised and subjected to in-gel trypsin digestion after reduction with

dithiothreitol and alkylation with iodoacetamide. Peptides eluted from the gel were lyophilized and re-suspended in 25  $\mu$ L of 5% acetonitrile (0.1% (v/v) TFA). A 1-2  $\mu$ L injection was loaded by a Waters NanoAcquity UPLC in 5% acetonitrile (0.1% formic acid) at 4.0  $\mu$ L/min for 4.0 min onto a 100  $\mu$ m I.D. fused-silica pre-column packed with 2 cm of 5  $\mu$ m (200 Å) Magic C18AQ (Bruker-Michrom). Peptides were eluted at 300 nL/min from a 75  $\mu$ m I.D. gravity-pulled analytical column packed with 25 cm of 3  $\mu$ m (100 Å) Magic C18AQ particles using a linear gradient from 5-35% of mobile phase B (acetonitrile + 0.1% formic acid) in mobile phase A (water + 0.1% formic acid) over 45-60 minutes. Ions were introduced by positive electrospray ionization via liquid junction at 1.4 kV into a Thermo Scientific Q Exactive hybrid mass spectrometer. Mass spectra were acquired over  $m/z$  300-1750 at 70,000 resolution ( $m/z$  200) with an AGC target of 1e6, and data-dependent acquisition selected the top 10 most abundant precursor ions for tandem mass spectrometry by HCD fragmentation using an isolation width of 1.6 Da, max fill time of 110ms, and AGC target of 1e5. Peptides were fragmented by a normalized collisional energy of 27, and fragment spectra acquired at a resolution of 17,500 ( $m/z$  200).

### *Data Analysis*

Raw data files were peak processed with Proteome Discoverer (version 2.1, Thermo) followed by identification using Mascot Server (version 2.1, Matrix Science) against the *Human* (Swissprot) FASTA file (downloaded 10/2016 and

04/2017). Search parameters included a fixed modification of carbamidomethyl cysteine, and variable modifications of oxidized methionine, pyroglutamic acid for Q, and N-terminal acetylation. Assignments were made using a 10 ppm mass tolerance for the precursor and 0.05 Da mass tolerance for the fragments. All non-filtered search results were processed by Scaffold (version 4.8.2, Proteome Software, Inc.) utilizing the Trans-Proteomic Pipeline (Institute for Systems Biology) with threshold values set at 80% for peptides (2.4% false-discovery rate) and **90%** for proteins (2 peptide minimum, 0.2% false-discovery rate), and quantitative comparisons made using the iBAQ quantitation method with all samples normalized by total ion current for the run.

## **Microscopy**

### **Negative stain TEM**

For negative staining, a single 8µL drop of protein is added to the grid (carbon-coated 400 mesh grids), and left on for 30 seconds, then wicked away with filter paper, leaving behind bound particles. In cases where sample concentration was low, the sample was fixed with a 2% glutaraldehyde solution prior to staining with a 1% uranyl acetate solution.

### **Scanning Electron Microscopy**

RBC ghosts treated with 2.5% SMA solution for 30 seconds, and fixed with 2.5% glutaraldehyde solution before evaluation using SEM.

## **Cytoskeleton dynamics**

Whole blood was incubated with latrunculin A (5  $\mu$ M) or jasplakinolide (2.5  $\mu$ M) at 37 °C for 4 hours. Following incubation, SMA extraction of RBC membrane proteins was performed. Thoroughly washed membranes underwent SMA solubilization and the material was purified on a Superdex 200 increase 10/300 SEC column. The resulting fractions were evaluated using SDS-PAGE (data not shown) and Native PAGE. Differences in GLUT1 and Band3 oligomerization could be seen with silver stain and western blotting,

## CHAPTER V: DISCUSSION

The body of work presented in this thesis represents a multi-pronged approach to the characterization of membrane protein structure and function. What began as a biochemical project focused on studying second-site suppressor mutations of CFTR quickly grew and evolved into a body of work far more rooted in structural biology and biophysics than I had anticipated. While the CFTR suppressor mutation aim of my proposal continued with success, I was unexpectedly drawn to the challenge of studying membrane proteins at large. Fortunately, I was permitted to follow the work where it led, even when it perhaps didn't necessarily stray, but ran a parallel track alongside the one we had originally laid. This slight change in course led me not only to some valuable science and a global network of welcoming academics who were excited to share their science, it also led to some wonderful collaborations and lifelong friendships, which ultimately became more valuable to me than the structure we were seeking.

My goals for this work were wide-ranging. The initial project that I embarked on had two main focuses. The first was to gain a better understanding of second-site suppression of the CF-causing  $\Delta F508$  CFTR mutation. The second was to validate the molecular modeling and dynamics work that served



as the basis for our approach. When this work began, there was not yet a full-length structure of CFTR to refer to, so the basis for all hypotheses required a solid starting model. Based on what was gleaned from the model, we were able to answer some questions regarding suppressor mutation V510D, as well as ask others about novel suppressor mutations that were uncovered in this work, namely P1050R and Q1042K. There are still many unanswered questions surrounding the concept of helical unraveling in  $\Delta F508$ -CFTR; for example, whether the inclusion of those charged residues does act to stabilize them based on the formation of salt bridges, or if a separate mechanism is involved which effectively acts as a chaperone. If this hypothesis is true, it would provide greater insight into the repair and improved stabilization of  $\Delta F508$ -CFTR with small molecule ligands that target TMs 10 and 11. A thorough understanding of the impact of Q1042K will require evaluation of this mutation in the same combinations as were tested for P1050R. Another valuable component of this work would be the implementation of a double-mutant cycle for a more quantitative understanding of the impact that each mutation is having on  $\Delta F508$ -CFTR correction, and whether combining two or more stabilizing mutations results in an additive effect (Ibarra-Molero *et al.*, 2004). For this analysis to be done effectively, it should involve a quantitative output of each mutation.

To facilitate this, and to determine whether the P1050R mutation is functional, it is my intent to evaluate the P1050R constructs in the electrophysiology assay to evaluate whether the helical stabilization hinders

activity, and will rerun the panel of mutations to obtain quantitative data that can be used for the double-mutant analysis. I will also incorporate the HRP-trafficking assay data to determine whether that data set provides similar conclusions, and whether a correlation between trafficking and function can be made with this work. As such, repeat of the electrophysiology data and Q1042K mutational analysis comprise next steps for this work.

Working with the members of the Hurlbut lab and with our colleagues on the Integrated Drug Discovery team, I was able to learn and apply a wide range of methods to show how V510D interacted with other residues within NBD1 as well as on ICL4 to support second-site suppression of  $\Delta F508$ . We definitively demonstrated the presence of a K564-V510D salt bridge using several different approaches including crystallography to generate a structure of  $\Delta F508/V510D$ -NBD1. With this, as well as several full-length CFTR studies, were able to better characterize the dual interaction V510D has with both NBD1 and ICL4. Our work with TMD2 stabilization successfully validated the hypothesis that helical unraveling of TMs 10 and 11, which together form ICL4, may be a significant aspect of the thermal instability and dysfunction characteristic of the  $\Delta F508$ -CFTR molecular pathology. Through our TMD2 helical stabilization work, we have identified a new set of second-site suppressor mutations, and by combining these with NBD1 and ICL4 stabilizers, we made a solid case for the requirement of NBD1 stabilization in  $\Delta F508$  rescue.

Perhaps equally as important, however, was the step-wise validation of the molecular dynamics simulation upon which these hypotheses were built. When this work began, the highest resolution structure was a 9Å model obtained through electron crystallography that relied on homologous protein Sav1866 for context. This modeling and MD simulation work was initiated in the hope of not only learning about  $\Delta F508$ -CFTR molecular pathology, but also as a potential tool for drug discovery in the absence of a full-length atomic resolution structure of  $\Delta F508$ -CFTR, which has yet to be published. That this body of work so conclusively supports the predictions made about  $\Delta F508$ -CFTR as well as its counterparts  $\Delta F508/V510D$ - and  $\Delta F508/R1070W$ -CFTR suggests that computer modeling may serve as a tangible asset to drug discovery.

Of course, the work on second-site suppression represents only one aspect of my thesis. My initial goal with regard to CFTR purification (which at the time was rooted in detergent solubilization) was to obtain a fully wild-type, native, glycosylated form that I could use for biophysical characterization. Early in the project, our team had been focused on crystallizing the protein, which meant producing sufficient quantities to facilitate concentrating the protein - without aggregating it – in anticipation of a crystal screen. This required stabilizing mutations, detergent screens, production of homologous CFTR (namely the more

stabilized chicken isoform), and removing the (presumably) unstructured R-domain.

In the course of my rotation with the Biologics Discovery group, which was focused on the aforementioned CFTR protein purification, I became curious about the approach we were taking and the utility of what was being produced, specifically the protein's stability and structural accuracy. TEM analysis of the protein was somewhat difficult to interpret, and aggregation appeared to be a serious concern. This led me to investigate alternative methods for the purification of CFTR. After some time researching Sligar's protocol for lipid nanodiscs - a method much better suited for robust and easily-produced bacterial proteins – I came across a paper published by Alice Rothnie's lab at Aston University in Birmingham, UK (Gulati *et al.*, 2014). In this publication, she outlines the detergent-free purification of a series of ABC transports; of which, CFTR was one. Her approach involved purifying CFTR from *S.cerevisiae* microsomes using styrene-maleic acid, or SMA. While the result was modest, it represented the first publication of a completely detergent-free approach to CFTR purification.

At that point, the focus of my work shifted to SMA purification of CFTR, and included attempting to obtain a high-resolution structure of human CFTR in its native form – a milestone that had not yet been reached when this work began. However despite our dedicated effort, that goal was not fully realized. This is perhaps in part due to the drought of precedent surrounding high-

resolution cryo-EM analysis of an SMA-purified protein, especially one as structurally sensitive as CFTR. What this work did represent, however, was the opportunity to contribute to a new and growing aspect of membrane protein purification involving SMA and its companion polymers. By attending several SMALP conferences over the last three years, I have both learned a great deal about biophysics and MP structural biology and offered up my own insights based on my successes and failures of adapting SMA-purified proteins for cryo-EM analysis. This has included a thorough evaluation of optimal grid prep methods such as graphene oxide coating and single-sided blotting from the 'back' of the grid to draw the protein to the GO surface and avoid harmful exposure of the protein to the air-liquid interface. I have had the opportunity to share my experience and thoughts surrounding all of this work with members of the UMass cryo-EM community as well as my collaborators in the SMALP network; and have in-turn learned a great deal from them.

While several factors may have impeded my ability to obtain a high-resolution CFTR-SMALP structure to date, it remains a goal that I am committed to. Perhaps my best chance for success relies upon my ability to utilize not just my own successes and failures, but also those of others in pursuit of a similar goal. Although my personal body of work involves SMA purification, it cannot be ignored that success has been met through the use of detergent purification. In the last three years, the Chen lab at Rockefeller University has published human and zebrafish CFTR structures in both open and closed conformations (Zhang

and Chen, 2016; Zhang *et al.*, 2017; Zhang *et al.*, 2018b). While their protocol involved several familiar aspects (DDM solubilization, baculovirus transduction, LMNG resuspension), it also included steps I had not considered previously myself, but may have been the key to their success (for example GFP nanobody purification and the addition of fluorinated detergent to increase variability in particle orientation). In one of my most recent attempts at CFTR-SMALP cryo-EM analysis, I adapted the Chen lab's grid preparation protocol for my own use, specifically the technique of adding fluorinated Fos-Choline-8 at 3mM (roughly 40 x's lower than its CMC of ~114mM). While this initial attempt proved only modestly successful (it does bear repeating), it highlights the importance of considering multiple approaches. As we develop our toolbox of methods suitable for working with lipid nanoparticles, we must be mindful of the fact that similar to detergent purification, there likely will not be one set path to success. The best we can do is be open-minded to where success may come from and learn from those opportunities.

My CFTR-SMALP work has also represented an exhaustive exercise in learning to identify where certain limitations may exist for both a protein and the polymer being used to solubilize it. For example, despite several publications suggesting that Diisobutylene Maleic Acid co-polymer (DIBMA) is impervious to divalent cations (despite no true protein-based evidence to support this) my personal experience with the polymer suggests this is not the case. While this body of work did not afford for that particular line of exploration, it is something

that I feel warrants investigating. Another avenue of investigation I look forward to pursuing is the functionalization of polymers to make them more compatible with specific downstream analysis. This would allow for the use of SMA-purified proteins with methods like surface plasmon resonance (SPR) to evaluate ligand binding and fluorescently-tagged particles for FRET-based studies of protein interaction.

The emphasis of my SMA purification work on CFTR was primarily focused on cryo-EM structural analysis and lipidomics analysis of CFTR-SMALPs. However the application of this method to the purification of GLUT1 highlighted its utility as a way to discern structural components without the need for microscopy. By utilizing SMA for the purification of GLUT1 expressed in Expi293 cells, I was able to detect a repeatable banding pattern of three distinct GLUT1 bands, as visible by Native PAGE separation and GLUT1 western blotting analysis. This data represents the first compelling native gel electrophoresis data demonstrating GLUT1 oligomeric forms. Moreover, this result was repeatable in human primary erythrocytes. By applying this approach to red blood cells that had been treated with latrunculin A and jasplakinolide, I was also able to provide supporting evidence for the theory of actin-dependence of GLUT1/Band3 higher-order complex formation.

This work has the potential to be expanded to a number of tissue types and primary cells in search of information on physiologically relevant interactions

that may not be reproducible through the use of recombinant expression. In instances where information cannot be duplicated in an artificial system or it is unclear what all the components of an interaction are, SMA solubilization may provide a path to characterization through proteomic and lipidomic evaluation.



## **APPENDIX I**

### **6.1 Appendix I**

Appendix I encompasses a collaborative effort toward CFTR-SMALP characterization and structural determination. Within this appendix is data collected on CFTR-SMALP characterization and structure, including cryo-EM grid preparation and microscopy. For this work, I performed all TEM and cryo-EM grid preparation and assay development with continued input and guidance from Chen Xu, who also acquired cryo-EM data on the Titan Krios. Kangkang Song provided assistance with grid screening on the Talos Arctica. Gregory Hendricks and Lara Strittmatter provided training and continued technical support (as needed) with all TEM work performed. Joe Batchelor oversaw the CFTR-SMALP cryo-EM data analysis.

### **6.2 CFTR Cryo-EM**

Once the basic assay parameters had been determined for SMA solubilization and purification of CFTR, modifications were made to the protocol to increase purity and homogeneity of the particles, and to ensure sample compatibility with cryo-EM analysis. This included removal of glycerol from the solubilization and purification step (Figure 6.1), dialyzing out excess SMA prior to

affinity column binding and dialyzing excess imidazole after elution from the affinity column prior to gel filtration. No changes to purity or stability were seen when glycerol was removed from the protocol (Figure 6.1), and removal of excess SMA allowed for tighter binding to the affinity column, and cleaner elution.

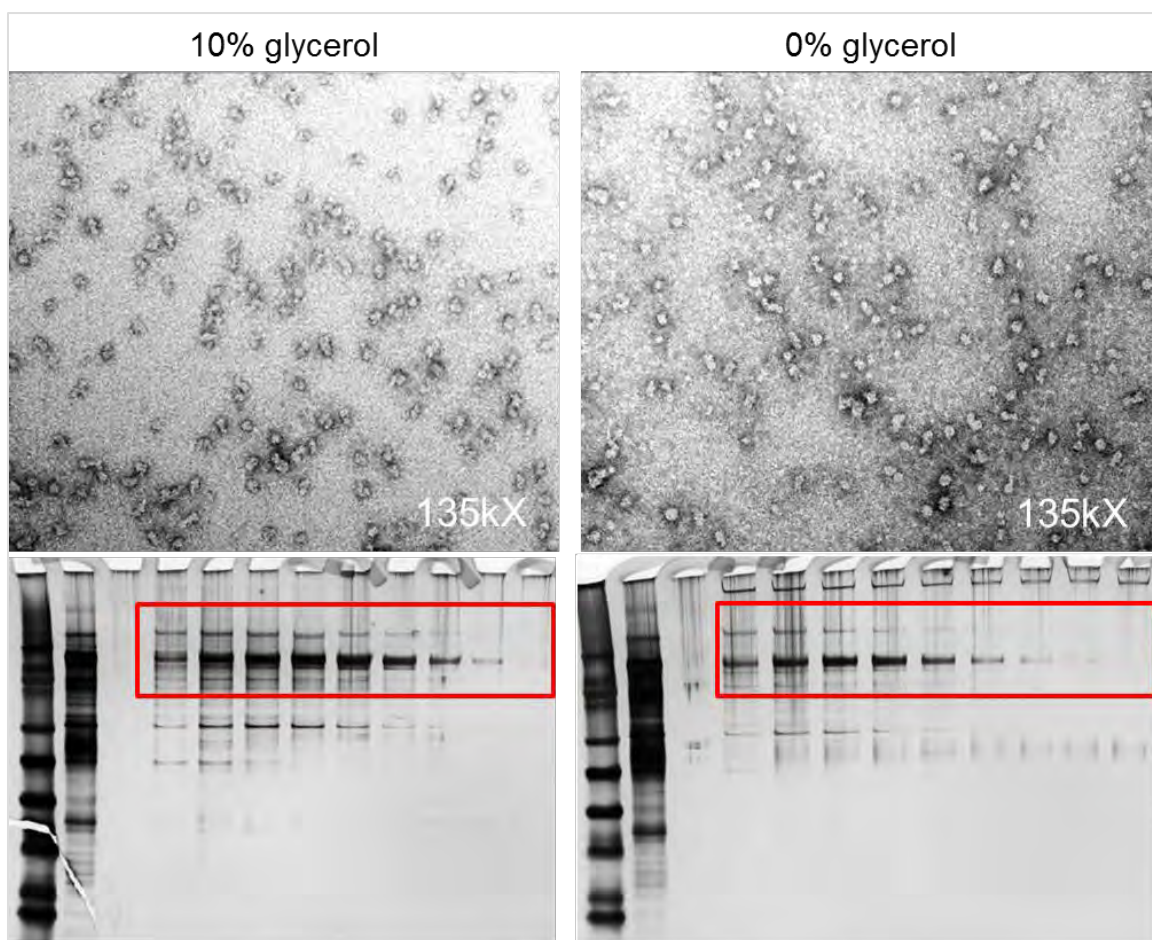


**Figure 6.1 Evaluation of the impact of glycerol removal on CFTR-SMALPs using negative stain TEM analysis and SDS-PAGE silver staining.** A side-by-side comparison of hCFTR-SMALPs in buffer with and without glycerol shows no differences in particle integrity. Because it interferes with the formation of vitreous ice during the cryo grid preparation process, it was necessary to remove glycerol from the sample buffer. For TEM, sample was added to carbon-coated 400 mesh grids and stained with 1% uranyl acetate staining.

One of the major challenges inherent in working with SMA-purified particles was obtaining sufficient particle count on the grids. It was unclear whether the SMA was interfering with the ability of the particles to reside in the vitreous ice, or whether they prefer to stay localized to the grid due to their charge. To combat this issue, I incorporated a graphene oxide grid-coating step into my grid preparation protocol. While this did improve particle count, initial 2D class averages pointed to a potential issue with particle heterogeneity in my sample, which may have been preventing better refinement of the class averages.

### **6.2.1 Reduction of particle heterogeneity with stabilizing modifications**

#### *The evaluation of non-hydrolyzable nucleotides*

Because HEK-293 cells partially phosphorylate CFTR, particles were purified in both the “closed” (de-phosphorylated) and “open” (phosphorylated with NBDs in contact) conformations. To minimize ATP hydrolysis, which triggers a closure of the CFTR channel, I added AMP-PNP as a non-hydrolyzable ATP analog in an effort to stabilize open CFTR. However, I also examined the effects of ATP- $\gamma$ -S, as AMP-PNP may bind to CFTR at a much slower rate. Working with David Stepp at Sanofi, I compared the affinity of NBD1 for ATP, ADP, AMP-PNP and ATP- $\gamma$ -S surface plasmon resonance. Our results suggest that NBD1 binds ATP- $\gamma$ -S, ATP and ADP with similar affinities (Table 6.1), and despite not

being impervious to hydrolysis; ATP- $\gamma$ -S is hydrolyzed at a rate approximately ten times slower than ATP. The protocol was therefore adjusted to include 1 mM ATP- $\gamma$ -S to the SEC/storage buffer in place of AMP-PNP.

### Nucleotide binding to NBD1-1d

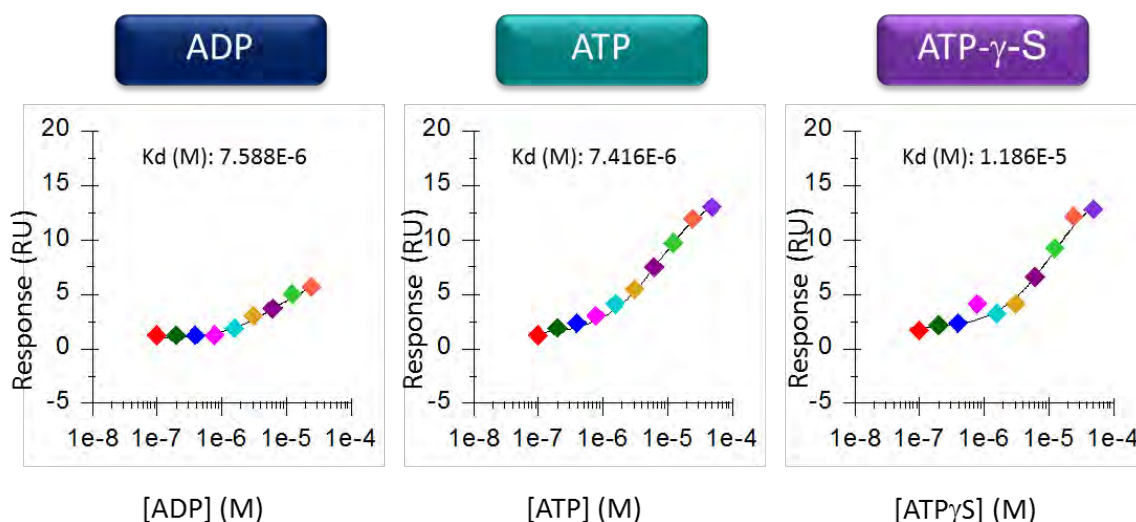


**Figure 6.2 Comparison of affinity binding of ATP, ADP and ATP- $\gamma$ -S to NBD1 using surface plasmon resonance.** Results indicate that ATP- $\gamma$ -S, a slowly hydrolyzing nucleotide, has a binding affinity to WT-NBD1 of 11.86  $\mu$ M, which is comparable to that of ATP (7.416  $\mu$ M) and ADP (7.588  $\mu$ M), making it suitable as a stabilizing ligand for structural studies of purified CFTR.

**Table 6.1 Binding affinities ( $K_d$ ) of ADP, ATP and ATP- $\gamma$ -S to WT-NBD1**

ADP	ATP	ATP- $\gamma$ -S
7.588 $\mu$ M	7.416 $\mu$ M	11.86 $\mu$ M

### *Phosphorylation of CFTR using PKA*

To further alleviate some of the heterogeneity, a phosphorylation step using the catalytic subunit of protein kinase A (PKA) was added prior to SEC. A protocol was adapted from a recent publication by the Chen lab (Zhang *et al.*, 2018b), involving detergent-purified CFTR, as well as communication with New England Biolabs. Initial evaluation involved adding PKA to either the purified membrane preparation prior to the addition of SMA (to circumvent the limitation on  $\text{MgCl}_2$  added to the reaction) or the “SMALPed” protein prior to SEC purification. Owing to the abundance of other proteins likely found in the membrane prep, it was difficult to discern whether any meaningful changes in the level of CFTR phosphorylation were occurring, whereas visible differences were seen via western blotting between phosphorylation of CIP treated and PKA treated CFTR when the isolated protein was treated at RT (21°C) for one hour.

A side-by-side comparison was also performed to determine the appropriate combination of nucleotides to add to ensure efficient phosphorylation. We observed that adding ATP and ATP- $\gamma$ -S at 1 mM each, and  $\text{MgCl}_2$  at 2 mM was most effective.

- a. Combination of nucleotides to add to the reaction
  - i. ATP
  - ii. ATP + ATP- $\gamma$ -S
  - iii. ATP- $\gamma$ -S

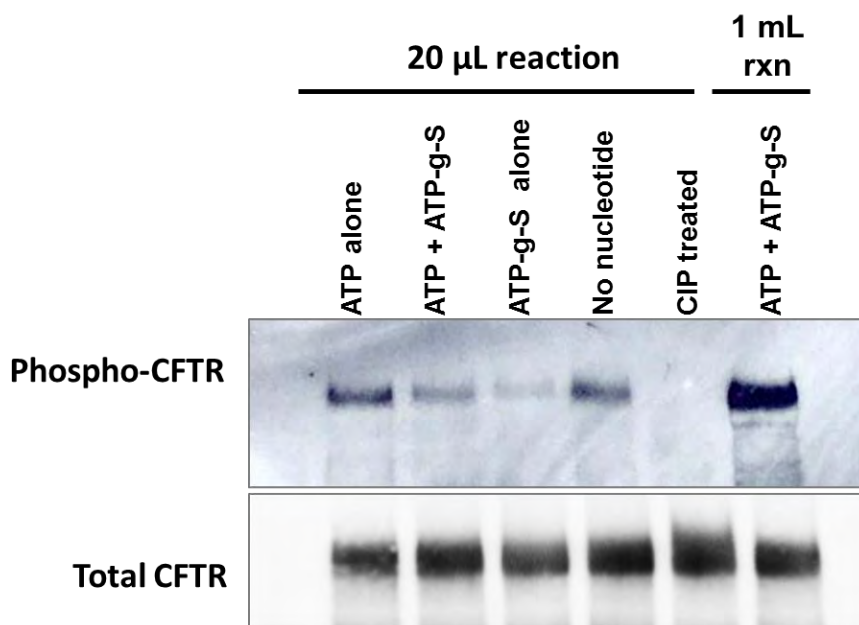


**Figure 6.3 Phosphorylation of CFTR-SMALPs with PKA catalytic subunit**  
 CFTR-SMALP samples were treated with the catalytic subunit of PKA with either 2mM ATP (lane 1), 1mM ATP + 1mM ATP- $\gamma$ -S (lane 2), 1mM ATP- $\gamma$ -S (lane 3), or no additional nucleotide (lane 4, residual ATP may still exist in the culture). A 20  $\mu$ L reaction volume was set up for each condition, as well as a 20  $\mu$ L CIP dephosphorylation treatment. The remaining 1 mL of purified CFTR-SMALPs were treated with the combination of ATP (1 mM) and ATP- $\gamma$ -S (1 mM). Following treatment with PKA to induce phosphorylation under different nucleotide conditions, CFTR-SMALP samples were subject to immunoblotting to evaluate levels of phosphorylated CFTR using a rabbit polyclonal antibody targeting Ser767. Results suggest that PKA treatment with ATP present results in the highest level of phosphorylation and that dephosphorylation using calf intestinal alkaline phosphatase treatment is effective at complete removal of phosphorylation at Ser767. Despite very modest levels of phosphorylation seen when ATP- $\gamma$ -S is the primary exogenously added nucleotide (which may be due to residual ATP in the sample), the combination of ATP + ATP- $\gamma$ -S when the full 1mL prep was treated with equal parts of each nucleotide and PKA was heavily phosphorylated when evaluated via anti-phosCFTR western blotting.

### **6.2.2 Optimization of cryo-EM grid preparation for CFTR-SMALP structural analysis**

As mentioned earlier in this chapter, a major limitation to the development of the grid preparation method for CFTR-SMALPs was the issue of limited particle count seen on the CFTR cryo grids. Several rounds of grid optimization were done to establish the ideal blotting conditions, which have improved ice formation, particle count and overall distribution of the particles across the grid. In the process of trouble-shooting this issue, several parameters were evaluated. They included cryo-EM grid type and preparation, blotting parameters, and protein stabilization. The following grid types were evaluated for their impact on ice formation and particle distribution:

- C-flat Holey Carbon
- QuantiFoil R 1.2/1.3 (Copper grid with Holey Carbon film)
- QuantiFoil R 1.2/1.3 and R 2/1 (Gold grid with Holey Carbon film)
- UltrAuFoil R 1.2/1.3 (Gold grid with Holey Gold Films 500Å thick)

Grid screening suggested that the UltrAuFoil grids provided the most consistent ice formation and particle distribution for SMALPs.

### **Blotting conditions and filter paper considerations**

A recent publication by Postis *et al.* (2018) describing the first sub-nanometer cryo-EM structure of a protein-SMALP mentions that blotting grids with ash-free filter paper that is low in divalent metal ion content is critical to avoid destabilizing the SMALPs. To address this, two additional types of filter paper that are low-ash and known to contain low levels of divalent cations were tested with the VitroBot during grid prep and analyzed for ice formation.

- Filter paper on VitroBot
  - Standard blotting paper - Whatman Ø55/20mm, Grade 595
  - Whatman grade 41 quantitative filter paper, ash-less
  - Whatman grade 50 quantitative filter paper, hardened low-ash

The Whatman grade 50 hardened, low-ash filter paper did not blot as efficiently as the grade 41, which was more absorbent; grade 41 was used going forward.

### **Graphene Oxide coating procedure to increase particle dispersity**

Perhaps the most significant change to the grid preparation procedure was the inclusion of a graphene oxide coating on the grids. In 2017, a manuscript was published outlining work done at Rockefeller University's New York Structural Biology Center (NYSBC) that suggests that approximately 90% of particles added to a cryo-EM grid are adsorbed to the air-water interface, rendering them structurally compromised (Noble *et al.*, 2017). This finding,



coupled with the challenges I experienced with limited particle count, led me to investigate the addition of a graphene oxide (GO) surface coating to my grids.

*Martin lab protocol*

Working with Dr. Chen Xu, I first tried a protocol adapted from Pantelic *et al.*, with slight modifications made to the glow discharging step (both sides are glow discharged for 45 seconds at 20 mA) and washing step (1 wash, rather than 3) (Pantelic *et al.*, 2010). This protocol appeared to work well, and greatly increased particle number on the grids in some areas. There were, however, large areas of the grid that didn't appear sufficiently coated, and thus had little to no particles in the ice, and variability in GO grid coating and particle distribution were a concern.

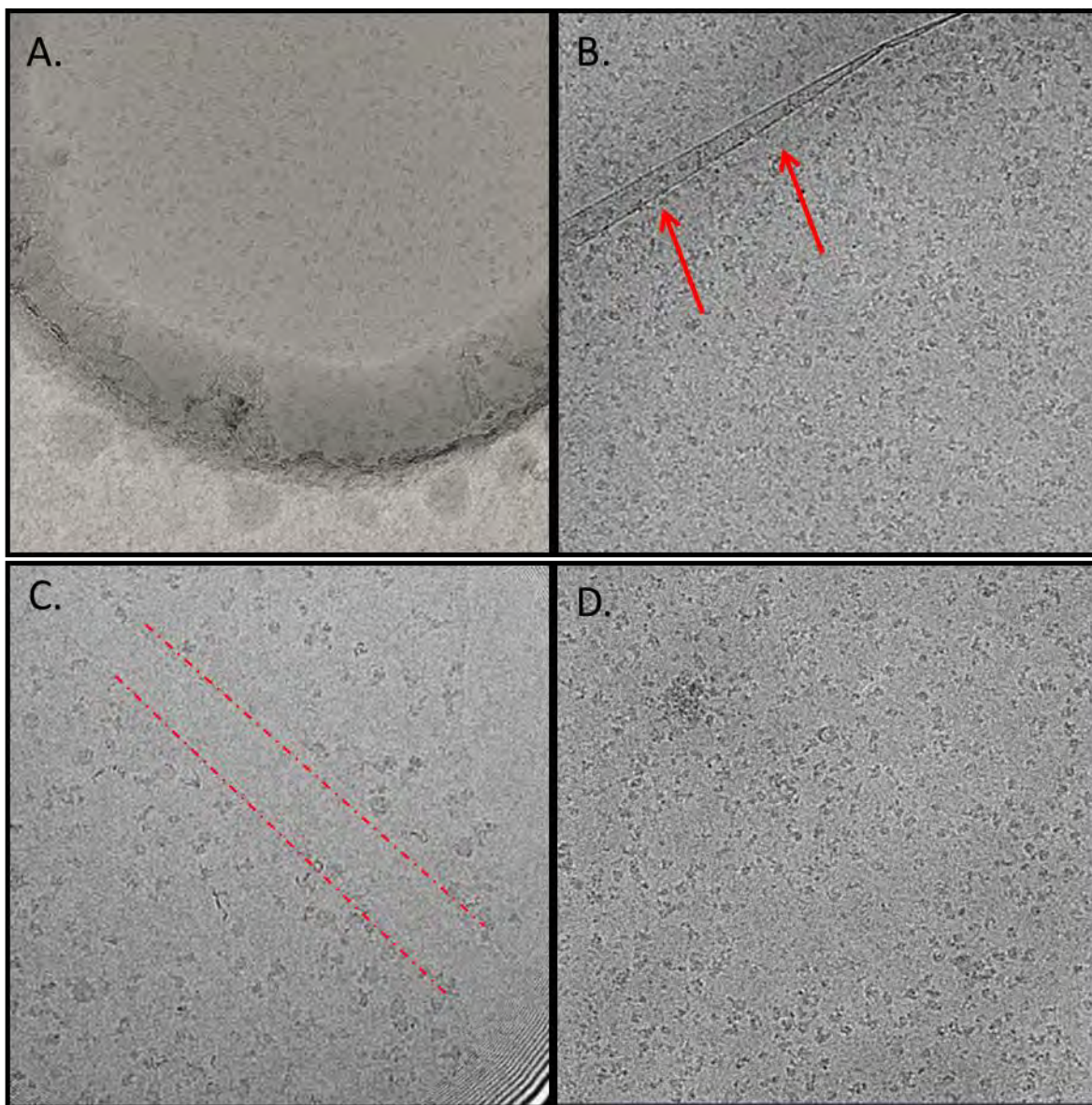


**Figure 6.4 Inconsistencies in graphene oxide grid coating led to variation in particle distribution.** Grids were coated with GO per the Martin Lab protocol and prepared with CFTR-SMALPs before evaluation on the Titan Krios (CFTR preparation was previously frozen; prepared August 2017). Particles tended to reside on the outer edge of holes in the gold film (A), overlaps in GO sheets caused areas of darker background (B), breaks in particle distribution can be seen where sheets of graphene oxide did not coat the grid (C) and overall particle dispersal was patch in places.

### *Agard/Cheng protocol*

To avoid the variability in GO coating seen using this protocol, I researched other methods and found a protocol developed in the labs of David Agard and Yifan Cheng at UCSF (Palovcak *et al.*, 2018). This method uses an 80% methanol solution as a dispersant to dissolve the GO suspension, which is dispersed into a thin layer across a water subphase. The water is subsequently pumped out of the petri dish it is contained in, effectively lowering the GO layer onto grids that are submerged in the subphase (Figure 6.5). After several attempts using this protocol - with changes made to grid type, GO quantity added, methanol content, and timing of preparation - and after approximately 36 grids had been prepared and screened using both TEM and cryo-EM - it was determined that this method was not an improvement over the original method provided by Dr. Xu.

One issue that arose while using the Agard/Cheng protocol was the disruption of ice formation. While the GO did appear to coat the grids, I was unable to obtain the consistent formation of vitreous ice I had seen previously, as several holes were empty. After discussing this with our project consultant, I re-introduced glycerol to my buffer at approximately 2% (a component I had previously removed). Unfortunately, this protocol modification led to the formation of non-vitreous ice that appeared wavy and uneven, and no particles were visible on the grids. I have since returned to the Martin lab protocol, increased the number of additions of GO to the grids (from 1 to 3), and

preferentially solubilize only larger GO flakes when preparing my 0.2 mg/mL solution in an effort to reduce variability of the coating. Evaluation of the Agard/Cheng protocol involved testing concentrations of graphene oxide from 50-80  $\mu$ g, comparing Quantifoil and UltrAuFoil grids, day-of prep compared to 24 hours prior to use, and the percent methanol content used as a dispersant (80%, 50%, 0%). A schematic can be seen in Figure 6.5.

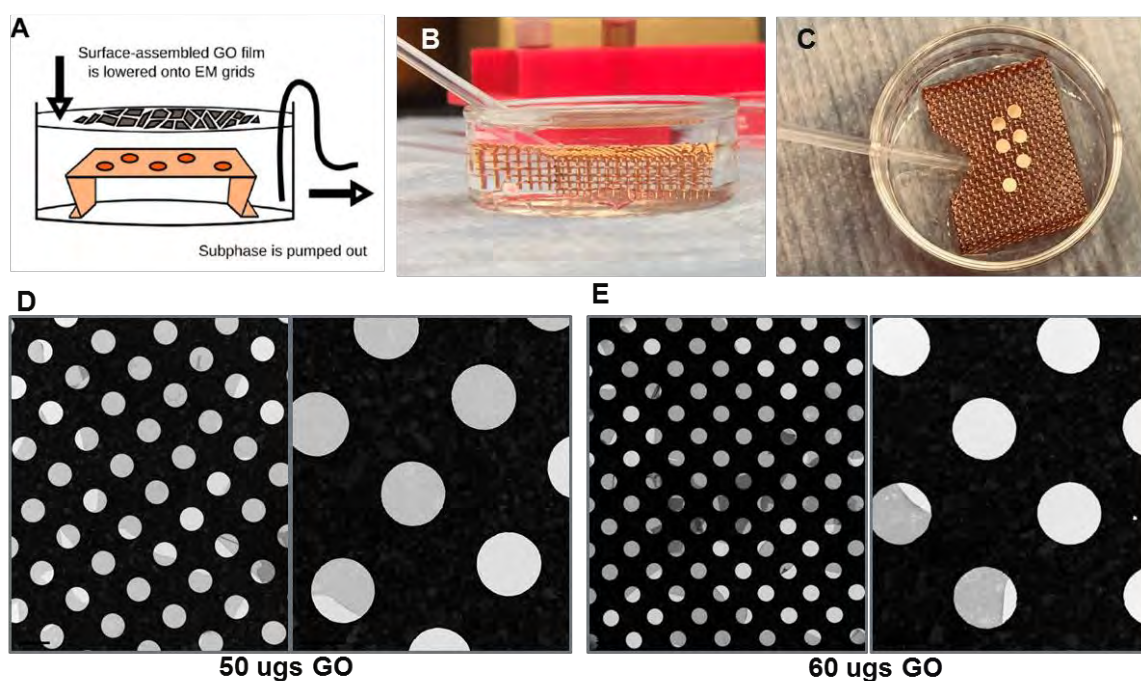


**Figure 6.5 Agard/Cheng graphene oxide coating protocol.** Dosing of GO was tested at solution (50 – 80  $\mu$ g). Grid type used (Quantifoil vs UltrAuFoil). Prepped 24 hours prior vs. fresh (1 hr prior to use). Change in methanol % used as dispersant (80%, 50% and 0%). Panel A of this figure originally appeared in Palovcak *et al*, 2018, A simple and robust procedure for preparing graphene-oxide cryo-EM grids (Palovcak *et al.*, 2018).



### 6.2.3 Current 2D and 3D cryo-EM models of hCFTR-SMALPs show both open and closed conformations of the protein

Despite extensive grid preparation work and several rounds of cryo-EM with CFTR-SMALPs, we had limited success obtaining an *ab initio* 3D model of our protein. One data set looked very promising early on, and gave reasonable 2D class averages of what appeared to be CFTR in two conformations. This collection of particles was only able to get to an estimated 15 Å of resolution (Figures 6.6 and 6.7).

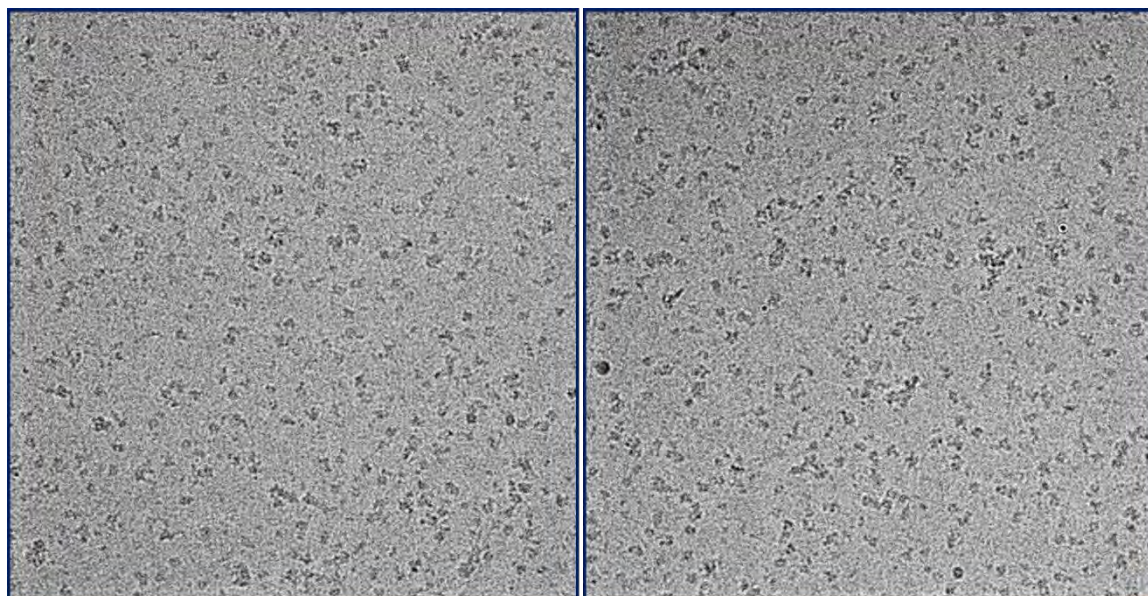


**Figure 6.6** Cryo-EM micrograph images of hCFTR-SMALPs captured using the Talos Arctica (200 kVa) by Chen Xu and KangKang Song. Grids prepared using UltrAuFoil® Holey Gold Films (500 Å thick, R 1.2/1.3).

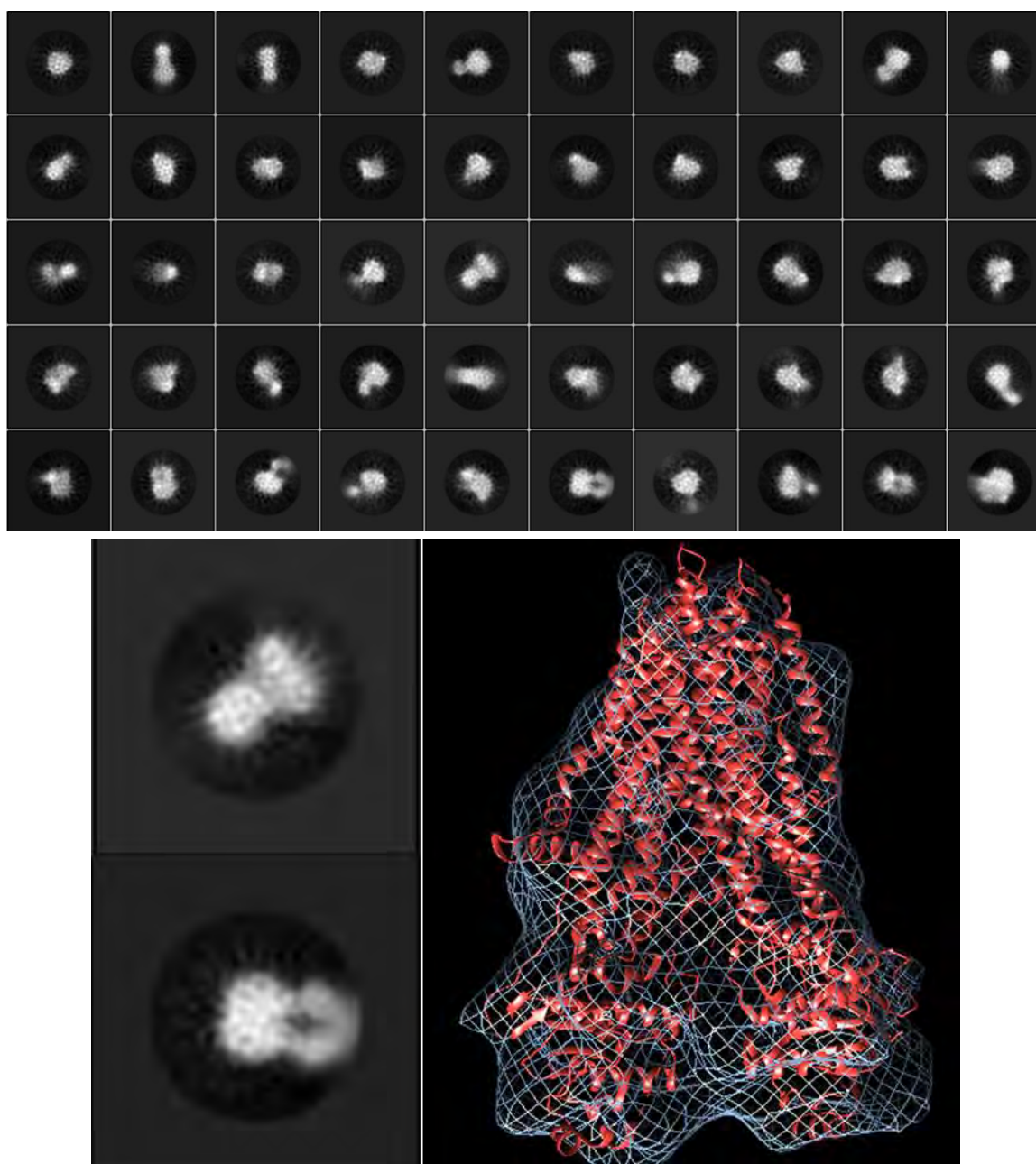


**Figure 6.7 2D class averaging of CFTR-SMALP cryo-EM particles and the resulting 3D model.** 3D classification and refinement was performed and the subsequent model (panel at right, blue mesh overlay at approximately 15 Å) was created. This model was derived by using zebrafish hCFTR cryoEM structure (PDB 5UAR, (Zhang and Chen, 2016)) as a reference model.

## 2D class averaging of negative stain TEM micrographs

In order to determine whether the protein was too heterogeneous for successful 3D modeling with cryo-EM, or whether the particles might be subject to damage during the process of image capture, thus preventing effective averaging, I performed two rounds of negative-stained particle 2D class-averaging on transmission electron micrographs. The first set of images was collected from grids that had been prepared with previously frozen CFTR-SMALPs (Figure 6.8).

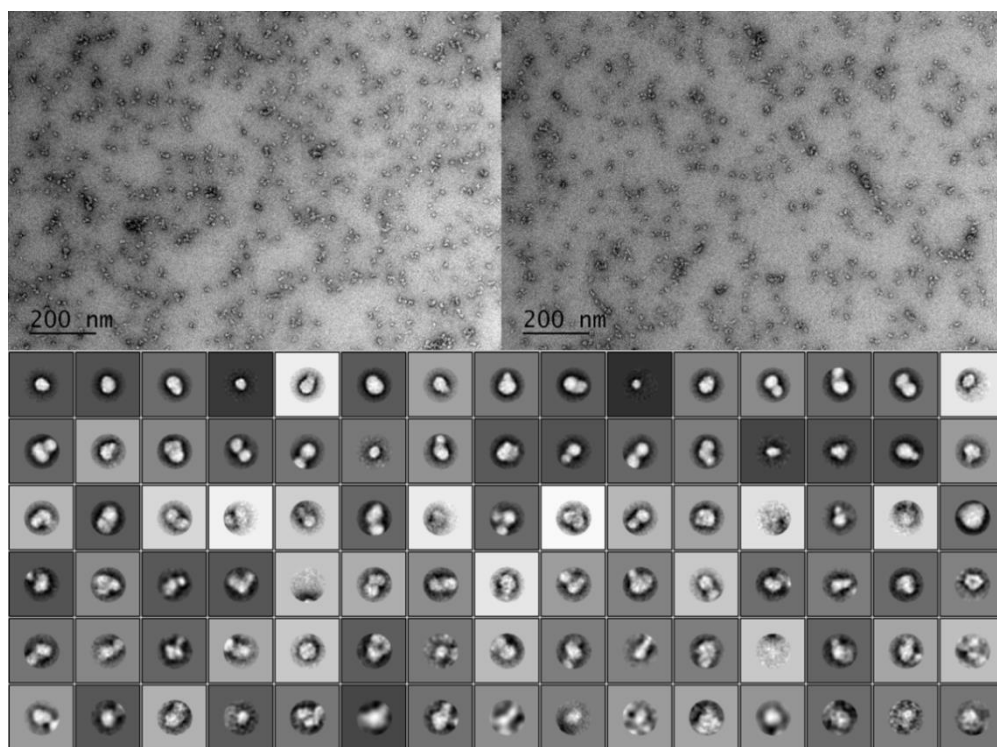


**Figure 6.8 2D class averages of CFTR-SMALPs from ~3,000 negatively stained TEM particles.** Protein was previously frozen (February 2018 prep) and had undergone 2 freeze/thaw cycles prior to grid prep. Several of the classes

resemble previously published negatively stained CFTR micrographs (Alzahrani *et al.*, 2015).

The second round of images collected came from grids of freshly-prepared CFTR-SMALPs that had a stabilizing ligand added just prior to being added to the grid. In both cases, only 50 images were used to collect particles (roughly 3,000 in total). The averages appear to resemble an ABC transporter although no structural detail is evident. Qualitative assessment of the images indicated that the sample with a ligand present had a slight advantage over the non-ligand bound, as did the use of a fresh prep (Figure 6.9).

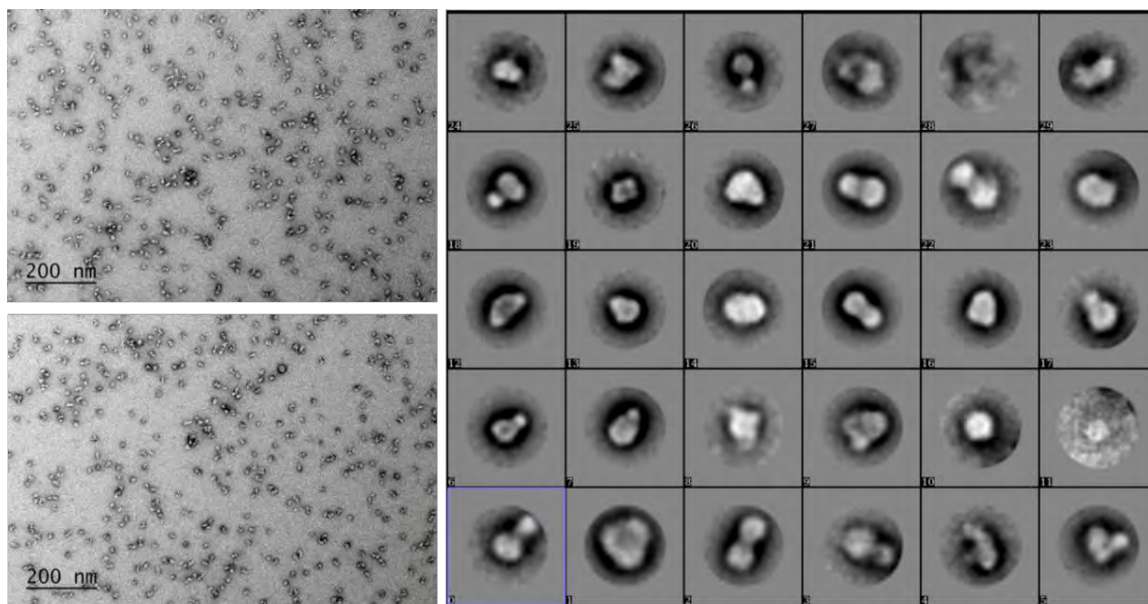


**Figure 6.9** 2D Class Averages from negatively stained TEM particles of CFTR-SMALPs with stabilizing ligand bound. Material was prepared fresh prior to analysis, and a stabilizing ligand was added immediately prior to grid prep.



The final attempt at obtaining cryoEM images of CFTR-SMALPs was with freshly-prepared protein. UltrAuFoil grids were coated with graphene oxide and used same-day. Grids had good particle distribution, which led to three days of imaging on the Krios. During the first day of image acquisition, 931 images were collected (roughly 16 hours of data collection). This series covered about half of the selected mesh areas that were chosen during screening. The grid was saved for future analysis, and was revisited about two weeks later. We realigned the grid in an attempt to cover regions not previously covered during the first session. At that point, an additional 616 images were obtained. Results from the second session were not as good as the first. During grid preparation I made a couple of grids for each condition to serve as back-ups in the event conditions were favorable. The set of grids had been loaded into the grid holder and unloaded on the two prior occasions. So on a third day of data collection, images were taken from a second grid that looked satisfactory during screening. Particles were analyzed using cisTEM software. A combination of all three data sets led to a ~20 Å structure. There were clear issues with degradation of the grid by the third set, so particles from the second and third round of imaging, where the grids had already been exposed to the beam and loaded/unloaded twice, were removed from analysis. By focusing on only the first set, we were able to get to ~11 Å at best (based on cisTEM's prediction), although our *ab initio* model does not resemble CFTR. However, when Jue Chen's open and closed zebrafish CFTR models (PDB IDs: 5W81 and 5UAR respectively (Zhang and Chen, 2016; Zhang

*et al.*, 2017)) are used as a starting point, we do obtain structures that resemble the protein in both conformations (Figure 6.10).

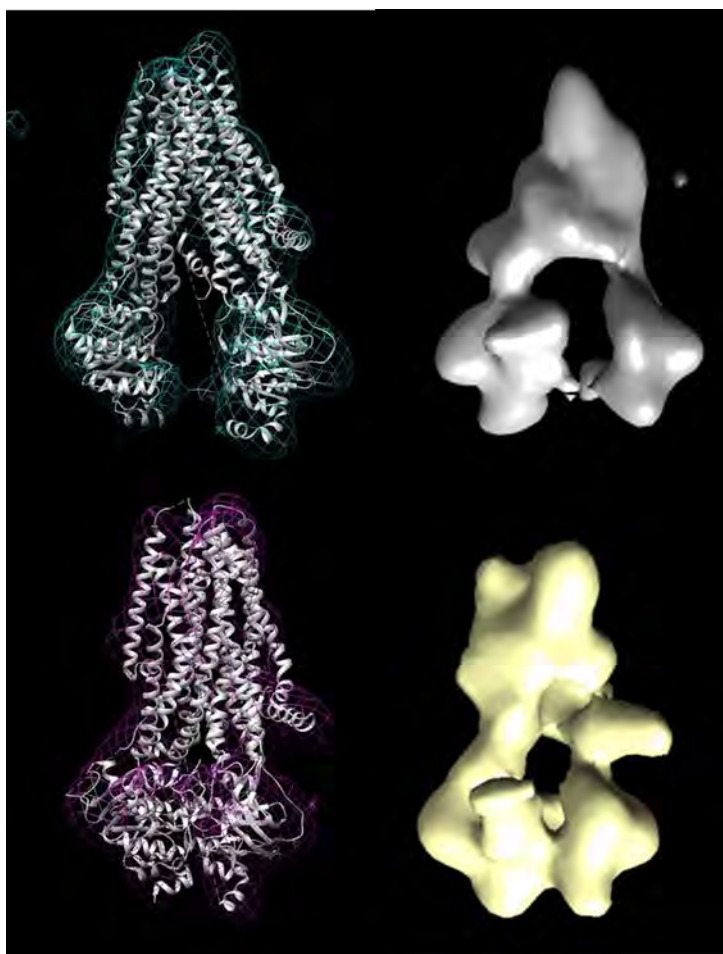


**Figure 6.10** Cryo-EM class-averaging of CFTR-SMALP particles in the open and closed conformations visible to 11 Å. The mesh structure represents our progress when the Chen lab structures were introduced as a starting point.

### 6.3 Discussion

The ultimate aim of this chapter was to obtain a high-resolution structure of CFTR-SMALPs by cryo-EM. As might be expected, sample and cryo-EM grid preparation are paramount. CFTR-SMALP grid preparation remains somewhat variable, likely owing to the properties that SMA introduces to the process such as the negatively charged, outward-facing maleic acid moieties on SMA and the sensitivity to divalent cations. Currently, my parameters include using UltrAuFoil grids coated with graphene oxide, 3.5  $\mu$ L sample addition, a force of 5, wait of 0 or 1 second (both appear to work), and a 4.5 second blotting time using Whatman grade 41 low-ash filter paper. Ice formation appears consistent and particle count is largely driven by the presence of GO, which appears necessary for particles to reside on the grid surface and away from the damaging air-liquid interface.

This body of work represents a collection of 8 cryo-EM data sets, primarily using the Titan Krios. Using a template based on predicted structure, refinements on 70k particles picked from our best data collection resolve to  $\sim 15$  Å. If we utilize a starting model, it is further refined to  $\sim 11$  Å. However this is not sufficient to identify structural components past general channel shape, which may be due to particle heterogeneity. Further, the use of a starting model has the potential to bias the data, thus it is always preferable to derive structural models *ab initio*.

Interestingly, both open- and closed-conformation structures were

obtained during class averaging of a dataset collected in February on the Talos Arctica. This occurred prior to implementation of the phosphorylation step as it currently stands, which was added to reduce such heterogeneity. Considering the limited particle count used to generate the 2D-class averages and 3D model, considerable gains in resolution should be made simply through a greater volume of data collection, indicating that this system shows promise for obtaining a high resolution structure.

## BIBLIOGRAPHY

(2015). The PyMOL Molecular Graphics System (Schrödinger, LLC.).

(2016). Schrödinger Suite 2019-1. In Protein Preparation Wizard: Epik, S. Impact, ed. (New York, NY: Schrödinger, LLC).

Ababou, A., and Koronakis, V. (2016). Structures of Gate Loop Variants of the AcrB Drug Efflux Pump Bound by Erythromycin Substrate. *PLOS ONE* *11*, e0159154.

Abrahams, J.P., Leslie, A.G., Lutter, R., and Walker, J.E. (1994). Structure at 2.8 Å resolution of F1-ATPase from bovine heart mitochondria. *Nature* *370*, 621-628.

Abreu, B., Lopes, E.F., AS, F.O., and Soares, C.M. (2019). F508del disturbs the dynamics of the nucleotide binding domains of CFTR before and after ATP hydrolysis. *Proteins*.

Abu-Arish, A., Pandzic, E., Goepp, J., Matthes, E., Hanrahan, J.W., and Wiseman, P.W. (2015). Cholesterol modulates CFTR confinement in the plasma membrane of primary epithelial cells. *Biophysical journal* *109*, 85-94.

Adams, P.D., Afonine, P.V., Bunkóczi, G., Chen, V.B., Davis, I.W., Echols, N., Headd, J.J., Hung, L.-W., Kapral, G.J., Grosse-Kunstleve, R.W., *et al.* (2010). PHENIX: a comprehensive Python-based system for macromolecular structure solution. *Acta crystallographica Section D, Biological crystallography* *66*, 213-221.

Aitken, M.L., Burke, W., McDonald, G., Shak, S., Montgomery, A.B., and Smith, A. (1992). Recombinant Human DNase Inhalation in Normal Subjects and Patients With Cystic Fibrosis: A Phase 1 Study. *JAMA* *267*, 1947-1951.

Aleksandrov, A.A., Kota, P., Aleksandrov, L.A., He, L., Jensen, T., Cui, L., Gentzsch, M., Dokholyan, N.V., and Riordan, J.R. (2010). Regulatory Insertion Removal Restores Maturation, Stability and Function of  $\Delta$ F508 CFTR. *Journal of Molecular Biology* *401*, 194-210.

Aleksandrov, A.A., Kota, P., Cui, L., Jensen, T., Alekseev, A.E., Reyes, S., He, L., Gentzsch, M., Aleksandrov, L.A., Dokholyan, N.V., *et al.* (2012). Allosteric modulation balances thermodynamic stability and restores function of  $\Delta$ F508 CFTR. *Journal of molecular biology* *419*, 41-60.

Aleksandrov, L.A., Jensen, T.J., Cui, L., Kousouros, J.N., He, L., Aleksandrov, A.A., and Riordan, J.R. (2015). Thermal stability of purified and reconstituted CFTR in a locked open channel conformation. *Protein expression and purification* 116, 159-166.

Aller, S.G., Yu, J., Ward, A., Weng, Y., Chittaboina, S., Zhuo, R., Harrell, P.M., Trinh, Y.T., Zhang, Q., Urbatsch, I.L., *et al.* (2009). Structure of P-glycoprotein reveals a molecular basis for poly-specific drug binding. *Science* 323, 1718-1722.

Alvarez, F.J.D., Orelle, C., and Davidson, A.L. (2010). Functional Reconstitution of an ABC Transporter in Nanodiscs for Use in Electron Paramagnetic Resonance Spectroscopy. *Journal of the American Chemical Society* 132, 9513–9515.

Alzahrani, A., Cant, N., Kargas, V., Rimington, T., Aleksandrov, A., Riordan, J., and Ford, R. (2015). Structure of the cystic fibrosis transmembrane conductance regulator in the inward-facing conformation revealed by single particle electron microscopy, Vol 2.

Amann, T., Kirovski, G., Bosserhoff, A.K., and Hellerbrand, C. (2011). Analysis of a promoter polymorphism of the GLUT1 gene in patients with hepatocellular carcinoma. *Mol Membr Biol* 28, 182-186.

Amaral, M.D., and Kunzelmann, K. (2011). Cystic Fibrosis: Diagnosis and Protocols, Vol Volume 1: Approaches to study and Correct CFTR Defects (New York: Springer).

Amir Shaghaghi, M., Zhouyao, H., Tu, H., El-Gabalawy, H., Crow, G.H., Levine, M., Bernstein, C.N., and Eck, P. (2017). The SLC2A14 gene, encoding the novel glucose/dehydroascorbate transporter GLUT14, is associated with inflammatory bowel disease. *Am J Clin Nutr* 106, 1508-1513.

Asano, T., Katagiri, H., Takata, K., Lin, J.L., Ishihara, H., Inukai, K., Tsukuda, K., Kikuchi, M., Hirano, H., and Yazaki, Y. (1991). The role of N-glycosylation of GLUT1 for glucose transport activity. *J Biol Chem* 266, 24632-24636.

Atwell, S., Brouillette, C.G., Conners, K., Emtage, S., Gheyi, T., Guggino, W.B., Hendle, J., Hunt, J.F., Lewis, H.A., Lu, F., *et al.* (2010). Structures of a minimal human CFTR first nucleotide-binding domain as a monomer, head-to-tail homodimer, and pathogenic mutant. *Protein Engineering, Design and Selection* 23, 375-384.

Baeza-Delgado, C., Marti-Renom, M.A., and Mingarro, I. (2013). Structure-based statistical analysis of transmembrane helices. *European biophysics journal : EBJ* 42, 199-207.

Baker, G.F., and Naftalin, R.J. (1979). Evidence of multiple operational affinities for D-glucose inside the human erythrocyte membrane. *Biochim Biophys Acta* 550, 474-484.

Baker, J.A., Wong, W.-C., Eisenhaber, B., Warwicker, J., and Eisenhaber, F. (2017). Charged residues next to transmembrane regions revisited: "Positive-inside rule" is complemented by the "negative inside depletion/outside enrichment rule". *BMC biology* 15, 66-66.

Baldwin, S.A. (1992). Probing the structure and function of the human erythrocyte glucose transporter. [Review]. *Biochemical Society transactions* 20, 533-537.

Baldwin, S.A. (1993). Mammalian passive glucose transporters: members of an ubiquitous family of active and passive transport proteins. [Review]. *Biochim Biophys Acta* 1154, 17-49.

Baldwin, S.A., Barros, L.F., and Griffiths, M. (1995). Trafficking of glucose transporters--signals and mechanisms. *Biosci Rep* 15, 419-426.

Bammes, B.E., Rochat, R.H., Jakana, J., Chen, D.-H., and Chiu, W. (2012). Direct electron detection yields cryo-EM reconstructions at resolutions beyond 3/4 Nyquist frequency. *Journal of structural biology* 177, 589-601.

Baneres, J.L., Popot, J.L., and Mouillac, B. (2011). New advances in production and functional folding of G-protein-coupled receptors. *Trends in biotechnology* 29, 314-322.

Bang, O., and Orskov, S.L. (1937). Variations in the permeability of red blood cells in man with particular reference to the conditions obtaining in pernicious anaemia. *J Clin Invest* 16, 279-288.

Barrera, N.P., and Robinson, C.V. (2011). Advances in the Mass Spectrometry of Membrane Proteins: From Individual Proteins to Intact Complexes. *Annual Review of Biochemistry* 80, 247-271.

Basketter, D., and Widdas, W. (1978). Asymmetry of the hexose transfer system in human erythrocytes. Comparison of the effects of cytochalasin B, phloretin and maltose as competitive inhibitors. *J Physiol* 278, 389-401.

Battle, A.R., Ridone, P., Bavi, N., Nakayama, Y., Nikolaev, Y.A., and Martinac, B. (2015). Lipid-protein interactions: Lessons learned from stress. *Biochimica et Biophysica Acta (BBA) - Biomembranes* 1848, 1744-1756.

- Bayburt, T.H., and Sligar, S.G. (2010). Membrane protein assembly into Nanodiscs. *FEBS letters* 584, 1721-1727.
- Berg JM, Tymoczko JL, and L., S. (2002). Each Organ Has a Unique Metabolic Profile. In *Biochemistry*, W. Freeman, ed. (New York).
- Bigay, J., and Antonny, B. (2012). Curvature, Lipid Packing, and Electrostatics of Membrane Organelles: Defining Cellular Territories in Determining Specificity. *Developmental Cell* 23, 886-895.
- BIOVIA, D.S. (2016). *Discovery Studio* (San Diego: Dassault Systèmes).
- Birch, J., Axford, D., Foadi, J., Meyer, A., Eckhardt, A., Thielmann, Y., and Moraes, I. (2018). The fine art of integral membrane protein crystallisation. *Methods* (San Diego, Calif) 147, 150-162.
- Birket, S.E., Chu, K.K., Houser, G.H., Liu, L., Fernandez, C.M., Solomon, G.M., Lin, V., Shastry, S., Mazur, M., Sloane, P.A., *et al.* (2016). Combination therapy with cystic fibrosis transmembrane conductance regulator modulators augment the airway functional microanatomy. *Am J Physiol Lung Cell Mol Physiol* 310, L928-939.
- Bisignano, P., and Moran, O. (2010). Molecular dynamics analysis of the wild type and dF508 mutant structures of the human CFTR-nucleotide binding domain 1. *Biochimie* 92, 51-57.
- Biswas, R., Kumar, P., and Pollard, H.B. (2017). Regulation of mRNA turnover in cystic fibrosis lung disease. *Wiley interdisciplinary reviews RNA* 8.
- Blodgett, D., Graybill, C., and Carruthers, A. (2008). Analysis of glucose transporter topology and structural dynamics. *J Biol Chem* 283, 36416-36424.
- Blodgett, D.M., De Zutter, J.K., Levine, K.B., Karim, P., and Carruthers, A. (2007). Structural basis of GLUT1 inhibition by cytoplasmic ATP. *J Gen Physiol* 130, 157-168.
- Bloor, W.R., and Knudson, A. (1916). The Separate Determination of Cholesterol and Cholesterol Esters in Small Amounts of Blood. *Journal of Biological Chemistry* 27, 107-112.
- Bompadre, S.G., Sohma, Y., Li, M., and Hwang, T.-C. (2007). G551D and G1349D, two CF-associated mutations in the signature sequences of CFTR, exhibit distinct gating defects. *The Journal of general physiology* 129, 285-298.



Bon, C.L., Popot, J.-L., and Giusti, F. (2014). Labeling and Functionalizing Amphipols for Biological Applications. *The Journal of membrane biology* 247, 797-814.

Booth, P.J., Flitsch, S.L., Stern, L.J., Greenhalgh, D.A., Kim, P.S., and Khorana, H.G. (1995). Intermediates in the folding of the membrane protein bacteriorhodopsin. *Nature Structural Biology* 2, 139-143.

Bowers, K.J., Chow, D.E., Xu, H., Dror, R.O., Eastwood, M.P., Gregersen, B.A., Klepeis, J.L., Kolossvary, I., Moraes, M.A., Sacerdoti, F.D., *et al.* (2006). Scalable Algorithms for Molecular Dynamics Simulations on Commodity Clusters. Paper presented at: SC '06: Proceedings of the 2006 ACM/IEEE Conference on Supercomputing.

Brodlie, M., Haq, I.J., Roberts, K., and Elborn, J.S. (2015). Targeted therapies to improve CFTR function in cystic fibrosis. *Genome medicine* 7, 101-101.

Brodsky, J.L. (2001). Chaperoning the maturation of the cystic fibrosis transmembrane conductance regulator. *American Journal of Physiology-Lung Cellular and Molecular Physiology* 281, L39-L42.

Broecker, J., Eger, B.T., and Ernst, O.P. (2017). Crystallogenes of Membrane Proteins Mediated by Polymer-Bounded Lipid Nanodiscs. *Structure* 25, 384-392.

Brüggeller, P., and Mayer, E. (1980). Complete vitrification in pure liquid water and dilute aqueous solutions. *Nature* 288, 569-571.

Butler, R., Hunt, T., and Smith, N.J. (2015). ENaC inhibitors for the treatment of cystic fibrosis. *Pharmaceutical patent analyst* 4, 17-27.

Calabrese, A.N., Watkinson, T.G., Henderson, P.J.F., Radford, S.E., and Ashcroft, A.E. (2015). Amphipols Outperform Dodecylmaltoside Micelles in Stabilizing Membrane Protein Structure in the Gas Phase. *Analytical Chemistry* 87, 1118-1126.

Callaway, E. (2015). The revolution will not be crystallized: a new method sweeps through structural biology. *Nature* 525, 172-174.

Callebaut, I., Eudes, R., Mornon, J.P., and Lehn, P. (2004). Nucleotide-binding domains of human cystic fibrosis transmembrane conductance regulator: detailed sequence analysis and three-dimensional modeling of the heterodimer. *Cellular and molecular life sciences : CMLS* 61, 230-242.

Callebaut, I., Hoffmann, B., Lehn, P., and Morion, J.-P. (2017). Molecular modelling and molecular dynamics of CFTR. *Cellular and Molecular Life Sciences* 74, 3-22.

Cantor, R.S. (1999). Lipid Composition and the Lateral Pressure Profile in Bilayers. *Biophysical journal* 76, 2625-2639.

CFF (2017). Types of CFTR Mutations. In About CF (<http://www.cff.org/What-is-CF/Genetics/Types-of-CFTR-Mutations/>).

CFF.org (2017). 2016 Annual Data Report (Bethesda, MD).

CFF.org (2018). 2017 Annual Data Report. In Cystic Fibrosis Foundation Patient Registry

(Bethesda, Maryland).

CFF.org (2019a). Cystic Fibrosis-Related Diabetes. In Life With CF, C.F. Foundation, ed.

CFF.org (2019b). Drug Development Pipeline.

Chae, P.S., Rasmussen, S.G., Rana, R.R., Gotfryd, K., Chandra, R., Goren, M.A., Kruse, A.C., Nurva, S., Loland, C.J., Pierre, Y., *et al.* (2010). Maltose-neopentyl glycol (MNG) amphiphiles for solubilization, stabilization and crystallization of membrane proteins. *Nature methods* 7, 1003-1008.

Chan, D.A., Sutphin, P.D., Nguyen, P., Turcotte, S., Lai, E.W., Banh, A., Reynolds, G.E., Chi, J.T., Wu, J., Solow-Cordero, D.E., *et al.* (2011). Targeting GLUT1 and the Warburg effect in renal cell carcinoma by chemical synthetic lethality. *Sci Transl Med* 3, 94ra70.

Chappe, V., Hinkson, D.A., Howell, L.D., Evagelidis, A., Liao, J., Chang, X.B., Riordan, J.R., and Hanrahan, J.W. (2004). Stimulatory and inhibitory protein kinase C consensus sequences regulate the cystic fibrosis transmembrane conductance regulator. *Proceedings of the National Academy of Sciences of the United States of America* 101, 390-395.

Chen, C., Pore, N., Behrooz, A., Ismail-Beigi, F., and Maity, A.C. (2001). Regulation of glut1 mRNA by Hypoxia-inducible Factor-1. *INTERACTION BETWEEN H-ras AND HYPOXIA. J Biol Chem* 276, 9519-9525.

Chen, T.-Y., and Hwang, T.-C. (2008). CLC-0 and CFTR: Chloride Channels Evolved From Transporters. *Physiological Reviews* 88, 351-387.

Cheng, S., Rich, D.P., Marshall, J., Gregory, R.J., Welsh, M.J., and Smith, A.E. (1991). Phosphorylation of the R domain by cAMP-dependent protein kinase regulates the CFTR chloride channel. *Cell* 66, 1027-1036.

Cheng, S.H., Gregory, R.J., Marshall, J., Paul, S., Souza, D.W., White, G.A., O'Riordan, C.R., and Smith, A.E. (1990). Defective intracellular transport and processing of CFTR is the molecular basis of most cystic fibrosis. *Cell* 63, 827-834.

Chiaw, P.K., Eckford, P.D.W., and Bear, C.E. (2011). Insights into the mechanisms underlying CFTR channel activity, the molecular basis for cystic fibrosis and strategies for therapy. *Essays In Biochemistry* 50, 233-248.

Chmiel, J.F., Konstan, M.W., and Elborn, J.S. (2013). Antibiotic and anti-inflammatory therapies for cystic fibrosis. *Cold Spring Harbor perspectives in medicine* 3, a009779-a009779.

Cloherty, E.K., Levine, K.B., and Carruthers, A. (2001). The red blood cell glucose transporter presents multiple, nucleotide-sensitive sugar exit sites. *Biochemistry* 40, 15549-15561.

Colas, C., Ung, P.M.-U., and Schlessinger, A. (2016). SLC Transporters: Structure, Function, and Drug Discovery. *MedChemComm* 7, 1069-1081.

Contreras, F.-X., Ernst, A.M., Wieland, F., and Brügger, B. (2011). Specificity of Intramembrane Protein–Lipid Interactions. *Cold Spring Harbor Perspectives in Biology* 3.

Corradi, V., Mendez-Villuendas, E., Ingólfsson, H.I., Gu, R.-X., Siuda, I., Melo, M.N., Moussatova, A., DeGagné, L.J., Sejdiu, B.I., Singh, G., *et al.* (2018). Lipid–Protein Interactions Are Unique Fingerprints for Membrane Proteins. *ACS Central Science* 4, 709-717.

Cosson, P., and Bonifacio, J. (1992). Role of transmembrane domain interactions in the assembly of class II MHC molecules. *Science* 258, 659-662.

Cuevas Arenas, R., Danielczak, B., Martel, A., Porcar, L., Breyton, C., Ebel, C., and Keller, S. (2017). Fast Collisional Lipid Transfer Among Polymer-Bounded Nanodiscs. *Scientific Reports* 7, 45875.

Cuevas Arenas, R., Klingler, J., Vargas, C., and Keller, S. (2016). Influence of lipid bilayer properties on nanodisc formation mediated by styrene/maleic acid copolymers. *Nanoscale* 8, 15016-15026.

Cura, A.J., and Carruthers, A. (2012). Role of Monosaccharide Transport Proteins in Carbohydrate Assimilation, Distribution, Metabolism, and Homeostasis. *Comprehensive Physiology* 2, 863-91439.

Dalton, J., Kalid, O., Schushan, M., Ben-Tal, N., and Villa-Freixa, J. (2012). New Model of Cystic Fibrosis Transmembrane Conductance Regulator Proposes Active Channel-like Conformation. *Journal of Chemical Information and Modeling* 52, 1842-1853.

Daruwalla, J., Nikfarjam, M., Greish, K., Malcontenti-Wilson, C., Muralidharan, V., Christophi, C., and Maeda, H. In vitro and in vivo evaluation of tumor targeting styrene-maleic acid copolymer-pirarubicin micelles: Survival improvement and inhibition of liver metastases. *Cancer Science* 101, 1866-1874.

Dawson, R.J., and Locher, K.P. (2007). Structure of the multidrug ABC transporter Sav1866 from *Staphylococcus aureus* in complex with AMP-PNP. *FEBS letters* 581, 935-938.

Dawson, R.J.P., and Locher, K.P. (2006). Structure of a bacterial multidrug ABC transporter. *Nature* 443, 180.

De Boeck, K., and Amaral, M.D. (2016). Progress in therapies for cystic fibrosis. *The Lancet Respiratory Medicine* 4, 662-674.

de Felipe, P. (2002). Polycistronic viral vectors. *Current gene therapy* 2, 355-378.

de Jonge, N., Pfaff, M., and Peckys, D.B. (2014). Chapter One - Practical Aspects of Transmission Electron Microscopy in Liquid. In *Advances in Imaging and Electron Physics*, P.W. Hawkes, ed. (Elsevier), pp. 1-37.

De Zutter, J., Levine, K., Deng, D., and Carruthers, A. (2013). Sequence determinants of GLUT1 oligomerization: analysis by homology-scanning mutagenesis. *J Biol Chem* 288, 20734-20744.

Dean, M., Hamon, Y., and Chimini, G. (2001). The human ATP-binding cassette (ABC) transporter superfamily. *Journal of Lipid Research* 42, 1007-1017.

Deisenhofer, J., Epp, O., Miki, K., Huber, R., and Michel, H. (1985). Structure of the protein subunits in the photosynthetic reaction centre of *Rhodospseudomonas viridis* at 3Å resolution. *Nature* 318, 618-624.

Deng, D., Sun, P., Yan, C., Ke, M., Jiang, X., Xiong, L., Ren, W., Hirata, K., Yamamoto, M., Fan, S., *et al.* (2015). Molecular basis of ligand recognition and transport by glucose transporters. *Nature* 526, 391-396.

Deng, D., Xu, C., Sun, P., Wu, J., Yan, C., Hu, M., and Yan, N. (2014). Crystal structure of the human glucose transporter GLUT1. *Nature* **510**, 121-125.

Denisov, I.G., and Sligar, S.G. (2017). Nanodiscs in Membrane Biochemistry and Biophysics. *Chemical reviews* **117**, 4669-4713.

Dörk T, W.U., Richter T, Neumann T, Wolfes H, Wulf B, Maass G, Tümmler B. (1991). Cystic fibrosis with three mutations in the cystic fibrosis transmembrane conductance regulator gene. *Human Genetics* **87**, 441-446.

Dörr, J.M., Scheidelaar, S., Koorengevel, M.C., Dominguez, J.J., Schäfer, M., van Walree, C.A., and Killian, J.A. (2016). The styrene–maleic acid copolymer: a versatile tool in membrane research. *European Biophysics Journal* **45**, 3-21.

Dorr, J.M., van Coevorden-Hameete, M.H., Hoogenraad, C.C., and Killian, J.A. (2017). Solubilization of human cells by the styrene-maleic acid copolymer: Insights from fluorescence microscopy. *Biochimica et biophysica acta* **1859**, 2155-2160.

Drew, L., Green, O., Villella, A., McEwan, B., Patel, N., Qiu, D., Bhalla, A., Bastos, C., Parks, D., Giuliano, K., *et al.* (2016). CFTR Amplifiers: A New Class of CFTR Modulator that Complements the Substrate Limitations of Other CF Therapeutic Modalities. In C60 ALL ABOUT CYSTIC FIBROSIS, pp. A5574-A5574.

Dubochet, J. (2012). Cryo-EM—the first thirty years. *Journal of Microscopy* **245**, 221-224.

Dubochet, J., Adrian, M., Chang, J.J., Homo, J.C., Lepault, J., McDowell, A.W., and Schultz, P. (1988). Cryo-electron microscopy of vitrified specimens. *Q Rev Biophys* **21**, 129-228.

Dubochet, J., and McDowell, A.W. (1981). VITRIFICATION OF PURE WATER FOR ELECTRON MICROSCOPY. *Journal of Microscopy* **124**, 3-4.

Eckford, P.D.W., Li, C., Ramjeesingh, M., and Bear, C.E. (2012). Cystic fibrosis transmembrane conductance regulator (CFTR) potentiator VX-770 (ivacaftor) opens the defective channel gate of mutant CFTR in a phosphorylation-dependent but ATP-independent manner. *The Journal of biological chemistry* **287**, 36639-36649.

Ege, R. (1919). Studier over Glukosens Invandring i Minneskets rode Blodlegemer. Thesis. . *Hospitalstid 1xi*, 993.

Eggermont, E. (1996). Gastrointestinal manifestations in cystic fibrosis. *European journal of gastroenterology & hepatology* **8**, 731-738.

Emsley, P., Lohkamp, B., Scott, W.G., and Cowtan, K. (2010). Features and development of Coot. *Acta crystallographica Section D, Biological crystallography* **66**, 486-501.

Ermund, A., Recktenwald, C.V., Skjåk-Bræk, G., Meiss, L.N., Onsøyen, E., Rye, P.D., Dessen, A., Myrset, A.H., and Hansson, G.C. (2017). OligoG CF-5/20 normalizes cystic fibrosis mucus by chelating calcium. *Clinical and Experimental Pharmacology and Physiology* **44**, 639-647.

Etzkorn, M., Raschle, T., Hagn, F., Gelev, V., Rice, Amanda J., Walz, T., and Wagner, G. (2013). Cell-free Expressed Bacteriorhodopsin in Different Soluble Membrane Mimetics: Biophysical Properties and NMR Accessibility. *Structure* **21**, 394-401.

Fang, D., West, R.H., Manson, M.E., Ruddy, J., Jiang, D., Previs, S.F., Sonawane, N.D., Burgess, J.D., and Kelley, T.J. (2010). Increased plasma membrane cholesterol in cystic fibrosis cells correlates with CFTR genotype and depends on de novo cholesterol synthesis. *Respiratory Research* **11**, 61.

Fang, W., Cai, Y., Chen, X., Su, R., Chen, T., Xia, N., Li, L., Yang, Q., Han, J., and Han, S. (2009). Poly(styrene-alt-maleic anhydride) derivatives as potent anti-HIV microbicide candidates. *Bioorganic & Medicinal Chemistry Letters* **19**, 1903-1907.

Feng, W., Cui, G., Tang, C.W., Zhang, X.L., Dai, C., Xu, Y.Q., Gong, H., Xue, T., Guo, H.H., and Bao, Y. (2017). Role of glucose metabolism related gene GLUT1 in the occurrence and prognosis of colorectal cancer. *Oncotarget* **8**, 56850-56857.

Fernandez-Moran, H. (1960). Low-temperature preparation techniques for electron microscopy of biological specimens based on rapid freezing with liquid helium II. *Ann N Y Acad Sci* **85**, 689-713.

Frank, J. (2006). Three-Dimensional Electron Microscopy of Macromolecular Assemblies: Visualization of Biological Molecules in Their Native State. In (Oxford University Press).

Gao, X., and Hwang, T.C. (2016). Spatial positioning of CFTR's pore-lining residues affirms an asymmetrical contribution of transmembrane segments to the anion permeation pathway. *J Gen Physiol* **147**, 407-422.

Gao, Y., Cao, E., Julius, D., and Cheng, Y. (2016). TRPV1 structures in nanodiscs reveal mechanisms of ligand and lipid action. *Nature* **534**, 347-351.

Gilljam, M., Ellis, L., Corey, M., Zielenski, J., Durie, P., and Tullis, D.E. (2004). Clinical manifestations of cystic fibrosis among patients with diagnosis in adulthood. *Chest* **126**, 1215-1224.

Giusti, F., Popot, J.L., and Tribet, C. (2012). Well-defined critical association concentration and rapid adsorption at the air/water interface of a short amphiphilic polymer, amphipol A8-35: a study by Forster resonance energy transfer and dynamic surface tension measurements. *Langmuir : the ACS journal of surfaces and colloids* **28**, 10372-10380.

Goor, F., Hadid, S., Grootenhuys, P.D.J., Burton, B., Cai, D., Neuberger, T., Turnbull, A., Singh, A., Joubran, J., Hazlewood, A., *et al.* (2009). Rescue of CF airway epithelial cell function in vitro by a CFTR potentiator, VX-770. *Proceedings of the National Academy of Sciences* **106**, 18825-18830.

Gordon, R.E. (2014). Electron microscopy: a brief history and review of current clinical application. *Methods in molecular biology (Clifton, NJ)* **1180**, 119-135.

Gorga, F., and Lienhard, G. (1981). Equilibria and kinetics of ligand binding to the human erythrocyte glucose transporter. Evidence for an alternating conformation model for transport. *Biochemistry* **20**, 5108-5113.

Gras, D., Roze, E., Caillet, S., Méneret, A., Doummar, D., Billette de Villemeur, T., Vidailhet, M., and Mochel, F. (2014a). GLUT1 deficiency syndrome: An update. *Revue Neurologique* **170**, 91-99.

Gras, D., Roze, E., Caillet, S., Méneret, A., Doummar, D., Billette de Villemeur, T., Vidailhet, M., and Mochel, F. (2014b). GLUT1 deficiency syndrome: an update. *Rev Neurol (Paris)* **170**, 91-99.

Graybill, C., van Hoek, A., Desai, D., Carruthers, A., and Carruthers, A. (2006). Ultrastructure of Human Erythrocyte GLUT1. *Biochemistry* **45**, 8096-8107.

Greish, K., Sawa, T., Fang, J., Akaike, T., and Maeda, H. (2004). SMA–doxorubicin, a new polymeric micellar drug for effective targeting to solid tumours. *Journal of Controlled Release* **97**, 219-230.

Grethen, A., Glueck, D., and Keller, S. (2018). Role of Coulombic Repulsion in Collisional Lipid Transfer Among SMA(2:1)-Bounded Nanodiscs. *The Journal of membrane biology* **251**, 443-451.

Gulati, S., Jamshad, M., Knowles, Timothy J., Morrison, Kerrie A., Downing, R., Cant, N., Collins, R., Koenderink, Jan B., Ford, Robert C., Overduin, M., *et al.* (2014). Detergent-free purification of ABC (ATP-binding-cassette) transporters. *Biochemical Journal* 461, 269-278.

Gupta, K., Li, J., Liko, I., Gault, J., Bechara, C., Wu, D., Hopper, J.T.S., Giles, K., Benesch, J.L.P., and Robinson, C.V. (2018). Identifying key membrane protein lipid interactions using mass spectrometry. *Nature protocols* 13, 1106.

Haber, E., and Anfinsen, C.B. (1962). Side-chain interactions governing the pairing of half-cystine residues in ribonuclease. *J Biol Chem* 237, 1839-1844.

Hahn, F., Etzkorn, M., Raschle, T., and Wagner, G. (2013). Optimized phospholipid bilayer nanodiscs facilitate high-resolution structure determination of membrane proteins. *Journal of the American Chemical Society* 135, 1919-1925.

Haines, T.H. (2001). Do sterols reduce proton and sodium leaks through lipid bilayers? *Progress in lipid research* 40, 299-324.

Hall, S.C.L., Tognoloni, C., Charlton, J., Bragginton, E.C., Rothnie, A.J., Sridhar, P., Wheatley, M., Knowles, T.J., Arnold, T., Edler, K.J., *et al.* (2018). An acid-compatible co-polymer for the solubilization of membranes and proteins into lipid bilayer-containing nanoparticles. *Nanoscale* 10, 10609-10619.

Hamill, S., Cloherty, E.K., and Carruthers, A. (1999). The human erythrocyte sugar transporter presents two sugar import sites. *Biochemistry* 38, 16974-16983.

Harik, S.I., Kalaria, R.N., Andersson, L., Lundahl, P., and Perry, G. (1990). Immunocytochemical localization of the erythroid glucose transporter: abundance in tissues with barrier functions. *Journal of Neuroscience* 10, 3862-3872.

He, L., Aleksandrov, A.A., An, J., Cui, L., Yang, Z., Brouillette, C.G., and Riordan, J. (2014). Restoration of NBD1 thermal stability is necessary and sufficient to correct  $\Delta F508$  CFTR folding and assembly. *Journal of Molecular Biology* 427, 106-120.

He, L., Aleksandrov, A.A., An, J., Cui, L., Yang, Z., Brouillette, C.G., and Riordan, J.R. (2015). Restoration of NBD1 Thermal Stability Is Necessary and Sufficient to Correct  $\Delta F508$  CFTR Folding and Assembly. *Journal of Molecular Biology* 427, 106-120.

He, L., Aleksandrov, L.A., Cui, L., Jensen, T.J., Nesbitt, K.L., and Riordan, J.R. (2010). Restoration of domain folding and interdomain assembly by second-site



suppressors of the DeltaF508 mutation in CFTR. *FASEB journal : official publication of the Federation of American Societies for Experimental Biology* 24, 3103-3112.

He, L., Kota, P., Aleksandrov, A.A., Cui, L., Jensen, T., Dokholyan, N.V., and Riordan, J.R. (2013). Correctors of  $\Delta F508$  CFTR restore global conformational maturation without thermally stabilizing the mutant protein. *FASEB journal : official publication of the Federation of American Societies for Experimental Biology* 27, 536-545.

Hebert, D.N., and Carruthers, A. (1991). Cholate-solubilized erythrocyte glucose transporters exist as a mixture of homodimers and homotetramers. *Biochemistry* 30, 4654-4658.

Hebert, D.N., and Carruthers, A. (1992). Glucose transporter oligomeric structure determines transporter function. Reversible redox-dependent interconversions of tetrameric and dimeric GLUT1. *J Biol Chem* 267, 23829-23838.

Hediger, M.A., Cl  men  on, B., Burrier, R.E., and Bruford, E.A. (2013). The ABCs of membrane transporters in health and disease (SLC series): introduction. *Molecular aspects of medicine* 34, 95-107.

Hediger, M.A., Romero, M.F., Peng, J.-B., Rolfs, A., Takanaga, H., and Bruford, E.A. (2004). The ABCs of solute carriers: physiological, pathological and therapeutic implications of human membrane transport proteins. *Pfl  gers Archiv* 447, 465-468.

Heged  s, T., Aleksandrov, A., Mengos, A., Cui, L., Jensen, T.J., and Riordan, J.R. (2009). Role of individual R domain phosphorylation sites in CFTR regulation by protein kinase A. *Biochimica et Biophysica Acta (BBA) - Biomembranes* 1788, 1341-1349.

Helenius, A., and Simons, K. (1975). Solubilization of membranes by detergents. *Biochim Biophys Acta* 415, 29-79.

Helms, J.B., and Rothman, J.E. (1992). Inhibition by brefeldin A of a Golgi membrane enzyme that catalyses exchange of guanine nucleotide bound to ARF. *Nature* 360, 352-354.

Henderson, R. (1977). THE PURPLE MEMBRANE FROM HALOBACTERIUM HALOBIUM. *Annual Review of Biophysics and Bioengineering* 6, 87-109.

Henderson, R., and Unwin, P.N. (1975). Three-dimensional model of purple membrane obtained by electron microscopy. *Nature* 257, 28-32.

Hertz, L., Peng, L., and Dienel, G.A. (2007). Energy metabolism in astrocytes: high rate of oxidative metabolism and spatiotemporal dependence on glycolysis/glycogenolysis. *J Cereb Blood Flow Metab* 27, 219-249.

Heydenreich, F.M., Vuckovic, Z., Matkovic, M., and Veprintsev, D.B. (2015). Stabilization of G protein-coupled receptors by point mutations. *Front Pharmacol* 6, 82-82.

Hildebrandt, E., Khazanov, N., Kappes, J.C., Dai, Q., Senderowitz, H., and Urbatsch, I.L. (2017). Specific stabilization of CFTR by phosphatidylserine. *Biochim Biophys Acta Biomembr* 1859, 289-293.

Hildebrandt, E., Zhang, Q., Cant, N., Ding, H., Dai, Q., Peng, L., Fu, Y., DeLucas, L.J., Ford, R., Kappes, J.C., *et al.* (2014). A survey of detergents for the purification of stable, active human cystic fibrosis transmembrane conductance regulator (CFTR). *Biochim Biophys Acta* 1838, 2825-2837.

Hinkle, P., Sogin, D., Wheeler, T., Teleford, J., and Vivo, D. (1976). Studies of the glucose transporter from human erythrocytes reconstituted in liposomes. In *Function and Molecular Aspect of Biomembrane Transport*, E.e.a.o. Quagliariello, SK, ed. (Amsterdam: Elsevier/North-Holland Biomedical Press), p. 487-494

Hirama, T., Lu, S.M., Kay, J.G., Maekawa, M., Kozlov, M.M., Grinstein, S., and Fairn, G.D. (2017). Membrane curvature induced by proximity of anionic phospholipids can initiate endocytosis. *Nature communications* 8, 1393.

Hirayama, H., Kimura, Y., Kioka, N., Matsuo, M., and Ueda, K. (2013). ATPase activity of human ABCG1 is stimulated by cholesterol and sphingomyelin. *Journal of Lipid Research* 54, 496-502.

Huang, K.S., Bayley, H., Liao, M.J., London, E., and Khorana, H.G. (1981). Refolding of an integral membrane protein. Denaturation, renaturation, and reconstitution of intact bacteriorhodopsin and two proteolytic fragments. *J Biol Chem* 256, 3802-3809.

Humphrey, W., Dalke, A., and Schulten, K. (1996). VMD: Visual molecular dynamics. *Journal of Molecular Graphics* 14, 33-38.

Hunt, J.F., Wang, C., and Ford, R.C. Cystic Fibrosis Transmembrane Conductance Regulator (ABCC7) Structure. *Cold Spring Harbor Perspectives in Medicine* 3, a009514.

- Hunt, J.F., Wang, C., and Ford, R.C. (2013). Cystic fibrosis transmembrane conductance regulator (ABCC7) structure. *Cold Spring Harb Perspect Med* 3, a009514.
- Huynh, K.W., Cohen, M.R., and Moiseenkova-Bell, V.Y. (2014). Application of amphipols for structure-functional analysis of TRP channels. *The Journal of membrane biology* 247, 843-851.
- Ibarra-Molero, B., Zitzewitz, J.A., and Matthews, C.R. (2004). Salt-bridges can Stabilize but do not Accelerate the Folding of the Homodimeric Coiled-coil Peptide GCN4-p1. *Journal of Molecular Biology* 336, 989-996.
- Jamshad, M., Charlton, J., Lin, Y.-P., Routledge, Sarah J., Bawa, Z., Knowles, Timothy J., Overduin, M., Dekker, N., Dafforn, Tim R., Bill, Roslyn M., *et al.* (2015). G-protein coupled receptor solubilization and purification for biophysical analysis and functional studies, in the total absence of detergent. *Bioscience Reports* 35.
- Jardetzky, O. (1966). Simple allosteric model for membrane pumps. *Nature* 211, 969-970.
- Jin, L., Milazzo, A.-C., Kleinfelder, S., Li, S., Leblanc, P., Duttweiler, F., Bouwer, J.C., Peltier, S.T., Ellisman, M.H., and Xuong, N.-H. (2008). Applications of direct detection device in transmission electron microscopy. *Journal of Structural Biology* 161, 352-358.
- Jones, D.A., Ros, J., Landolt, H., Fillenz, M., and Boutelle, M.G. (2000a). Dynamic Changes in Glucose and Lactate in the Cortex of the Freely Moving Rat Monitored Using Microdialysis. *J Neurochem* 75, 1703-1708.
- Jones, P.M., and George, A.M. (2004). The ABC transporter structure and mechanism: perspectives on recent research. *Cell Mol Life Sci* 61, 682-699.
- Jones, P.M., George, A.M.i., M., and Boutelle, M.G. (2000b). Symmetry and structure in P-glycoprotein and ABC transporters. *European Journal of Biochemistry* 267, 5298-5305.
- Joost, H.G., Bell, G.I., Best, J.D., Birnbaum, M.J., Charron, M.J., Chen, Y.T., Doege, H., James, D.E., Lodish, H.F., Moley, K.H., *et al.* (2002). Nomenclature of the GLUT/SLC2A family of sugar/polyol transport facilitators. *Am J Physiol Endocrinol Metab* 282, E974-976.
- Kabsch, W., and Sander, C. (1983). Dictionary of protein secondary structure: pattern recognition of hydrogen-bonded and geometrical features. *Biopolymers* 22, 2577-2637.

Kalid, O., Mense, M., and Fischman, S. (2010). Small molecule correctors of F508del-CFTR discovered by structure-based virtual screening. *Journal of computer-aided molecular design* 24, 971-991.

Kapoor, K., Finer-Moore, J., Pedersen, B., Caboni, L., Waight, A., Hillig, R., Bringmann, P., Heisler, I., Müller, T., Siebeneicher, H., *et al.* (2016). Mechanism of inhibition of human glucose transporter GLUT1 is conserved between cytochalasin B and phenylalanine amides. *Proceedings of the National Academy of Sciences of the United States of America* 113, 4711-4716.

Kasahara, M., and Hinkle, P.C. (1977). Reconstitution and purification of the D-glucose transporter from human erythrocytes. *J Biol Chem* 252, 7384-7390.

Kayano, T., Burant, C.F., Fukumoto, H., Gould, G.W., Fan, Y.S., Eddy, R.L., Byers, M.G., Shows, T.B., Seino, S., and Bell, G.I. (1990). Human facilitative glucose transporters. Isolation, functional characterization, and gene localization of cDNAs encoding an isoform (GLUT5) expressed in small intestine, kidney, muscle, and adipose tissue and an unusual glucose transporter pseudogene-like sequence (GLUT6). *J Biol Chem* 265, 13276-13282.

Kendrew, J.C., Bodo, G., Dintzis, H.M., Parrish, R.G., Wyckoff, H., and Phillips, D.C. (1958). A Three-Dimensional Model of the Myoglobin Molecule Obtained by X-Ray Analysis. *Nature* 181, 662-666.

Kendrew, J.C., Dickerson, R.E., Strandberg, B.E., Hart, R.G., Davies, D.R., Phillips, D.C., and Shore, V.C. (1960). Structure of myoglobin: A three-dimensional Fourier synthesis at 2 Å. resolution. *Nature* 185, 422-427.

Kerem, B., Rommens, J., Buchanan, J., Markiewicz, D., Cox, T., Chakravarti, A., Buchwald, M., and Tsui, L. (1989). Identification of the cystic fibrosis gene: genetic analysis. *Science* 245, 1073-1080.

Kim, S., Kim, D.H., Jung, W.-H., and Koo, J.S. (2013). Metabolic phenotypes in triple-negative breast cancer. *Tumor Biology* 34, 1699-1712.

Klepper, J., Scheffer, H., Elsaid, M., Kamsteeg, E., Leferink, M., and Ben-Omran, T. (2009). Autosomal recessive inheritance of GLUT1 deficiency syndrome. *Neuropediatrics* 40, 207-210.

Klepper, J., and Voit, T. (2002). Facilitated glucose transporter protein type 1 (GLUT1) deficiency syndrome: impaired glucose transport into brain-- a review. *Eur J Pediatr* 161, 295-304.

Knowles, T.J., Finka, R., Smith, C., Lin, Y.-P., Dafforn, T., and Overduin, M. (2009). Membrane Proteins Solubilized Intact in Lipid Containing Nanoparticles

Bounded by Styrene Maleic Acid Copolymer. *Journal of the American Chemical Society* **131**, 7484-7485.

Komar, J., Alvira, S., Schulze, R.J., Martin, R., Lycklama a Nijeholt, J.A., Lee, S.C., Dafforn, T.R., Deckers-Hebestreit, G., Berger, I., Schaffitzel, C., *et al.* (2016). Membrane protein insertion and assembly by the bacterial holo-translocon SecYEG–SecDF–YajC–YidC. *Biochemical Journal* **473**, 3341-3354.

Korkeila, E., JAAKKOLA, P.M., SYRJÄNEN, K., PYRHÖNEN, S., and SUNDSTRÖM, J. (2011). Pronounced Tumour Regression after Radiotherapy is Associated with Negative/Weak Glucose Transporter-1 Expression in Rectal Cancer. *Anticancer Research* **31**, 311-315.

Krasnov, K.V., Tzetis, M., Cheng, J., Guggino, W.B., and Cutting, G.R. (2008). Localization studies of rare missense mutations in cystic fibrosis transmembrane conductance regulator (CFTR) facilitate interpretation of genotype-phenotype relationships. *Human mutation* **29**, 1364-1372.

Kuijper, M., van Hoften, G., Janssen, B., Geurink, R., De Carlo, S., Vos, M., van Duinen, G., van Haeringen, B., and Storms, M. (2015). FEI's direct electron detector developments: Embarking on a revolution in cryo-TEM. *Journal of structural biology* **192**, 179-187.

Kurisu, G., Zhang, H., Smith, J.L., and Cramer, W.A. (2003). Structure of the cytochrome b6f complex of oxygenic photosynthesis: tuning the cavity. *Science* **302**, 1009-1014.

Laganowsky, A., Reading, E., Hopper, J.T.S., and Robinson, C.V. (2013). Mass spectrometry of intact membrane protein complexes. *Nature protocols* **8**, 639.

Landreh, M., Marty, M.T., Gault, J., and Robinson, C.V. (2016). A sliding selectivity scale for lipid binding to membrane proteins. *Current opinion in structural biology* **39**, 54-60.

Laursen, M., Yatime, L., Nissen, P., and Fedosova, N. (2013). Crystal structure of the high-affinity Na<sup>+</sup>K<sup>+</sup>-ATPase-ouabain complex with Mg<sup>2+</sup> bound in the cation binding site. *Proceedings of the National Academy of Sciences of the United States of America* **110**, 10958-10963.

Le Bon, C., Marconnet, A., Masscheleyn, S., Popot, J.-L., and Zoonens, M. (2018). Folding and stabilizing membrane proteins in amphipol A8-35. *Methods (San Diego, Calif)* **147**, 95-105.

Lee, A.G. (2004). How lipids affect the activities of integral membrane proteins. *Biochimica et biophysica acta* **1666**, 62-87.

Lee, A.G. (2005). How lipids and proteins interact in a membrane: a molecular approach. *Molecular bioSystems* 1, 203-212.

Lee, S.C., Khalid, S., Pollock, N.L., Knowles, T.J., Edler, K., Rothnie, A.J., O, R.T.T., and Dafforn, T.R. (2016a). Encapsulated membrane proteins: A simplified system for molecular simulation. *Biochimica et biophysica acta* 1858, 2549-2557.

Lee, S.C., Knowles, T.J., Postis, V.L., Jamshad, M., Parslow, R.A., Lin, Y.P., Goldman, A., Sridhar, P., Overduin, M., Muench, S.P., *et al.* (2016b). A method for detergent-free isolation of membrane proteins in their local lipid environment. *Nature protocols* 11, 1149-1162.

Lee, S.C., and Pollock, N.L. (2016). Membrane proteins: is the future disc shaped? *Biochemical Society transactions* 44, 1011-1018.

LeFevre, P.G. (1948). Evidence of active transfer of certain non-electrolytes across the human red cell membrane. *J Gen Physiol* 31, 505-527.

Levy, H., Kalish, L.A., Huntington, I., Weller, N., Gerard, C., Silverman, E.K., Celedon, J.C., Pier, G.B., and Weiss, S.T. (2007). Inflammatory markers of lung disease in adult patients with cystic fibrosis. *Pediatr Pulmonol* 42, 256-262.

Lew, S., Caputo, G.A., and London, E. (2003). The Effect of Interactions Involving Ionizable Residues Flanking Membrane-Inserted Hydrophobic Helices upon Helix-Helix Interaction. *Biochemistry* 42, 10833-10842.

Lewis, H., Buchanan, S.G., Burley, S.K., Connors, K., Dickey, M., Dorwart, M., Fowler, R., Gao, X., Guggino, W.B., Hendrickson, W.A., *et al.* (2004). Structure of nucleotide-binding domain 1 of the cystic fibrosis transmembrane conductance regulator. *The EMBO journal* 23, 282-293.

Lewis, H.A., Wan, C., Zhao, X., Hamuro, Y., Connors, K., Kearins, M.C., Lu, F., Sauder, M.J., Molnar, K.S., Koales, S.J., *et al.* (2010). Structure and dynamics of NBD1 from CFTR characterized using crystallography and hydrogen/deuterium exchange mass spectrometry. *Journal of Molecular Biology* 396, 406-430.

Liberti, M.V., and Locasale, J.W. (2016). The Warburg Effect: How Does it Benefit Cancer Cells? *Trends in biochemical sciences* 41, 211-218.

Lindhoud, S., Carvalho, V., Pronk, J.W., and Aubin-Tam, M.E. (2016). SMA-SH: Modified Styrene-Maleic Acid Copolymer for Functionalization of Lipid Nanodiscs. *Biomacromolecules* 17, 1516-1522.

Linsdell, P. (2014). Cystic fibrosis transmembrane conductance regulator chloride channel blockers: Pharmacological, biophysical and physiological relevance. *World journal of biological chemistry* 5, 26-39.

Lippman, M.E., Bates, S., Huff, K.K., Davidson, N., and Dickson, R.B. (1987). Estrogens regulate production of specific growth factors in hormone-dependent human breast cancer. *The Journal of Laboratory and Clinical Medicine* 109, 230-235.

Littlewood, J.M. (1992). Cystic fibrosis: gastrointestinal complications. *British medical bulletin* 48, 847-859.

Liu, F., Zhang, Z., Csanády, L., Gadsby, D.C., and Chen, J. (2017). Molecular Structure of the Human CFTR Ion Channel. *Cell* 169, 85-95.e88.

Liu, Y., Gonen, S., Gonen, T., and Yeates, T.O. (2018). Near-atomic cryo-EM imaging of a small protein displayed on a designed scaffolding system. *Proceedings of the National Academy of Sciences* 115, 3362-3367.

Liu, Z., Yan, H., Wang, K., Kuang, T., Zhang, J., Gui, L., An, X., and Chang, W. (2004). Crystal structure of spinach major light-harvesting complex at 2.72 Å resolution. *Nature* 428, 287-292.

Lloyd, K., Ojelabi, O., Simon, A., De Zutter, J., and Carruthers, A. (2017). Kinetic Basis of Cis- and Trans-Allostery in GLUT1-Mediated Sugar Transport. *The Journal of membrane biology*.

Logez, C., Damian, M., Legros, C., Dupré, C., Guéry, M., Mary, S., Wagner, R., M'Kadmi, C., Nosjean, O., Fould, B., *et al.* (2016). Detergent-free Isolation of Functional G Protein-Coupled Receptors into Nanometric Lipid Particles. *Biochemistry* 55, 38-48.

London, E., and Khorana, H.G. (1982). Denaturation and renaturation of bacteriorhodopsin in detergents and lipid-detergent mixtures. *J Biol Chem* 257, 7003-7011.

Long, S., Campbell, E., and Mackinnon, R. (2005). Crystal structure of a mammalian voltage-dependent Shaker family K<sup>+</sup> channel. *Science* 309, 897-903.

Loo, T.W., Bartlett, M.C., and Clarke, D.M. (2010). The V510D suppressor mutation stabilizes  $\Delta$ F508-CFTR at the cell surface. *Biochemistry* 49, 6352-6357.

Looyenga, B., VanOpstall, C., Lee, Z., Bell, J., Lodge, E., Wrobel, K., Arnoys, E., and Louters, L. (2016). Determination of GLUT1 Oligomerization Parameters

using Bioluminescent Förster Resonance Energy Transfer. *Scientific Reports* 6, 29130.

Lu, B., Li, L., Schneider, M., Hodges, C.A., Cotton, C.U., Burgess, J.D., and Kelley, T.J. (2019). Electrochemical measurement of membrane cholesterol correlates with CFTR function and is HDAC6-dependent. *Journal of Cystic Fibrosis* 18, 175-181.

Luiken, J., Coort, S., Koonen, D., van der Horst, D., Bonen, A., Zorzano, A., and Glatz, J. (2004). Regulation of cardiac long-chain fatty acid and glucose uptake by translocation of substrate transporters. *Pflügers Arch* 448, 1-15.

Lukacs, G.L., and Verkman, A.S. (2012). CFTR: folding, misfolding and correcting the  $\Delta F508$  conformational defect. *Trends in molecular medicine* 18, 81-91.

Lundahl, P., Mascher, E., Andersson, L., Englund, A.K., Greijer, E., Kameyama, K., and Takagi, T. (1991). Active and monomeric human red cell glucose transporter after high performance molecular-sieve chromatography in the presence of octyl glucoside and phosphatidylserine or phosphatidylcholine. *Biochimica et biophysica acta* 1067, 177-186.

Lux, S.E. (2016). Anatomy of the red cell membrane skeleton: unanswered questions. *Blood* 127, 187-199.

Macheda, M.L., Rogers, S., and Best, J.D. (2005). Molecular and cellular regulation of glucose transporter (GLUT) proteins in cancer. *Journal of Cellular Physiology* 202, 654-662.

Maestro (2016). Schrödinger Release 2016-3 (Schrödinger, LLC New York, NY).

Maher, F., Vannucci, S., and Simpson, I., IA (1994). Glucose transporter proteins in brain. *FASEB journal : official publication of the Federation of American Societies for Experimental Biology* 8, 1003-1011.

Mailhot, G., Rabasa-Lhoret, R., Moreau, A., Berthiaume, Y., and Levy, E. (2010). Correction: CFTR Depletion Results in Changes in Fatty Acid Composition and Promotes Lipogenesis in Intestinal Caco 2/15 Cells. *PLOS ONE* 5, 10.1371/annotation/f1379b1378a1379d1372-1374be1373-4981-1392f1374-a1373b1374cb1370b1370bf1375.

Maiz-Carro, L., and Navas-Elorza, E. (2002). Nontuberculous mycobacterial pulmonary infection in patients with cystic fibrosis: diagnosis and treatment. *American journal of respiratory medicine : drugs, devices, and other interventions* 1, 107-117.



- Manavalan, P., Dearborn, D.G., McPherson, J.M., and Smith, A.E. (1995). Sequence homologies between nucleotide binding regions of CFTR and G-proteins suggest structural and functional similarities. *Federation of European Biochemical Societies* 366, 87-91.
- Mann, G.E., Yudilevich, D.L., and Sobrevia, L. (2003). Regulation of Amino Acid and Glucose Transporters in Endothelial and Smooth Muscle Cells. *Physiol Rev* 83, 183-252.
- Marinko, J.T., Huang, H., Penn, W.D., Capra, J.A., Schleich, J.P., and Sanders, C.R. (2019). Folding and Misfolding of Human Membrane Proteins in Health and Disease: From Single Molecules to Cellular Proteostasis. *Chemical reviews*.
- Marson, F.A.L., Bertuzzo, C.S., and Ribeiro, J.D. (2016). Classification of CFTR mutation classes. *The Lancet Respiratory Medicine* 4, e37-e38.
- Martin, C., Hamard, C., Kanaan, R., Boussaud, V., Grenet, D., Abély, M., Hubert, D., Munck, A., Lemonnier, L., and Burgel, P.-R. (2016). Causes of death in French cystic fibrosis patients: The need for improvement in transplantation referral strategies! *Journal of Cystic Fibrosis* 15, 204-212.
- McCoy, A.J., Grosse-Kunstleve, R.W., Adams, P.D., Winn, M.D., Storoni, L.C., and Read, R.J. (2007). Phaser crystallographic software. *Journal of applied crystallography* 40, 658-674.
- McKoy, N.A., Wilson, L.M., Saldanha, I.J., Odelola, O.A., and Robinson, K.A. (2016). Active cycle of breathing technique for cystic fibrosis. *The Cochrane database of systematic reviews* 7, Cd007862.
- Meng, X., Clews, J., Ciuta, A.D., Martin, E.R., and Ford, R.C. (2019). CFTR structure, stability, function and regulation. *Biological chemistry*.
- Meng, X., Clews, J., Kargas, V., Wang, X., and Ford, R.C. (2017a). The cystic fibrosis transmembrane conductance regulator (CFTR) and its stability. *Cellular and molecular life sciences : CMLS* 74, 23-38.
- Meng, X., Wang, Y., Wang, X., Wrennall, J.A., Rimington, T.L., Li, H., Cai, Z., Ford, R.C., and Sheppard, D.N. (2017b). Two Small Molecules Restore Stability to a Sub-population of the Cystic Fibrosis Transmembrane conductance Regulator with the Predominant Disease-causing Mutation. *Journal of Biological Chemistry*.

Mijnders, M., Kleizen, B., and Braakman, I. (2017). Correcting CFTR folding defects by small-molecule correctors to cure cystic fibrosis. *Current Opinion in Pharmacology* 34, 83-90.

Milazzo, A.-C., Cheng, A., Moeller, A., Lyumkis, D., Jacovetty, E., Polukas, J., Ellisman, M.H., Xuong, N.-H., Carragher, B., and Potter, C.S. (2011). Initial evaluation of a direct detection device detector for single particle cryo-electron microscopy. *Journal of Structural Biology* 176, 404-408.

Minskaia, E., and Ryan, M.D. (2013). Protein coexpression using FMDV 2A: effect of "linker" residues. *BioMed research international* 2013, 291730-291730.

Mirtajani, S., Farnia, P., Hassanzad, M., Ghanavi, J., Farnia, P., and Velayati, A. (2017). Geographical distribution of cystic fibrosis; The past 70 years of data analyzis. *Biomedical and Biotechnology Research Journal (BBRJ)* 1, 105-112.

Mitra, N. (2013). Nanodiscs: membrane protein research in near-native conditions. In *Materials and Methods*.

Modok, S., Heyward, C., and Callaghan, R. (2004). P-glycoprotein retains function when reconstituted into a sphingolipid- and cholesterol-rich environment. *J Lipid Res* 45, 1910-1918.

Molenaar, D., van Berlo, R., de Ridder, D., and Teusink, B. (2009). Shifts in growth strategies reflect tradeoffs in cellular economics. *Molecular systems biology* 5, 323.

Moore, P.J., and Tarran, R. (2018). The epithelial sodium channel (ENaC) as a therapeutic target for cystic fibrosis lung disease. *Expert Opinion on Therapeutic Targets* 22, 687-701.

Moraes, I., Evans, G., Sanchez-Weatherby, J., Newstead, S., and Stewart, P.D. (2014). Membrane protein structure determination - the next generation. *Biochimica et biophysica acta* 1838, 78-87.

Mornon, J.-P., Lehn, P., and Callebaut, I. (2008). Atomic model of human cystic fibrosis transmembrane conductance regulator: Membrane-spanning domains and coupling interfaces. *Cellular and Molecular Life Sciences* 65, 2594-2612.

Morrison, K., Akram, A., Mathews, A., Khan, Z.A., Patel, J.H., Zhou, C., Hardy, D.J., Moore-Kelly, C., Patel, R., Odiba, V., *et al.* (2016a). Membrane protein extraction and purification using styrene-maleic acid (SMA) co-polymer: Effect of variations in polymer structure. *Biochemical Journal*.

Morrison, K.A., Akram, A., Mathews, A., Khan, Z.A., Patel, J.H., Zhou, C., Hardy, D.J., Moore-Kelly, C., Patel, R., Odiba, V., *et al.* (2016b). Membrane protein extraction and purification using styrene-maleic acid (SMA) co-polymer. *Biochemical Journal* 473, 4349-4360.

Mueckler, M., and Thorens, B. (2013). The SLC2 (GLUT) family of membrane transporters. *Molecular aspects of medicine* 34, 121-138.

Muhlebach, M.S., Clancy, J.P., Heltshe, S.L., Ziady, A., Kelley, T., Accurso, F., Pilewski, J., Mayer-Hamblett, N., Joseloff, E., and Sagel, S.D. (2016). Biomarkers for cystic fibrosis drug development. *Journal of Cystic Fibrosis* 15, 714-723.

Mulkidjanian, A.Y., Galperin, M.Y., and Koonin, E.V. (2009). Co-evolution of primordial membranes and membrane proteins. *Trends in biochemical sciences* 34, 206-215.

Murakami, S., Nakashima, R., Yamashita, E., and Yamaguchi, A. (2002). Crystal structure of bacterial multidrug efflux transporter AcrB. *Nature* 419, 587-593.

Murata, K., and Wolf, M. (2018). Cryo-electron microscopy for structural analysis of dynamic biological macromolecules. *Biochimica et Biophysica Acta (BBA) - General Subjects* 1862, 324-334.

Niesen, M.J.M., Marshall, S.S., Miller, T.F., and Clemons, W.M. (2017). Improving membrane protein expression by optimizing integration efficiency. *Journal of Biological Chemistry* 292, 19537-19545.

Noble, A.J., Dandey, V.P., Wei, H., Brasch, J., Chase, J., Acharya, P., Tan, Y.Z., Zhang, Z., Kim, L.Y., Scapin, G., *et al.* (2017). Routine Single Particle CryoEM Sample and Grid Characterization by Tomography. *bioRxiv*.

Nomura, N., Verdon, G., Kang, H., Shimamura, T., Nomura, Y., Sonoda, Y., Hussien, S., Qureshi, A., Coincon, M., Sato, Y., *et al.* (2015a). Structure and mechanism of the mammalian fructose transporter GLUT5. *Nature* 526, 397-401.

Nomura, N., Verdon, G., Kang, H.J., Shimamura, T., Nomura, Y., Sonoda, Y., Hussien, S.A., Qureshi, A.A., Coincon, M., Sato, Y., *et al.* (2015b). Structure and mechanism of the mammalian fructose transporter GLUT5. *Nature* 526, 397-401.

Okino, S.T., Chichester, C.H., and Whitlock, J.P., Jr. (1998). Hypoxia-inducible mammalian gene expression analyzed in vivo at a TATA-driven promoter and at an initiator-driven promoter. *J Biol Chem* 273, 23837-23843.

Oluwole, A.O., Danielczak, B., Meister, A., Babalola, J.O., Vargas, C., and Keller, S. (2017). Solubilization of Membrane Proteins into Functional Lipid-Bilayer Nanodiscs Using a Diisobutylene/Maleic Acid Copolymer. *Angewandte Chemie (International Ed in English)* 56, 1919-1924.

Orenti, A., Zolin, A., Naehrlich, L., and van Rens, J. (2018). ECFSPR Annual Report 2016, E.C.F. Society, ed. (Denmark).

Orwick-Rydmark, M., Lovett, J.E., Graziadei, A., Lindholm, L., Hicks, M.R., and Watts, A. (2012). Detergent-Free Incorporation of a Seven-Transmembrane Receptor Protein into Nanosized Bilayer Lipodisc Particles for Functional and Biophysical Studies. *Nano Letters* 12, 4687-4692.

Otwinowski, Z., and Minor, W. (1997). [20] Processing of X-ray diffraction data collected in oscillation mode. In *Methods in Enzymology* (Academic Press), pp. 307-326.

Palczewski, K., Kumasaka, T., Hori, T., Behnke, C.A., Motoshima, H., Fox, B.A., Le Trong, I., Teller, D.C., Okada, T., Stenkamp, R.E., *et al.* (2000). Crystal structure of rhodopsin: A G protein-coupled receptor. *Science* 289, 739-745.

Palovcak, E., Wang, F., Zheng, S.Q., Yu, Z., Li, S., Bulkley, D., Agard, D.A., and Cheng, Y. (2018). A simple and robust procedure for preparing graphene-oxide cryo-EM grids. *bioRxiv*.

Pankow, S., Bamberger, C., Calzolari, D., Martinez-Bartolome, S., Lavalleye-Adam, M., Balch, W.E., and Yates, J.R., 3rd (2015). F508 CFTR interactome remodelling promotes rescue of cystic fibrosis. *Nature* 528, 510-516.

Pantelic, R.S., Meyer, J.C., Kaiser, U., Baumeister, W., and Plitzko, J.M. (2010). Graphene oxide: a substrate for optimizing preparations of frozen-hydrated samples. *Journal of structural biology* 170, 152-156.

Pao, S.S., Paulsen, I.T., and Saier, M.H., Jr. (1998). Major facilitator superfamily. *Microbiol Mol Biol Rev* 62, 1-34.

Park, K.-H., Billon-Denis, E., Dahmane, T., Lebaupain, F., Pucci, B., Breyton, C., and Zito, F. (2011). In the cauldron of cell-free synthesis of membrane proteins: playing with new surfactants. *New Biotechnology* 28, 255-261.

Parmar, M., Rawson, S., Scarff, C.A., Goldman, A., Dafforn, T.R., Muench, S.P., and Postis, V.L.G. (2018). Using a SMALP platform to determine a sub-nm single particle cryo-EM membrane protein structure. *Biochimica et Biophysica Acta (BBA) - Biomembranes* 1860, 378-383.

Pebay-Peyroula, E., Rummel, G., Rosenbusch, J.P., and Landau, E.M. (1997). X-ray Structure of Bacteriorhodopsin at 2.5 Angstroms from Microcrystals Grown in Lipidic Cubic Phases. *Science* 277, 1676-1681.

Peng, Y., Xing, S.N., Tang, H.Y., Wang, C.D., Yi, F.P., Liu, G.L., and Wu, X.M. (2019). Influence of glucose transporter 1 activity inhibition on neuroblastoma in vitro. *Gene* 689, 11-17.

Pezzulo, A.A., Tang, X.X., Hoegger, M.J., Alaiwa, M.H., Ramachandran, S., Moninger, T.O., Karp, P.H., Wohlford-Lenane, C.L., Haagsman, H.P., van Eijk, M., *et al.* (2012). Reduced airway surface pH impairs bacterial killing in the porcine cystic fibrosis lung. *Nature* 487, 109-113.

Phuan, P.-W., Veit, G., Tan, J.-A., Roldan, A., Finkbeiner, W.E., Haggie, P.M., Lukacs, G.L., and Verkman, A.S. (2018).  $\Delta F508$ -CFTR Modulator Screen Based on Cell Surface Targeting of a Chimeric Nucleotide Binding Domain 1 Reporter. *SLAS discovery : advancing life sciences R & D* 23, 823-831.

Phuan, P.-W., Veit, G., Tan, J., Roldan, A., Finkbeiner, W.E., Lukacs, G.L., and Verkman, A.S. (2014). Synergy-based small-molecule screen using a human lung epithelial cell line yields  $\Delta F508$ -CFTR correctors that augment VX-809 maximal efficacy. *Molecular pharmacology* 86, 42-51.

Pocanschi, C.L., Dahmane, T., Gohon, Y., Rappaport, F., Apell, H.-J., Kleinschmidt, J.H., and Popot, J.-L. (2006). Amphipathic Polymers: Tools To Fold Integral Membrane Proteins to Their Active Form. *Biochemistry* 45, 13954-13961.

Pollock, N.L., Rimington, T.L., and Ford, R.C. (2015). Characterizing diverse orthologues of the cystic fibrosis transmembrane conductance regulator protein for structural studies. *Biochemical Society transactions* 43, 894-900.

Popot, J.-L., Althoff, T., Bagnard, D., Banères, J.-L., Bazzacco, P., Billon-Denis, E., Catoire, L.J., Champeil, P., Charvolin, D., Cocco, M.J., *et al.* (2011). Amphipols From A to Z. *Annual Review of Biophysics* 40, 379-408.

Postis, V., Rawson, S., Mitchell, J.K., Lee, S.C., Parslow, R.A., Dafforn, T.R., Baldwin, S.A., and Muench, S.P. (2015). The use of SMALPs as a novel membrane protein scaffold for structure study by negative stain electron microscopy. *Biochimica et Biophysica Acta (BBA) - Biomembranes* 1848, 496-501.

Prabudiansyah, I., Kusters, I., Caforio, A., and Driessen, A.J.M. (2015). Characterization of the annular lipid shell of the Sec translocon. *Biochimica et Biophysica Acta (BBA) - Biomembranes* 1848, 2050-2056.

Prinz, N., Zolin, A., Konrad, K., Nährlich, L., Laubner, K., Olesen, H.V., Bauer, M., Jung, A., Frischer, T., Holl, R.W., *et al.* (2019). Characteristics of cystic fibrosis-related diabetes: Data from two different sources the European cystic fibrosis society patient registry and German/Austrian diabetes prospective follow-up registry. *Pediatric Diabetes*, 1-8.

Protasevich, I., Yang, Z., Wang, C., Atwell, S., Zhao, X., Emtage, S., Wetmore, D., Hunt, J.F., and Brouillette, C.G. (2010). Thermal unfolding studies show the disease causing F508del mutation in CFTR thermodynamically destabilizes nucleotide-binding domain 1. *Protein science : a publication of the Protein Society* 19, 1917-1931.

Qiu, W., Fu, Z., Xu, G.G., Grassucci, R.A., Zhang, Y., Frank, J., Hendrickson, W.A., and Guo, Y. (2018). Structure and activity of lipid bilayer within a membrane-protein transporter. *Proceedings of the National Academy of Sciences* 115, 12985-12990.

Rabeh, M.W., Bossard, F., Xu, H., Okiyoned, T., Bagdany, M., Mulvihill, C.M., Du, K., Bernardo, S., Liu, Y., Konermann, L., *et al.* (2012a). Correction of both NBD1 energetics and domain interface is required to restore  $\Delta F508$  CFTR folding and function. *Cell* 148, 150-163.

Rabeh, W., Bossard, F., Xu, H., Okiyoned, T., Bagdany, M., Mulvihill, Cory M., Du, K., di Bernardo, S., Liu, Y., Konermann, L., *et al.* (2012b). Correction of Both NBD1 Energetics and Domain Interface Is Required to Restore  $\Delta F508$  CFTR Folding and Function. *Cell* 148, 150-163.

Ravula, T., Hardin, N.Z., Ramadugu, S.K., Cox, S.J., and Ramamoorthy, A. (2018). Formation of pH-Resistant Monodispersed Polymer-Lipid Nanodiscs. *Angew Chem Int Ed Engl* 57, 1342-1345.

Reading, E., Hall, Z., Martens, C., Haghighi, T., Findlay, H., Ahdash, Z., Politis, A., and Booth, P.J. (2017). Interrogating Membrane Protein Conformational Dynamics within Native Lipid Compositions. *Angew Chem Int Ed Engl* 56, 15654-15657.

Reddy, V.S., Shlykov, M.A., Castillo, R., Sun, E.I., and Saier Jr, M.H. (2012). The major facilitator superfamily (MFS) revisited. *FEBS Journal*.

Ren, H.Y., Grove, D.E., De La Rosa, O., Houck, S.A., Sopha, P., Van Goor, F., Hoffman, B.J., and Cyr, D.M. (2013). VX-809 corrects folding defects in cystic fibrosis transmembrane conductance regulator protein through action on membrane-spanning domain 1. *Molecular biology of the cell* 24, 3016-3024.

Rich, D., Berger, H.A., Cheng, S.H., Travis, S.M., Saxena, M., Smith, A.E., and Welsh, M.J. (1993). Regulation of the cystic fibrosis transmembrane conductance regulator Cl<sup>-</sup> channel by negative charge in the R domain. *Journal of Biological Chemistry* 268, 20259-20267.

Rich, D.P., Anderson, M.P., Gregory, R.J., Cheng, S.H., Paul, S., Jefferson, D.M., McCann, J.D., Klinger, K.W., Smith, A.E., and Welsh, M.J. (1990). Expression of cystic fibrosis transmembrane conductance regulator corrects defective chloride channel regulation in cystic fibrosis airway epithelial cells. *Nature* 347, 358–363.

Richter, E.A. (2010). *Glucose Utilization* (John Wiley & Sons, Inc.).

Riordan, J., Rommens, J., Kerem, B., Alon, N., Rozmahel, R., Grzelczak, Z., Zielenski, J., Lok, S., Plavsic, N., Chou, J., *et al.* (1989a). Identification of the cystic fibrosis gene: cloning and characterization of complementary DNA. *Science* 245, 1066-1073.

Riordan, J.R. (2008). CFTR function and prospects for therapy. *Annu Rev Biochem* 77, 701-726.

Riordan, J.R., Rommens, J.M., Kerem, B., Alon, N., Rozmahel, R., Grzelczak, Z., Zielenski, J., Lok, S., Plavsic, N., Chou, J.L., *et al.* (1989b). Identification of the cystic fibrosis gene: cloning and characterization of complementary DNA. *Science* 245, 1066-1073.

Ritchie, T.K., Grinkova, Y.V., Bayurt, T.H., Denisov, I.G., Zolnerciks, J.K., Atkins, W.M., and Sligar, S.G. (2009). Reconstitution of Membrane Proteins in Phospholipid Bilayer Nanodiscs. *Methods in Enzymology* 464, 211-232.

Robichaud, T., Appleyard, A., Herbert, R., Henderson, P., and Carruthers, A. (2011). Determinants of ligand binding affinity and cooperativity at the GLUT1 endofacial site. *Biochemistry* 50, 3137-3148.

Romano, A.H., and Conway, T. (1996). Evolution of carbohydrate metabolic pathways. *Research in Microbiology* 147, 448-455.

Rosenberg, M.F., Kamis, A.B., Aleksandrov, L.A., Ford, R.C., and Riordan, J.R. (2004). Purification and Crystallization of the Cystic Fibrosis Transmembrane Conductance Regulator (CFTR). *Journal of Biological Chemistry* 279, 39051-39057.

Rosenberg, M.F., O’Ryan, L.P., Hughes, G., Zhao, Z., Aleksandrov, L.A., Riordan, J.R., and Ford, R.C. (2012). The Cystic Fibrosis Transmembrane Conductance Regulator (CFTR): THREE-DIMENSIONAL STRUCTURE AND

LOCALIZATION OF A CHANNEL GATE. *The Journal of Biological Chemistry* 286, 42647-42654.

Rothnie, A., Theron, D., Soceneantu, L., Martin, C., Traikia, M., Berridge, G., Higgins, C.F., Devaux, P.F., and Callaghan, R. (2001). The importance of cholesterol in maintenance of P-glycoprotein activity and its membrane perturbing influence. *European biophysics journal* : EBJ 30, 430-442.

Rungaldier, S., Oberwagner, W., Salzer, U., Csaszar, E., and Prohaska, R. (2013). Stomatin interacts with GLUT1/SLC2A1, band 3/SLC4A1, and aquaporin-1 in human erythrocyte membrane domains. *Biochim Biophys Acta* 1828, 956-966.

Sakai, H., and Tsukihara, T. (1998). Structures of membrane proteins determined at atomic resolution. *J Biochem* 124, 1051-1059.

Sanders, C.R., and Myers, J.K. (2004). Disease-Related Misassembly of Membrane Proteins. *Annual Review of Biophysics and Biomolecular Structure* 33, 25-51.

Schechter, M.S. (2018). Reevaluating approaches to cystic fibrosis pulmonary exacerbations. *Pediatric Pulmonology* 53, S51-S63.

Schmidt, A., Mendoza, J.L., and Thomas, P.J. (2011). Biochemical and biophysical approaches to probe CFTR structure. *Methods in molecular biology* (Clifton, NJ) 741, 365-376.

Schmidt, V., and Sturgis, J.N. (2018). Modifying styrene-maleic acid co-polymer for studying lipid nanodiscs. *Biochimica et biophysica acta* 1860, 777-783.

Schneider, E., and Hunke, S. (1998). ATP-binding-cassette (ABC) transport systems: Functional and structural aspects of the ATP-hydrolyzing subunits/domains. *FEMS Microbiology Reviews* 22, 1-20.

Schurmann, A., Doege, H., Ohnimus, H., Monser, V., Buchs, A., and Joost, H.G. (1997). Role of conserved arginine and glutamate residues on the cytosolic surface of glucose transporters for transporter function. *Biochemistry* 36, 12897-12902.

Scott, D.J., Kummer, L., Tremmel, D., and Plückthun, A. (2013). Stabilizing membrane proteins through protein engineering. *Current Opinion in Chemical Biology* 17, 427-435.



Seddon, A.M., Curnow, P., and Booth, P.J. (2004). Membrane proteins, lipids and detergents: not just a soap opera. *Biochimica et biophysica acta* 1666, 105-117.

Seibert, F.S., Linsdell, P., Loo, T.W., Hanrahan, J.W., Clarke, D.M., and Riordan, J.R. (1996). Disease-associated Mutations in the Fourth Cytoplasmic Loop of Cystic Fibrosis Transmembrane Conductance Regulator Compromise Biosynthetic Processing and Chloride Channel Activity. *Journal of Biological Chemistry* 271, 15139-15145.

Serohijos, A.W., Hegedus, T., Aleksandrov, A., He, L., Cui, L., Dokholyan, N., and Riordan, J. (2008). Phenylalanine-508 mediates a cytoplasmic-membrane domain contact in the CFTR 3D structure crucial to assembly and channel function. *Proceedings of the National Academy of Sciences* 105, 3256-3261.

Shak, S., Capon, D.J., Hellmiss, R., Marsters, S.A., and Baker, C.L. (1990). Recombinant human DNase I reduces the viscosity of cystic fibrosis sputum. *Proceedings of the National Academy of Sciences of the United States of America* 87, 9188-9192.

Sharma, R., Gupta, S., Ahmad, H., Ansari, G.A., and Awasthi, Y.C. (1990). Stimulation of a human erythrocyte membrane ATPase by glutathione conjugates. *Toxicol Appl Pharmacol* 104, 421-428.

Sheppard, D.N., and Welsh, M.J. (1999). Structure and function of the CFTR chloride channel. *Physiol Rev* 79, S23-45.

Singer, S.J., and Nicolson, G.L. (1972). The fluid mosaic model of the structure of cell membranes. *Science* 175, 720-731.

Smirnova, I., Kasho, V., and Kaback, H. (2011). Lactose permease and the alternating access mechanism. *Biochemistry* 50, 9684-9693.

Smith, S.O., Smith, C.S., and Bormann, B.J. (1996). Strong hydrogen bonding interactions involving a buried glutamic acid in the transmembrane sequence of the neu/erbB-2 receptor. *Nat Struct Biol* 3, 252-258.

Southern, K.W., Clancy, J.P., and Ranganathan, S. (2019). Aerosolized agents for airway clearance in cystic fibrosis. *Pediatric Pulmonology* 0.

Southern, K.W., Patel, S., Sinha, I.P., and Nevitt, S.J. (2018). Correctors (specific therapies for class II CFTR mutations) for cystic fibrosis. *Cochrane Database of Systematic Reviews*.

Spoonhower, K.A., and Davis, P.B. (2016). Epidemiology of Cystic Fibrosis. *Clinics in Chest Medicine* 37, 1-8.

Stein, W.D. (1986). *Transport and diffusion across cell membranes* (New York: Academic Press).

Stratford, Fiona L., Ramjeesingh, M., Cheung, Joanne C., Huan, L.-J.U.N., and Bear, Christine E. (2007). The Walker B motif of the second nucleotide-binding domain (NBD2) of CFTR plays a key role in ATPase activity by the NBD1-NBD2 heterodimer. *Biochemical Journal* 401, 581-586.

Stroud, Z., Hall, S.C.L., and Dafforn, T.R. (2018). Purification of membrane proteins free from conventional detergents: SMA, new polymers, new opportunities and new insights. *Methods* (San Diego, Calif).

Sun, C., Benlekber, S., Venkatakrishnan, P., Wang, Y., Hong, S., Hosler, J., Tajkhorshid, E., Rubinstein, J.L., and Gennis, R.B. (2018). Structure of the alternative complex III in a supercomplex with cytochrome oxidase. *Nature* 557, 123-126.

Sun, J., Bankston, J.R., Payandeh, J., Hinds, T.R., Zagotta, W.N., and Zheng, N. (2014). Crystal structure of the plant dual-affinity nitrate transporter NRT1.1. *Nature* 507, 73-77.

Swainsbury, D.J.K., Proctor, M.S., Hitchcock, A., Cartron, M.L., Qian, P., Martin, E.C., Jackson, P.J., Madsen, J., Armes, S.P., and Hunter, C.N. (2018). Probing the local lipid environment of the *Rhodobacter sphaeroides* cytochrome bc1 and *Synechocystis* sp. PCC 6803 cytochrome b6f complexes with styrene maleic acid. *Biochimica et biophysica acta* 1859, 215-225.

Szczesniak, R., Heltshe, S.L., Stanojevic, S., and Mayer-Hamblett, N. (2017). Use of FEV(1) in cystic fibrosis epidemiologic studies and clinical trials: A statistical perspective for the clinical researcher. *Journal of cystic fibrosis : official journal of the European Cystic Fibrosis Society* 16, 318-326.

Takakuwa, Y. (2000). Protein 4.1, a multifunctional protein of the erythrocyte membrane skeleton: structure and functions in erythrocytes and nonerythroid cells. *International journal of hematology* 72, 298-309.

Takakuwa, Y., and Manno, S. (1996). [Structure of erythrocyte membrane skeleton]. *Nippon Rinsho* 54, 2341-2347.

Takata, K., Kasahara, T., Kasahara, M., Ezaki, O., and Hirano, H. (1990). Erythrocyte/HepG2-type glucose transporter is concentrated in cells of blood-

tissue barriers. *Biochemical & Biophysical Research Communications* 173, 67-73.

Taylor, K.A., and Glaeser, R.M. (1974). Electron diffraction of frozen, hydrated protein crystals. *Science* 186, 1036-1037.

Taylor, K.A., and Glaeser, R.M. (1976). Electron microscopy of frozen hydrated biological specimens. *Journal of ultrastructure research* 55, 448-456.

Teem, J.L., Berger, H.A., Ostedgaard, L.S., Rich, D.P., Tsui, L.-C., and Welsh, M.J. (2007). Identification of revertants for the cystic fibrosis  $\Delta$ F508 mutation using STE6-CFTR chimeras in yeast. *Cell* 130, 335-346.

Teo, A.C.K., Lee, S.C., Pollock, N.L., Stroud, Z., Hall, S., Thakker, A., Pitt, A.R., Dafforn, T.R., Spickett, C.M., and Roper, D.I. (2019). Analysis of SMALP co-extracted phospholipids shows distinct membrane environments for three classes of bacterial membrane protein. *Scientific Reports* 9, 1813.

Thibodeau, P.H., Brautigam, C.A., Machius, M., and Thomas, P.J. (2005). Side chain and backbone contributions of Phe508 to CFTR folding. *Nature structural & molecular biology* 12, 10-16.

Thibodeau, P.H., Richardson, J.M., Wang, W., Millen, L., Watson, J., Mendoza, J.D., K., Fischman, S., Senderowitz, H., Lukacs, G.L., Kirk, K., *et al.* (2010). The Cystic Fibrosis-causing Mutation F508 Affects Multiple Steps in Cystic Fibrosis Transmembrane Conductance Regulator Biogenesis. *Journal of Biological Chemistry* 285, 35825-35835.

Thomas, J.L., Barton, S.W., and Tirrell, D.A. (1994). Membrane solubilization by a hydrophobic polyelectrolyte: surface activity and membrane binding. *Biophysical journal* 67, 1101-1106.

Thorens, B., and Mueckler, M. (2010). Glucose transporters in the 21st Century. *Am J Physiol Endocrinol Metab* 298, E141-145.

Tribet, C., Audebert, R., and Popot, J.-L. (1996). Amphipols: Polymers that keep membrane proteins soluble in aqueous solutions. *Proceedings of the National Academy of Sciences* 93, 15047-15050.

Tsui, L.-C. (1992). The spectrum of cystic fibrosis mutations. *Trends in Genetics* 8, 392-398.

Uhlen, M., Fagerberg, L., Hallstrom, B.M., Lindskog, C., Oksvold, P., Mardinoglu, A., Sivertsson, A., Kampf, C., Sjostedt, E., Asplund, A., *et al.* (2015). Proteomics. Tissue-based map of the human proteome. *Science* 347, 1260419.

Uldry, M., Steiner, P., Zurich, M.-G., Beguin, P., Hirling, H., Dolci, W., and Thorens, B. (2004). Regulated exocytosis of an H<sup>+</sup>/myo-inositol symporter at synapses and growth cones. *EMBO J* 23, 531-540.

Vaidehi, N., Grisshammer, R., and Tate, C.G. (2016). How Can Mutations Thermostabilize G-Protein-Coupled Receptors? *Trends Pharmacol Sci* 37, 37-46.

Vallièrès, E., and Elborn, J.S. (2014). Cystic fibrosis gene mutations: evaluation and assessment of disease severity. *Advances in Genomics and Genetics* 4, 161-172.

van 't Hag, L., Knoblich, K., Seabrook, S.A., Kirby, N.M., Mudie, S.T., Lau, D., Li, X., Gras, S.L., Mulet, X., Call, M.E., *et al.* (2016). Exploring the in meso crystallization mechanism by characterizing the lipid mesophase microenvironment during the growth of single transmembrane alpha-helical peptide crystals. *Philosophical transactions Series A, Mathematical, physical, and engineering sciences* 374.

van Meer, G., Voelker, D.R., and Feigenson, G.W. (2008). Membrane lipids: where they are and how they behave. *Nat Rev Mol Cell Biol* 9, 112-124.

Vargas, C., Arenas, R.C., Frotscher, E., and Keller, S. (2015). Nanoparticle self-assembly in mixtures of phospholipids with styrene/maleic acid copolymers or fluorinated surfactants. *Nanoscale* 7, 20685-20696.

Vergani, P., Lockless, S.W., Nairn, A.C., and Gadsby, D.C. (2005). CFTR channel opening by ATP-driven tight dimerization of its nucleotide-binding domains. *Nature* 433, 876-880.

Viviani, L., Harrison, M.J., Zolin, A., Haworth, C.S., and Floto, R.A. (2016). Epidemiology of nontuberculous mycobacteria (NTM) amongst individuals with cystic fibrosis (CF). *Journal of cystic fibrosis : official journal of the European Cystic Fibrosis Society* 15, 619-623.

von Heijne, G. (1992). Membrane protein structure prediction. Hydrophobicity analysis and the positive-inside rule. *J Mol Biol* 225, 487-494.

Walker, J. (2015). FDA Panel Backs Vertex Cystic-Fibrosis Drug Orkambi.

Wang, D., Pascual, J.M., Yang, H., Engelstad, K., Jhung, S., Sun, R.P., and De Vivo, D.C. (2005). Glut-1 deficiency syndrome: clinical, genetic, and therapeutic aspects. *Ann Neurol* 57, 111-118.

Wang, W., and Linsdell, P. (2012). Relative movements of transmembrane regions at the outer mouth of the cystic fibrosis transmembrane conductance regulator channel pore during channel gating. *J Biol Chem* 287, 32136-32146.

Wang, Y., Loo, T.W., Bartlett, M.C., and Clarke, D.M. (2007). Correctors promote maturation of cystic fibrosis transmembrane conductance regulator (CFTR)-processing mutants by binding to the protein. *J Biol Chem* 282, 33247-33251.

Ward, A., Reyes, C.L., Yu, J., Roth, C.B., and Chang, G. (2007). Flexibility in the ABC transporter MsbA: Alternating access with a twist. *Proceedings of the National Academy of Sciences of the United States of America* 104, 19005-19010.

Wark, P., and McDonald, V.M. (2018). Nebulised hypertonic saline for cystic fibrosis. *Cochrane Database of Systematic Reviews*.

Wasserman, D.H. (2009). Four grams of glucose. *American journal of physiology Endocrinology and metabolism* 296, E11-E21.

Wellberg, E.A., Johnson, S., Finlay-Schultz, J., Lewis, A.S., Terrell, K.L., Sartorius, C.A., Abel, E.D., Muller, W.J., and Anderson, S.M. (2016). The glucose transporter GLUT1 is required for ErbB2-induced mammary tumorigenesis. *Breast Cancer Research* 18, 131.

Welsh, M.J., and Smith, A.E. (1993a). Molecular mechanisms of CFTR chloride channel dysfunction in cystic fibrosis. *Cell* 73, 1251-1254.

Welsh, M.J., and Smith, A.E. (1993b). Molecular mechanisms of CFTR chloride channel dysfunction in cystic fibrosis. *Cell* 73, 1251-1254.

White, N.M., Jiang, D., Burgess, J.D., Bederman, I.R., Previs, S.F., and Kelley, T.J. (2007). Altered cholesterol homeostasis in cultured and in vivo models of cystic fibrosis. *American Journal of Physiology-Lung Cellular and Molecular Physiology* 292, L476-L486.

White, S.H. (2019). *Membrane Proteins of Known 3D Structure* (UC Irvine).

Widdas, W.F. (1952). Inability of diffusion to account for placental glucose transfer in the sheep and consideration of the kinetics of a possible carrier transfer. *J Physiol (London)* 118, 23–39.

Wilbrandt, E.M., Guensberg, E., and Lauener, J.u., H. (1947). *Helv Physiol Acta* 5, C20.

Wilkinson, D.J., Strong, T.V., Mansoura, M.K., Wood, D.L., Smith, S.S., Collins, F.S., and Dawson, D.C. (1997). CFTR activation: additive effects of stimulatory and inhibitory phosphorylation sites in the R domain. *Am J Physiol* 273, L127-133.

Wilson, T.H., and Lin, E.C. (1980). Evolution of membrane bioenergetics. *J Supramol Struct* 13, 421-446.

Winn, M.D., Ballard, C.C., Cowtan, K.D., Dodson, E.J., Emsley, P., Evans, P.R., Keegan, R.M., Krissinel, E.B., Leslie, A.G.W., McCoy, A., *et al.* (2011). Overview of the CCP4 suite and current developments. *Acta crystallographica Section D, Biological crystallography* 67, 235-242.

Wood, R., and Morgan, H. (1969). Regulation of sugar transport in avian erythrocytes. *J Biol Chem* 244, 1451-1460.

Wright (2009). Diseases of Renal Glucose Handling.

Wu, X., and Freeze, H.H. (2002). GLUT14, a duplicon of GLUT3, is specifically expressed in testis as alternative splice forms. *Genomics* 80, 553-557.

Xuong, N.-H., Milazzo, A.-C., LeBlanc, P., Duttweiler, F., Bouwer, J., Peltier, S., Ellisman, M., Denes, P., Bieser, F., Matis, H.S., *et al.* (2004). First use of a high-sensitivity active pixel sensor array as a detector for electron microscopy, Vol 5301 (SPIE).

Yan, N. (2017). A Glimpse of Membrane Transport through Structures-Advances in the Structural Biology of the GLUT Glucose Transporters. *J Mol Biol* 429, 2710-2725.

Yang, Z., Hildebrandt, E., Jiang, F., Aleksandrov, A.A., Khazanov, N., Zhou, Q., An, J., Mezzell, A.T., Xavier, B.M., Ding, H., *et al.* (2018). Structural stability of purified human CFTR is systematically improved by mutations in nucleotide binding domain 1. *Biochim Biophys Acta Biomembr* 1860, 1193-1204.

Yang, Z., Wang, C., Zhou, Q., An, J., Hildebrandt, E., Aleksandrov, A., Riordan, J., L Urbatsch, I., F Hunt, J., and G Brouillette, C. (2014). Membrane protein stability can be compromised by detergent interactions with the extramembranous soluble domains, Vol 23.

Yeagle, P.L. (2016). Chapter 13 - Membrane Transport. In *The Membranes of Cells* (Third Edition), P.L. Yeagle, ed. (Boston: Academic Press), pp. 335-378.

Zhang, J., Yu, Y.-C., Yeh, J.-T., and Hwang, T.-C. (2018a). Functional characterization reveals that zebrafish CFTR prefers to occupy closed channel conformations. *PloS one* *13*, e0209862-e0209862.

Zhang, J.Z., Behrooz, A., and Ismail-Beigi, F. (1999). Regulation of glucose transport by hypoxia. *Am J Kidney Dis* *34*, 189-202.

Zhang, K., and Liu, Z. (2018). A brief introduction of cryo-EM revolution—the Nobel Prize in Chemistry 2017. *Science China Life Sciences* *61*, 368-370.

Zhang, W., Liu, Y., Chen, X., and Bergmeier, S. (2010). Novel inhibitors of basal glucose transport as potential anticancer agents. *Bioorg Med Chem Lett* *20*, 2191-2194.

Zhang, Z., and Chen, J. (2016). Atomic Structure of the Cystic Fibrosis Transmembrane Conductance Regulator. *Cell* *167*, 1586-1597.e1589.

Zhang, Z., Liu, F., and Chen, J. (2017). Conformational Changes of CFTR upon Phosphorylation and ATP Binding. *Cell* *170*, 483-491.e488.

Zhang, Z., Liu, F., and Chen, J. (2018b). Molecular structure of the ATP-bound, phosphorylated human CFTR. *Proceedings of the National Academy of Sciences* *115*, 12757-12762.

Zhao, F., Ming, J., Zhou, Y., and Fan, L. (2016). Inhibition of Glut1 by WZB117 sensitizes radioresistant breast cancer cells to irradiation. *Cancer chemotherapy and pharmacology* *77*, 963-972.

Zhao, G., and London, E. (2006). An amino acid "transmembrane tendency" scale that approaches the theoretical limit to accuracy for prediction of transmembrane helices: relationship to biological hydrophobicity. *Protein science : a publication of the Protein Society* *15*, 1987-2001.

Zhenin, M., Noy, E., and Senderowitz, H. (2015). REMD Simulations Reveal the Dynamic Profile and Mechanism of Action of Deleterious, Rescuing, and Stabilizing Perturbations to NBD1 from CFTR. *Journal of chemical information and modeling* *55*, 2349-2364.

Zhong, Z., Wilson, K.L., and Dahl, K.N. (2010). Chapter 5 - Beyond Lamins: Other Structural Components of the Nucleoskeleton. In *Methods in Cell Biology*, G.V. Shivashankar, ed. (Academic Press), pp. 97-119.

Zhou, J.J., Li, M.S., Qi, J., and Linsdell, P. (2010). Regulation of conductance by the number of fixed positive charges in the intracellular vestibule of the CFTR chloride channel pore. *J Gen Physiol* *135*, 229-245.

Zoonens, M., Giusti, F., Zito, F., and Popot, J.-L. (2007). Dynamics of Membrane Protein/Amphipol Association Studied by Förster Resonance Energy Transfer: Implications for in Vitro Studies of Amphipol-Stabilized Membrane Proteins. *Biochemistry* 46, 10392-10404.

Zoonens, M., and Popot, J.-L. (2014a). Amphipols for Each Season. *The Journal of membrane biology* 247, 759-796.

Zoonens, M., and Popot, J.-L. (2014b). Amphipols for Each Season. *The Journal of Membrane Biology* 247, 759-796.

Zoonens, M., Zito, F., Martinez, K., and Popot, J.-L., eds. (2014). *Amphipols: A General Introduction and Some Protocols* (New York: Springer).

Zottola, R.J., Cloherty, E.K., Coderre, P.E., Hansen, A., Hebert, D.N., and Carruthers, A. (1995). Glucose transporter function is controlled by transporter oligomeric structure. A single, intramolecular disulfide promotes GLUT1 tetramerization. *Biochemistry* 34, 9734-9747.